Development of an original 10 kHz Ti : Sa regenerative cavity allowing 17 fs CEP stable 1 kHz TW-class amplification or wavelength tunability

Anna Golinelli

université PARIS-SACLAY

NNT : 2019SACLS018

Thèse de doctorat

Development of an original 10 kHz Ti:Sa regenerative cavity allowing 17 fs CEP stable 1 kHz TW-class amplification or wavelength tunability

Thèse de doctorat de l'Université Paris-Saclay
préparée à l'Université Paris-Sud

École doctorale n°572 Ondes et Matière (EDOM)
Spécialité de doctorat: Lasers, molécules, rayonnement atmosphérique

Thèse présentée et soutenue à l'Orme des Merisiers, le 21 Janvier 2019, par

Mme Anna Golinelli

Composition du Jury :

M. Salvatore Stagira Professeur associé, Politecnico di Milano	Rapporteur
Mme Aurélie Jullien Chargée de Recherche, CNRS (INPHYNI)	Rapporteuse
M. Marc Hanna Chargé de recherche, CNRS, (Laboratoire Charles Fabry)	Examinateur
M. Eric Cormier Professeur, Université de Bordeaux	Président
M. Milutin Kovacev Professeur associé, Hannover University	Examinateur
M. Jean-François Hergott Ingénieur - chercheur, CEA (LIDYL)	Directeur de thèse
Mme Xiaowei Chen Ingénieure Sénior, Amplitude Laser Group	Invitée

Acknowledgements

This manuscript crowns three years of stimulating challenges. First of all I want to express my deepest gratitude to two people who made this possible: my thesis director Jean-François Hergott and my supervisor Xiaowei Chen. Their constant help and strong expertise, the fruitful discussions and advices accompanied and definitely upgraded my work of these years. I particularly recognize and appreciate the comprehension and support demonstrated during the last months. I would like to thank the european network Medea, that financed the thesis and enriched it with international scientific exchanges, transversal formation opportunities and engaging activities.
Special thanks to Benoit Bussière and Emilien Gontier from Amplitude Laser Group for their priceless skills and competences: together with Xiaowei they taught me everything I know about laser operation and alignment and they have been (more than once) the first aid in laser-emergency cases. Their contagious enthusiasm creates an invaluable positive working environment. Thank also to all the R&D team of Amplitude, and to all the qualified and willing colleagues of different teams I had the opportunity to work with. Many thanks to Olivier Tcherbakoff and Pascal d'Oliveira, for the precious advices and help, to David Garzella for coaching, and to all the equipe SLIC of CEA for their warm welcoming in the group. I would like to thank Salvatore Stagira and Caterina Vozzi for welcoming me in their laboratory in Politecnico di Milano during two months and giving me the opportunity to enrich my PhD experience (and to revive my university years). I express my gratitude to the colleagues of the ATTO group for the scientific and non-scientific discussions, during a coffee break or an apero. A special mention to Christiana Alexandridi, with who I shared in the past months, beside the office, also the experience of writing our two thesis: chapter by chapter, one by one, we made it!
A special thought to my enthusiastic and always present friends and to my family, for being my model of courage, initiative and tireless fortitude.
My warmest thanks to Julius, for his exemplary and inspiring creativity, sharp brilliance and unstoppable vivacity that strongly support me.
...and to not forget anything and anybody, a special mention to Kamal!

Contents

French summary

Au cours de dix dernières années la Physique en champ-fort et en particulier la science attoseconde ont été l'objet d'un fort dèveloppement. La production d'impulsions laser énergétiques de courte durée à haute cadence et stabilisées en CEP (position de la porteuse par rapport au maximum de l'enveloppe temporelle) constitue la première étape pour accéder aux dynamiques ultra-rapides caractérisant l'interaction de la matière avec une source de lumière cohérente, intense et ultra-rapide. Le travail de cette thèse a consisté à améliorer les performances d'un système laser Ti:Sa à haute cadence (10 kHz) optimisé pour la génération des impulsions attosecondes. La production d'un rayonnment UVX optimal impose des exigences sur les performances du laser. Ces dernières incluent la courte durée d'impulsion ($<$ 20 fs), le taux de répétition élevé ($\geq$ 10 kHz) et un niveau d'énergie multi-millijoule, pour assurer une brillance significative du signal harmonique et réduire les temps d'acquisition des expériences associées. Un système laser CPA Ti:Sa utilisant des réseaux en reflection dans les modules dispersifs semble toujours être, pour le moment, le choix le plus approprié pour obtenir des impulsions à haute énergie, de courte durée, tout en maintenant la valeur d'intégrale B en sortie d'amplificateur final aussi faible que possible. Cependant, répondre à ces exigences implique la nécessité de résoudre deux difficultés principales au sein de l'amplification dans le Ti:Sa. D'une part, les effets thermiques dans le milieu amplificateur réduisent la puissance moyenne atteignable en sortie de la chaine laser lorsque les taux de répétition dépassent le kHz. D'autre part, le rétrécissement spectral par le gain induit par la configuration multi-passages des amplificateurs limite la largeur spectrale des impulsions amplifiées; plus particulièrement dans le cas d'une cavité régénérative la douzaine d'allers-retours dans le milieu amplificateur limite le spectre amplifié à une largeur mi-hauteur de l'ordre de 30 nm correspondant à une durée minimale d'impulsion de plus de 35 fs. Nous avons développé une nouvelle configuration de cavité régénérative fonctionnant à 10 kHz qui permet une meilleure gestion des effets thermiques dans le cristal. La nouveauté réside dans le design utilisant deux cristaux amplificateurs afin de répartir les effets thermiques. On peut ainsi pomper chaque cristal à sa puissance de pompe limite et multiplier par deux la puissance de pompe globale. La puissance extraite de l'amplificateur atteint près de 5 W en bande étroite (35 nm), soit près de trois fois la puissance extraite d'une cavité typique à cristal unique. La compensation du rétrécissement spectral par le gain est réalisée avec l'insertion d'un filtre acousto-optique de contrôle de gain programmable intra-cavité (Mazzler). Nous avons obtenu un élargissement du spectre jusqu'à 110 nm en $1/e^2$, impliquant une perte de puissance extraite; elle atteint alors 2.7 W (0.3% de stabilité RMS) pour 28.5 W de pompe. La large bande spectrale amplifiée permet une compression des impulsions à près de 17 fs. Cette courte durée d'impulsion, qui peut encore être réduite après un système de post-

compression à des durées de moins de 3 cycles optiques, implique la nécessité de contrôler le champ électrique à la cadence du laser afin de garantir une parfaite reproductibilité des impulsions et donc l'efficacité de la génération d'impulsions attosecondes isolées. Ce contrôle du champ électrique peut être réalisé en stabilisant la CEP tir-à-tir, effectué à l'aide d'un système de détection totalement analogique et d'une boucle de correction rapide appliquée à un actuateur acousto-optique présent dans le système laser. En sortie d'amplificateur, le bruit résiduel mesuré tir-à-tir est réduit à 210 mrad pendant trois heures, et 170 mrad sur une plus courte durée de 20 secondes. Paralèllement à ce mode de fonctionnement, nous avons démontré que l'amplificateur régénératif peut fonctionner efficacement en mode accordable. En plus du filtre programmable intra-cavité qui permet un profil de gain sur une large étendue spectrale un second filtre spectral programmable permet de sélectionner des spectres de 30 à 40 nm de largeur à mi-hauteur et de longueur d'onde centrale accordable des impulsions injectées dans l'amplificateur. Il est ainis possible de produire des impulions amplifiées avec une longueur d'onde centrale accordable dans une gamme de $\pm$50 nm autour de 800 nm et avec un niveau de précision nanométrique. Nous avons conçu et mis en fonctionnement un amplificateur multi-passages non-cryogéné à imagerie par lentille thermique pour accroître la puissance des impulsions jusqu'à 10 W à une cadence de 1 kHz (amplification de 200 J à 10 mJ). Le régime de forte saturation de l'amplificateur garantit une variation négligeable ($\pm$3% pic à pic) de la puissance des impulsions en sortie du module, face à une variation importante de la puissance en entrée ($\pm$25% pic à pic) en mode d'opération accordable. Associer ce front-end à double mode d'opération à une ligne d'amplification à refroidissement cryogénique permet d'atteindre des puissances au niveau TW, à la cadence de 1 kHz (16 mJ à 17.8 fs) avec une stabilisation en CEP (350 mrad de bruit résiduel tir-à-tir). Les éléments dispersifs comme l'étireur et le compresseur sont extrêmement sensible aux diverses vibrations imposant une forte dérive de la CEP. Les résultats expérimentaux obtenus sur les compresseurs et la compléxité de reproduire ces expériences sur les étireurs nous ont conduit à proposer une étude numérique de l'influence des diverses sources de vibration sur le bruit de CEP dans ces modules hautement dispersifs. La littérature propose des formules analytiques pour évaluer l'influence sur la CEP de perturbations appliquées à un couple des réseaux. Nous avons conçu une nouvelle approche numérique sur la base d'un logiciel de tracé de rayon commercial (Zemax) pour évaluer les variations de CEP dans tous types de modules dispersifs, même ceux qui, de conception plus complexe, ne peuvent pas être modélisés par un couple des réseaux. Notre approche numérique a d'abord été validée en utilisant un design de compresseur, qui peut être directement approximé par un couple de réseaux et dont la littérature fournit des formules pour évaluer l'impact des différentes perturbations sur le bruit de CEP. Une fois notre algorithme de calcul validé par la comparaison de nos résultats aux calculs analytiques, nous avons appliqué ce dernier à un étireur d'Öffner, pour lequel l'approximation à un couple de réseaux proposé par la littérature est trop forte. Nous avons démontré que la nouvelle approche numérique peut être appliquée à tous types de design et qu'elle permet d'évaluer l'impact sur la stabilité de CEP des diverses sources de perturbations, appliquées aux réseaux mais aussi aux diverses optiques composant le module.

Chapter 1

Introduction

Since ancient times, humans have been fascinated by the concept of light. The word *light* derives etymologically from the root *leuk*, corresponding to the ancient Greek word $\lambda\varepsilon\upsilon\kappa\acute{o}\varsigma$, meaning "bright, shining". Greeks had also another term to indicate light, $\varphi\tilde{\omega}\varsigma$, from the root $\varphi\alpha\acute{\iota}\nu\omega$, meaning "to bring to light, to reveal". Since the third century B.C. the Greek philosopher Plato gave an interpretation of light as a revealing element, associating it to the transcendent disclosing of knowledge to humans. The "revealing" symbolism of light became a recurrent theme in different religions across centuries and lands, identifying light with the divine epiphany[1], but also in art[2] and literature.

Besides the metaphysical meaning of light, the Greek philosopher Aristotle, in his work *Physics* dating from the third century B.C, gave one of the first scientific theory of light that is on record, associating it to one of the five constituent Elements of nature. Across the centuries light has been widely studied in its physical properties, from the corpuscular theory firstly proposed by Newton (17th century) and the undulatory theory by Huygens (published in 1690 in *Traité de la Lumière*), to the classical electromagnetic theory of Maxwell (end of 19th century) and the Quantum theory of Planck (1900).

Since the invention of the flash photography by Talbot in 1851, light pulses have been used to freeze the temporal evolution of physical phenomena, and study their dynamics. In 1866 the German physics Toepler, pioneer in the study of shock waves [1], used a spark discharge to create an acoustic wave in air, and a flash of light, synchronized to the spark, to take a picture of the acoustic wave. Varying the delay between the two events allowed to reconstruct the dynamics of the acoustic wave. Since the oscillation period of the acoustic wave is of the order of the ms, a μs flash is appropriate to monitor the whole dynamics of the wave evolution. In general, to detect the dynamics of a physical phenomenon, it is necessary to dispose of a light flash whose duration is equal or shorter than the process under analysis. The wish of understanding faster and faster natural processes pushed the technology to develop detection systems based on shorter and shorter light flashes. Nowadays, spectroscopy techniques that can capture events down to the attosecond time scale have been demonstrated, making it

[1] One can think about two religious architectures: the Saint-Chapelle (Paris, France 1248) and the Nasi-il-molk Mosque (Shiraz, Iran 1888). Built in completely different historical and geographical contests, their architecture is equally conceived around the idea of diffusing light

[2] Light in art recalls the mean to reach knowledge; cf. *Young man reading at candlelight* by Matthias Stom, 1628/1632, Nationalmuseum, Stockholm.

possible to follow the dynamics of the "birth of a photoelectron" [2].
What is the key factor that allowed to scale the temporal resolution from the shock waves to the motion of electrons time scale? If generating μs light pulses is possible with standard photographic flash, nanosecond light pulses became accessible only after the demonstration of the first solid state laser based on ruby in 1960 [3] and the validation of the Q-switching regime in 1962 [4]. Picosecond light pulses were demonstrated shortly later upon introduction of mode-locking technique in 1965 [5] and the first solid-state (ruby, Nd:YAG, Nd:glass) lasers emitting pulses of duration less than 100 ps. In 1976 mode-locking through saturable absorbers was applied to dye laser, allowing scaling the pulse duration down to 1 ps and later on, across 1980, the pulse duration of dye lasers reached 100 fs [6]. In parallel, new amplifier solid-state materials emerged, and among these the Ti:Sa crystal, characterized by enormous bandwidth that allowed to decrease the pulse duration below 100 fs. The discovery of Kerr-lens mode-locking (KLM) [7] in Ti:Sa laser [8] coupled with dispersion compensation through a pair of prisms [9] or chirped multilayer dielectric mirrors [10] revolutionized ultrafast laser technology. Compact mirror-dispersion-controlled (MDC) KLM Ti:Sa oscillators routinely generated sub 10-fs pulses [11, 12] with peak powers exceeding MW level [13, 14]. Figure 1.1a reproduces the evolution of passively-mode locked dye laser and Ti:Sa laser in terms of pulse duration from 1960 to 2000.

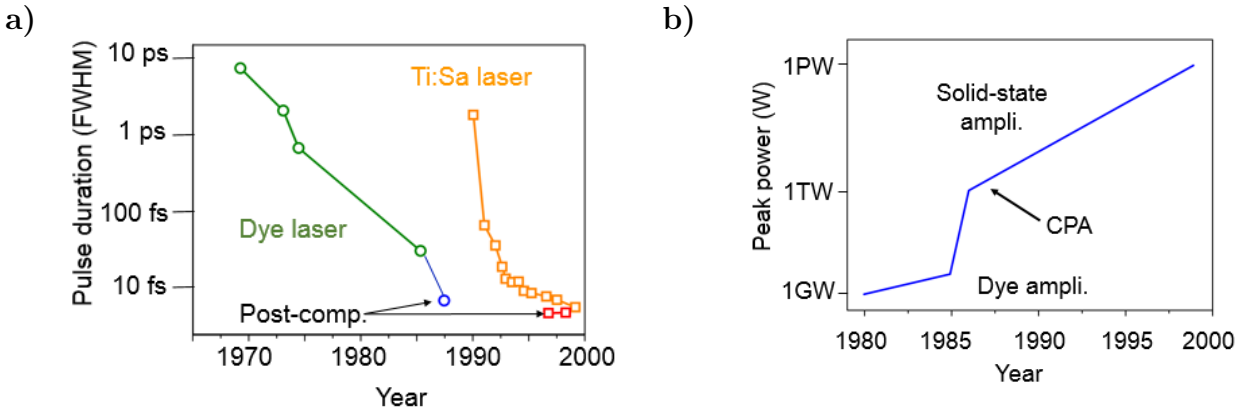

Figure 1.1: Evolution of a) pulse duration of dye and Ti:Sa laser and b) Peak power from 1960 to 2000.

In parallel to pulse duration scaling, the introduction in 1985 of the Chirped Pulse Amplification [15] made possible to increase the pulse peak power of several orders of magnitude (figure 1.1b), leading to nowadays commercially available systems at the PW (Petawatt) level.

As soon as multiterawatt laser sources became available, the strong field regime became easily accessible, quickly producing many demonstrations of high harmonics generation from interaction between atoms [16, 17], atoms clusters [18, 19] or molecules [20, 21] with the laser pulse. High harmonics generation is the key factor for producing XUV pulses, with pulse duration in the attosecond regime [22, 23]. Technological advancement in laser science became the prerequisite for accessing ultrafast phenomena.

Beside the above mentioned performances in terms of energy and pulse duration, the wide success of these lasers was also due to their possibility of fitting on a table-top system. Thus, at the beginning of the Century, ultrashort, high peak power laser system, exceeding 100 TW were commercially available, and many laboratories around the world were equipped with this kind of source [24].

The Ti:Sa CPA systems remained over the last decades the dominant driving sources for ultrafast high-intensity experiments. Not only high peak power but also high average power pulses were easily generated. The average power scales as the pulse energy and the repetition rate. Increasing the repetition rate to the kHz level ensures W-level average power for mJ level pulses, and brings together the advantage of decreasing the acquisition time and increasing the brightness of the signal from strong field experiments [25].
Further improvements in the performances of Ti:Sa sources are quite challenging due to mainly two effects. The first one is represented by thermal effects taking place in the amplification crystal [26, 27]. The accumulated heat inside the medium induces a change of the refractive index due to thermal and mechanical distortion of the material. This effect depends critically on the repetition rate and on the pumping energy [28] and in this terms it limits the average reachable power. Water cooling and cryogenically cooling of high power amplifier helped containing these detrimental effects [29]. Cryo cooled regenerative amplifier has been demonstrated delivering 26 W at 10 kHz [30]. The cryogenically cooling remains however a rather expensive and cumbersome solution, that affects the compactness of the amplification line.
The second effect deals with the lower limit for pulse duration. Gain narrowing in the amplification medium [31] limits the minimum pulse duration to 35-40 fs. Introduction of spectral filters for gain narrowing compensation [32, 33, 34] can solve this problem and decreases the pulse duration from 30 fs to 15 fs depending on the amplification level. The advent of the post-compression technique [35], via spectral broadening of the pulse by coupling it in hollow-core fibers filled with rare gas [36, 37, 38] or filamentation-based self-compression [39, 40] allowed to shorten even more the pulse duration. Pulses down to 4 fs at the mJ level were generated, and the road to the quasi-single cycle pulse became feasible.
As soon as the pulse duration approaches the single cycle regime, the envelope of the electric fields evolves almost as fast as the electric field itself. Since strong field applications depend directly on the electric field rather than on the envelope itself, they are significantly influenced by the so-called carrier-envelope phase (CEP). CEP stabilization, i.e. fixing the carrier wave position within the temporal envelope, is a key factor for producing isolated attosecond pulses [41].

An alternative technology to Ti:Sa is Optical Parametric Chirped Pulse Amplification (OPCPA)[42]. The architecture is equivalent to a CPA system but the amplification happens through energy transfer from a pump beam to the seed beam, mediated by a non-linear crystal, rather than through stimulated emission. As opposite to Ti:Sa laser system, no energy is directly stored in the amplification medium: the energy conversion happens instantaneously from pump to signal. Consequently no heat load is in principle accumulated in the amplification medium and the output power can be scaled without influence on the beam profile. The OPCPA amplification bandwidth spans over an octave, and single cycle pulses can be generated at different central wavelengths, depending on the non-linear crystal.

Nevertheless, OPCPA systems are limited by energy and average power of the commercially available pump lasers, and by parasitic effects showing up at high repetition rate. OPCPA technique largely benefits during last years from the development of pump lasers with good beam quality, which in the past represented a limiting factor. The last improvements in this field yields to 1 kHz OPCPA laser systems delivering pulses at the TW level in the mid-IR range [43] and in the IR range, close to 800 nm [44, 45]. OPCPA systems can easily achieve the mid-IR wavelength range, with benefits of strong field experiement. The performances of the OPCPA are similar to those of CPA Ti:Sa laser, and nowadays the two technologies are competing on the same field of high repetition rate, high average power laser systems. However, some implementation of the OPCPA technique cannot be totally decoupled from Ti:Sa improvements. We can find some example of OPCPA systems seeded by Ti:Sa laser[43], or using frequency doubled Ti:Sa emission as pump [45] or again consisting in a hybrid system [46, 47] comprising Ti:Sa amplifiers. For this reason, a continuous development of the Ti:Sa technique is of primary importance for next generation of high peak and average power lasers.
Fiber lasers [48, 49], where amplification occurs in a optical fiber doped with rare-earth elements (erbium, ytterbium, neodymium) deserve also to be mentioned. Thanks to the high surface to volume ratio and the small quantum defect, thermal effects are minimized with benefit for beam quality. However, the small saturation fluence compromises the energy storage and consequently the high energy operation. Recent advancements in fiber laser techniques together with efficient post-compression methods [50] allow nowadays to generate pulses with more than 100 μJ energy and 33 fs or even shorter pulse duration, thus suitable for accessing strong field applications.
The three technologies offer valid alternatives depending on the application.

The laser system that will be presented in this work has been conceived for being the most suitable Ti:Sa 10 kHz front-end for strong field applications. The thesis project has been founded by the MEDEA network[3] in partnership with the enterprise Amplitude Laser Group[4]. The practical goal of our work is to reach high pulse intensity within the first stages of amplification, thus simplifying the design of our source, making it accessible at lower price and allowing the possibility of coupling cryogenically cooled amplifiers for further amplification. Our method can be identified in conceiving an original front-end delivering mJ level pulses below 20 fs. As mentioned above, as the repetition rate exceeds the kHz level, non negligible thermal effects limit the amplification and new design for the regenerative amplifier must be adopted for scaling the energy to the mJ level in the first amplification stages. For ultrashort pulses gain narrowing effects must be considered and prevented with programmable spectral filters. Many efforts have also been dedicated to the characterization and stabilization of the CEP.

The manuscript is organized in two parts. The first, which consists in the first three chapters, is dedicated to fundamentals, methods and experimental demonstration of a high peak power, 10 kHz repetition rate Ti:Sa CPA laser, working in different spectral bandwidth

[3]http://www.medea-horizon2020.eu/
[4]http://http://www.amplitude-laser.com//

regimes. The second part deals with theory, simulation and results of CEP characterization, detection and stabilization of the laser system described in the first part.

Chapter 2: This chapter introduces the theoretical basics of femtosecond pulses propagation. The Chirped Pulse Amplification technique will be described detailing each modules. Finally the spectroscopic properties of Ti:Sa crystal will be resumed.

Chapter 3: In this chapter our 10 kHz Ti:Sa front-end will be presented. The performances of the newly designed double crystal regenerative amplifier for thermal lensing management will be compared to those of a standard regenerative amplifier. The new design allows to generate pulses three times more powerful than in standard design, reaching 5 W in narrow band mode. The method of spectral broadening through programmable filter will be presented together with the results of pulse compression with a grating based module, resulting in 17 fs short pulses. A section will be dedicated to spectral tuning at the regenerative amplifier output. We then present a complete water-cooled multipass Ti:Sa amplifier boosting the pulse power up to 10 W at 1 kHz repetition rate for 17 fs pulse duration, approaching the TW level. Spectral tunability is also demonstrated at the output of the regenerative cavity as well as at the output of 1 kHz amplifier. This allows the system to work in three different regimes: tunable, narrow band and broad band mode. Finally we present the results obtained by coupling the 10 kHz front-end output to two different cryogenically cooled amplifiers, for further amplification at 1 and 10 kHz repetition rate, leading to the new FAB1/10 laser equipping the ATTOlab facility.

Chapter 4: The thermal effect study of the regenerative cavity will be presented by reporting the results of thermal lens focal length measurements for different functioning regime of our double crystal regenerative amplifier.

Chapter 5: A review of theoretical basics of CEP detection and stabilization will be proposed, with a highlight on the active stabilization method.

Chapter 6: After describing the complete analog method used for CEP detection and stabilization, the experimental results of CEP stabilization of the 10 kHz front-end based on the newly-design double crystal cavity, with or without additional amplification stages, will be reported. A comparison between two compressor's configurations will be provided, in order to study the influence of the module's design on the CEP stability. Finally a numerical approach for predicting the CEP shift in grating based dispersive modules, allowing to study their sensitivity to environmental vibration sources, will be proposed.

Chapter 2

Femtosecond lasers

2.1 Introduction

Since laser invention in 1960, the introduction of the mode-locking technique in 1965 [5] triggered the development of Ultrafast Optics. Concentrating all the energy of the laser resonator in a time slot of hundreds of picoseconds provides an appropriate way to access physical processes that happen in the same time scale. The first generation of mode-locked laser used solid-state material such as ruby, Nd:YAG and Nd:Glass as gain media and the mode-locking was achieved either actively through external electronic control [51] or passively through saturable absorber [52], producing pulses with duration less than 100 ps.

The race to shorten the pulse duration gave raise in 1970 to the second generation of lasers, based on organic dye gain media [53]. These media exhibit large gain bandwidth, which, thanks to the mode locking technique through saturable absorber, allows generation of pulses with duration below the picosecond. Organic dye based amplifiers producing up to GW, 300 fs pulses were demonstrated [54]. Despite the above-mentioned demonstrations, not negligible drawbacks make the dye laser technology unsuitable for high power operation. One can cite short energy storage time and strong amplified spontaneous emission, competing with the laser emission and downgrading its profile, as some of the dye laser drawbacks. Moreover organic dyes are often toxic or carcinogen.

During the eighties the investigation of alternative suitable gain media resulted in new promising solid-state materials. Host crystals (YAG, sapphire, forsterite) doped with transition-metals (titanium, chromium) exhibit an incredibly broad gain bandwidth and small value of stimulated emission cross section (10^{-20} cm^2), holding the promise of breaking down the GW peak power limit imposed by dye lasers. The third generation of ultrafast lasers was rising.

However the direct amplification of picosecond pulses in solid-state media produces catastrophic effects due to an accumulated intensity-dependent wavefront distortion caused by the so called *Kerr effect*. When amplifying directly an ultrashort pulse, intensity values widely exceed the medium damage threshold long before the saturation fluence can be reached. Keeping the intensity at acceptable level while injecting enough energy for efficient amplification seemed an insurmountable problem. The solution came with the invention of the Chirped Pulse Amplification technique in 1985 [15], consisting in stretching the pulse du-

ration by a factor of thousand up to hundred thousand. This process does not change the pulse fluence but it lowers down the intensity. The pulse can be efficiently amplified from the nanojoule to the millijoule or even joule level without the risk of damaging the medium. Subsequently a dispersive module compresses the pulse down to as close as possible its initial duration.

The pioneer applications if this technique demonstrated the generation of single ps pulses amplified to the TW level [55].

In the early '90s, the introduction of high dispersive modules, as gratings-based stretcher [56] and compressor [57], allowed to quickly generate pulses as short as 100 fs, at the mJ level from table-top systems [17]. Peak powers above the TW level became easily achievable, and intensity at focus reached 10^{18} W/cm^2. The main actor of this fast rising of the peak power was the use of Titanium Sapphire as gain medium thanks to its broad gain bandwidth.

The promise of increasing the peak power triggered many advances in each of the CPA module. Aberration free stretcher [58] and compressor [59] associated to spectral shaping made possible to push the Titanium Sapphire amplifiers to the multiterawatt level in the 30 fs regime, limited to 10 Hz repetition rate [60]. The exceptional thermo-optical properties of the Ti:Sa made quickly possible to implement chirped pulse amplification up to the kHz regime.

This chapter will introduce the fundamentals of femtosecond laser systems based on Titanium Sapphire gain medium. The principles of light matter interaction will be firstly discussed, focusing on femtosecond pulse propagation. The Chirped Pulse Amplification will be introduced and detailed. Finally, the main spectroscopic properties of the Titanium Sapphire (Ti:Sa) crystal will be described.

2.2 Femtosecond pulses

2.2.1 Formalism

Before discussing the interaction between an ultrashort pulse and matter, it is necessary to introduce some relevant physical quantities that will be mentioned in the following chapters. The electric field of a short pulse can be written as (bold letters indicate a vector notation):

$$\boldsymbol{E}(t) = \boldsymbol{E}_0(t)cos[\omega_0 t + \varphi_{ce}] \tag{2.1}$$

A short pulse is defined as the product of two functions: the carrier, a sinusoidal wave that oscillate at the frequency ω_0 and an envelope $E_0(t)$, that is defined as a packet of waves and is localized where all the waves of its spectrum interact constructively. The position of the carrier wave with respect to the maximum of the envelope is defined as the *Carrier Envelope Phase* (CEP) symbolized by φ_{ce}. In first approximation the envelope is slowly varying compared with the carrier and it modulates the carrier defining the temporal and spatial profile of the pulse.

In the following text, the electric field is referenced to using the complex notation omitting the real part operator

$$E(t) = E_0(t)e^{i(\omega_0 t+\varphi_{ce})} \tag{2.2}$$

The electric field of equation (2.2) is in time-domain; the same quantity can be described in the frequency domain by Fourier-transforming the time electric field:

$$\tilde{E}(\omega) = FT\{E(t)\} = \int_{-\infty}^{+\infty} E(t)e^{-i\omega t}dt \tag{2.3}$$

The intensity of the pulse is defined from the amplitude of the envelope and is measured in W/cm^2:

$$I(t) = \frac{1}{2}\varepsilon_0 cn|E_0(t)|^2 \qquad I(\omega) = \frac{1}{2}\varepsilon_0 cn|E_0(\omega)|^2 \tag{2.4}$$

where ε_0 is the vacuum permittivity, c is the speed of light and n is the refractive index of the propagation medium.
For a Gaussian pulse, the intensity can be expressed as:

$$I(t) = E_0^2 e^{-\left(\frac{t}{\tau_p}\right)^2} = E_0^2 e^{-2\left(\frac{t}{\Delta t_0}\right)^2} = E_0^2 e^{-4ln2\left(\frac{t}{\Delta T_0}\right)^2} \tag{2.5}$$

where τ_p is the half width at 1/e of the intensity, Δt_0 is the half width at 1/e^2 and ΔT_0 is the full width half maximum (FWHM). The different durations are correlated as follow:

$$\Delta T_0 = 2\sqrt{ln2}\tau_p = \sqrt{2ln2}\Delta t_0 \tag{2.6}$$

The pulse duration is defined as the FWHM of the intensity. For the Fourier theorem, the pulse spectral content defines the shortest envelope duration (*transform limited duration*) according to the relation:

$$\Delta T_0 \Delta\nu \geq 2\sqrt{ln2}/\pi$$

where $\Delta\nu$ is the FWHM of the spectral intensity in the frequency domain.
The fluence (J/cm^2) is defined as the integral of the intensity in time:

$$F(t) = \int_{-\infty}^{t} I(\tau)d\tau$$

The peak power (W) is the integral of the intensity in surface:

$$P(t) = \int\int I(x,y,t)dxdy$$

The energy (J) is the integral of the intensity in surface and in time:

$$E = \int\int\int I(x,y,t)dxdydt$$

2.2.2 Light matter interaction

The propagation of light in a medium is described by a set of partial differential equations also known as the Maxwell equations:

$$\begin{cases} \nabla \cdot \mathbf{D} = \rho & \nabla \times \mathbf{E} = -\dfrac{\partial \mathbf{B}}{\partial t} \\ \nabla \cdot \mathbf{B} = 0 & \nabla \times \mathbf{H} = \mathbf{J} + \dfrac{\partial \mathbf{D}}{\partial t} \end{cases} \tag{2.7}$$

where ρ and $\mathbf{J}$, known as charge and as current density, are the sources of the electric field in the material. Vectors magnetic induction $\mathbf{B}$ and electric induction $\mathbf{D}$ are described by following equations:

$$\begin{cases} \mathbf{D} = \varepsilon_0 \mathbf{E} + \mathbf{P} \\ \mathbf{B} = \mu_0 (\mathbf{H} + \mathbf{M}) \end{cases} \tag{2.8}$$

ε_0 and μ_0 are the vaccum permittivity and permeability, vectors $\mathbf{E}$ and $\mathbf{H}$ are the electric and magnetic fields and vectors $\mathbf{P}$ and $\mathbf{M}$ the electric polarization and magnetization fields. In order to simplify the equations, a set of hypothesis is assumed: the light propagates in an isotropic material, without charge density or currents ($\rho = 0$ and $\mathbf{J} = 0$); the material behaves like in vacuum in terms of magnetization field ($\mathbf{M} = 0$).

The interaction between light and matter is defined by the electrical properties of the material and an insight of these properties is proposed here. When the electric field $\mathbf{E}$ associated with the light radiation interacts with the dielectric medium, it induces the formation of oriented dipoles. The electronic distribution is modified and it acts as a source of electric field inside the medium. This phenomenon is macroscopically described by the polarization field $\mathbf{P}$. In the case of non-intense incident electric field the polarization can be described by the following formula:

$$\mathbf{P}(\omega) = (\varepsilon_r(\omega) - 1)\varepsilon_0 \mathbf{E}(\omega) \tag{2.9}$$

with ε_r, the relative permittivity of the material. If we define the electric susceptibility tensor as $\chi_e(\omega) = \varepsilon_r(\omega) - 1$ then

$$\mathbf{P}(\omega) = \chi_e(\omega)\varepsilon_0 \mathbf{E}(\omega) \tag{2.10}$$

From the definition of $\chi_e(\omega)$ it is also possible to derive the definition of the refractive index:

$$n(\omega) = \sqrt{1 + \chi_e(\omega)} = \sqrt{\varepsilon_r} \tag{2.11}$$

The frequency dependence of the refractive index is the source of the dispersive nature of the material. Dispersion will be discussed further in this chapter.
In presence of intense electric field, higher order terms, depending non-linearly on the electric field, cannot be neglected and the definition of the polarization becomes:

$$\mathbf{P} = \varepsilon_0 [\chi_e^{(1)} \mathbf{E} + \chi_e^{(2)} \mathbf{E}^2 + \chi_e^{(3)} \mathbf{E}^3 + ...] \tag{2.12}$$

In general, for intense electric field, the polarization can be defined as the sum of two terms: a linear one, depending linearly on the electric field, and a non-linear one, depending on increasing powers of the electric field.

$$\mathbf{P} = \mathbf{P}_L + \mathbf{P}_{NL} \tag{2.13}$$

With the above-mentioned hypothesis the system of equations (2.7) can be developed as the *wave equation*

$$\nabla^2\mathbf{E} = \frac{1}{c_0^2}\frac{\partial^2\mathbf{E}}{\partial t^2} + \mu_0\frac{\partial^2\mathbf{P}}{\partial t^2} \tag{2.14}$$

where $c_0 = \dfrac{1}{\sqrt{\mu_0\varepsilon_0}}$ is the speed of light in vacuum.
This equation can be solved for short pulses propagating in a medium with linear and non linear response. Further approximations are needed to simplify the problem and an expression for the electric field of the pulse and polarization must be proposed. The electric field is assumed to propagate in the z-direction (scalar approximation) and is polarized and constant in the xy-plane (plane wave). The wave equation can now be written as follows:

$$\frac{\partial^2 E(z,t)}{\partial z^2} - \frac{1}{c_0^2}\frac{\partial^2 E(z,t)}{\partial t^2} = \mu_0\frac{\partial^2 P_L(z,t)}{\partial t^2} \tag{2.15}$$

In order to solve the equation (2.15), we need to assume an analytical expression for the pulse's electric field. Referring to equation (2.2), in the particular case of an electric field linearly polarized along the y direction and propagating along the z direction, the electric field can be written as follows:

$$E(z,t) = E_0(z,t)e^{i(\omega_0 t - k_0 z)} \tag{2.16}$$

where $k_0 = \dfrac{2\pi}{\lambda}n(\omega_0) = \dfrac{\omega_0}{c_0}n(\omega_0)$ is the wave vector. The same formalism can be adopted for the polarization fields:

$$\begin{cases} P_L(z,t) = p_l(z,t)e^{i(\omega_0 t - k_0 z)} \\ P_{NL}(z,t) = p_{nl}(z,t)e^{i(\omega_0 t - k_p z)} \end{cases} \tag{2.17}$$

where the wave vector of the non linear polarization k_p is in general different from the wave vector of the linear polarization. We proceed applying the Fourier transform to the equation (2.16) and (2.17) in order to switch to the frequency domain:

$$\begin{cases} \widetilde{E}(z,\omega) = \widetilde{E}_0(z,\omega')e^{ik_0 z} \\ \widetilde{P}_L(z,\omega) = \widetilde{p}_l(z,\omega')e^{ik_0 z} \\ \widetilde{P}_{NL}(z,\omega) = \widetilde{p}_{nl}(z,\omega')e^{ik_p z} \end{cases} \tag{2.18}$$

where $\omega' = \omega - \omega_0$. We now substitute the equations (2.18) in the wave equation (2.15) previously Fourier-transformed:

$$e^{-ik_0 z}\left[\frac{\partial^2\widetilde{E}_0}{\partial z^2} - 2ik_0\frac{\partial\widetilde{E}_0}{\partial z} - k_0^2\tilde{E}_0\right] + \frac{\omega^2}{c_0^2}e^{-ik_0 z}\widetilde{E}_0 = -\mu_0\omega^2 p_l e^{-ik_0 z} - \mu_0\omega^2 p_{nl}e^{-ik_p z} \tag{2.19}$$

We can unfold the envelope of the linear polarization term remembering that:

$$\begin{cases} \widetilde{P}_L(z,\omega) = \widetilde{p}_l(z,\omega')e^{ik_0 z}, & \text{from (2.18)} \\ \widetilde{P}_L(z,\omega) = \varepsilon_0[n_0^2(\omega) - 1]\widetilde{E_0}(z,\omega')e^{-ik_0 z}, & \text{from (2.9) and (2.18)} \end{cases} \tag{2.20}$$

then $\widetilde{p}_l(z,\omega') = \varepsilon_0[n_0^2(\omega)-1]\widetilde{E}_0(z,\omega')$.
In the *slowly varying envelope approximation* we consider negligible the envelope variations that happen in a space of the order of the carrier wavelength, leading to:

$$\frac{\partial^2 \widetilde{E}_0}{\partial z^2} \ll \frac{2\pi}{\lambda_0}\frac{\partial \widetilde{E}_0}{\partial z} \tag{2.21}$$

The equation (2.19) can finally be written in a more compact way:

$$-2ik_0\frac{\partial \widetilde{E}_0}{\partial z} + [k^2(\omega)-k_0^2]\widetilde{E}_0 = -\mu_0\omega_0^2\tilde{p}_{nl}e^{-i(k_p-k_0)z} \tag{2.22}$$

2.2.3 Propagation in media with linear response to the electric field of the pulse: dispersion

Until now we assumed a general description of the polarization comprising a linear and a non linear terms. The following section will analyse the propagation in a linear medium: the polarization can be described by the single linear term and the wave equation (2.22) can be further simplified:

$$-2ik_0\frac{\partial \widetilde{E}_0}{\partial z} + [k^2(\omega)-k_0^2]\widetilde{E}_0 = 0 \tag{2.23}$$

Remembering that $k(\omega) = \dfrac{\omega}{c}n(\omega)$ and that the spectrum of the pulse is centred at ω_0, if $n(\omega)$ is slowly varying with the frequency, the difference between k_0 and $k(\omega)$ is small and the following approximations can be used:

$$k^2(\omega)-k_0^2 = [k(\omega)-k_0][k(\omega)+k_0] \simeq 2k_0[k(\omega)-k_0] \tag{2.24}$$

and

$$\begin{aligned} k(\omega) &\simeq \sum_{n=0}^{\infty}\frac{k^{(n)}(\omega_0)}{n!}(\omega-\omega_0)^n \\ &\simeq k(\omega_0) + \left.\frac{\partial k}{\partial\omega}\right|_{\omega_0}(\omega-\omega_0) + \frac{1}{2!}\left.\frac{\partial^2 k}{\partial\omega^2}\right|_{\omega_0}(\omega-\omega_0)^2 + \frac{1}{3!}\left.\frac{\partial^3 k}{\partial\omega^3}\right|_{\omega_0}(\omega-\omega_0)^3 + ... \end{aligned} \tag{2.25}$$

that is the Taylor expansion of $k(\omega)$.
Further physical quantities may now be introduced for describing the pulse propagation, before substituting these approximations in the wave equation. The propagation on the medium has a direct influence on the phase of each single spectral component of the pulse. Considering that for a specific spectral component ω the phase can be written as $\varphi(\omega) = k(\omega)z$, then:

$$\begin{aligned} \varphi(\omega) &\simeq \sum_{n=0}^{\infty}\frac{\varphi^{(n)}(\omega_0)}{n!}(\omega-\omega_0)^n \\ &\simeq \varphi(\omega_0) + \left.\frac{\partial \varphi}{\partial\omega}\right|_{\omega_0}(\omega-\omega_0) + \frac{1}{2!}\left.\frac{\partial^2 \varphi}{\partial\omega^2}\right|_{\omega_0}(\omega-\omega_0)^2 + \frac{1}{3!}\left.\frac{\partial^3 \varphi}{\partial\omega^3}\right|_{\omega_0}(\omega-\omega_0)^3 + ... \end{aligned} \tag{2.26}$$

The *phase velocity* is the speed rate at which the wavefront of a single wave, defined by a specific value of frequency ω and wave vector k, propagates in space:

$$v_p = \frac{\omega}{k} = \frac{c_0}{n(\omega)} \tag{2.27}$$

Waves with different frequencies propagate with different velocities due to the dependency of the medium's refractive index on the frequency. A light pulse is described as the product of a carrier, with a defined frequency ω_0 propagating at $v_p(\omega_0)$, and an envelope. Since this last one is not described by a single wave but rather by a packet of waves, its propagation cannot be defined by a phase velocity but rather by the *group velocity*:

$$v_g = \frac{\partial \omega}{\partial k} \tag{2.28}$$

that is the reciprocal of the second term of the Taylor expansion for $k(\omega)$. The propagation in a medium causes the so called *dispersion*: different spectral components propagate with different velocities and the pulse stretches in time. This temporal distortion can be quantified by the *group velocity dispersion (GVD)*:

$$GVD = \left.\frac{\partial^2 k}{\partial \omega^2}\right|_{\omega_0} = \frac{\partial}{\partial \omega}\frac{1}{v_g} \tag{2.29}$$

In terms of phase, the effects of the propagation can be evaluated by each term of the Taylor series.

2.2.3.1 First order dispersion

At the first order, the propagation of the pulse over a defined length simply introduces a delay in the spectral components; the time interval that the pulse takes to travel a certain length L is quantified by the *group delay*:

$$\tau_g = \left.\frac{\partial \varphi}{\partial \omega}\right|_{\omega_0} \tag{2.30}$$

The group delay does not induce any deformation in the shape of the envelope. If the propagation medium is not dispersive over its length L then the phase varies linearly with the frequency and the group delay is constant for all spectral components.

2.2.3.2 Second order dispersion

On the contrary the second derivative of the phase quantifies the stretching factor that the pulse undergoes due to second order dispersion, i.e. due to propagation through a dispersive medium of length L; this quantity is called *group delay dispersion (GDD)*:

$$GDD = \left.\frac{\partial^2 \varphi}{\partial \omega^2}\right|_{\omega_0} = GVD \cdot L \tag{2.31}$$

The effect of the second order dispersion can be demonstrated by solving the wave equation (2.23), considering the second order of the Taylor expansion of $k(\omega)$. The equation (2.24) can be re-written:

$$k^2(\omega) - k_0^2 \simeq 2k_0 \left[\frac{1}{v_g}(\omega - \omega_0) + \frac{GVD}{2}(\omega - \omega_0)^2 \right] \tag{2.32}$$

and the wave equation is then simplified to the *parabolic equation*:

$$\frac{\partial \tilde{E}_0}{\partial z} = -i\frac{GVD}{2}\omega^2 \tilde{E}_0 \tag{2.33}$$

If the propagation medium is not dispersive and its refractive index is constant then :

$$\frac{\partial k}{\partial \omega} = \frac{\partial}{\partial \omega}\left[\frac{\omega}{c_0}n\right] = \frac{n}{c_0} \Longrightarrow GVD = \frac{\partial^2 k}{\partial \omega^2} = 0 \tag{2.34}$$

and the envelope does not exhibit any deformation since $\dfrac{\partial \tilde{E}_0}{\partial z} = 0$.
In order to solve the parabolic equation we assume that before propagation ($z = 0$) the envelope is described by a Gaussian shape with temporal width τ_p at 1/e of the intensity (see equation (2.6)):

$$\tilde{E}_0(0, \omega) = \sqrt{2\pi}\tau_p e^{-\dfrac{\omega^2 \tau_p^2}{2}} \tag{2.35}$$

After integrating the parabolic equation (2.33) over the propagation length z and substituting the envelope equation (2.35), the pulse envelope after propagation becomes:

$$\tilde{E}_0(z, \omega) = A_0\sqrt{2\pi}\tau_p e^{-\dfrac{\omega^2}{2}(\tau_p^2 + GDD)} \tag{2.36}$$

and in time domain:

$$E_0(z,t) = \frac{A_0\tau_p}{\sqrt{\tau_p^2 + iGDD}} \underbrace{e^{-\dfrac{t^2\tau_p^2}{2(\tau_p^4 + GDD^2)}}}_{\text{amplitude}} \underbrace{e^{-\dfrac{i}{2}\dfrac{t^2 GDD}{(\tau_p^4 + GDD^2)}}}_{\text{phase}} \tag{2.37}$$

As underlined in the last equation, the dispersion influences the envelope adding an amplitude and a phase term. The amplitude term can be re-written introducing the pulse duration after propagation τ_{out}:

$$\frac{t^2\tau_p^2}{2(\tau_p^4 + GDD^2)} = \frac{t^2}{2\tau_{out}^2} \Longrightarrow \tau_{out} = \tau_p\sqrt{1 + \left(\frac{GDD}{\tau_p^2}\right)^2} \tag{2.38}$$

It is often more convenient to describe the temporal profile of the pulse in terms of FWHM:

$$\Delta T_{out} = \Delta T_0\sqrt{1 + 16(ln2)^2\left(\frac{GDD}{\Delta T_0^2}\right)^2} \tag{2.39}$$

We can conclude that, for a defined propagation medium, the shorter the input pulse, the more important is the effect of dispersion.

We consider now the phase term:

$$\phi = \frac{t^2 GDD}{2(\tau_p^4 + GDD^2)} \tag{2.40}$$

which allows to re-write the pulse electric field after propagation as follows:

$$E(z,t) = E_0(z,t)e^{i[\omega_0 t + \phi(t) - k_0 z]} = E_0(z,t)e^{i\Phi(t)} \tag{2.41}$$

Considering that the *instantaneous frequency* $\omega_i(t)$ is the derivative of the phase:

$$\omega_i(t) = \frac{d\Phi}{dt} = \omega_0 + \frac{t\ GDD}{\tau_p^4 + GDD^2} \tag{2.42}$$

in the case of dispersion, different spectral components exit the propagation medium at different moments; this effect is called *frequency chirp* and is the reason why the pulse results stretched after propagation. If the GDD is positive, at the output of the propagation medium the instantaneous frequency increases with increasing time: longer wavelength components of the spectrum propagate faster than shorter wavelengths and the pulse is *up-chirped*. The opposite case corresponds to a negative value of GDD and the pulse is *down-chirped*. Figure

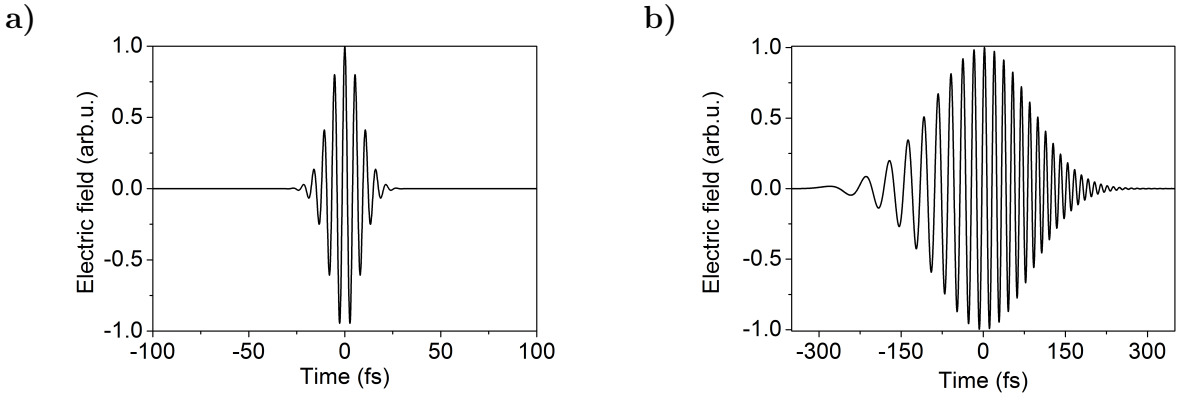

Figure 2.1: Electric fields for a 50 nm broad pulse (FWHM) centred at 800nm. a) Transform limited pulse, b) *upchirped* pulse induced by a GDD of 1000 fs^2.

2.1 represents the electric fields of a 50 nm broad pulse centred at 800 nm in the transform limited condition (2.1a) and after a propagation through a medium inducing a GDD of 1000 fs^2 (2.1b). Figure 2.2 shows the effect of the GDD on the temporal profile of an ultrashort pulse. Figure 2.2a represents the spectral content of a 40 nm broad pulse (FWHM) centred at 800 nm (black line). The dashed line represents its spectral phase after propagation through 1 cm of SF10, which introduces a GDD of 1565 fs^2. The stretching of the temporal profile due to the second order dispersion is shown in figure 2.2b: the black line corresponds to the transform limited pulse duration, 23 fs at FWHM, and the dashed line is the profile after propagation (185 fs FWHM).

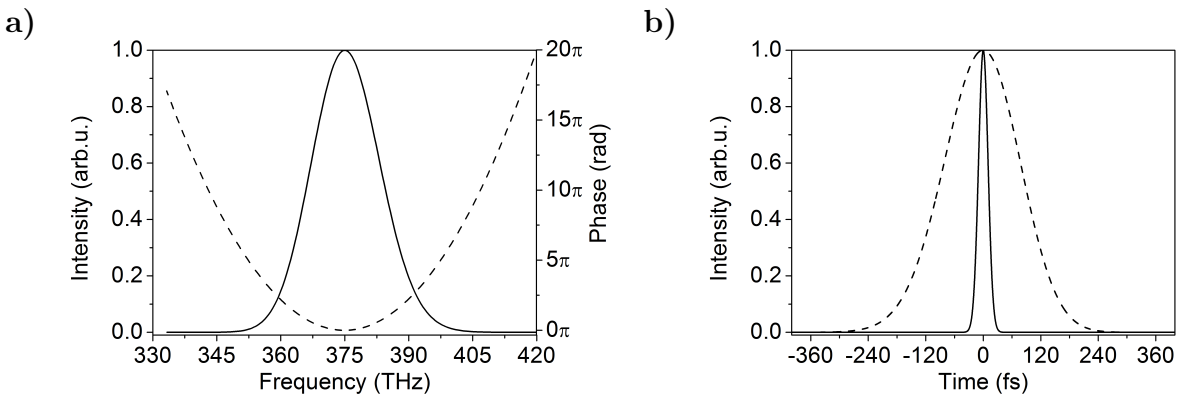

Figure 2.2: a) Pulse spectrum (black line) centered at 800 nm with 40 nm bandwidth (FWHM) and spectral phase (dashed line) after propagation through 1 cm of SF10, inducing $GDD = 1565$ fs^2. b) Corresponding temporal profiles in case of flat phase, equivalent to a transform limited pulse (black line) and in case of parabolic phase of figure 2.2a (dashed line).

2.2.3.3 Third order dispersion and higher orders

The wave equation has been solved for the wave vector $k(\omega)$ approximated to the second order of the Taylor polynomial. However, the broader the spectrum, the more important are the effects of higher order dispersion in defining the temporal profile of the pulse.
The *third order dispersion (TOD)* is defined as:

$$TOD = \left.\frac{\partial^3 \varphi}{\partial \omega^3}\right|_{\omega_0} \tag{2.43}$$

This dispersion has a small effect on the pulse duration after propagation but it can affect the temporal profile of the pulse. It induces a modulation on the tails of the gaussian and reduces the slope of the raising or descenting front, according to the sign. Figure 2.3 shows the effect of a third order phase (dashed line on figure 2.3a) on a 80 nm broad spectrum centred at 800 nm (black line on figure 2.3a). The phase shows a cubic trend with frequencies, corresponding to a TOD equal to 4100 fs^3 due to propagation through 4 cm of SF10. As shown on figure 2.3b, the temporal stretching factor induced on the 11 fs transform limited pulse (black line) is negligible whereas modulations appear on the rising temporal front and a slope smoothing on the descending front (dashed line).
Higher order dispersion terms induce as well distortions of the temporal profile that represent a limit to the pulse compression down to the minimal pulse duration.

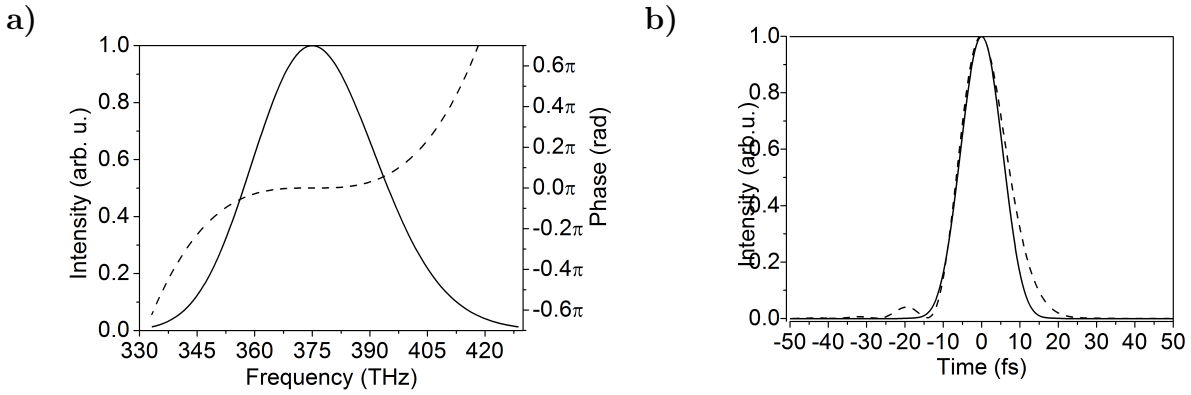

Figure 2.3: Temporal profile distortion induced on a 80 nm width pulse centred at 800 nm by $TOD = 4100fs^3$, equivalent to propagation through 4 cm of SF10.a) Pulse spectrum (black line) centered at 800 nm, 80 nm bandwidth (FWHM), and spectral phase (dashed line) after propagation through 4 cm of SF10, inducing $TOD = 4100fs^3$. b) Corresponding temporal profiles in case of flat phase, equivalent to a transform limited pulse (black line) and in case of cubic phase of figure 2.3a (dashed line).

2.2.3.4 Dispersion and refractive index

In the previous discussion it has been underlined that the origin of dispersion is the dependency of the medium refractive index on the frequency. It is straightforward that each terms of dispersion can be developed once the function $n = n(\omega)$ or equivalently $n = n(\lambda)$ is known.
The *Sellmeier equation* provides an empirical relationship between a specific material refractive index and the wavelength:

$$n(\lambda)^2 = 1 + \frac{B_1\lambda^2}{\lambda^2 - C_1} + \frac{B_2\lambda^2}{\lambda^2 - C_2} + \frac{B_3\lambda^2}{\lambda^2 - C_3} \tag{2.44}$$

where $B_{1,2,3}$ and $C_{1,2,3}$ are experimentally determined coefficients.
It is possible now to re-write each term of the phase expansion as a function of the refractive index of a material with length L.

$$\begin{aligned} \tau_g &= \frac{\partial\varphi}{\partial\omega} = \frac{L}{c_0}\left(n - \lambda\frac{dn}{d\lambda}\right) \\ GDD &= \frac{\partial^2\varphi}{\partial\omega^2} = \left(\frac{L\lambda^3}{2\pi c_0^2}\right)\frac{\partial^2 n}{\partial\lambda^2} \\ TOD &= \frac{\partial^3\varphi}{\partial\omega^3} = -\frac{L\lambda^4}{4\pi c_0^3}\left(3\frac{\partial^2 n}{\partial\lambda^2} + \lambda\frac{\partial^3 n}{\partial\lambda^3}\right) \end{aligned} \tag{2.45}$$

2.2.4 Propagation in media with non linear response to the electric field of the pulse

If the electric field interacting with the material is intense, higher order terms of polarization influence the interaction between light and matter. The material polarization can then be described as follows:

$$\mathbf{P} = \underbrace{\varepsilon_0 \chi_e^{(1)} \mathbf{E}}_{P_L} + \underbrace{\varepsilon_0 \chi_e^{(2)} \mathbf{E}^2 + \varepsilon_0 \chi_e^{(3)} \mathbf{E}^3 + ..}_{P_{NL}} \tag{2.46}$$

where the linear and non linear terms are underlined.

In the previous section we discussed the effect induced by the linear term of polarization. In the following section we will discuss the effect of the non linear term on the pulse propagating in the material.

Most of the material are centrosymmetric, meaning that the direction of the polarization changes according to the direction of the incident electric field. As a consequence, even terms of susceptibility have a zero value and the polarization equation can be written as:

$$\mathbf{P} = \varepsilon_0 \chi_e^{(1)} \mathbf{E} + + \varepsilon_0 \chi_e^{(3)} \mathbf{E}^3 \tag{2.47}$$

The interaction of an intense field with the material implies that the refractive index depends on the field intensity according to the expression:

$$n(I) = n_0 + n_2 I(z,t) \tag{2.48}$$

where n_0 is the linear refractive index, n_2 is the second-order nonlinear refractive index that depends on $\chi^{(3)}$ and I is the radiation intensity. The dependency of the refractive index on the pulse intensity is called *Kerr effect*.

The pulse intensity is assumed to be described by a Gaussian distribution in time and space. Subsequently the refractive index inherits the time and space dependency from the intensity, causing two different but simultaneous effects on the propagating pulse. In particular the time-varying refractive index induces the so called *self-phase modulation*, whereas the space dependency gives rise to *self-focusing*.

2.2.4.1 Self-Phase Modulation (SPM)

In the following discussion we will simplify the equations adopting the considerations made in the previous section, i.e. the condition of incident plane wave and scalar approximation. Moreover we consider for now negligible the spatial distortion of the pulse, focusing only on the temporal impact of the Kerr effect.

In first approximation, the third order non linear polarization term can be written as:

$$P(z,t) = 2\varepsilon_0 n_0 \tilde{n}_2 |E(z,t)|^2 E(z,t) \tag{2.49}$$

where $\tilde{n}_2 |E|^2 = n_2 I$. Considering that $E(z,t) = E_0(z,t) e^{i(\omega_0 t - k_0 z)}$, the previous equation becomes:

$$P(z,t) = 2\varepsilon_0 n_0 \tilde{n}_2 |E_0(z,t)|^2 E(z,t) e^{i(\omega_0 t - k_0 z)} \tag{2.50}$$

With these considerations, the time dependent wave equation for a pulse propagating in a material showing a linear and a third order non linear term of polarization is:

$$i\frac{\partial E_0}{\partial z} = -\frac{GVD}{2}\frac{\partial^2 E_0}{\partial t^2} + \gamma|E_0|^2 E_0 \tag{2.51}$$

with $\gamma = \frac{\omega_0}{c_0}\tilde{n}_2$.

The effect of the GVD has already been developed in the previous section and it can be neglected in the following discussion. Integrating equation (2.51) leads to the following solution for the pulse envelope:

$$E_0(z,t) = E_0(0,t)e^{-i\gamma|E_0(0,t)|^2} = E_0(0,t)e^{-i\phi_{nl}(z,t)} \tag{2.52}$$

The third order polarization introduces a term of phase $\phi(z,t)$ in the time dependent envelope; this term depends on the third order susceptibility $\chi^{(3)}$ and on the intensity of the propagating field.
The electric field can then be written as:

$$E(z,t) = E_0(0,t)e^{i(\omega_0 t - \phi_{nl}(z,t) - k_0 t} = E_0(0,t)e^{i\Phi_{nl}(z,t)} \tag{2.53}$$

The instantaneous frequency is then:

$$\omega_i(z,t) = \frac{\partial \Phi_{nl}(z,t)}{\partial \omega} = \omega_0 - \gamma z\frac{\partial|E_0(0,t)|^2}{\partial t} = \omega_0 - n_2\frac{\omega_0}{c_0}z\frac{\partial I(0,t)}{\partial t} \tag{2.54}$$

In conclusion the third order susceptibility causes the instantaneous frequency to shift with time. The pulse spectrum gains new frequency components that are temporally stretched. If $n_2 > 0$ initially new frequencies below ω_0 are generated (*red-shift*), and later frequencies greater than ω_0 (*blue-shift*). Each new component ω_i is generated in two different times during the pulse propagation. The two sinusoidal waves at the same frequency interfere constructively or destructively according to their reciprocal phase causing the final spectrum to be modulated.

2.2.4.2 Self focusing

Another consequence of Kerr effect originates from the dependency of the refractive index on the spatial coordinates. This dependency is inherited from the gaussian profile of the propagating pulse in the material.
Due to the spatial gaussian profile of the intensity, the pulse experiences a higher refractive index in its center according to the Kerr equation $n = n_0 + n_2 I(x,y,z,t)$. The spatial-depending refractive index acts like a focusing lens and as a consequence the pulse wavefront undergoes a deformation. As the spatial profile converges due to wavefront distortion, the intensity increases in the center of the beam, increasing rapidly the focusing process. It is possible to quantify the wavefront distortion in terms of λ by the so-called *B-integral*:

$$B = \frac{2\pi}{\lambda}\int_0^L n_2 I(z)dz \tag{2.55}$$

The induced convergence due to the Kerr effect is opposed to the natural divergence of the beam. The critical power P_c is defined as the value of input beam power at which the two phenomena compensate each other [61].

$$P_c = \frac{\lambda^2}{2\pi n_0 n_2} \tag{2.56}$$

Above the critical power, the B-integral causes the beam to self focus. As an example, for a Ti:Sa crystal $n_2 = 5 \cdot 10^{-16}$ cm^2/W and the critical power at 800 nm is of the order of MW.

In general for ultrashort pulses self-focusing becomes critical when the *B-integral* value exceeds 3 to 5: the beam collapses to a small radius and the peak intensity exceeds the damage threshold of the material. Strong field applications requiring high temporal and spatial quality of the pulse impose *B-integral* values below 0.3.

2.3 Chirped Pulse Amplification

The key for achieving high peak powers is amplification of sub-picosecond pulses. During the ten years following the first laser demonstration in 1960, the pulse duration saw a promising decrease thanks to the introduction of the mode-locking technique and the discovery of solid state gain material whose bandwidth can support femtosecond pulses. These materials have also the benefit of high energy storage due to their low stimulated emission cross section according to the equation for the saturation fluence

$$F_{sat} = \frac{\hbar\omega}{\sigma_{21}} \tag{2.57}$$

where $\hbar$ is the Planck's constant, ω is the central laser frequency and σ_{21} is the stimulated emission cross section. In solid state material the value of the cross section spans from 10^{-19} cm^2 to 10^{-21}cm^2 compared with large values of cross section of dyes and excimers lasers (10^{-16} cm^2).

The condition for efficient amplification requires that the beam propagating in the gain medium carries a fluence of the order of F_{sat}. In a solid state material as Ti:Sa $\sigma_{21} = 3.8{\cdot}10^{-19}$ and saturation fluence is of the order of 1J/cm^2 that corresponds to an intensity value of 10^{12}W/cm^2 for picosecond pulse duration. This intensity corresponds to a B-integral of few thousand, much higher than the limit established in the previous section.
As the pulse duration decreases, it becomes impossible to amplify the pulse without producing unwanted non linear effects or damages due to the high intensities propagating in the gain medium. Consequently the laser peak power and the intensity plateaued until 1985.

This limiting quandary was solved with the introduction of the Chirped Pulse Amplification technique in 1985 [15]. The working principle is represented in figure 2.4. The femtosecond, nJ energy level pulses produced by a primary source are first temporally stretched by a factor of a thousand to hundred thousand. Enlarging the temporal profile of the pulse does not change its energy fluence whereas it does decrease its intensity keeping the B-integral to acceptable values. The pulse can then be amplified from the nJ to the J level in subsequent

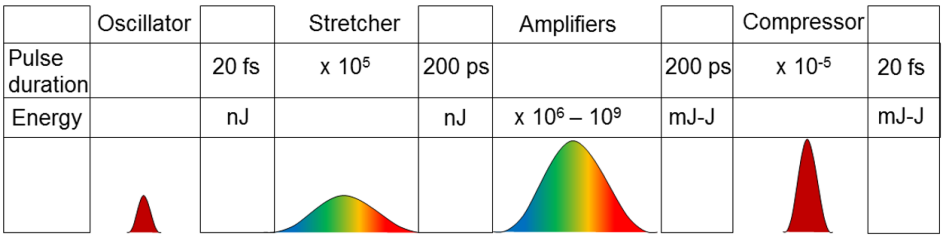

Figure 2.4: Schematic representation of the Chirped Pulse Amplification technique.

amplification stages and finally the energetic pulse is recompressed to ideally its transform limited duration.

In the next section each module composing a CPA chain will be analyse.

2.3.1 Femtosecond oscillators

A laser cavity supports an evenly-spaced comb of self-consisted longitudinal modes defined by their frequency $\omega = \pi cn/L$, where L is the length of the cavity. However the longitudinal modes that are actually oscillating in the cavity are selected by the spectral width of the gain material. Figure 2.5 represents the longitudinal modes selection induced by the spectral gain.

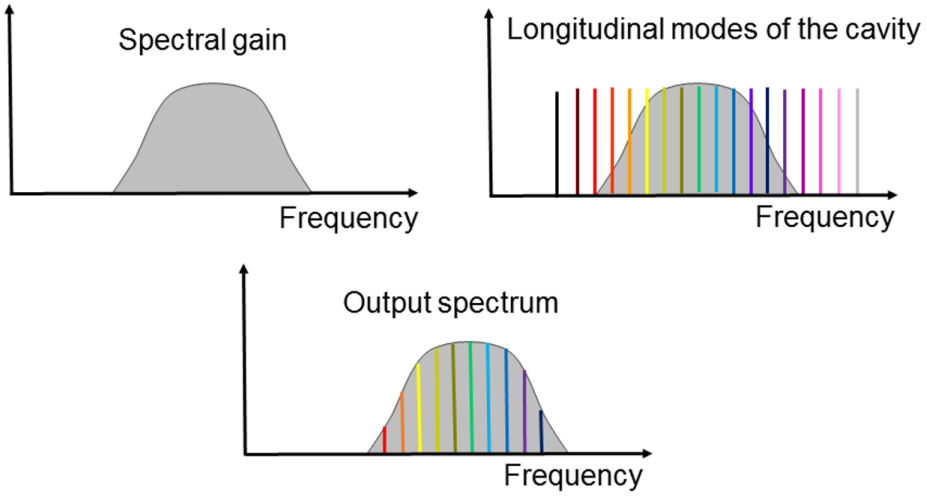

Figure 2.5: Schematic representation of longitudinal modes selection by spectral gain

.

If the modes oscillate without any phase relation, the laser emission is temporally continuous. On the contrary, if the modes oscillate with a defined phase relation, the laser emission is pulsed. In order to generate ultrashort pulses, it is necessary to lock in phase a large spectrum of modes: the larger the spectrum allowed by the cavity and the gain medium, the shorter the pulse resulting from the mode-locking.

Femtosecond pulses are generated with passive mode locking technique; here only the Kerr lens mode locking technique will be briefly presented, that is the most frequently

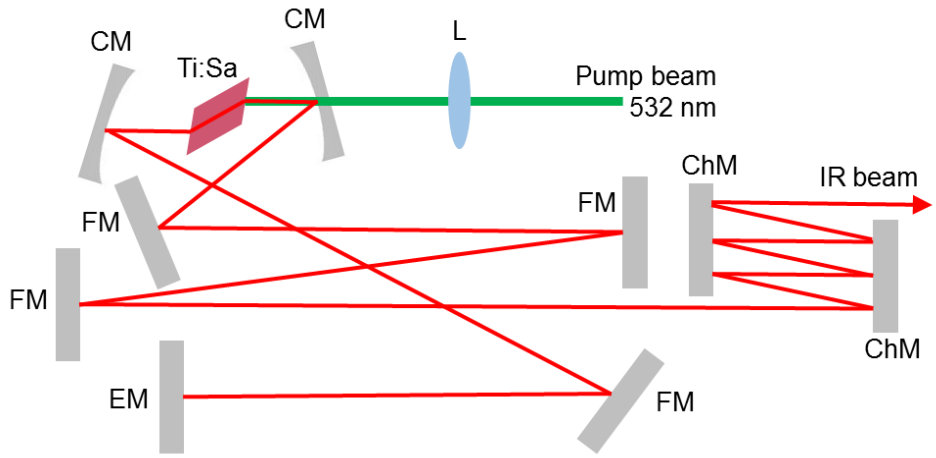

Figure 2.6: Scheme of a commercial femtosecond oscillator; CM-concave mirror, L-focusing lens, FM-flat mirror, EM-cavity end mirror, ChM-chirped mirror.

used in Ti:Sa oscillators. This technique consists in discriminating the pulsed regime from the continuum background and promoting only the amplification of short pulses. For this purpose, the Kerr effect is employed. In the previous section it has been demonstrated that the refractive index of the gain material is space dependent according to the intensity variation; this causes wavefront distortion and beam focusing during propagation in material. This effect is triggered by a sufficiently high value of intensity, i.e. by the pulsed regime. It follows that the pulsed beam undergoes a focusing effect and its diameter is reduced, whereas the continuum regime is not concerned by self focusing effects. The discrimination between the pulsed and continuous regimes is then operated on their different beam sizes. It is sufficient to place a spatial filter, like a slit, after the gain material to select only the pulsed beam. Moreover, the pulsed beam amplification at the expenses of the continuum regime is implemented also with a spatial adjustment of the gain to the beam size of the pulsed beam. The gain is spatially distributed according to the longitudinal pump. The diameter narrowing due to the Kerr effect promotes a better size match between the pulsed beam and the gain channel. Mode locking is achieved with an initial perturbation of the cavity.
The positive dispersion accumulated over all the spectral components due to the Kerr effect and to the propagation in the gain material is compensated by a negative dispersive line like a couple of prisms or chirped mirrors. Figure 2.6 shows schematically an oscillator design.

Commercial oscillators deliver pulses with energy at the nJ level, pulse duration on the fs regime and repetition rate of tens of MHz.

2.3.2 Dispersive modules: stretcher and compressor

The working principle of dispersive modules consists in adding second and third order dispersion to the pulse in order to stretch or re-compress its duration. In order to properly conceive the dispersive modules, one needs to know how far the pulse should be stretched

and estimate the necessary GDD. The compressor should be design so that it compensates the dispersion added by both stretcher and propagation in the amplification line.
As already mentioned, the pulse duration before amplification should be stretched in order to avoid unacceptable values of B-integral and permanent damages of the gain material. On the other side, the condition of efficient energy extraction is fulfilled when the fluence circulating in the amplifier reaches at least the value of the saturation fluence (1 J/cm^2). These requirements together quantify how far a pulse should be stretched. We suppose for example that the damage threshold (I_{damage}) for an optical components is 5 GW/cm^2 for a pulse width of 100 ps. If 2 J/cm^2 is the desired pulse fluence (F_{pulse}), the chirped pulse duration can roughly be estimated as:

$$\Delta T_{out} = \frac{F_{pulse}}{I_{damage}} = 400 \quad ps \tag{2.58}$$

Most of the Ti:Sa systems are operating with chirped pulse duration in the range from 100 ps to 400 ps.

Equation (2.39) in the first section can be used to estimate the necessary GDD to stretch an initial femtosecond pulse to the above mentioned pulse duration of hundreds of ps. Typical values of 10^6 fs^2 for the GDD are thus necessary. The same order of magnitude of GDD will be necessary to recompress the pulse after amplification. Common glasses add in general much lower dispersion. Comparing different dispersive modules on the absolute value of GDD induced, a pair of prisms is not usable either, since a spacing of few meters between the prisms would be necessary and the compactness of the module would suffer. Grisms pair [62], a combination of transmission gratings and prisms, can induce a higher value of GDD (10^5 fs^2) but a good compromise between input energy and beam size should be found in order to avoid damages. Diffraction grating pairs are highly dispersive and can match high values of GDD in a relatively compact geometry. In addition, grating pairs can be use for both the stretcher and the compressor, ensuring opposite signs and matching values of second and third dispersions that can be finely adjusted with distances and angles tuning. Table 2.1 resumes typical values of GDD and TOD for different dispersive modules.

Device	λ (nm)	GDD (fs^2)	TOD fs^3
Bulk glass	620	550	240
Fused Silica (L= 1 cm)	800	362	280
Prism pair	620	-760	-1300
Fused Silica (L = 50 cm)	800	-523	-612
Grating pair (L = 20 cm)	620	$-8.2 \cdot 10^{4}$	$1.1 \cdot 10^{5}$
groove density = 1200 l/mm	800	$-3 \cdot 10^{6}$	$6.8 \cdot 10^{6}$

Table 2.1: Second and Third order dispersion induced by three different dispersive modules for two wavelengths.

The following discussion will firstly detail the equations for the grating based compressor and then for the stretcher. This order is justified by the fact that naturally a grating pair adds negative dispersion, that is induced to compress the pulse. Once the equation for the

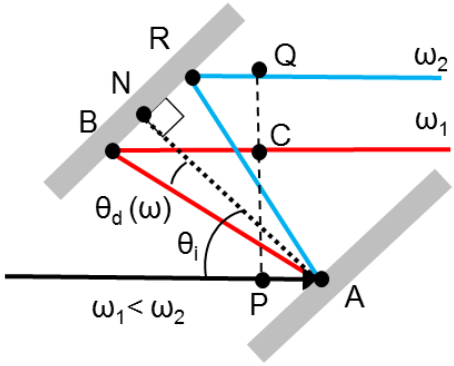

Figure 2.7: Negative dispersion from a grating pair

grating pair in double pass configuration will be unfold, the method to reverse the sign of dispersion and design the stretcher will be explained.

2.3.2.1 Grating compressor

A grating based compressor is composed by two parallel gratings. The first grating diffracts the pulse spectral components causing the collimated input beam to diverge due to the angular chirp; the second grating compensates the angular divergence. As depicted in figure 2.7, shorter wavelengths (blue components, higher frequency) travel shorter paths than longer wavelengths (red components, lower frequency) and the GDD is negative. After one pass in the grating pair the beam still suffers spatial chirp so a second pass is necessary to spatially reshape the beam.
The diffraction through a grating is ruled by following equation:

$$\sin\theta_d = \frac{m}{d}\frac{2\pi c}{\omega} - \sin\theta_i \tag{2.59}$$

where θ_i and θ_d are respectively the incidence and the diffracted angles with respect to the normal of the grating surface, ω is the frequency, $1/d$ is the groove density and m is the diffraction order that from now on will be considered equal to 1.
From figure 2.7 the optical path $\overline{PABC}$ is:

$$\overline{PABC} = b + b \cdot cos(\theta_i - \theta_d) \tag{2.60}$$

where $b = G(cos\theta_d)^{-1}$, with G the perpendicular distance ($\overline{NA}$) between gratings. The point P and C are arbitrarily chosen since their positioning does not affect the phase difference between different frequencies. Similar consideration can be done for each frequency, defining its optical path p as a function of the diffraction angle.
The total phase shift for a spectral component propagating along path p is therefore:

$$\varphi(\omega) = \frac{\omega}{c}p + R(\omega) \tag{2.61}$$

The necessity of the correction factor $R(\omega)$ is illustrated in figure 2.8 where diffraction of a plane wave is qualitatively depicted (taken from[57]).

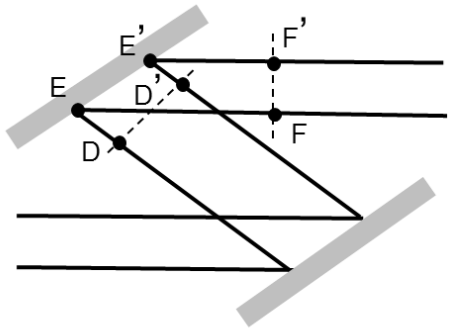

Figure 2.8: Illustration of wavefronts in a grating compressor (taken from[57]).

$\overline{DD'}$ and $\overline{FF'}$ are wavefronts, i.e. surfaces of equal phase. However, path $\overline{DEF}$ is longer than path $\overline{E'D'F'}$. Necessarily the path difference should be an integer multiple of 2π and thus necessarily we should consider that each groove within the distance $\overline{EE'}$ introduces a -2π phase jump. Similar assumptions should be considered while computing the phase shift between the two different frequencies of figure 2.7 propagating along $\overline{PABC}$ and $\overline{PARQ}$ where we should now account for the number of grooves in the segment $\overline{BR}$. This can be done considering for each frequency the additional phase in the segment from the point N (intersection between second grating and the perpendicular from A to the second grating) and the intersection point between the diffracted ray and the second grating (for example B for ω_1).

$$R(\omega) = -2\pi\frac{G}{d}tan(\theta_d) \tag{2.62}$$

The point N is arbitrarily but uniquely chosen for all the frequencies, since its positioning does not influence the phase shift between components.
The spectral phase induced by a grating pair is then:

$$\varphi(\omega) = \frac{\omega}{c}p - 2\pi\frac{G}{d}tan(\theta_d) \tag{2.63}$$

Differentiating this equation gives the time delay:

$$\tau_g = \frac{\partial\varphi}{\partial\omega} = \frac{p}{c} + \frac{\omega}{c}\frac{\partial p}{\partial\omega} - 2\pi\frac{G}{d}\frac{\partial tan(\theta_d)}{\partial\omega} \tag{2.64}$$

The second term is shown to be equal in module and opposite in sign to the third term, providing that

$$\tau_g = \frac{p}{c} \tag{2.65}$$

Differentiating the group delay yields to the expression for the second and third order spectral phases as a function of the wavelength for a single pass in the grating pair:

$$GDD = \frac{\partial^2 \varphi}{\partial \omega^2} = -\frac{\frac{G\lambda^3}{d^2}}{2\pi c^2 cos^3(\theta_d)} \tag{2.66}$$

$$TOD = \frac{\partial^3 \varphi}{\partial \omega^3} = \frac{3G}{4d^2}\frac{\lambda^4}{\pi^2 c^3 cos^5(\theta_d)}(1 + sin(\theta_i)sin(\theta_d)) \tag{2.67}$$

Note that, since $-\pi/2 < \theta_d < \pi/2$, the GDD is always negative and can compensate positive dispersion induced by propagation in normal material. Similarly it can be demonstrated that the TOD is always positive.
Equations (2.66) and (2.67) can be used to estimate the GDD induced by a compressor with double pass on the grating pair, using the following parameters:

$$\begin{cases} G = 380 \text{ mm} & \\ \frac{1}{d} = 1480 \text{ lines/mm} & \\ \lambda = 800 \text{ nm} & GDD = -2.22 \cdot 10^6 \text{ fs}^2 \\ \theta_i = 45° & TOD = 4.89 \cdot 10^6 \text{ fs}^3 \\ \theta_d = 28.5° & \end{cases} \tag{2.68}$$

2.3.2.2 Stretcher

The major trouble in developing a grating based stretcher is to find a way to reverse the natural negative sign of the GDD introduced by a gratings pair. Flipping the sign is achieved with an imaging system within the grating pair in order to create a virtual negative distance between the two gratings. The concept is schematically depicted in figure 2.9. The input pulse is diffracted by the first grating at an angle $\theta_d(\omega)$ and propagates through the imaging system which creates the image of the first grating at a distance L_{eff} behind the position of the second grating. This configuration corresponds to a situation where the grating distance is negative. Shorter wavelengths propagate through longer paths and positive GDD values are added to the spectral phase. The GDD induced by a grating based stretcher follows the same equation demonstrated for the grating compressor where the perpendicular distance is $L_{eff}cos(\theta_d)$.

As the spectral components undergo an important dispersion, it is necessary to use large aperture optics and to avoid clipping of the spectrum. In order to totally exploit the aperture, the spatially dispersed spectrum fills the imaging optics, causing spatial aberrations that can induce temporal distortions in the compressed beam. In order to avoid chromatic aberrations it is preferable to use an all-reflective triplet design, better known as the Öffner triplet [58]. In this configuration, depicted in figure 2.10, the imaging system is composed by a couple of concave and convex mirrors. The grating diffracts the spectral components of the input pulse that propagates towards the imaging system. The couple of mirrors reflects back the pulse to the grating which deviates it towards a dihedral retroreflector for the second pass in the system. If we denote as R_{conc} the radius of curvature of the concave mirror ($f_{conc} = R_{conc}/2$), the convex mirror should be chosen so that its radius of curvature

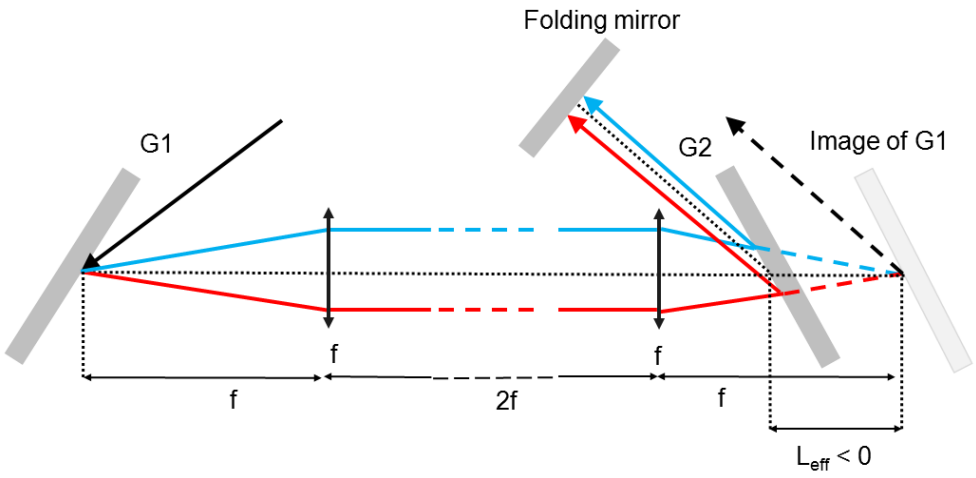

Figure 2.9: Stretcher principle for positive dispersion. $G1$ and $G2$ are the gratings, f the lenses focal length of the imaging system and L_{eff} the negative distance between the gratings.

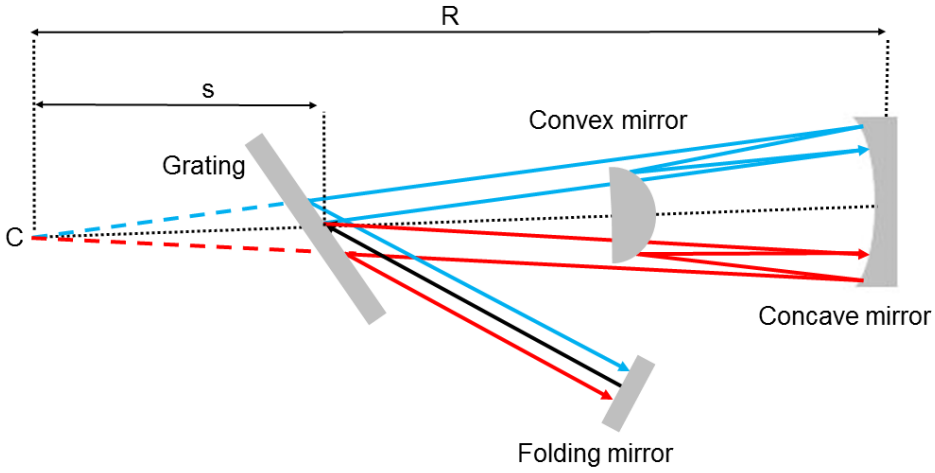

Figure 2.10: Öffner configuration for stretcher. C is the center of curvature, R the radius of the concave mirror, d the distance between the position of the grating and the center of curvature.

is half of that of the concave mirror: $R_{conv} = -R_{conc}/2$ so that $f_{conv} = -f_{conc}/2$. The two mirrors are placed at a mutual distance of f_{conc} and the grating is placed at a distance s from the center of curvature. Figure 2.11 shows the equivalent Öffner configuration where the complete reflective imaging system is replaced by refractive optics.
The equivalent distance between the two gratings L_{eff} is twice the distance s from the center of curvature to the position of the first grating, and it is negative so that $L_{eff} = -2s$.
Recalling equation (2.66) and (2.67), and considering that the equivalent perpendicular distance between the stretcher gratings is $G_s = -L_{eff}cos\theta_d = -2scos\theta_d$, is possible to estimate

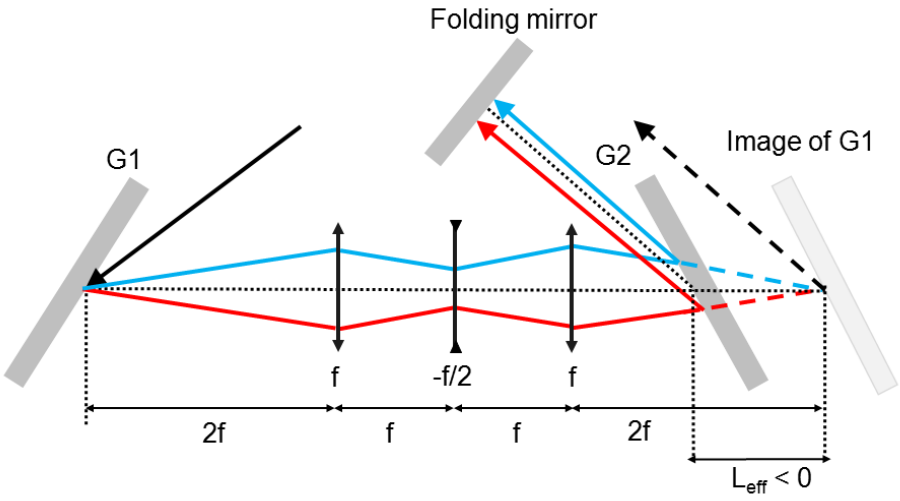

Figure 2.11: Equivalent configuration of the Öffner triplet with refractive optics. $G1$ and $G2$ are the two grating.

the GDD and TOD induced by module:

$$\begin{cases} s = 200\text{mm} \rightarrow G_s = -2scos\theta_d = 297 \text{ mm} \\ \dfrac{1}{d} = 1200 \text{ lines/mm} \\ \lambda = 800 \text{ nm} \qquad\qquad GDD = 1.88 \cdot 10^6 \text{ fs}^2 \\ \theta_i = 17° \qquad\qquad TOD = -5.16 \cdot 10^6 \text{ fs}^3 \\ \theta_d = 42° \end{cases} \tag{2.69}$$

The equivalent mirrored configuration of the compressor with respect to the stretcher ensures a complete compensation of the second and third dispersion orders. Additional dispersion induced by the propagation in the gain media or other optical devices can be compensated by slightly changing the parameters of the compressor. In particular, adjusting the grating distance and the grating angle allow the fine tuning of GDD and TOD respectively. As the pulse duration approaches the single-cycle, higher dispersion orders become not negligible and need to be compensated. It has been demonstrated [63, 64, 65] that groove mismatch between stretcher and compressor's gratings allows better correction of fourth order dispersion.

2.3.3 Amplification

A properly temporally stretched pulse propagating in the gain medium undergoes energy amplification. In the specific case of Ti:Sa, firstly optical pumping creates the condition of population inversion, then the signal extracts the stored energy. The pulse fluence at the output of an amplifier F_{out} is given by the Frantz-Nodvik equation [66]:

$$F_{out} = F_{sat} ln\left\{ G_0 \left[exp\left(\frac{F_{in}}{F_{sat}} \right) - 1 \right] + 1 \right\} \tag{2.70}$$

F_{sat} is the already mentioned saturation fluence (2.57), F_{in} is the fluence of the input signal to the amplifier and G_0 is the small signal gain defined as:

$$G_0 = exp\left(\frac{F_{stored}}{F_{sat}}\right) \tag{2.71}$$

where F_{stored} is the fluence stored by the gain medium; for a single pass amplifier it is equal to the pump fluence F_{pump}. In general the *gain* is defined as the ratio of the output fluence to

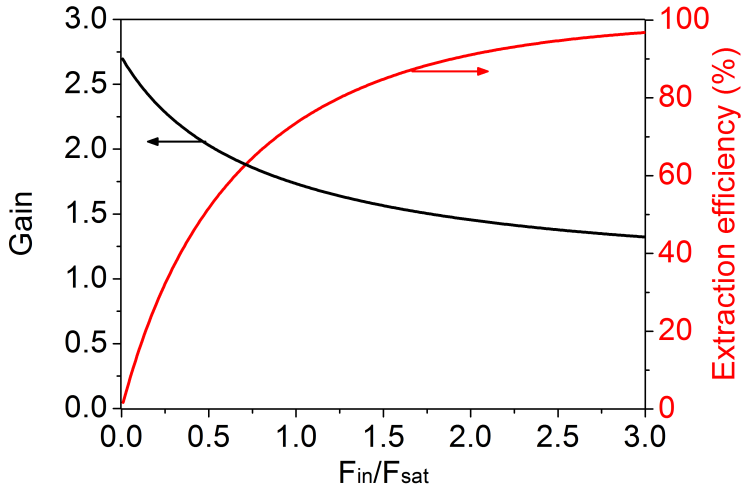

Figure 2.12: Energy extraction efficiency (red line) and amplifier gain (black line) as a function of the ratio between input fluence and saturation fluence

.

the input fluence, $G = F_{out}/F_{in}$. If the input fluence is small compared with the saturation fluence (condition of small signal), the gain can be approximated to G_0.
Another significant parameter used to classify the amplifiers is the extraction efficiency η. In general we can affirm that:

$$F_{out} = \eta F_{pump} + F_{in}$$
and
$$\eta = \frac{F_{out}}{F_{pump}} - \frac{F_{in}}{F_{pump}}$$

In the particular case of $F_{pump} = F_{sat}$ we can simplify the equation for gain G and extraction efficiency η:

$$G = \frac{F_{sat}}{F_{in}} ln\left\{e^1\left[exp\left(\frac{F_{in}}{F_{sat}}\right) - 1\right] + 1\right\} \tag{2.72}$$

$$\eta = ln\left\{e^1\left[exp\left(\frac{F_{in}}{F_{sat}}\right) - 1\right] + 1\right\} - \frac{F_{in}}{F_{sat}} \tag{2.73}$$

Figure 2.12 reproduces the trend of the above mentioned quantity as a function of F_{in}/F_{sat}.

For small values of F_{in}/F_{sat} the gain is maximal (approaching the value of G_0) and the extraction efficiency is low. On the contrary as F_{in} approaches or even exceeds F_{sat}, the gain decreases and the extraction efficiency plateaus to its maximum values corresponding to the saturation condition.
It follows that an amplifier can either give a high value of gain or a high extraction efficiency. Based on this consideration the amplifiers can be classified in two categories. High gain amplifiers are typically used a the first stages of the amplification line when F_{in} is still at low energy values (nJ), ensuring net gain of the order of 10^6; the regenerative amplifier is a common design of high gain amplifier. High power amplifiers, typically at the end of the amplification chain due to the greater value of F_{in}, ensure the saturation condition. High power amplifier are mostly designed in a multipass configuration.

Increasing the energy of the pulse means scaling the amplifier to bigger size. High power amplifiers often require bigger and more expensive optics, as well as cooling systems to avoid thermal distortion. [30].

2.3.3.1 Regenerative amplifier

Figure 2.12 shows that if the input fluence to the amplifier is much lower than the saturation fluence, the condition of saturation and efficient extraction cannot be reached. A method to circumvent this limitation is to multipass the gain medium. The regenerative amplifier is a specific design which permits an arbitrarily number of passes through the gain medium, while conserving a good spatial beam quality after a very long propagation distance. Its basic configuration is shown in figure 2.13. The regenerative cavity is a stable resonator with two high reflectivity ending mirrors and the gain medium. Two additional components are needed for injecting and extracting the pulse: a Pockels cell and thin-film polarizers. All the components are centred on the axis of the cavity except for the Pockels cell that is a bit tilted, equivalent to a quarter wave plate on single pass. The polarizer reflects one linear polarization component (for example S-polarization) and transmits the other (P-polarization). With zero voltage applied to the Pockels cell, it behaves like a quarter wave plate for single pass and a half wave plate for double pass: every pulse entering the cavity is rejected after one round trip in the cavity. The operation of the regenerative amplifier proceeds as follow. The pump laser is absorbed by the gain medium creating inversion of population. The Pockels cell is timed so that it remains off untill all the pump energy is absorbed by the medium and it starts emitting fluorescence due to spontaneous emission: the medium has stored enough energy to amplify the injected beam. After the signal is injected and after the first double pass in the Pockels cell, a quarter wave voltage is applied. In this condition the Pockels cell acts like a half wave plate for single pass and is transparent for double pass. The beam is trapped in the cavity until the voltage is switched off again.

Ti:Sa regenerative amplifier requires typically 10 to 15 round trips for extracting all the stored energy, considering that each round trip corresponds to a double pass in the crystal. If the signal is kept inside the cavity for further round trips, since the stored energy is completely extracted, the cavity losses are not compensated anymore by the round trip gain and the signal energy slowly decays to zero.

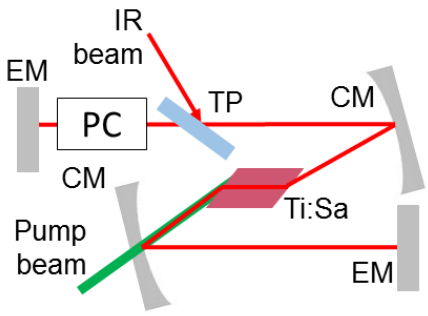

Figure 2.13: One regenerative amplifier configuration; CM-concave mirror, TP-thin polarizer, PC-Pockles cell, EM-cavity end mirror.

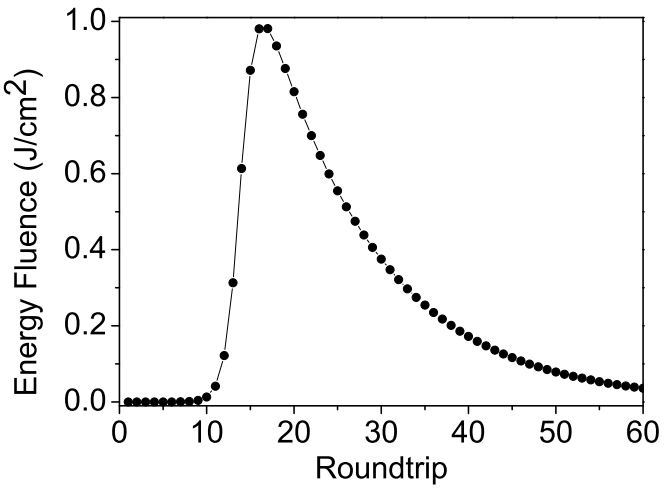

Figure 2.14: Extracted energy fluence as a function of the round trip for $F_{pump} = 1.25$ J/cm^2, input signal energy = 1 nJ over a beam size of 1 mm^2 at 1/e^2.

The behaviour of a regenerative cavity is modelled by the Lowdermilk and Murray [67] expansion:

$$F_{out}^{(k)} = F_{sat}^{(k)} ln\left\{G_0^{(k)}\left[exp\left(\frac{F_{in}^{(k)}}{F_{sat}}\right) - 1\right] + 1\right\} \tag{2.74}$$

where the index k indicates the round trip number. $G_0^{(k)}$ and $F_in^{(k)}$ are dynamic quantities:

$$G_0^{(k)} = exp\left[\frac{F_{stored}^{(k)}}{F_{sat}}\right] \quad \text{where } F_{stored}^{(k+1)} = F_{stored}^{(k)} - F_{out}^{(k)} + F_{in}^{(k)}$$

$$F_{in}^{(k+1)} = TF_{out}^{(k)} \quad \text{where T is the amplifier transmission}$$

Figure 2.14 represents the energy build-up of a pulse in the regenerative cavity. It has been plotted from the Lowdermilk-Murray's equations supposing an input signal energy of 1 nJ

over a beam size of 1 mm^2 at $1/e^2$. The pump fluence, 1.25 J/cm^2, slightly exceeds the saturation fluence. The maximal energy corresponds to the 17th round-trip. For further passes the losses become more important than the gain.

2.3.3.2 Multipass amplifier

Differently from the regenerative cavity, the multipass amplifier is not based on a resonator design but rather on a set of mirrors precisely positioned that allows the signal to multipass the gain medium. The design of a multipass amplifier is determined by the number of passes needed to reach saturation. Differently from the regenerative amplifier where the spatial overlap of pump and signal is ensured by the design, the conception of a multipass amplifier is a trade-off between keeping the incidence angle of each pass at the minimum to ensure pump-signal overlap, and fitting all the necessary passes. Typical configurations we use for multipass amplifiers are the "bow-tie" and the "3-mirror ring", both depicted in figure 2.15.

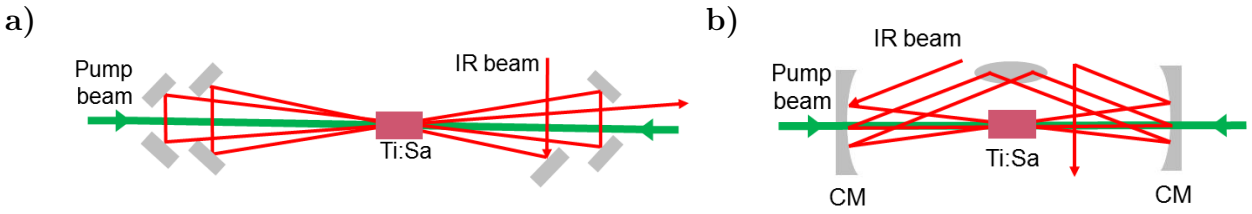

Figure 2.15: Two common multipass amplifier configurations: a) the bow-tie, b) the 3-mirror ring. CM-concave mirror.

Here below a comparison between regenerative and multipass amplifiers, underlining advantages and disadvantages:

- The multipass configuration minimizes the propagation through dispersive optics which is on the contrary unavoidable in the regenerative configuration, where the beam propagates through Pockels cell and polarizers. After a multipass amplifier the pulse recompression benefits from less higher dispersion order terms which are difficult to compensate.

- Opposite to the regenerative configuration, the multipass design doesn't require any polarizer, avoiding any possible stray reflection which may lead to prepulses and deteriorate the temporal contrast.

- In the multipass amplifier the output IR beam profile depends on the pump and on the input seed mode, on the optics and on the gain profile. Different causes might then contribute to deteriorate the output profile quality. On the other side, in the regenerative configuration the output profile depends mostly on the cavity design and it is insensitive to the seed mode, providing a high quality output beam profile.

- Often the multipass configuration makes use of curved optics or lenses for adapting the beam size to the pump mode; this might induce astigmatism. The regenerative amplifier is design as a stable cavity and does not need any additional refractive optics.

2.4 Ti:Sa Spectroscopy

In the same period the Chirped Pulse Amplification was proposed, Ti:Sa lasers were firstly demonstrated [8]. Despite the first experiments showed a critical low efficiency due to scattering and re-absorption of the laser wavelength [68], the promising large spectral bandwidth exhibited by the Ti:Sa pushed the technology to grow higher-quality crystals with smaller losses [69]. This crystal was quickly demonstrated to have excellent mechanical, thermal and optical properties that allow the laser system to be scaled to high average powers and short pulse duration.

In the next section the spectroscopy of the Titanium Sapphire and its lasing properties will be briefly discussed.

In the Titanium-doped Sapphire, Ti:Al_2O_3, Ti^{3+} ions substitute for aluminum ions in the sapphire host crystal Al_2O_3. The outermost shell of the titanium ion is occupied by a single d-electron, while the remaining 18 electrons completely fill the innermost shells. As depicted in figure 2.16a the titanium ion occupies the central part of the octahedron whose corners are defined by six oxygen ions. The d-electron interacts with the electronic charges of the surrounding ions and this electrostatic field, called the *crystal field*, removes the five-fold degeneracy of the single d-electron. In particular, depending on the direction of their orbitals, the five degenerate ground state levels of the d-electron are splitted into a triplet ground state T with lower energy and a doublet excited state E with higher energy (see 2.16b). The energy difference between the degenerate T-levels and the E-levels corresponds to the energy of a photon with a wavelength around 500 nm, and absorption of light in this spectral region causes the transition from the ground state to the excited state.

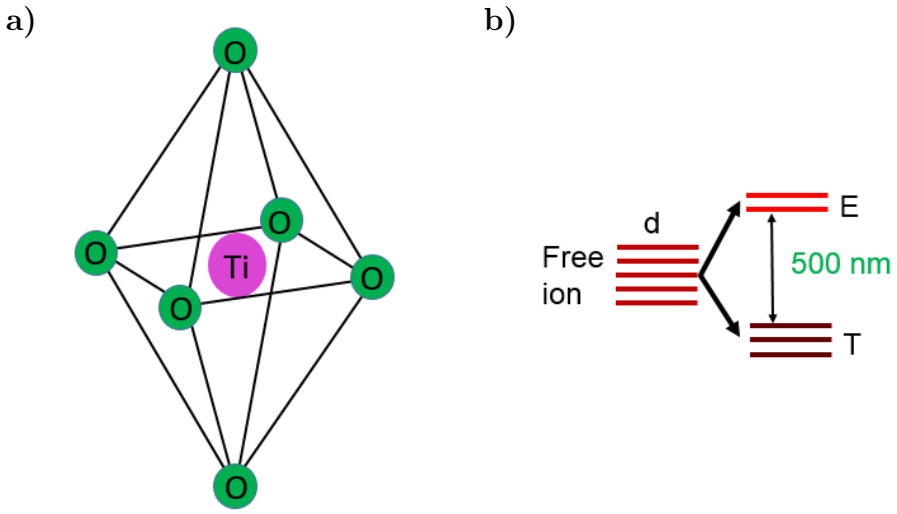

Figure 2.16: a) Octahedric geometry of Ti:Al_2O_3; Ti-titanium ion, O-oxygen ions. b) The crystal field of the sapphire lattice removes the fivefold degeneracy of the 3d electron of the free ion T^{3+} to a doublet excited state E and a triplet ground state T.

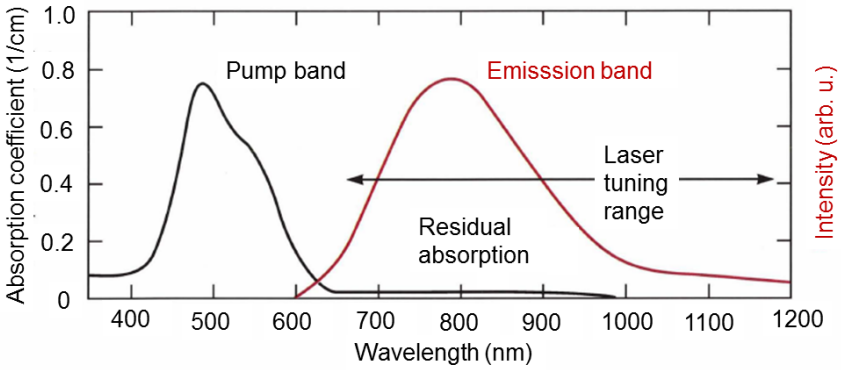

Figure 2.17: Absorption and emission band of Ti:Al_2o_3. The absorption band peaks near 490 nm; the spectral broadening results form the Jahn-Teller splitting. The emission band is peaked near 790 nm. A weak residual absorption overlaps the emission band [71].

According to the so-called Jahn-Teller effect [70], the Ti^{3+} ion in its excited state E can displace itself with respect to the surrounding oxygen lattice, lowering the overall energy of the system. The displacement removes the degeneracy of the E-doublet and the absorption band is spectrally broadened around the green peak. The Jahn-Teller splitting is not completely resolved and the absorption band spectrally appears as a main peak with a side bump.
The same displacement causes the titanium ion to excite vibrations, or phonons, in the surrounding lattice. The coupling of electronic energy with vibrational states causes relaxation of the ion to lower energy excited levels. From this vibrational level, the electron decades to another vibrational level of the ground state, emitting a photon with a wavelength in the red spectrum. Again the electron relaxes quickly to the lowest energy ground level emitting a phonon. The tuning of the emission spectrum to longer wavelengths with respect to the absorption is called *Stokes shift*. Figure 2.17 [71] shows the absorption band from T-level to E-level and the fluorescence spectrum.

The absorption spectrum spans from 400 nm to 600 nm while the emission spectrum from 600 nm to 1 μm, with a spectral width at FWHM of 180 nm. Figure 2.18 represents schematically the lasing dynamics of the crystal in terms of energy. The Gaussian-shaped curves, C and A, represent the probability of finding the Ti^{3+} ion in a particular vibrational level, defined by its energy, of the excited and ground states, respectively. The probability spread of the Ti^{3+} ion position in vibrational levels of both excited and ground states causes the emission to spread over a large range of energies, resulting in a broad band emission spectrum. Finally, higher excited levels lie far above the E-level, and neither the green pump photons nor the lasing red photons can cause transitions from the E level to higher levels.
The lasing properties of Ti:Sa crystal depend on the lifetimes of the energy levels taking part in the above-described dynamics. The lifetime of the population in the excited level, also called fluorescence lifetime, is denoted as τ_r and for Ti:Sa at room temperature is 3.2 μs. This is the time limit for the pump to create population inversion and to store energy in the excited level.

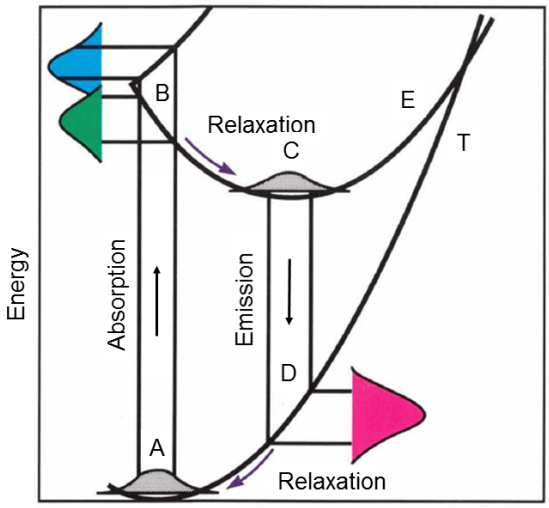

Figure 2.18: Schematic of the laser dynamic of Ti:Al_2o_3 in terms of energy levels.

Another parameter for evaluating a gain medium is its stimulated emission cross section σ, that defines, in units of area, the number of transitions from the upper to the lower level caused by a specific flux of photons. It follows that the gain per length unit of the medium is $N\sigma$, with N the population inversion density. As already mentioned, higher values of σ are preferable for efficient amplification. The stimulated emission cross section can be estimated performing spectroscopic measurement of the spectral fluorescence profile and of the fluorescence lifetime:

$$\sigma = \frac{3}{4\pi^2}\frac{\lambda^2}{n^2\tau\Delta f} \tag{2.75}$$

where τ_r is the fluorescence time, λ is the peak of the fluorescence curve, n is the refractive index of the crystal and Δf is the full width at half maximum of the fluorescence curve in frequency. For Ti:Sa σ is $3.8{\cdot}10^{-19}$ cm^{-2}.
According to its spectrally broad absorption cross section, Ti:Sa can be optically pumped by different methods. Argon-ion lasers emitting at 515 nm and 488 nm can be used for continuous-wave pumping. Pulsed operation have been demonstrated with dye-laser pumping emitting at 503 nm and frequency-double Nd:YAG or Nd:YLF lasers emitting at 532 nm and 527 nm respectively.

Chapter 3

Ti:Sa amplification: An original 10 kHz front-end coupled to a 1 kHz amplifier

3.1 Introduction

Upon introduction of the Chirped Pulse Amplification Technique [15], countless improvements on the Ti:Sa laser system promote this technology to the dominant driving laser source for ultrafast, high-intensity experiments. The recognition of this technology as a breakthrough in laser science has been formalized early this year with the Nobel Prize award to Strickland[1] and Mourou[2]. At the beginning of the century, TW laser systems were demonstated delivering pulses with duration below 35 fs and 10 Hz repetition rate [72, 73]. Ti:Sa based laser systems with 100 TW peak power at 10 Hz, sub-50 fs, appeared shortly after [74], paving the way to sub-PW laser systems. At this point, further improvements of the Ti:Sa based laser became challenging due to two main reasons. First, the amplification bandwidth of the Ti:Sa is limited by gain narrowing effect. Spectral filtering techniques [60, 34, 75, 76, 32] have been successfully employed to extend the amplification bandwidth and reach sub-20 fs pulse duration for 10 to 100 Hz repetition rate systems. Alternatively, propagation methods, like spectral broadening in hollow-core fibers [77, 36, 38], or filamentation-based self-compression[78, 79], can be used to generate single-cycle regime pulses with non negligible energy losses.
Ultra-broad band amplified spectra not only allow to generate sub-20 fs pulse duration but they can also support spectral tunability [80, 75], adding a degree of flexibility to the driving source for strong field experiments [81, 80].

Driving sources with high energy and high repetition rate are particularly advantageous for strong field applications, in order to reduce the acquisition time, increase the experimental statistic and the brightness of the detected signal. Moreover, disposing of a mJ, kHz level

[1]Donna Strickland Facts 2018. NobelPrize.org. Nobel Media AB 2018. Tue. 16 Oct 2018. ¡https://www.nobelprize.org/prizes/physics/2018/strickland/facts/

[2]Grard Mourou Facts 2018. NobelPrize.org. Nobel Media AB 2018. Tue. 16 Oct 2018. ¡https://www.nobelprize.org/prizes/physics/2018/mourou/facts/

train of pulses extends the range of strong field applications to coincidence spectroscopy [82]. As the repetition rate increases, thermal effects inside the crystal become more crucial and detrimental for the beam profile; the output average power is then limited to few tens of Watt. Several solutions have been proposed to overcome thermal effect limitations at the kHz repetition rate. Cryo-cooling systems can be employed to compensate for the heat accumulation and allow high-average power working of the laser [29, 83]. A new design for the amplification medium has also been proposed [84], resulting in the Thin-Disk Ti:Sa, allowing heat management for high power sources. This technology has been proven on a 10 Hz sub-PW laser [85] and demonstrated to be scalable to hundreds Hertz [86].

The state of the art for Ti:Sa based laser offers still some room of improvement, especially for high repetition rate, high average power system. As already mentioned, approaching the mJ level with sub-20 fs pulse duration at high repetition rate without cryo-cooling the Ti:Sa crystal is quite challenging due to thermal effect and gain narrowing limitations. Part of the engagement of Amplitude Laser Group, in collaboration with the research institute CEA, consists in exploring new solutions for Ti:Sa based laser enabling an improvement of the system performances. Here we present the results obtained on a Ti:Sa 10 kHz laser front-end, completely water-cooled, approaching the mJ energy level with sub-20 fs pulse duration. The novelty of the system consists in achieving both high average power and broadband spectrum without the need of expensive and cumbersome cryo-cooling chambers. Finally we demonstrate that our system supports also a spectral tunable mode.

3.2 Overview of the 10 kHz Ti:Sa front-end

The 10 kHz laser system has been developed by Amplitude Laser Group in collaboration with CEA-Saclay within the joint laboratory Impulse. The laser chain is schematically depicted in figure 3.1 and it is based on the Chirped Pulse Amplification technique. The 10 kHz

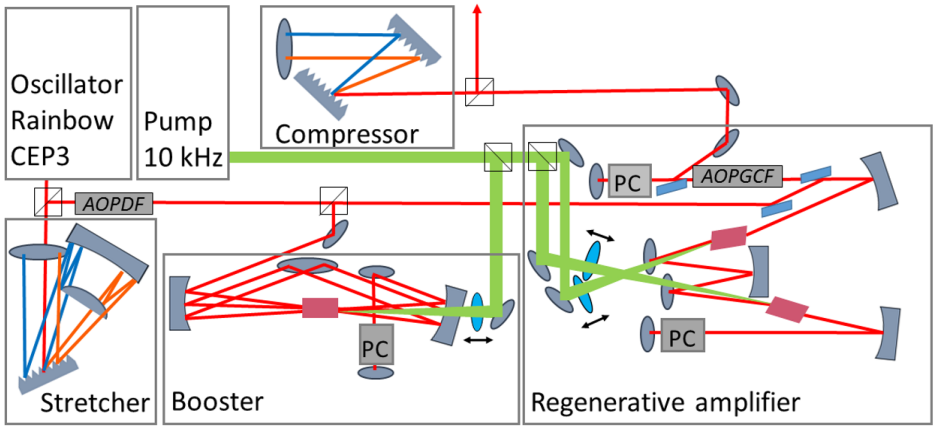

Figure 3.1: Scheme of the experimental 10 kHz front-end. The oscillator is CEP stabilized (Rainbow CEP3 - Spectra Physics). The Öffner stretcher is followed by two amplification stages: the booster and the double crystal regenerative amplifier. The compressor is grating based. The amplifiers are pumped by a 10 kHz prototype pump laser from Amplitude Laser Group.

front-end relies on a novel double-crystal design of the regenerative cavity for thermal load management at high average power. The primary source is a CEP stabilized oscillator; the train of pulses at 75 MHz emitted by the oscillator are stretched by an Öffner triplet stretcher and then amplified in two modules. The first high gain amplifier is in multipass configuration and boosts the pulse before further amplification in the newly designed double crystal regenerative amplifier. The final module of the laser front-end is the grating based compressor. As shown in the figure 3.1, two acousto-optics dispersive modules are inserted in the laser chain and their working principle will be described later. The acousto-optic programmable dispersive filter (AOPDF) is placed after the stretcher and is used to shape the spectral phase of the pulse and optimize compression. The acousto-optic programmable gain control filter (AOPGCF) is placed in the regenerative cavity and allows to attain spectrally broad amplified pulses. The AOPGCF module acts on the the spectral amplitude whereas the AOPDF can affect both the spectral phase and amplitude of the propagating pulse depending on the purpose defined.

In the next discussion we will describe the method that allows the system to produce 110 nm large spectrum after amplification up to 5 W, supporting 17 fs pulses after compression and spectral tunability. We will describe an additional amplifier working at 1 kHz repetition rate that boosts the pulse average power up to 9-10 W in broadband regime without cryo-cooling. Finally we will describe a high-average power system, based on the 10 kHz front-end and coupled to further stages of amplification, reaching the TW peak power level.

3.2.1 10 kHz pump laser prototype

The 10 kHz Ti:Sa front-end is optically pumped by a 10 kHz prototype pump laser developed by Amplitude Laser Group emitting at 532 nm. The final output wavelength is obtained through second harmonic generation of laser emission at 1064 nm, typically from a Nd:YAG crystal. The laser scheme is shown in figure 3.2. The dichroic mirror DM2 allows

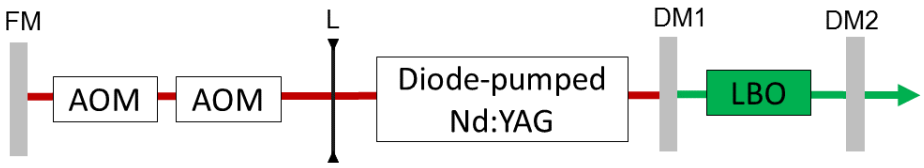

Figure 3.2: Schematic representation of the 10 kHz pump laser (Amplitude Laser Group prototype). FM-flat mirror; L-lens; AOM-acousto-optic modulator; DM1 and DM2-dichroic mirrors; LBO-second harmonic crystal.

high reflectivity at 1064 nm and high transmission at 532 nm and together with the flat mirror FM (high reflectivity 1064 nm) defines and closes the laser cavity. A convex lens L is placed in the cavity. The Nd:YAG crystal is diode-pumped and its infra-red emission is trapped in the cavity: two acousto-optic modulators (AOM), powered by an acoustic wave generated from RF signal and synchronized to a 10 kHz trigger, allow the Q-switch regime of the cavity. The 1064 nm laser emission is sent to a LBO crystal through the dichroic mirror DM1 (high transmission at 1064 nm and high reflection at 532 nm) for frequency doubling.

The LBO crystal and the diode-pumped Nd:YAG are water cooled at 21°. The generated second harmonic at 532 nm is finally emitted through the dichroic mirror DM2. Figure 3.3a shows the output power at 532 nm as a function of diode current. For maximal current of 32.5 A the pump delivers 93 W at 532 nm, with M^2 of 25 and pulse duration of 60 ns. The pump beam profile in the focus of a lens is shown in figure 3.3b.

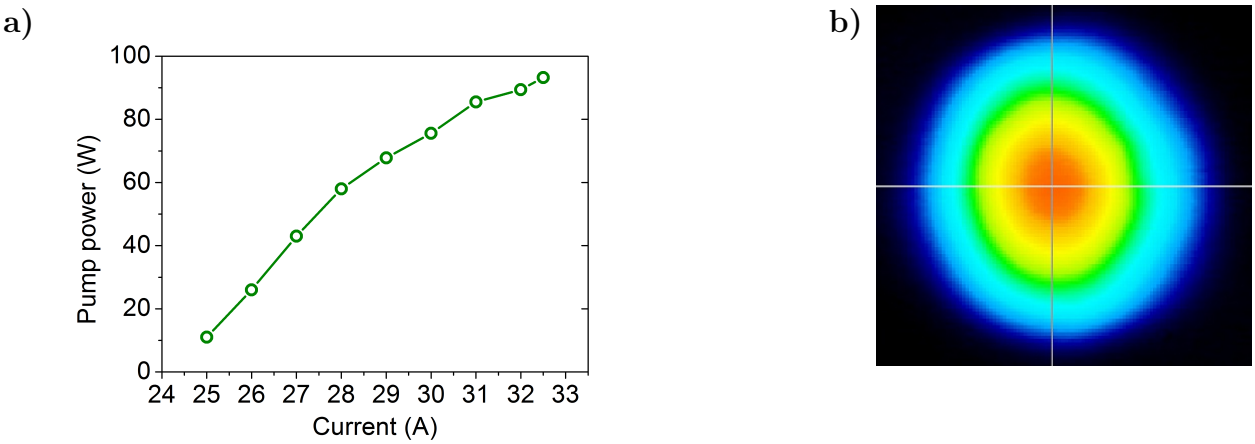

Figure 3.3: a) Extracted pump power at 532 nm as a function of the current applied to the diodes. b) Pump beam profile on the focus of a lens.

The pump laser can power different amplifiers so a distribution line is built at its output. This module consists on adjustable wave plates and polarizers. The fine tuning of the polarization allows to chose the amount of pump energy transmitted or reflected by the polarizers and consequently the amount of pump energy on each pumping line. The pump prototype is used on two amplification modules: the booster and the regenerative amplifier.

3.2.2 Femtosecond oscillator

The primary source is a 75 MHz, CEP stabilized commercial oscillator (Rainbow CEP3 from Spectra Physics). Ultrashort P-polarized pulses, with duration of 7 fs, are achieved via Kerr-lens mode-locking upon perturbation of the cavity length through the control of the position of a mirror in the cavity. Compression is performed with a pair of chirped mirrors. The output average power is 250 mW that corresponds to few nJ of pulse energy. The CEP stabilization is achieved with a commercial Menlo System interferometer and feedback loop. The CEP detection is performed with the difference frequency generation method and the acquired beat signal f_{CEO} is sent to a phase analyser. A second input $f_{rep}/4$ feeds the phase analyser which produce an error signal controlling a PID. The feedback for CEP stabilization relies on a piezoelectric motor that varies the insertion of a pair of wedges in the oscillator cavity and on a Acousto Optic Modulator (AOM) that varies the energy of the pump beam.

3.2.3 Öffner triplet stretcher

Before amplification the pulses are temporally extended in a grating based Öffner-triplet stretcher. The beam enters the dispersive module in P-polarization for maximizing the re-

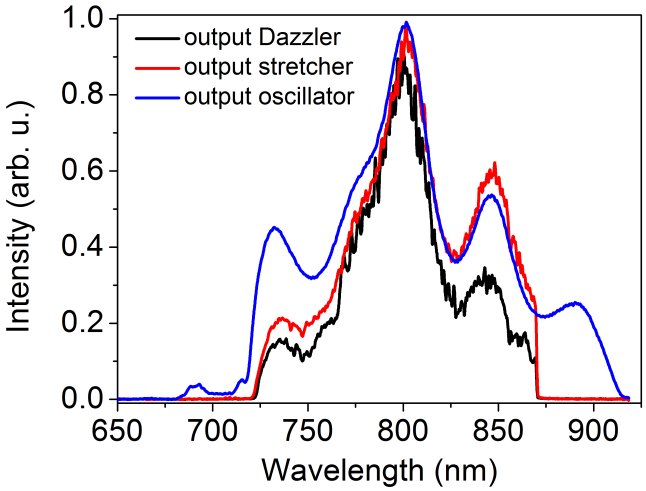

Figure 3.4: Spectra at the output of oscillator (blue line), stretcher (red line) and Dazzler (black line).

flectivity on optics surfaces. The radius of curvature of the silver concave and convex mirrors are respectively R_{conc} =1000 mm and $R_{conv} = -500$ mm. The grating is placed at 200 mm distance from the center of curvature and its groove density is 1200 lines/mm. The total grating distance is G_s = -299.23 mm. The incidence angle is 17.2° and the diffracted angle at 800 nm is 41.6°. Considering a double pass in the grating pair, the module induces a second order dispersion (GDD) of $1.8639 \cdot 10^6$ fs^2 and a third order dispersion (TOD) of $-5.0749 \cdot 10^6$ fs^3. The total stretching factor for double passing the grating pair is 5.5 ps/nm. Figure 3.4 shows the spectra at the output of the oscillator (blue line) and after propagation through the stretcher (red line). The dimension of the optics in the stretcher allows a spectral transmission of 145 nm at $1/e^2$. Proper dimensioning of the whole module, including optics size and distances, is a compromise between maintaining compactness and mechanical stability and providing enough dispersion without spherical aberration. In fact in order to avoid nonlinear phenomena during amplification, the equivalent grating distance should be scaled to provide enough dispersion. At the same time, increasing the distance between grating and concave mirror, as well as its radius of curvature, decreases the spherical aberration, but may induce some spectral losses at the concave surface because of the beam divergency. A certain encumbrance of the module is therefore unavoidable. The extended dimension of the stretcher and the size of the diffractive optics make the module sensitive to mechanical vibrations, that might cause variations of the induced dispersion and, more critically, CEP noise. Mechanical stability of the stretcher is improved with a proper design of grating and optics solid mounts which make the module less sensitive to mechanical vibrations, promoting CEP stability. A telescope for beam collimation is placed on the output line of the stretcher.
Considering a reflectivity of 90% on the grating surface, the module transmission is approximately 65%. Moreover an AOPDF (Dazzler by Fastlite) is placed on the output line of the stretcher. This device will be used to finely tune the pulse dispersion and optimize its temporal compression. An acoustic wave creates a transient diffraction grating in the Daz-

zler and imprints a specific spectral phase on the diffracted beam. The working principle of the Dazzler for pulse compression will be explained in the related section. For now we just cite that the useful output of the Dazzler is the diffracted beam and its diffraction efficiency is about 30%. As a consequence the pulse energy is further more decreased. The spectral transmission of the dispersive module spans over 145 nm bandwidth centered at 800 nm and allows the whole input spectrum to be diffracted, as shown in figure 3.4, where the black line represents the output spectrum of the Dazzler. The Dazzler turns the diffracted beam polarization by 90°, thus a half wave plate is necessary to bring the polarization back to the P-direction in order to seed the first amplification stage.

3.2.4 Enhancing the contrast: Booster

The main purpose of the booster amplifier is to enhance the seed energy before amplification in the regenerative cavity, in order to encourage the energy transfer from nanosecond to picosecond regime and improve the nanosecond-picosecond contrast after the regenerative amplifier. Moreover, a pulse picker is placed in the booster to select a train of 10 kHz pulses before further amplification.

The input line of the module includes an optical isolator, which protects the oscillator from stray reflections from the amplifier module. The isolator line is composed by a Faraday rotator included between two cube polarizers. The schematic is shown in figure 3.5. The

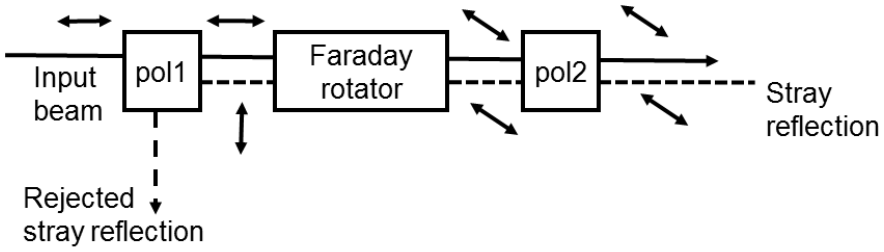

Figure 3.5: Schematic representation of optical isolator.

input pulse is P-polarized and the cube polarizer is aligned so that it transmits the p-component and rejects the S-component. The P-polarized pulse propagates into the Faraday rotator which turns the pulse polarization by 45° clockwise and a cube polarizer is aligned to completely transmit the pulse. A quarter wave plate turns the polarization again clockwise and the output beam is S-polarized and ready to be injected in the amplifier. If a S-polarized stray reflection comes back to the input line, first the quarter wave plate turns the polarization by 45°. The second cube polarizer completely transmits the stray beam. The Faraday rotator turns again the polarization clockwise and the output beam is again S-polarized, then deviated by 90° by the first cube polarizer.

The booster is a multipass amplifier in ring configuration and it is designed to allow in total 10 passes in the amplification medium, that is a flat surface Ti:Sa crystal, with antireflection coating, 15 mm long and 3 mm of radius and water cooled at 17°. The design of the booster is shown in figure 3.6. The pulse is sent to a concave silver mirror with a radius of curvature of R= 500 mm. The mirror focuses the beam on the Ti:Sa crystal at 250 mm

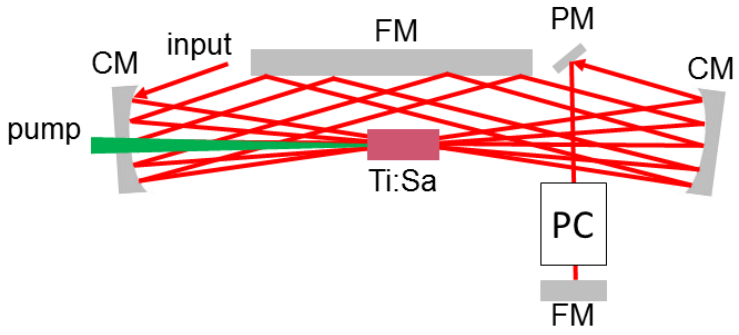

Figure 3.6: Schematic representation of booster. CM-concave mirror; FM-flat mirror; PM-pick-up mirror; PC-Pockels cell.

distance. After propagating through the crystal the beam is recollimated by a second concave mirror with the same features of the first one. The reflected beam propagates towards a flat silver mirror that folds the beam back to the first concave mirror. This mirror is placed beside the crystal at 50 mm from it. Depending on the input angle of the beam, it is possible to choose different number of passes, within the limit of the optics size. The incident angle in the crystal is kept as small as possible in order to maximize the spatial overlap between pump and seed mode. After 5 passes, the pulse is extracted by a pick up mirror. The following line includes a lens for adjusting the beam divergence and astigmatism and the pulse picker line: a cube polarizer for S-polarized pulse transmission and P-polarized pulse rejection, a Pockels cell and a quarter wave plate. The Pockels cell is aligned as a quarter wave plate with high voltage on (3 kV), and is used in double pass by means of a rear mirror. The signal powering the Pockels cell is a gate triggered by a 10 kHz signal. For double pass and high voltage on the Pockels cell turns the polarization by 90° of one pulse every 100 μs whereas the double pass in the static quarter wave plate turns back to S-polarization the 10 kHz train. After double passing the Pockels cell and quarter wave plate, the pulse train is composed by a MHz pulse train that is P-polarized including a 10 kHz train that is S-polarized. The MHz train is rejected by the cube polarizer and the 10 kHz train is again sent to the ring amplifier for 5 further passes in the crystal. After the 5 passes, the beam propagates through the Faraday isolator which at its end deviates the S-polarized beam by 90° towards the output line. This line is again equipped with another optical isolator to avoid stray reflection from the regenerative amplifier to the oscillator.

The booster amplifier works in small signal regime and is then far from the saturation condition. In this approximation we can consider that the crystal is not depleted during amplification. A telescope and a focusing lens on the 10 kHz pump line ensure the mode matching between IR and pump at the crystal surface. Figure 3.7 shows the IR and pump beam profile with corresponding beam diameters at $1/e^2$ at the crystal surface.

With a pumping power of 7.3 W and 10 total passes in the crystal, the total gain is 190. Since the pulse power is too weak for being measured with a powermeter, it has been measured with a photodiode and an oscilloscope, comparing the pulse amplitude before and after amplification. Without pump the signal level is really weak, about 2.9 mV in the oscilloscope. After amplification the signal amplitude reaches 550 mV.

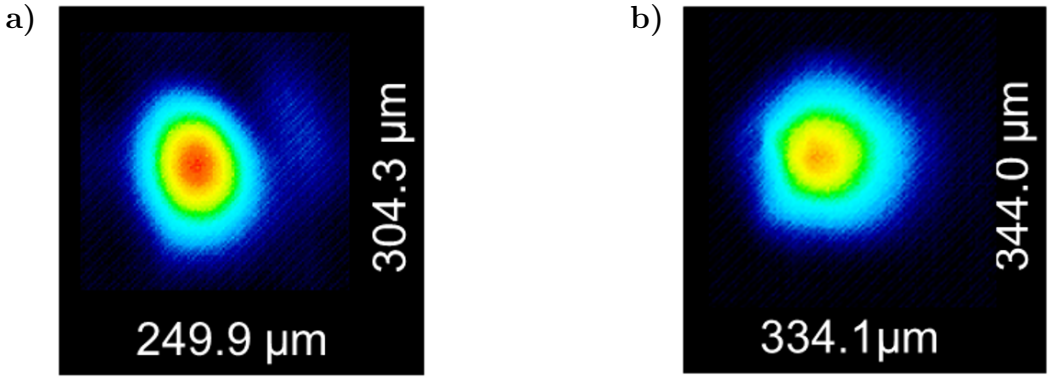

Figure 3.7: a) IR and b) pump beam profiles at the crystal surface of the booster amplifier. Beam diameters at $1/e^2$.

3.2.5 A novel design for the regenerative amplifier

In this section we present a novel configuration of the Ti:Sa regenerative cavity supporting 110 nm broad spectrum and delivering pulses three times more powerful than a single crystal cavity. The idea of a new design arises from the need of increasing the pulses average power without being limited by thermal effects that are detrimental for the pulse profile.

We will briefly describe the performances of a single crystal cavity, detailing its limitation in terms of power and profile quality, due to thermal effects. In this chapter we will give just few references of the thermal effects that will be largely discussed in chapter 4. Secondly a novel double-crystal design for regenerative amplifier will be proposed, showing its performances in comparison with those of the single crystal cavity. Lastly, the broadband working regime of the double-crystal cavity will be described, detailing the methods and results in terms of spectral width and power.
Double-crystal designs for regenerative amplifier have already been conceived and demonstrated for 1 kHz repetition rate in Yb:KYW [87] and Yb:CALGO [88] crystals. A double-slab configuration has also been designed for gain narrowing compensation in a multi-kHz (form 20 to 100 kHz) regenerative amplifier [89]. The idea is to combine different emission spectra of two Yb:KYW crystals aligned according to two different optical axis. The novelty introduced in our system consists in applying a double crystal configuration to a 10 kHz Ti:Sa based system.

3.2.5.1 Limit of single crystal regenerative amplifier

As already mentioned in chapter 2, the first stage of amplification is represented by the regenerative amplifier. In order to approach the demanded pulse requirements for strong field applications, many efforts are made to design and provide more and more efficient amplifiers in terms of pulse duration and average power. Obtaining pulses with at the same time broadband spectrum and high average power is not obvious because the two phenomena are in some terms competing with each other. The multipass configuration of the regenerative cavity sets a limit to the output spectral width due to the gain narrowing effect[31]. Due to its gaussian-like shape, the spectral emission band of the Ti:Sa promotes the amplification

of its central wavelengths, concentrating the gain on a 40 nm bandwidth centered at 800 nm. This phenomenon is emphasized in a regenerative amplifier due to the high number of passes inside the crystal. In order to counteract the spectral narrowing of the amplified pulses, spectral filters can be used to homogenize the amplification over the bandwidth of the injected signal, and obtain broad amplified pulses. The working principle of a programmable filter will be detailed in section 3.2.5.3 but the fundamental idea consists in creating spectral losses where the gain is maximal in order to encourage amplification of spectral components at the edge of the signal spectrum. As the filter creates losses, the average power of the amplified pulses decreases and a higher pumping power is needed to compensate for energy losses. At 10 kHz repetition rate pumping with high power causes thermal heat to accumulate in the Ti:Sa crystal. Two main phenomena arise as consequence: refractive index gradient through the length of the crystal and thermo-mechanic deformation of the crystal surfaces. These two effects are taken into account defining an equivalent thermal lens generated in the crystal, which is detail in chapter 4. Careful dimensioning of the crystal and cooling system can help reducing the heat load but the thermal effect remains critically influenced by the pump power.

Preliminary studies on the performances of a single crystal regenerative cavity have been conducted: figure 3.8 shows the evolution of the IR beam profile and output power for increasing pump power in a standard single crystal cavity. The cavity is designed considering

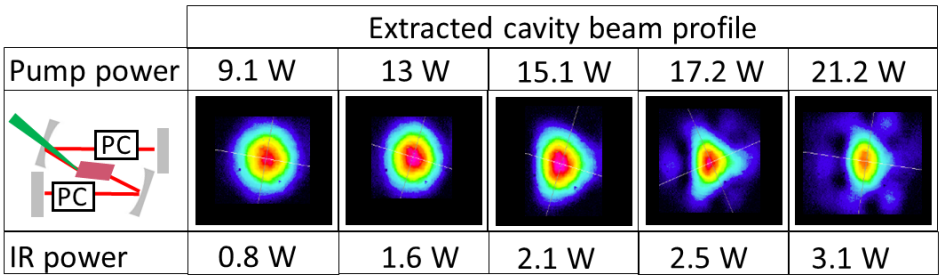

Figure 3.8: Evolution of the IR beam profile and output power as a function of the pump power for the standard single-crystal regenerative amplifier configuration.

a pump power of 15 W and beam radius at the crystal position of 150 μm at $1/e^2$. The Ti:Sa crystal is Brewster cut with 3 mm radius and 20 mm length and it is water-cooled at 19°. With this values, the thermal focal length is calculated to be as short as 180 mm. With this design, the performances of the cavity are tested for different pump values, from 9 W to 21 W. As the pump power increases the thermal lens focal length decreases. Figure 3.9 shows the stability parameter $(A+D)/2$ for an equivalent single crystal cavity as a function of the thermal lens focal length [90]. In order to design a stable resonator, the stability parameter value should be included between 1 and -1. As the focal length becomes shorter, the stability parameter decreases and the cavity approaches its stability limit. Figure 3.9 shows that for values of thermal lens focal length lower than 90 mm the stability parameter converge rapidly to -1. We can consider 90 mm as the lowest threshold value for the thermal lens focal length. The IR output power for increasing pump power (figure 3.8) is not limited by the thermal effect, in fact the cavity can deliver pulses up to 3.1 W output power. However

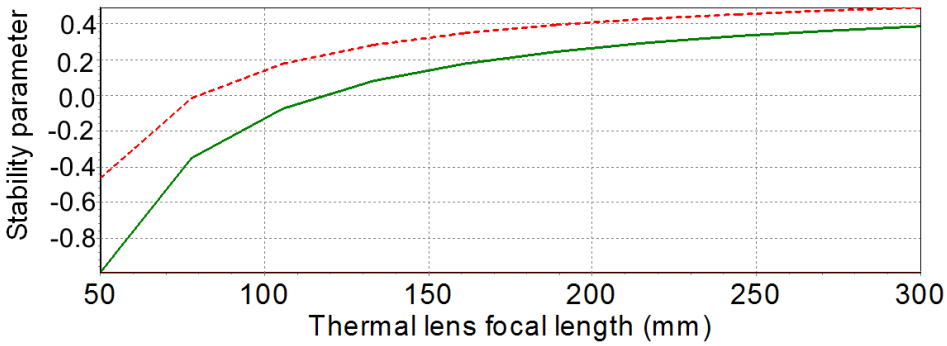

Figure 3.9: Stability parameter as a function of the thermal lens focal length for single crystal regenerative amplifier, for both beam dimensions, the vertical (S-dashed red line) and the horizontal (T-green line).

thermal effects and the loss of stability have a detrimental effect on the beam profile. The condition of a clean beam profile limits the pump power to 14 W and consequently the IR output power to 1.8 W.

3.2.5.2 Double-crystal regenerative amplifier

In order to overcome the power limit caused by the thermal effect we propose a new design of the regenerative cavity based on a double crystal configuration. Each crystal is pumped with maximum power of 14 W, maintaining a good beam profile and delivering pulses whose energy is up to three times higher than the standard regenerative cavity.

Design and methods The fundamental idea of the double-crystal amplifier consists in creating an imaging system inside the cavity. Figure 3.10 shows the equivalent optical system in terms of refractive optics. If a lens with focal length $f/2$ is interposed between two lenses

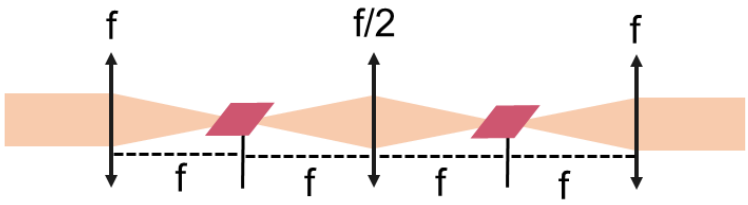

Figure 3.10: Concept of imaging system used in the design of double crystal regenerative cavity.

with focal length f at a distance $2f$ from each of them, the focus of the first lens is imaged in the focus of the second lens.
The innovative double crystal cavity design is shown in figure 3.11. Two concave mirrors, CM1 and CM3 with radius of curvature 500 mm define the cavity edges, whereas the concave mirror CM2 with radius of curvature 250 mm is used as the imaging optics. Each crystal is pumped by two independent arms. In order to maintain the compactness of the design and

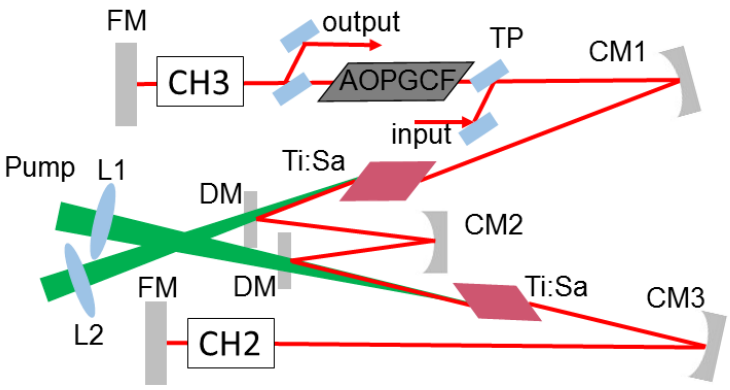

Figure 3.11: Double-crystal regenerative amplifier. CM-concave mirror, FM-flat mirror, CH2-injection and CH3-extraction Pockels cells, L1 and L2 pump focusing lens,TP-thin polarizers, DM- dichroic mirror, AOPGCF - Acousto-optic programmable gain control filter.

to not clip the pump beam propagating towards the crystals, two flat dichroic mirrors (DM) are used to fold and unfold the beam before and after reflection on the imaging mirror. The two mirrors allow high transmission at 532 nm and high reflection at 800 nm. The double-crystal cavity assumes then a W-like configuration. The mirrors employed in the cavity support high reflectivity over a bandwidth of about 140 nm at $1/e^2$ centered at 800 nm. The mirror reflectivity has been tested with P-polarized light, and the input spectrum was limited by the stretcher spectral transmission. Figure 3.12 shows the measured spectra after reflection on the dichroic mirror (DM) and on the concave mirror (CM). Two Ti:Sa

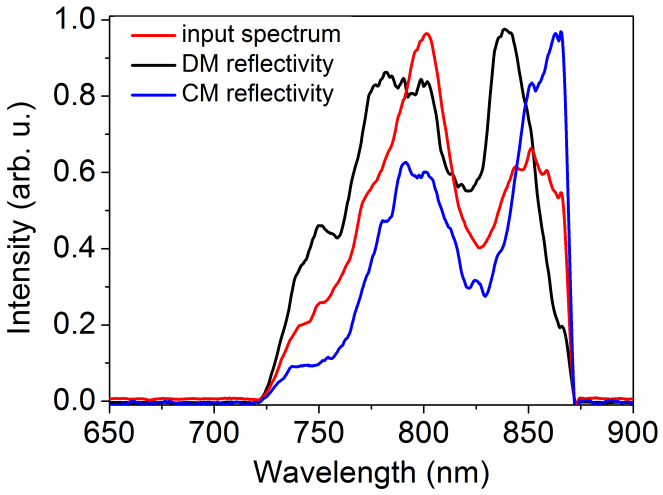

Figure 3.12: Spectral reflectivity of DM-dichroic mirror (back line) and CM-concave mirror (blue line); the testing input spectra is in red line.

brewster-cut crystals are used as amplification media, with round section of 3 mm radius and 20 mm length. The crystal doping ensures an absorption of 90% of the pump energy. The

two crystals as well as the two Pockels cells for injection and extraction are water cooled at 17°. This parameter is experimentally chosen as a compromise between keeping the crystal temperature low enough and avoiding condensation on the crystal surface. All the cooling mounts are designed to allow direct contact between water and optical component. As evident from figure 3.11, the double cavity is constituted by two single crystal sub-cavities. The novel double crystal design falls under the category of periodic resonators, i.e. resonators composed of optically equivalent subsections. Power scaling through multi-crystal design for circumventing the limit imposed by thermal effects has been theoretically demonstrated by Eggleston [91]. In his work Eggleston demonstrates two main concepts. First, for a single crystal resonator it exists a range of thermal lens focal length values defining the condition of resonator stability. Second, if the resonator is composed by equivalent and symmetrical sub-resonators, the power range for stable operation (which depends on pump power and as a consequence on thermal lensing) scales linearly with the number of periods (or sub-resonators). The symmetry requirement in a periodic resonator is strongly underlined in Eggleston work, as a prerequisite for optimal power scaling. In our Ti:Sa double crystal cavity symmetry is assured by the imaging mirror, as well as by same pumping conditions for the two crystals. However experimentally the position of the imaging mirror may differ from the perfect symmetric condition, as a reflect of the fact that the two sub-cavities may not be exactly equivalent (uncertainty from crystal fabrication) and the pump power may fluctuate in the two arms.

A preliminary simulation of the double cavity design has been performed with the software Rezonator in order to find the best distances and to study stability, collimation and divergence of the beam inside the cavity. The cavity has initially been designed to support a thermal lens focal length of 180 mm, in order to provide a comparison with the single crystal cavity, but if the cavity is well designed it can support a large range of thermal focal lengths. In particular the position of the imaging mirror CM2 is critical for preserving the stability of the cavity as well as for keeping the beam collimated, necessary condition to benefit from a homogeneous effect of the Pockels cell. Figure 3.13.a shows the evolution of the beam radius at $1/e^2$ propagating in the cavity for different values of thermal lenses and for optimal positioning of the imaging mirror CM2. Green line reproduces the evolution of the horizontal radius while the red line is the vertical radius. Even though the design is optimized for a thermal focal length of 180 mm, the cavity maintains its stability even for focal length values twice bigger (360 mm) or smaller (90 mm). Recalling figure 3.9, 90 mm corresponds to the lowest value of thermal lens focal length for preserving resonator stability in a single crystal regenerative amplifier. Since the double crystal cavity is composed by two independent and equivalent sub-cavities, for symmetrical reason the stability range as a function of the thermal lens focal length in the single crystal cavity is conserved in the double crystal cavity. Knowing that theoretically also the double crystal cavity is stable for $f_{th} \geq$90 mm, we decided to show here the evolution of the beam profile in the cavity, rather than the stability parameter that has been already shown in figure 3.9. Only for f_{th} =90 mm, the beam acquires a small ellipticity in the injection arm. Figure 3.13.b shows the same evolution but for a different cavity design, where the distance between the imaging mirror CM2 and each of the two crystals has been shortened by 1 cm. In this case, the cavity is optimized only for f_{th} =90 mm, whereas for higher values of focal lengths the IR beam becomes more and more astigmatic, both in the injection and in the extraction arm (f_{th} =180

mm). For higher values of focal lengths (f_{th} =360 mm) the radius diverges so much that the simulation cannot provide anymore its evolution and the cavity becomes unstable.

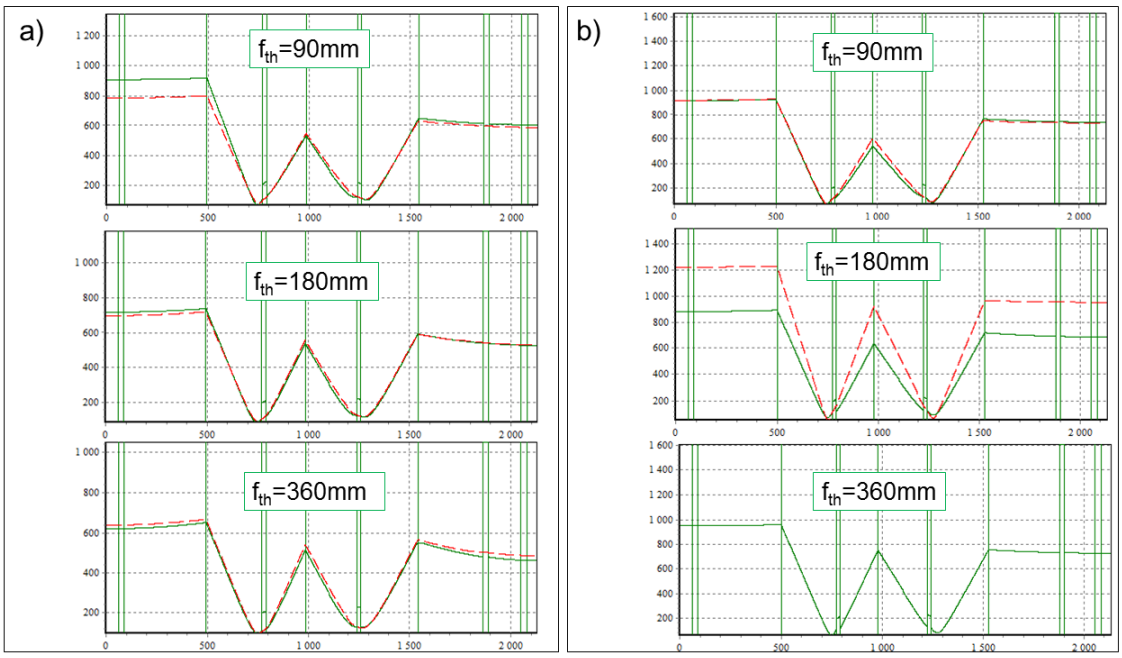

Figure 3.13: IR beam radius evolution for different values of focal lengths, 90 mm, 180 mm and 360 mm, for a) optimized cavity design and b) alternative cavity design whit 1 cm shift of imaging mirror CM2. Green line-horizontal radius, red line-vertical radius at $1/e^2$.

In the next discussion we will detail the narrowband mode regime of the cavity, considering that, even when not used but inserted in the cavity, the AOPGCF induces some energy losses on the IR beam.

Working principle Injection and extraction of the IR signal are triggered by two Pockels cells powered by 3 kV high voltage and coupled with two pairs of thin polarizers. The Pockels cell CH2 enables the injection of the chirped signal from the booster whereas the Pockels cell CH3 allows the extraction of the amplified signal. The injection Pockels cell CH2 is regulated as a quarter wave plate for single pass with high voltage off. With high voltage on it behaves as a half-wave plate on single pass. The extraction Pockels cell CH3 is transparent with high voltage off and behaves as a quarter wave plate with high voltage on. Two pairs of polarizers allow high reflectivity of S-polarized beam, and consequently transmission of P-polarized beam. The working process is the following:

- The Pockels cell CH2 is timed such that it remains off untill the pump energy is completely stored in the Ti:Sa crystals. When off, CH3 is transparent. In this time interval CH2 behaves like a quarter wave plate on single pass, and a half-wave plate on double pass. Any IR emission produced in this condition or any pulse injected in the cavity is rejected by the thin polarizers due to the periodical polarization switch for each round trip in CH2.

- When the pump energy is fully absorbed by the gain medium, the IR pulse to be amplified (i.e. the seed) can be injected and trapped in the cavity. The seed enters in S-polarization, propagates back and forward in CH2 causing a change in its polarization from S to P; in this moment high voltage is provided to CH2 that switches to half wave plate for single pass and that is transparent for double pass. Since CH3 does not induce any polarization switch, the pulse is trapped inside the cavity in P-polarization. If no seed is injected in the cavity, the configuration CH2 on - CH3 off still allows the cavity to lase: the P-polarized component of fluorescence spontaneous emission from the pumped crystals is trapped in the cavity and undergoes amplification. The characteristic time of this laser emission is on the nanosecond scale. In practice it is preferable to optimize the cavity alignment in nanosecond regime before injecting the picosecond seed. When the seed enters the cavity, a precise overlap between its propagation direction and the cavity axis is necessary to promote energy conversion from the nanosecond scale to the picosecond scale.

- At maximum of the pulse amplification, Pockels cell CH3 is switched on to attain a status of quarter-wave plate. On double passing through CH3 the pulse polarization changes from S to P and the pulse is extracted by the thin polarizers.

Performances The performances of the new designed regenerative cavity have been tested both in nanosecond regime and picosecond regime. The two crystals are optically pumped by the 10 kHz prototype pump laser from Amplitude Laser Group, with total average power of 30 W, 3 mJ pulse energy at 532 nm central wavelength, on the regenerative amplifier line. The pump is shared in two arms by mean of a 50%/50% beam splitter and focused on each crystal by two 333 mm focal length focusing lenses. The power reaching each crystal surface is reduced by losses on the pump focusing line: the first crystal is pumped by 14 W and the second crystal by 13.5 W, for a total pump power of 27.5 W. Figure 3.14a shows the seed beam profile and figure 3.14b the pump beam profile at the surface of the second crystal.

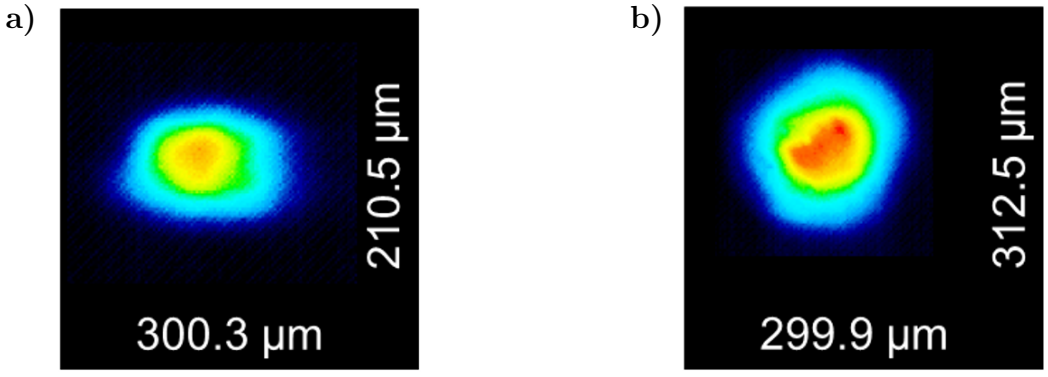

Figure 3.14: a) IR seed and b) pump profiles with corresponding diameters at $1/e^2$ at the crystal surface in the regenerative amplifier.

The ellipticity of the seed is not critical, since the beam profile of the amplified pulse is determined by the cavity design and the pump profile, that maintains a good ellipticity with a beam radius of 150 μm at $1/e^2$.

Figure 3.15a shows the output powers for both nanosecond and picosecond regimes for increasing pump powers.

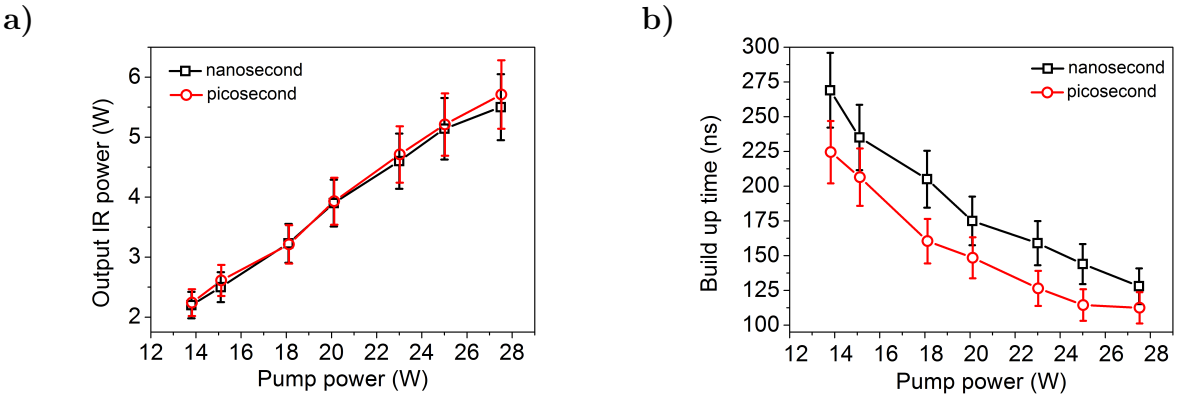

Figure 3.15: Performances of the double crystal regenerative amplifier in nanosecond and picosecond regimes in terms of a) IR output power and b) bulid up time. The error bars represents the 10% of incertitude in the measurement due to alignment optimization.

For a total pumping power of 27.5 W the new design regenerative amplifier delivers pulses with energy up to 5.5 W, with an RMS stability of 0.3 % over ten minutes, that is three times more power than the single crystal cavity. The double crystal cavity delivers the same output IR powers for the two regimes, meaning that the amplification process is mostly driven by the pump energy rather than the seed energy, that is at the nJ level, thus negligible compared with the pump. The energy conversion efficiency is 20% and the amplification factor is of the order of 10^6.

As shown in 3.15b, the build up time decreases for increasing pump power. The build up time is shorter for picosecond regime than for nanosecond regime. This can be explained as follows: in first approximation we consider the energy of the first spontaneous emission (not yet amplified) at the nJ level; the seed reaching the amplifier is also at the nJ level, and consequently the injection process increase twice or three times the injected energy on the crystal. As already demonstrated, the injected energy remains negligible compared with the energy conversion from the pump but since the injection is stronger, the amplification process will be faster and the build up time shorter. The cavity round trip time has been calculated to be around 14.5 ns, then the build up time difference between nanosecond and picosecond regime is equivalent to 2 or 3 cavity round-trip. For optimal working conditions, i.e. for total pump power of 27.5 W the build up time in picosecond regime is approximately 112 ns, which corresponds to 8 round trips in the cavity.

Figure 3.16 shows the IR amplified beam profile in picosecond regime as a function of the pump power.
The cavity design allows to generate pulses with a good beam profile quality over a broad range of pump power. The beam profile evolution shown in picture 3.16 corresponds to the pump power increment. At maximum pump power the ellipticity value for this series is 85% (third profile from the left on bottom). However optimization of Pockels alignment lead to a further optimization of the ellipticity value up to 91% (fourth profile from the left

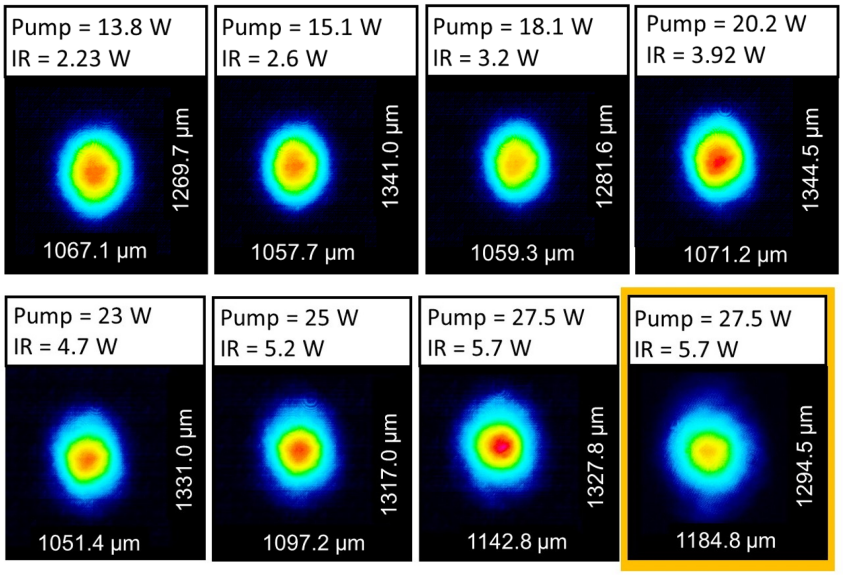

Figure 3.16: IR output profile with corresponding diameters at $1/e^2$, and power for increasing pump power for picosecond regime of the regenerative amplifier. The fourth profile from left on bottom corresponds to optimization of Pockels cell alignment.

on bottom). Due to shared thermal effect in the two crystals, the profile does not undergo detrimental effects, as is the case for the single crystal cavity (cf figure 3.8) and it maintains a good ellipticity, better than 85%. In terms of output power, the new design cavity delivers pulses with three times more power compared with a standard cavity, as shown in figure 3.17. In the same figure, one can note that the double crystal amplifier does not reach the saturation level, meaning that we could in principle increase the pump level also because, as we saw previously in the simulation, the cavity maintains its stability for even shorter thermal lens focal lengths, at the price of an increasing ellipticity on the injection arm. The limiting factor in increasing the pump power is actually the damaging threshold of the optics in the cavity. Particularly critical are the optics placed closer to the two crystals, i.e. the two folding flat mirrors around the imaging mirror. In this position the beam is small and the power density can reach dangerous levels that may induce damage on the optics. In conclusion, not only the position of the concave mirror is critical for the stability of the cavity but also the positioning of the two folding mirrors, for avoiding damaging.

Figure 3.18a shows the seed spectrum before amplification and 3.18b the nanosecond and picosecond amplified output spectra for 27.5 W total pump power. The seed spectrum has been taken after a first pass in the injection Pockels cells CH2, that cleans the 10 kHz pulse train from parasitic MHz pulses whereas the amplified spectra are taken after extraction. The nanosecond amplified spectrum is not larger than 38 nm at FWHH, even though the emission bandwidth of the Ti:Sa spans over 180 nm bandwidth at FWHM. This spectral shrinking is due to the gain narrowing that becomes critical when multi-passing the amplification medium. As consequence, even though the seed spans over a broad spectrum, only a 38 nm bandwidth around 800 nm can be amplified. Moreover the picosecond amplified spectrum shows a further spectral narrowing to 30 nm FWHM and a red-shift when compared to the nanosecond amplified spectrum. Because of its up-chirp, red spectral components of the

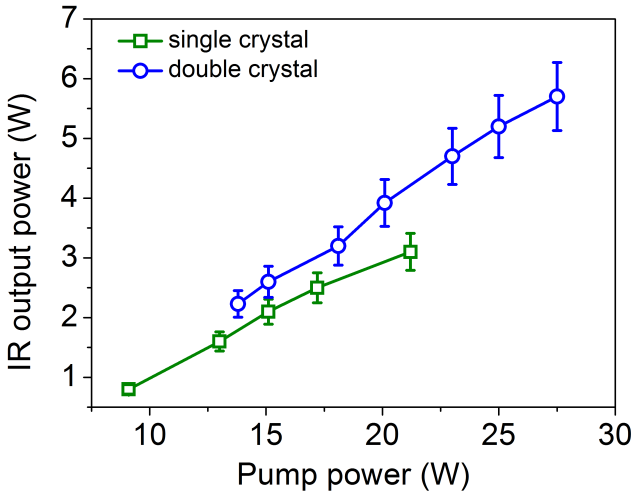

Figure 3.17: IR output power in picosecond regime as a function of pump power for single crystal (green line) and double crystal (blue line) regenerative amplifier. The error bars shows that measured values can vary of ±10% depending on alignment optimization.

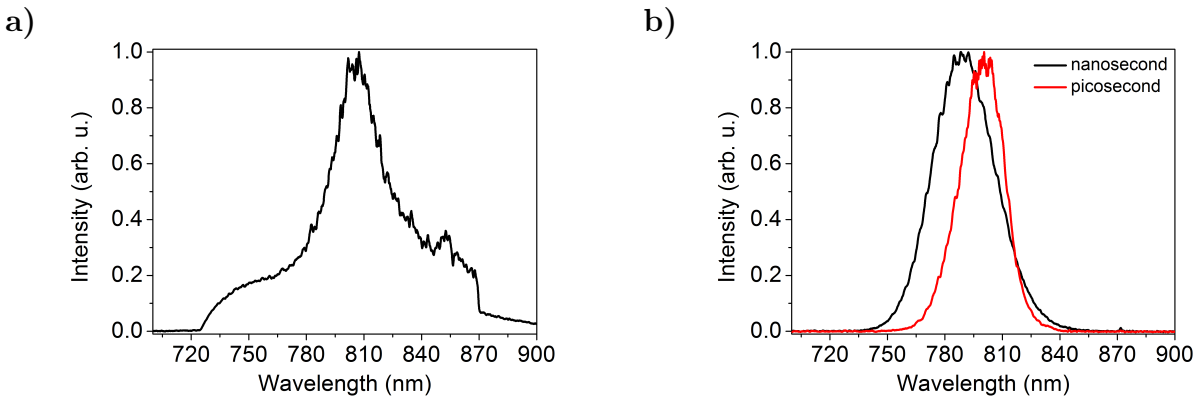

Figure 3.18: a) Seed spectrum and b) output spectra after amplification for nanosecond (black line) and picosecond (red line) regime.

seed spectrum are amplified earlier and as consequence more strongly, causing the whole spectrum to shift to higher wavelengths.

3.2.5.3 Double crystal regenerative amplifier in broadband mode

State of the art The gain narrowing effect in gain medium amplifier [31] limits the amplified pulse bandwidth to not more than 40 nm. The amplified spectral intensity $I_{out}(\omega)$ can be written as follows [32]:

$$I_{out}(\omega) = I_{in}(\omega)G^n(\omega)T^n(\omega) \tag{3.1}$$

where $G(\omega)$ is the frequency-dependent gain, $T(\omega)$ the frequency-dependent transmission function of the amplifier and n the number of passes through the amplification medium. Equation 3.1 suggests two ways to counteract gain narrowing. One way consists in enlarging the gain bandwidth. This has been proven in Nd:Glass laser [92, 93], where different amplification media with different peak gain wavelengths have been simultaneously used to broaden significantly the amplification bandwidth. The second method consists in inducing some frequency-dependent losses, reducing the amplification at the spectral peak of the gain. This concept has been successfully implemented in several ways that can be categorized in three concepts.

- The first one consists in using intra-cavity spectral filters. The bibliography provides several examples. Barty et al. [32] proposed an air-spaced, angle-tuned etalon, composed by two uncoated BK7 plates spaced by air. By finely adjusting the plates spacing to an odd multiple of quarter the central wavelength by means of a piezoelectic controller, it is possible to introduce relative attenuation at the spectrally central line of the medium gain. With this technique transform limited pulse duration below 18 fs has been proven. The same author proposed also two other alternative methods [76]. One is based on a single birefringent quartz plate as spectral filter introducing a fixed amount of loss for each pass of the pulse. The second way is based on using a spatial mask coupled to a prism pair at one end of the regenerative cavity. The prism pair induces a spatial chirp on the pulse; with a circular-shaped card with variable attenuation factor, different wavelengths undergo different attenuation factors. The three methods have been applied to the same laser system and demonstrate a spectral broadening of the amplified pulses up to nearly 100 nm, on a square shaped spectrum. Intracavity spectral filters are in general a quite simple and efficient solution for gain narrowing compensation; the main drawbacks are lack of programmability, and generation of artifacts.

- The second solution for inducing spectral losses consists in wavelength selective pumping. The concept has been originally proposed by Christov and Danailov [94, 95]: the idea consists in spatially disperse the seed beam inside the amplifier and choose the amount of energy to transfer to each wavelength. This method has been successfully demonstrated by Hauri et al. [96] in a Ti:Sa based amplifier, reaching 120 nm broad amplified spectra. This technique theoretically does not induce any loss, so that all the energy stored in the gain medium is ideally available for pulse amplification. The drawback consists on the implementation complexity.

- A third method is represented by programmable filters that can be intra or extra cavity. The first example is proposed by Weiner, based on a multielement liquid-crystal phase

modulator [97]. A pair of gratings is placed in the focal planes of a unit-magnification confocal lens pair and a liquid-crystal phase modulator is inserted midway between the lenses. The first grating and lens spatially separate the spectral component of the input pulse. The phase modulator modifies the spectrum according to the voltage applied to the liquid crystal. The second couple of lens and grating recombine the different frequencies into a single collimated beam. By this way, any user defined pulse shape can be imprinted in the spectrum.
Verluise et al.[98] proposed a different approach, based on an acosto-optic programmable dispersive filter (AOPDF). As it will be explained in the section about compressor, the acoustic wave in the acousto-optic crystal create a transient diffraction grating. A pulse propagating in the module undergoes diffraction. It is possible to shape the acoustic wave so that it acts as an amplitude gate. Programming an amplitude mask with a transmission minimum at the spectral maximum of the gain allows to counteract the gain narrowing. However the AOPDF output is the diffracted beam, so that a big part of the pulse energy is wasted. Pulse duration reduction in Ti:Sa systems has been demonstrated [99].

In the following discussion we will describe an alternative method proposed by Oksenhendler et al. [34] in order to counteract gain narrowing effect during amplification. The technique is based on an acousto optics programmable filter, where the usable output is the transmitted beam, not the diffracted beam, circumventing the problem of too high energy losses.

The Mazzler The acousto-optics programmable gain filter (AOPGCF - Mazzler by Fastlite) is an intracavity device. It is based on a 25 mm long Brewster-cut birefringent crystal (TeO_2). The crystal is seeded by an acoustic wave, generated by a transducer from an RF input signal and synchronized to the optical signal propagating in the Mazzler. The acoustic wave reproduces spatially the RF signal through the TeO_2 crystal, creating a diffraction grating with periodicity defined by the RF signal. The pulse propagating in the TeO_2 crystal is partially diffracted and partially transmitted. Since it is possible to finely regulate the spectral bandwidth of diffraction as well as the power of the acoustic wave, it is then possible to create tunable losses in the transmitted beam. If the losses are created where the gain of the Ti:Sa is higher, i.e. around 800 nm, then amplification of side spectral components is encouraged, leading to a broader amplified spectrum. Figure 3.19 shows the effect of the Mazzler on the propagating beam. The working principle of the Mazzler is quite simple: the controlling software acquires as input the amplified narrow spectrum and calculate the acoustic wave in order to diffract central components of the spectrum. The user can chose the power of the acoustic wave which is launched on the TeO_2 crystal and the propagating beam is spectrally shaped. In order to obtain a broad spectrum it is necessary to reiterate the process with increasing acoustic power until the desirable bandwidth is reached. The process itself is simple but few side-effects must be taken into account while applying it. First and foremost the energy losses: as part of the energy is diffracted, increasing the number of loops and broadening the spectral band of the pulse means decreasing its energy. Secondly, the synchronization of the acoustic wave should be finely chosen, to allow perfect temporal match between the acoustic wave and the pulse propagating in the Mazzler. Third, the alignment of the Mazzler is critical for efficient process, as well as for the stability of the

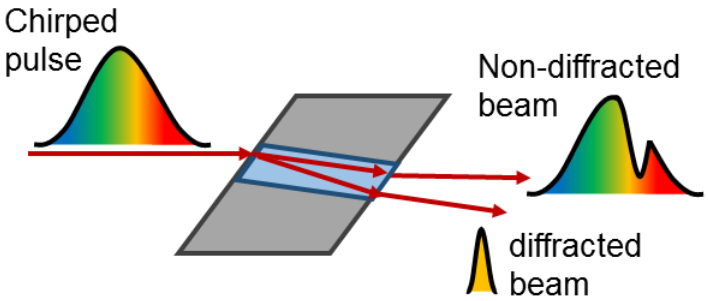

Figure 3.19: Schematic representation of Mazzler principle.

cavity.

Results Figure 3.20 shows the output spectra of the double crystal regenerative amplifier for increasing number or Mazzler loops. The bandwidth gets broader and reaches 110 nm at FWHM after 4 iterations.

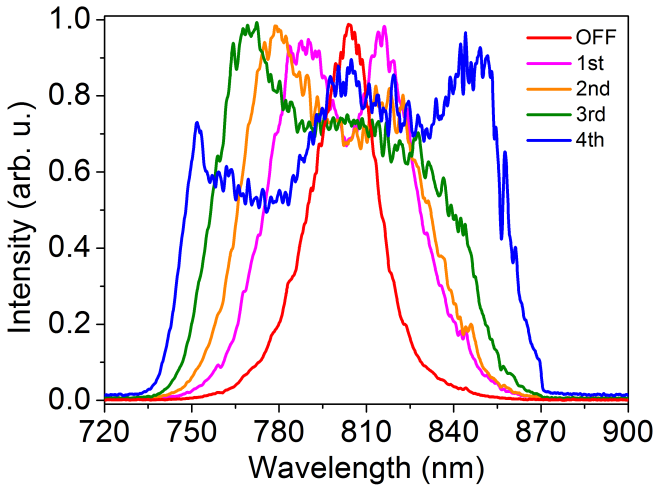

Figure 3.20: Regenerative amplifier output spectra for consecutive Mazzler loops.

Figure 3.21a and 3.21b resume the data in terms of respectively output power and FWHM bandwidth of the IR pulse for different number of iterations. Comparing the narrower spectrum (28 nm at FWHM for 5.5 W of output power) and the broader spectrum (110 nm at FWHM for 2.7 W of output power), we notice that after the 4 iterations, even if the pulse loses half of its power, its bandwidth is 4.5 times broader than the narrow band pulse. Finally, in order optimize the energy emission in broad band mode, the delay of the extraction Pockels cell CH3 needs to be increased by an amount of time equivalent to at least one round trip.

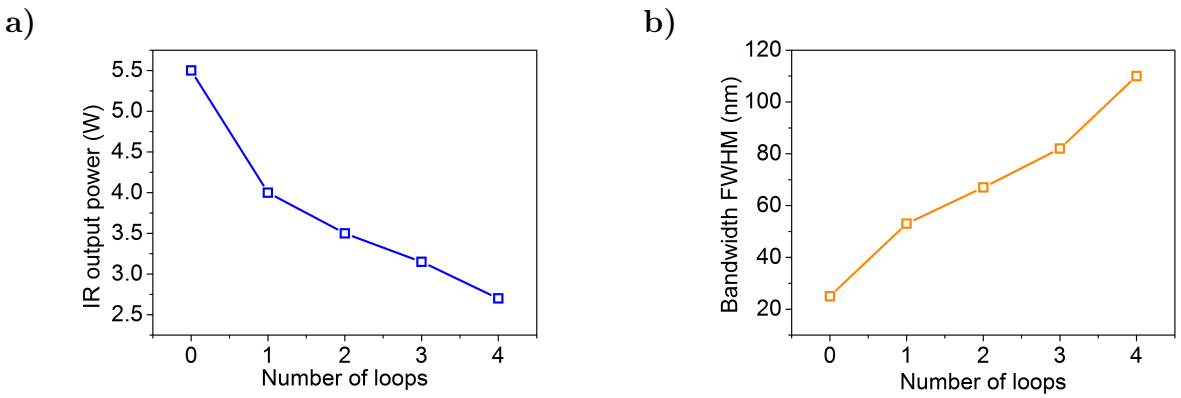

Figure 3.21: Performances of the regenerative amplifier for consecutive Mazzler loops in terms of a) IR output power and b) FWHM bandwidth.

3.2.6 Temporal compression

After amplification and spectral broadening the pulses are sent to the compressor to shorten their duration. The dispersive module is grating based and its configuration is designed in order to compensate the dispersion introduced by the stretcher as well as by the amplification stages. A telescope at the output of the regenerative amplifier magnifies the beam of a factor of 10, in order to keep the beam fluence on the grating surface below the damage threshold and limit the power density. The two gratings are spaced by 383 mm and their groove density is 1480 lines/mm. The literature provides studies [65] and examples [63, 64] that a groove mismatch between stretcher and compressor gratings allows better compensation of higher order dispersion. For this purpose, our couple stretcher-compressor is characterized by respectively 1200 groove/mm and 1480 groove/mm grating's groove density.
The incidence angle at 800 nm is 45.45°. With this parameters the total second order dispersion introduced by the compressor is -2.21·10^6 fs^2 and the third order is 4.84·10^6 fs^3. A picture of the compessor is shown in 3.22. The compressor includes newly-designed optical

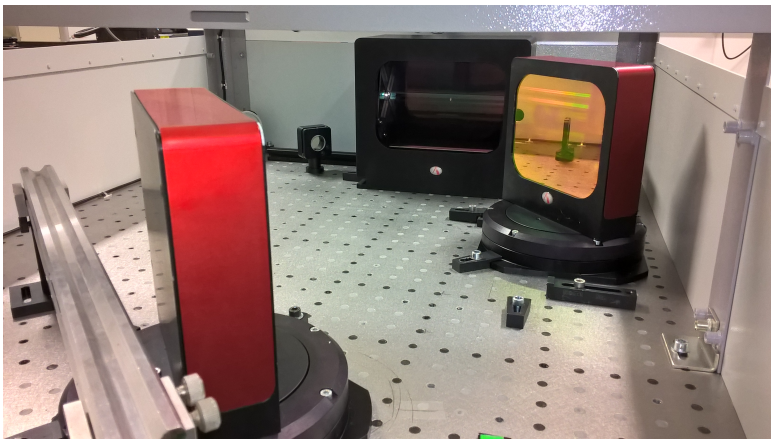

Figure 3.22: Picture of the grating-based compressor.

mounts, free of most of the adjustment settings, and particularly bulk and solid. These mounts are designed to make the compressor less sensitive to mechanical vibrations and compatible to a high degree of CEP stability. On the other hand, if the lack of regulation tools increases the mechanical stability of the module, it also makes it more challenging to align. In particular the grating mounts are equipped only with a rotation stage for regulating the incident angle and two aligners for tuning the diagonal position of the grating surface. There are no spring-based tools for micro-metric adjustment, that would be sensitive to vibrations. The alignment is made by hand, checking the compression optimisation through plasma generation and pulse duration measurement.

3.2.6.1 Wizzler: ultrafast pulse measurement system

The measure of the pulse duration is performed with the Wizzler by Fastlite. This tool is based on the so-called *XPW effect* or Cross-polarized Wave Generation [100, 101]. The XPW is a third order non-linear effect: when a high-intensity pulse propagates through a plate (usually BaF_2 or LiF), a replica of the pulse with orthogonal polarization is generated. The amplitude of the newly-generated wave is linked to the amplitude of the input wave by the relation:

$$E_{XPW}(t) =\propto |E_{IN}(t)|^2 \cdot E_{IN}(t) \tag{3.2}$$

The XPW replica is equivalent to the input pulse amplitude, filtered by its own temporal intensity. The XPW pulse is demonstrated to have a broader spectrum and a flatter phase with respect to the input pulse [102], and it can be used as a reference for measuring the pulse duration.
The Wizzler measurement technique is called Self-Referenced Spectral Interferometry (SRSI), shown schematically in figure 3.23. A replica of the main pulse to be measured is firstly gener-

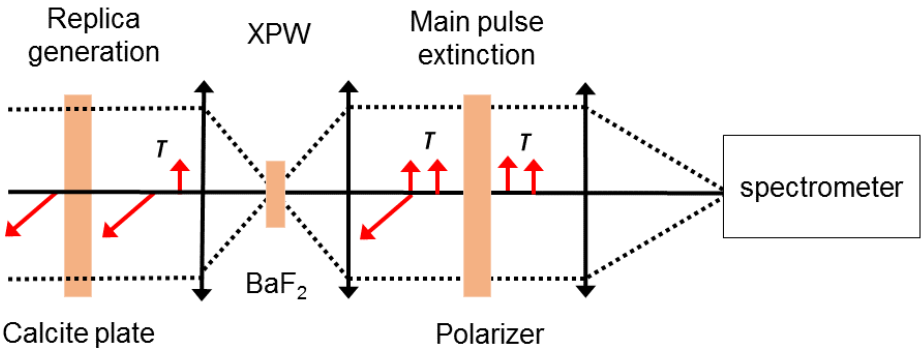

Figure 3.23: Schematic representation of Self-Reference Spectral Interferometry.

ated with perpendicular polarization and delayed by means of a birefringent plate (Calcite). The main pulse is used to create a XPW signal with broader spectrum, flatter phase and polarization parallel to the first replica. A polarizer transmits only the replica and the XPW signal that propagate towards a spectrometer with delay τ between each other. The spectrometer detects the interference spectrum between the first replica and the XPW reference signal. The Fourier Transform Spectral Interferometry algorithm (see chapter 5) is applied

and both spectral phase and intensity of the replica are extracted. Since it is based on a third order effect, the Wizzler technique works only for a rather compressed pulse, i.e. its duration should not exceed twice the transform limited duration. A preliminary accurate alignment of the compressor is then necessary for obtaining a valid measurement. On the other hand, the Wizzler system represents an extremely compact tool, allowing to measure pulse duration below 20 fs. It is particularly advantageous for efficient compression when coupled with the Dazzler, since it can apply an active spectral phase correction and match the transform limited pulse duration.

3.2.6.2 Dazzler

As already described in chapter 2, the compressor benefits of two degrees of freedom for dispersion compensation: the grating distance and the incidence angle. Tuning these parameters allows to finely compensate for second and third order dispersion, that are the most detrimental for pulse duration. However, as the pulse approaches the single cycle regime, higher dispersion orders become critical for efficient compression down to the transform limited duration. The groove density mismatch between stretcher and compressor grating allows better compensation of high order dispersion. In order to further optimize the compression we equipped our laser system of an acousto-optic programmable dispersive filter (AOPDF) or Dazzler (Fastlite). Since our compressor is designed to be on purpose bulky and not flexible, the Dazzler represents also a powerfull tool to introduce fine changes of second, third and fourth order dispersion.

The Dazzler is based on a 25 mm long birefringent crystal, the TeO_2 [98, 103]. A transducer generates an acoustic wave from an RF input signal. The acoustic wave propagates through the crystal in the ordinary z-axis and reproduces spatially the temporal shape of the RF signal, creating a diffraction grating. When an optical wave with frequency ω_1 propagates in the z-axis of the crystal, it undergoes diffraction at a certain position z_1 and part of its energy is transferred to the diffracted beam, propagating on the extraordinary axis. If the optical wave is composed by multiple frequencies, which is the case of a femtosecond pulse, each frequency is diffracted at different propagation lengths in the crystal. Since the refractive index for ordinary and extraordinary axis is different, and different spectral components are diffracted at different positions, they also see different time delays. By selecting the shape of the acoustic wave it is then possible to transfer specific values of second, third and fourth order dispersion to the pulse. The schematic principle of the Dazzler is shown in figure 3.24.
As already written, the Dazzler can support large spectral bandwidth (145 nm) but most of the input pulse energy is necessarily wasted because the useful part of the pulse is the diffracted one. Typical values of diffraction efficiency do not exceed 30%. Consequently the Dazzler is placed before any amplification stage for two reasons. First, an excessive input power may damage the birefringent crystal. Second, the regenerative amplifier output power does not depend critically on the injected power, and it provides the same output power even if it is not injected (see power curves for nanosecond and picosecond regimes): placing the Dazzler after the amplification would decrease drastically the disposable final power, whereas placing it before does not change the amplification efficiency. However, injecting less energy in the regenerative amplifier can slightly change the temporal contrast. Finally,

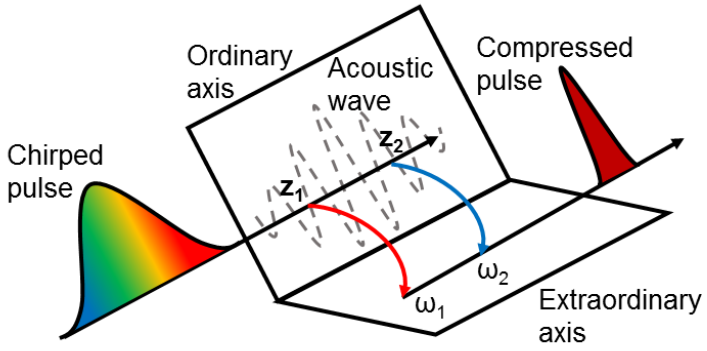

Figure 3.24: Schematic representation of Dazzler principle [98].

even though the Dazzler design is really compact (50X100 mm), the stretcher module output line is rather long and well collimated and represents the ideal place for placing the dispersive filter without impediments.

A further important benefit of the Dazzler is the possibility of coupling it easily with the Wizzler. The latter provides a measurement of residual spectral phase dispersion and feeds back on the first for dispersion compensation. The results proposed below have been obtained with careful alignment of compressor and feedback loop between Wizzler and Dazzler.

3.2.6.3 Compression results

In this section we propose the results obtained from pulse compression at the output of the regenerative amplifier upon performing subsequent Mazzler loops for spectral broadening.

Figure 3.25 shows on the left the measured spectra (black line) with corresponding spectral phase (blue line-measured phase, red line-fit of the measured phase) after best compression, on the right the pulse transform limited (black line) and measured (red line) duration. For all the spectra, the spectral phase is flat over the pulse bandwidth and the pulses approach closely the transform limited duration.

The power at the output of the compression is further decreased by the compressor transmission that is experimentally measured to be 75%.

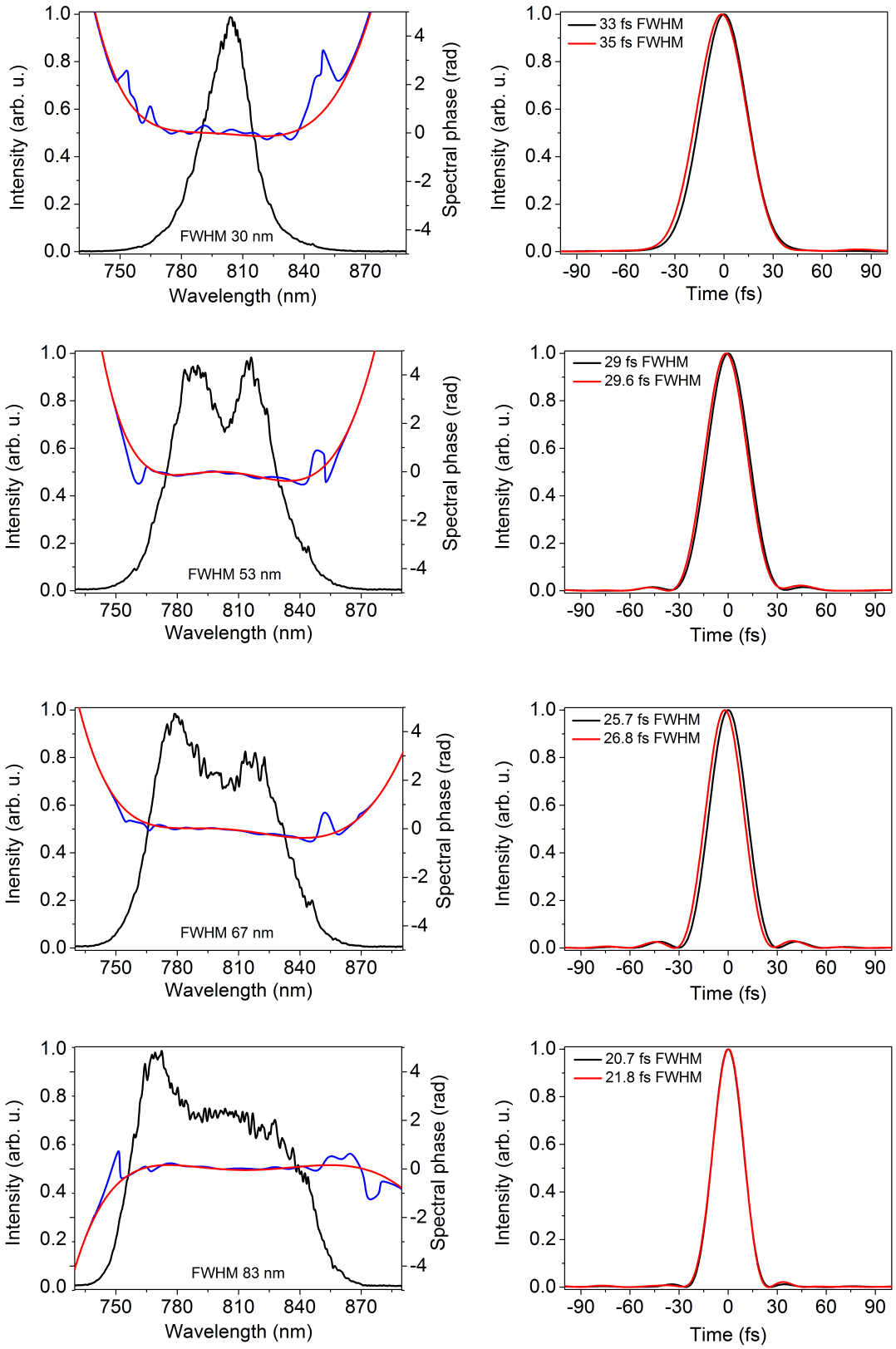
Intensity (arb. u.)
Spectral phase (rad)
Wavelength (nm)
FWHM 30 nm
33 fs FWHM
35 fs FWHM
Time (fs)
FWHM 53 nm
29 fs FWHM
29.6 fs FWHM
Inensity (arb. u.)
FWHM 67 nm
25.7 fs FWHM
26.8 fs FWHM
FWHM 83 nm
20.7 fs FWHM
21.8 fs FWHM

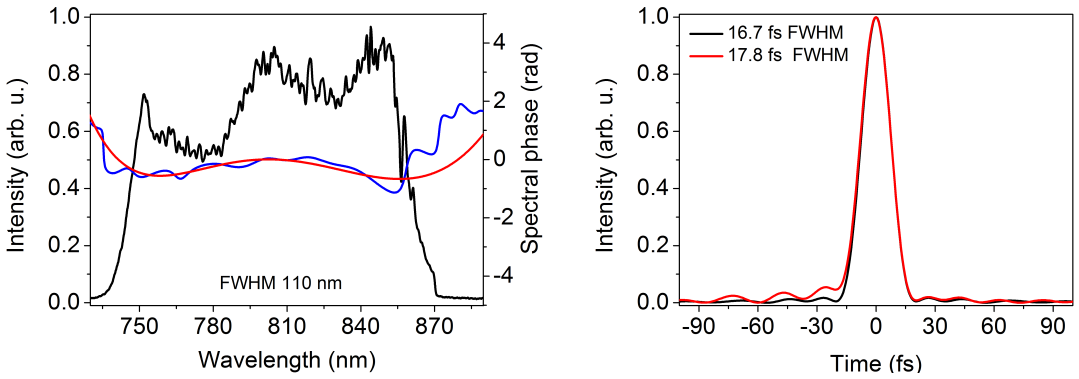

Figure 3.25: Pulse compression after consecutive Mazzler loops. On the left the spectra (black line) with measured (blue line) and fit (red line) spectral phase; on the right the transform limited (black line) and measured (red line) pulse duration.

3.3 Spectral tunability

High average power tunable lasers represent versatile tools for many strong field applications. Tuning the driver laser wavelength can be expanded to XUV and HHG increasing the flexibility of the strong field experiment [104]. We remind that the wavelength of a high order harmonic of order q depends on the wavelelngth of the driving pulse λ_0 according to the relation: $\lambda_q = \lambda_0/q$. As a consequence, the possibility of tuning the driving laser wavelength is translated into the possibility of adjusting the wavelength of the harmonics, which can be interesting in pump probe experiment in the deep UV. Other examples of experiments which benefit from spectral tunability are fine tuning wave mixing, coherent control in atomic or molecular physics experiments [80] or driving photo-injector electron guns on Free Electron Laser facilities [81]. Ti:Sa laser systems in principle do not offer wavelength tunability due to the gain narrowing, expecially when using a regenerative amplifier which is selecting the central wavelelngth. As we mentioned in the previous chapter, obtaining a broad spectrum preserving a sufficient output power is quite challenging, especially at 10 kHz repetition rate due to thermal effects. Tunable Ti:Sa laser systems have been demonstrated at 100 Hz [75] and 1 kHz [80] repetition rate. Alternatively, Optical Parametric Amplifiers have been used to demonstrate spectral tunability [105] over a large spectral range. Here we present the performances of our 10 kHz Ti:Sa front-end in terms of spectral tunability. As we described in the previous chapter, the broad band regime of the regenerative amplifier represents the starting point for performing spectral tunability. We demonstrate tunable spectra over 90 nm spectral range centered around 800 nm with 1 nm resolution and bandwidths spanning from 20 to 70 nm.

3.3.1 Methods

The key for performing spectral tunability over a large spectral range is disposing of a broad amplification spectrum. The broadband regime of the regenerative amplifier achieved with the Mazzler provides the starting point for performing spectral tunability at the re-

generative amplifier level. The method used is based on coupling the two programmable dispersive modules in the laser chain, i.e. the Dazzler and the Mazzler. The Mazzler creates the broad amplified spectrum whereas the Dazzler selects the seed bandwidth to be amplified. Thus, instead of injecting all the spectrum transmitted by the stretcher, only a portion of it is selected by the Dazzler and amplified in the regenerative amplifier. The Dazzler in this case is used only as a gate to select a defined part of the spectrum. If the seed spectrum counts less spectral components, its pulse duration is also shorter; the amplifier's gain is distributed among less spectral components and on a shorter time range: the peak power reaches higher values with respect to the broadband mode. While performing spectral tunability and especially while choosing the seed bandwidth, the time narrowing should be carefully taken into account in order to avoid serious damage of optics or amplification medium.

Figure 3.26 shows the spectral transfer function in the Dazzler for large band diffraction, the one of the Mazzler for spectral broadening and the corresponding 100 nm FWHM spectrum. As reminder, the Mazzler spectral transfer function represents the diffracted beam,

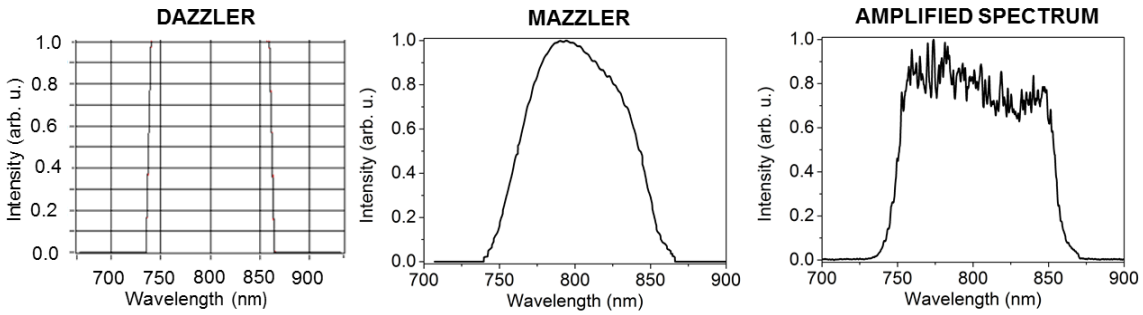

Figure 3.26: Dazzler (left) and Mazzler (center) spectral transfer function for broadband amplification, and corresponding IR spectrum after amplification in regenerative amplifier (right).

that is the losses inserted in the transmitted part of the beam, whereas the spectrum of the Dazzler corresponds to the diffracted wave. When performing spectral tunability, the Dazzler is configured to create a gate and diffracts only the selected bandwidth. Figure 3.27 shows the Dazzler configuration for 40 nm width pulse centered at 800 nm, the Mazzler in broadband configuration and the resulting amplified spectrum from the regenerative amplifier. Two unwanted effects appear. Firstly, the amplified spectrum presents a bump in a spectral range that is not injected. This unwanted spectral bump is due to amplified spontaneous emission (ASE). In fact, also spectral components that are not injected but are emitted spontaneously by the Ti:Sa undergo amplification due to the broad amplification spectrum created by the Mazzler. As a consequence, a part of the usable energy created by the pump is wasted in amplification of spontaneous emission and the temporal contrast between nanosecond and picosecond emission is deteriorated. In order to counteract the unwanted amplification of spontaneous emission, a second acoustic wave must be added to the broadband one. This second wave creates losses where the ASE is located, i.e. for those spectral ranges that are not transmitted by the Dazzler. Figure 3.28 shows separately the broadband wave and the user defined ASE-killer wave. The Mazzler software allows to select

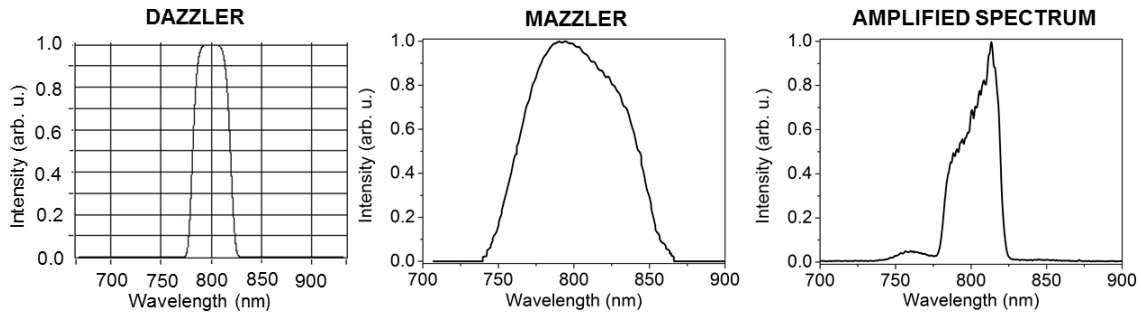

Figure 3.27: Dazzler (left) and Mazzler (center) spectral transfer function for tunable 40 nm width spectrum amplification, and corresponding IR spectrum after amplification in regenerative amplifier (right).

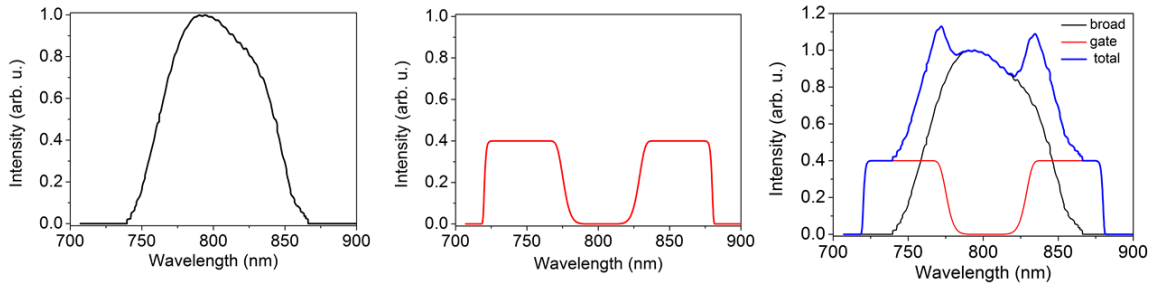

Figure 3.28: Combination of two transfer functions on the Mazzler for achieving broadband amplification and minimizing ASE. The two separate transfer functions (broadband on the left and ASE-killer on the center) gives the total wave shown in blue line on the right.

the weight of the second wave depending on the strength of the ASE to be corrected. Figure 3.28 shows in blue line the total wave applied to the Mazzler where the ASE-killer wave weight is 40%. Figure 3.29 shows the amplified spectrum after combining the two waves

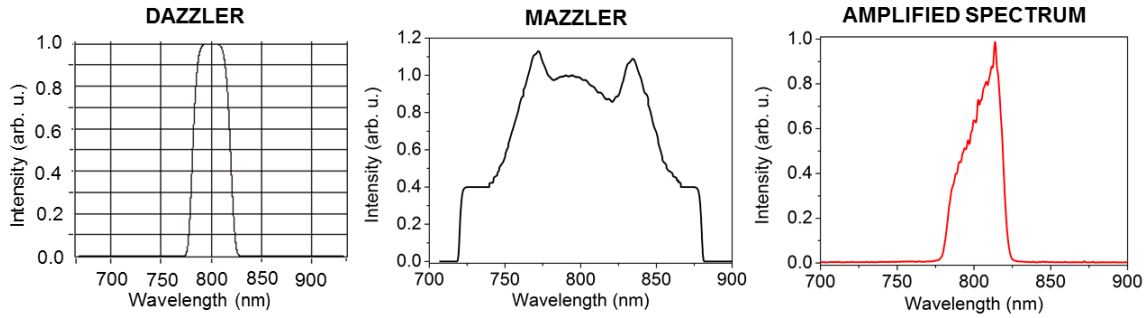

Figure 3.29: The new Mazzler transfer function (center) allows to minimize the ASE on the amplified spectrum (red line on the right).

in the Mazzler: thanks to the spectral shape of the total Mazzler wave, the side ASE is not amplified and the energy is more efficiently converted into picosecond emission. This evidence is supported also by the comparison of the two spectra of figure 3.30, before ap-

plication of ASE-killer (black line) and after application of the filter (red line). The ASE is totally converted into picosencod pulse, and the peak of the final spectrum in red results more intense than the previous spectrum in black line.

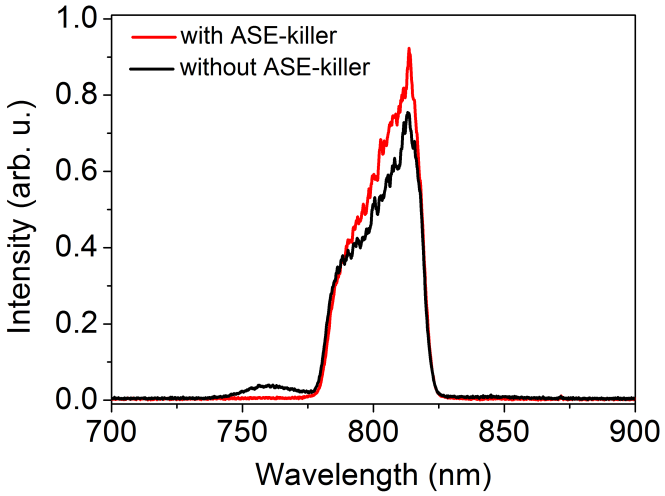

Figure 3.30: Comparison between the spectrum before (black line) and after application of the ASE killer (red line). The ASE is converted into picosecond energy.

Secondly, the amplification process causes the spectrum to shift to higher wavelengths (the so called red-shift) where a peak appears: the spectrum is narrower than the injected one (26 nm FWHM) and the peak power stronger. It is necessary then to modify the injected spectra in order to counteract the red-shift and consequently modify the spectral gate created by the Dazzler. In particular we pre-compensate the red-shift by creating an asymmetrical Dazzler gate. Figure 3.31 shows the amplified spectrum after changing the Dazzler gate in order to counteract the red-shift: the spectrum spans over a broader band (32 nm) and no peak is visible.

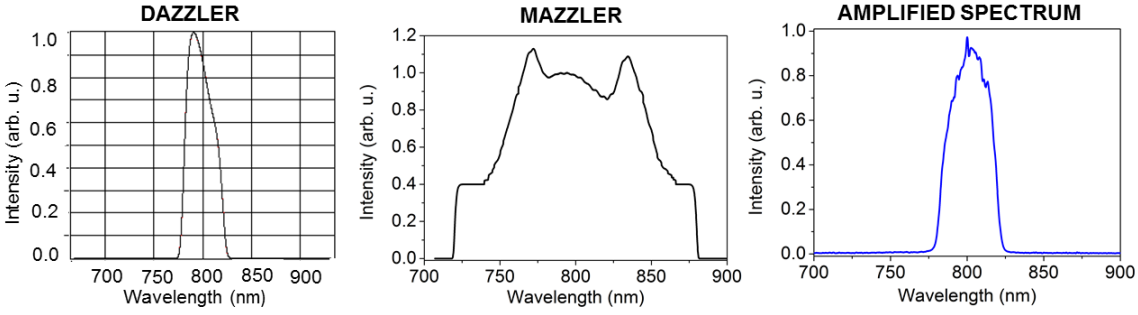

Figure 3.31: Combination of the asymmetrical Dazzler (on the left) and Mazzler (center) transfer function allows to obtain a symmetrical 32 nm braod amplified spectrum (blue line at the right) with ASE minimized and red-shift compensated.

3.3.2 Results

We performed a scan over the amplified broadband spectrum, tuning the central wavelength from 760 nm to 840 nm with 10 nm of resolution and 40 nm of bandwidth. Figure 3.32 shows the amplified spectra and their actual bandwidth measured at FWHM. The cen-

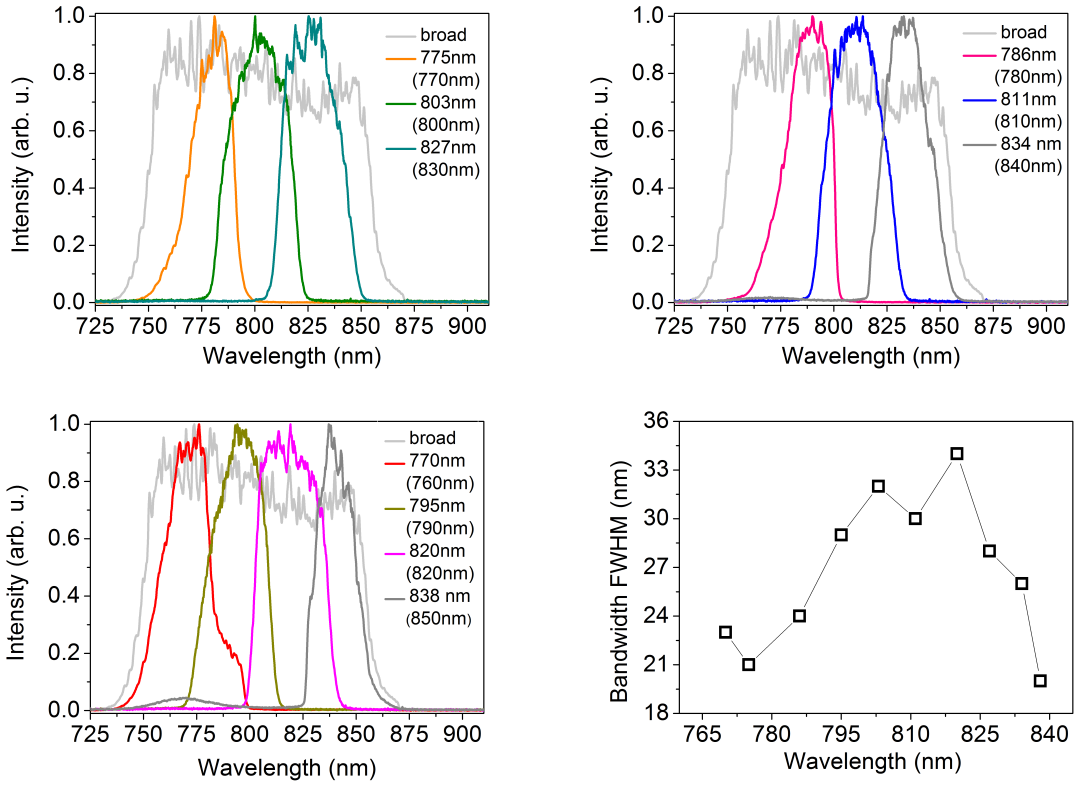

Figure 3.32: Amplified spectra, tuning the central wavelength from 760 to 840 nm with 10 nm of resolution. The Dazzler gate is programmed for injecting a pulse width of 40 nm. In the legend, the spectra central wavelength and in brackets the Dazzler selected one. On the bottom right the actual bandwidth for different central wavelength.

tral wavelengths for each spectrum is slightly shifted with respect to the central wavelength selected with the Dazzler. In figure3.32, the legends shows the actual central wavelength and in brackets the selected one. The spectra maintain a rather symmetrical shape and the ASE is minimized. However, even though the Dazzler is tuned to inject 40 nm bandwidth in the regenerative amplifier, the actual bandwidth of all the spectra is narrower. In particular spectra with central bandwidth closer to the peak of the spectral gain maintain a quite broader bandwidth (around 35 nm at FWHM) whereas spectra at the edges of the gain are narrower (minimal width is 21 nm). In order to demonstrate the need of pre-compensating the red shift, we measure three spectra selecting the Dazzler central wavelength at 800 nm, 770 nm and 840 nm in two cases, i.e. with symmetrical Dazzler gate centered on the chosen wavelengths, and with asymmetrical Dazzler gate.

If a symmetrical Dazzler gate is used (see figure 3.33a), we observe that the spectra centered at 740 nm and 800 nm undergo a strong red-shift, and higher wavelengths are

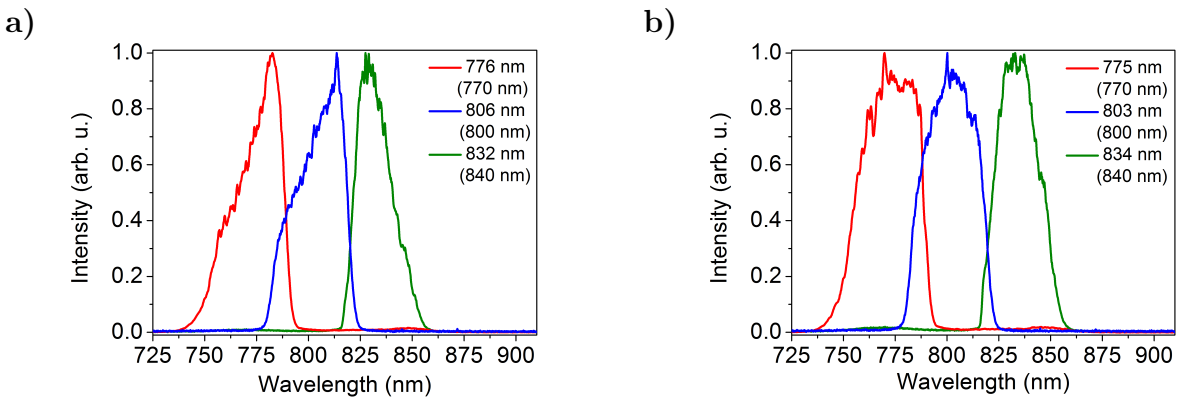

Figure 3.33: Tunability spectra with a) symmetrical and b) asymmetrical Dazzler gate. In the legend the spectra central wavelength and in brackets the Dazzler selected one.

amplified first and thus more strongly. Consequently for the spectra centered at 740 nm and 800 nm the red-shift effect pushes the spectrum towards higher wavelengths. For 840 nm we notice that the spectrum does not undergo red-shift, on the contrary it tends to shift towards 800 nm. For explaining this specific case, we need to take into account the spectral shape of the acoustic wave. In fact, for 840 nm, the Mazzler configuration induces less losses at 800 nm, and the gain is then higher for 800 nm than for further wavelengths. The red-shift competes with the effect of the Mazzler configuration: in particular the red-shift pushes the spectrum to higher wavelengths whereas the gain amplifies more wavelengths closer to 800 nm. The result is still an asymmetric spectrum, where the shift due to the gain appears to be predominant on the red-shift. Figure 3.33b shows on the contrary the three amplified spectra injected with an asymmetrical Dazzler gate. Thanks to the shaping of the Dazzler acoustic wave, we are able to compensate the two detrimental effects described below and obtain symmetrical and homogeneous spectra, where the spectra central wavelength approaches the central wavelength selected with Dazzler. Figure 3.34 shows the power for three spectral regimes: the narrow band mode (NB), where no Mazzler loop is applied nor spectral gating via Dazzler and as already saw in the previous sections, the gain narrowing reduces the bandwidth to 35 nm but, since no Mazzler loop is applied, no energy losses are created and the narrow spectrum conserves the maximum power of 5 W; the broadband mode (BB), where the broad spectrum resulting from consecutive Mazzler loops is amplified up to 2.5 W; and finally the tunable narrow band mode (TNB), corresponding to injection of 40 nm broad spectra achieved with spectral tuning of the central wavelength with Dazzler and amplified thanks to the broad spectrum achieved with Mazzler loops. The power of the tuned spectra changes considerably for different central wavelengths and in particular it increases as the central wavelength approaches the side of the amplification spectrum. This trend can be explained considering the shape of the Mazzler acoustic wave corresponding to each spectrum. Figure 3.35 reports the two Mazzler waves used for amplification of 40 nm injected spectra centered at 800 nm and 760 nm. We specify that the power set for all the waves is the same. However, from the comparison we can note that the Mazzler wave for 800 nm spans over a broader spectrum as well as the area covered by the wave is bigger than the wave used for 760 nm. The Mazzler configuration for 800 nm introduces more losses than

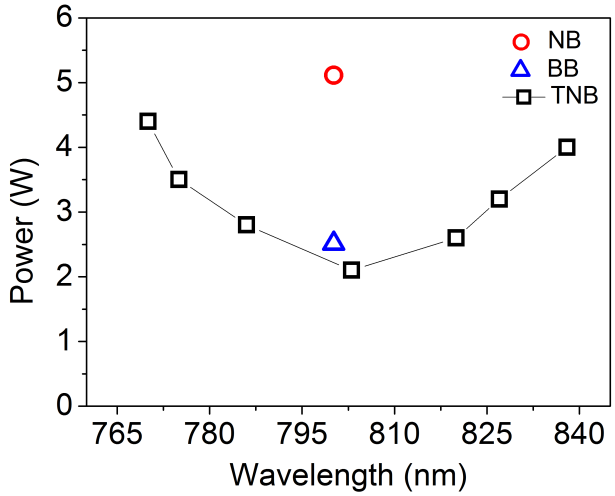

Figure 3.34: IR output power for different regenerative amplifier regimes as function of the central wavelength: NB-Narrow band mode; BB-Broadband mode; TNB-Tunable spectra shown in figure 3.32

those for 760 nm and its amplified spectrum benefits of more energy.

In order to demonstrate the accuracy of the tuning process, we performed spectral tuning with Dazzler of 40 nm broad spectrum with a resolution of 2 nm. Figure 3.36 (top left, top right and bottom left) shows the spectra for ±2 nm tuning around 800 nm, 770 nm and 830 nm. The wavelength in the legend corresponds to the real one and in bracket those chosen with the Dazzler . We push the technique even further by moving a 20 nm bandwidth centered at 800 nm of ±1 nm, as shown in figure 3.36 at the bottom right.

Finally we performed a tuning of the injected spectral width centered at 800 nm, as shown in figure 3.37. These results confirm the reliability, flexibility and precision of our method: the user can chose the central wavelength of the pulse within 80 nm spectral range, with a precision of ±1 nm, as well the pulse bandwidth. As already mentioned, we set 20 nm as lower limit for the bandwidth, to avoid eventual damage of the optics.

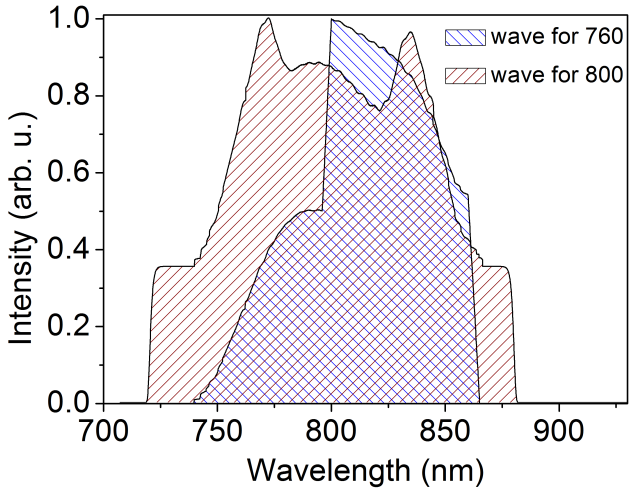

Figure 3.35: Comparison between Mazzler configuration for 40 nm width injected spectra centered at 800 nm and 760 nm.

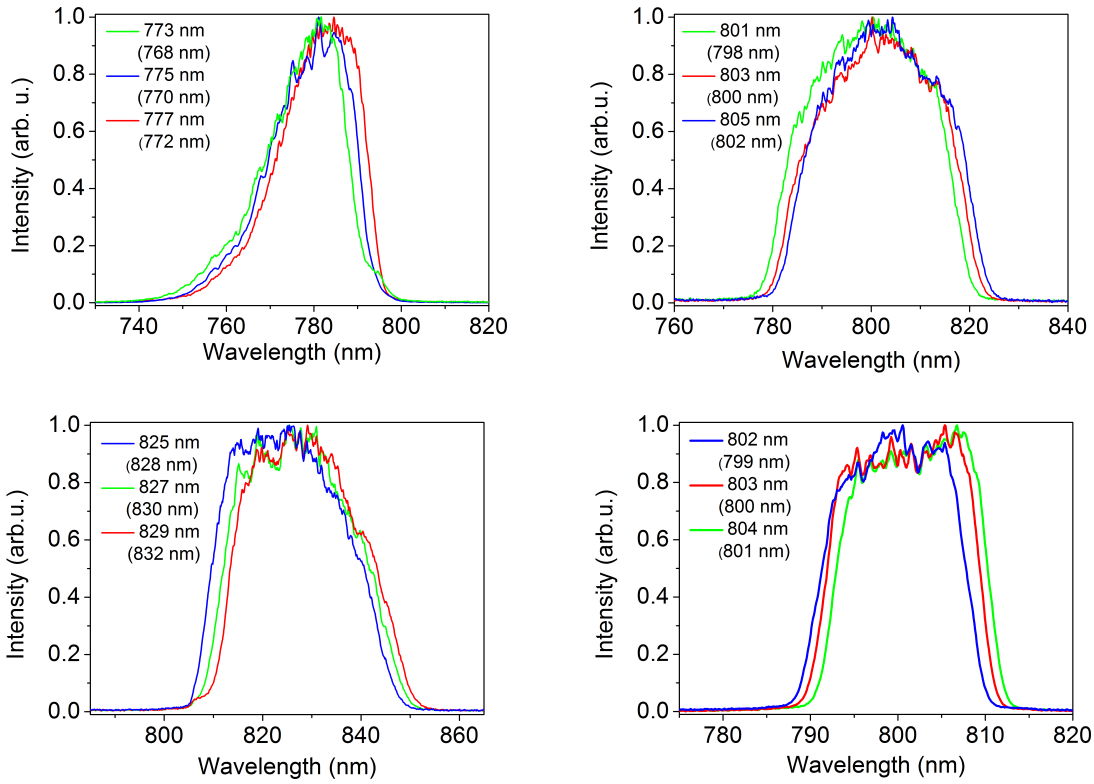

Figure 3.36: Spectral tuning with 2 nm of resolution of 40 nm width spectra centered at 770 nm (top left), 800 nm (top right) and 830 nm (bottom left). Spectral tuning with 1 nm of resolution of 20 nm width spectra centered at 800 nm (bottom right).

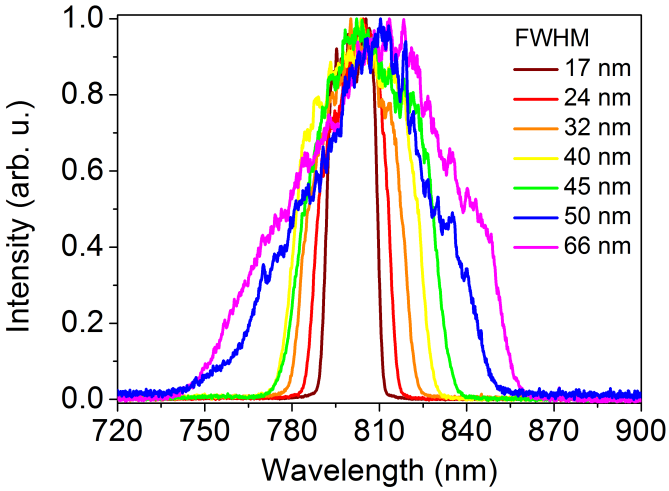

Figure 3.37: Bandwidth tuning around 800 nm.

3.4 The 1 kHz multipass amplifier

The pulse energy of the above described innovative front-end can be scaled to higher values by coupling at its output further amplification stages. We developed a high average power 1 kHz Ti:Sa amplifier delivering 10 mJ pulses in narrow band mode and 8.4 mJ pulses in broad band mode without cryogenical cooling.

3.4.1 Design and setup

The multipass amplifier is pumped by a commercial diode pumped Nd:YLF laser from Continuum (Amplitude Laser Group). The laser emission is peaked at 527 nm at 1 kHz repetition rate. The maximal output power is 28.8 W with an RMS stability of 0.4 % over one hour (measured with a powermeter). The distribution line consists of high reflectivity mirrors at 527 nm but also of a couple of adjustable waveplate and polarizers; this line is conceived for an eventual repartition of the pump energy that is not used in the following setup. The propagation line introduces some losses and the residual available power at the crystal surface is 23 W.
The setup is designed to attain a pump fluence of 2 J/cm^2 on the crystal surface with a pump power of 18 W, in order to set aside some pump power. The pump beam radius at 1/e^2 on the crystal should then measure around 535 μm. Considering an output beam profile of 1250 μm radius at 1/e^2 and a M^2 of 12, we design the pump propagation line in order to properly focus the beam on the Ti:Sa crystal surface. The scheme is shown in figure 3.38. The pump line consists of a magnifying telescope at a distance of 180 mm from the laser output, with lenses of - 300 mm and + 333 mm focal lengths spaced by a distance of 80 mm. A third lens with a focal length of 400 mm is placed at 930 mm distance from the telescope and the beam is focused at 450 mm distance, where the crystal is placed. The crystal absorption at 527 nm is measured to be 90%. A folding mirror is placed at the other end of the amplifier, at 420 mm distance from the crystal, in order to recycle the 10% of the power that is not

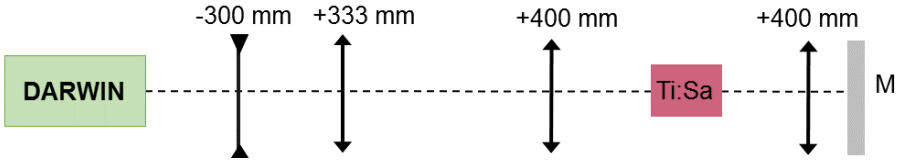

Figure 3.38: Propagation line for 1 kHz pump.

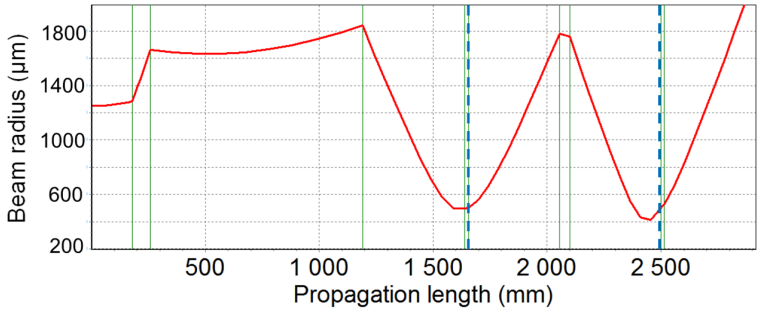

Figure 3.39: Pump beam radius evolution at $1/e^2$ as a function of propagation length. The blue dashed line represents the position of the Ti:Sa crystal.

absorbed in the first pass. A focusing lens is then necessary to compensate the pump beam divergence and re-image the pump focus after reflection: a 400 mm focusing lens is placed at 400 mm distance from the crystal. Figure 3.39 shows the Rezonator simulation of the pump beam radius evolution in the propagation line with the above-mentioned parameters: the pump beam measures around 500 μm in the first pass on the crystal and 530 μm in the second pass. Since the power is recycled after a first pass in the crystal, the total crystal absorption at the pump wavelength is considered to be 95%. Figure 3.40 shows the pump beam profile at the crystal surface: the radius at $1/e^2$ is 530 μm.

The 1 kHz multipass amplifier is placed five meters away from the output of the regenerative amplifier, because of the size of the available optical table. The IR beam divergence should be then taken into account while designing the IR injection line. The IR beam ex-

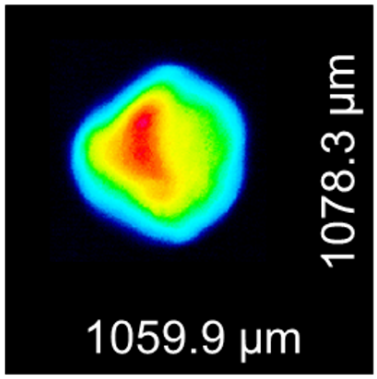

Figure 3.40: Pump beam profile (diameter at $1/e^2$) at the crystal surface.

tracted from the regenerative amplifier measures 800 μm of radius at $1/e^2$. The extraction line includes a periscope, in order to adapt the height of the regenerative amplifier module to the height of the 1 kHz amplifier module. Consequently the pulse polarization changes from S to P. In order to preserve the beam collimation during propagation towards the 1 kHz amplifier it is necessary to design a proper telescope that consists in two focusing lens, of 4000 mm each, spaced by 1350 mm distance. As shown in figure 3.41 representing the simulated beam radius evolution for the above-mentioned optical path, the IR beam maintains a good collimation during three meters propagation. A pulse picker Pockels cell is placed

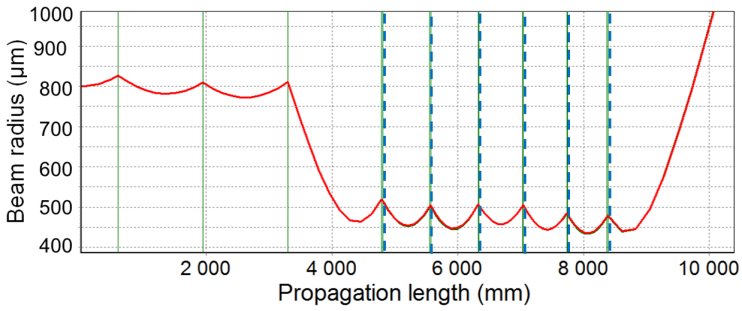

Figure 3.41: IR beam radius evolution at $1/e^2$ as function of the propagation length.The blue dashed line represents the position of the Ti:Sa crystal.

along this path for converting the 10 kHz pulse train into a 1 kHz train. The Pockels cell works as a polarization gate. It is powered by high voltage (6 kV) on a square-wave shape with duration of 20 μs and triggered by a 1 kHz signal. When receiving the high voltage signal, the Pockels cell behaves as a half-wave plate and rotate by 90° the polarization of the propagating beam: one pulse over ten of the 10 kHz train is then S-polarized. Two pairs (for better efficiency) of thin polarizers are used to reflect only the S-polarized beam and reject the P-polarized one. The 1 kHz train of S-polarized pulses is then transmitted and focused towards the crystal by a lens of 1333 mm focal length. In order to match pump and seed dimension, the focusing lens is placed at 1490 mm distance from the crystal. As show in the simulation of figure 3.41, at the crystal surface the IR beam radius is estimated to be 520 μm. As written in the previous chapter, in narrow band mode regime the regenerative amplifier generate pulses with average power of 5.5 W at 10 kHz, corresponding to 0.55 mJ. After propagation through the 1 kHz amplifier input line, the IR seed energy is 0.350 mJ, i.e. 0.35 W at 1 kHz repetition rate at the crystal surface.

In order to simulate the behaviour of the IR beam radius for the consecutive passes in the Ti:Sa crystal, the thermal lens created by the pump in the crystal should be taken into account. Considering a Ti:Sa crystal of 3 mm radius and 15 mm length with flat surfaces, water-cooled at 16°, and a pump beam radius of 530 μm for 18 W of power at 1 kHz, our simulations give a thermal lens focal length of 900 mm. Due to the multipass configuration of the amplifier, pump and IR seed are not perfectly collinear but they cross the crystal surface with a mutual angle of 5°. The thermal lens felt by the IR beam is then tilted by the same amount.

The IR beam radius evolution is again traced in figure 3.41 where the distance between each pass on the crystal varies, depending on the pass, between 625 and 740 mm. The blue

dashed lines represent the position of the Ti:Sa crystal. During propagation in the amplifier, the beam maintains on the crystal a radius of 520 μm at $1/e^2$ for the first four passes and becomes slightly smaller for the remaining two passes. We underline that this configuration does not include any lens to re-adapt the IR beam size form one pass to the consecutive. The re-imaging on the crystal surface for consecutive passes is obtained exploiting the thermal lens in the crystal. As a consequence the amplifier benefits from less energy losses (that can happen on the surface of a refractive optics) and compactness. This design has already been proposed on a 1 kHz laser amplifier [106].

The number of passes in the amplifier has been chosen upon previous simulation of the energy evolution during propagation in the amplifier. Figure 3.42 shows the IR power values for increasing number of passes in the Ti:Sa crystal. The simulation is based on the Frantz-

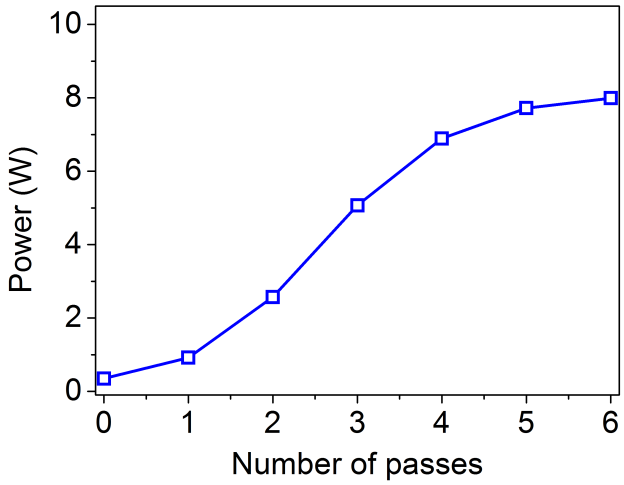

Figure 3.42: Simulated IR output power as function of number of passes in the crystal for the 1 kHz multipass amplifier. Parameters: pump power 18W, pump beam radius at $1/e^2$ 530 μm, IR injected power 0.35 W, IR beam radius at $1/e^2$ 520 μm, Ti:Sa pump absorption 90%.

Nodvik equation for the following input parameter: pump power 18 W at 1 kHz (18 mJ), 530 μm radius at $1/e^2$; IR input power 0.35 W at 1 kHz (0.35 mJ) and beam radius of 520 μm at $1/e^2$; crystal absorption of pump 95%. The desired regime of the amplifier is the saturation condition, where any fluctuation of the injected beam energy does not affect critically the final output power. As shown in the simulation, the amplifier reaches saturation after five or better six passes on the crystal. The 1 kHz amplifier configuration is depicted in figure 3.43. We decided to build the amplifier so that the angle between the IR beam and the pump increases with the number of passes. This choice may be quite dangerous but it also has a benefit. As shown in figure 3.43 the folding mirrors are placed closer to the crystal as the number of passes increases (for example M10 is closer to the Ti:Sa than M2). This means that, with increasing number of passes, the beam propagates and diverges less before hitting the folding mirror. The energy of the pulse increases with the number of passes and as a consequence a smaller beam with higher energy hits the mirror surface and may cause

damages. A careful positioning of the folding mirrors is then necessary in order to ensure the best efficiency of the amplifier while avoiding mirrors damage. On the other side, if the angle between pump and seed is smaller, the matching between the two modes is better and the amplification more efficient. This condition is particularly favourable for energy conversion in the first passes, where the amplifier is not saturated and the crystal stores the maximal pump energy.

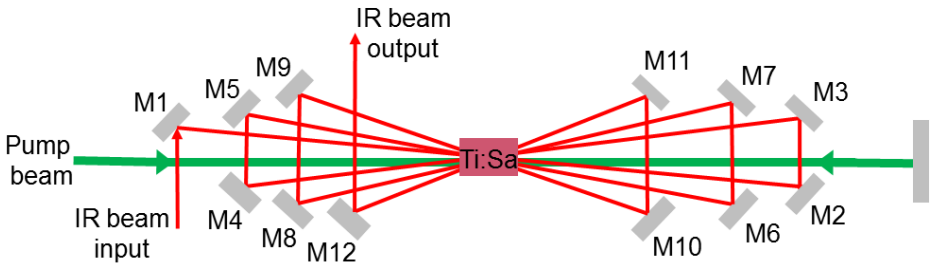

Figure 3.43: Schematic representation of the six passes 1 kHz amplifier.

3.4.2 Results

The 1 kHz amplifier is first seeded by the IR pulse in narrow band mode and pumped at 18 W. The IR profile at the crystal surface before amplification looks elliptical and not homogeneous due to the long propagation path between the regenerative amplifier and the amount of optics in the optical path. However, right after the first pass in the crystal, the beam profile quality increases, the beam is homogeneously amplified and maintains a small ellipticity for all the consecutive passes. After the fifth pass, the beam ellipticity is 94% at $1/e^2$. The beam profile evolution with increasing number of passes at the crystal surface is shown in figure 3.44. We first tested the amplifier performances on a five-passes configuration.

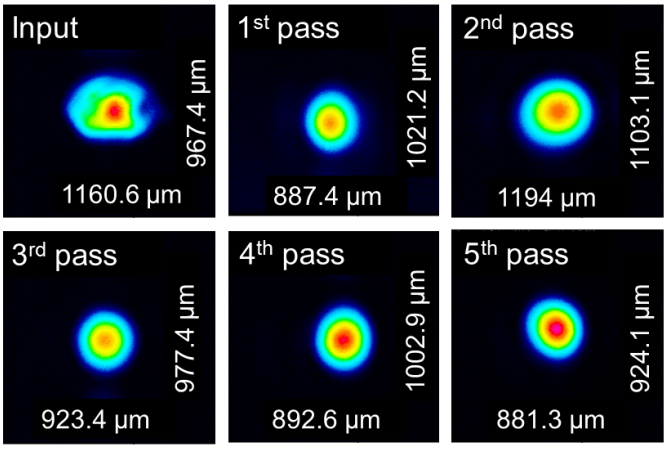

Figure 3.44: IR beam profile (beam diameter at $1/e^2$) evolution for consecutive passes on the Ti:Sa crystal.

The fact that the beam is re-imaged with nearly the same size for each pass without using any lens confirms the robustness of the amplifier configuration. Figure 3.45 shows the measured power evolution with increasing number of passes up to five. The experimental results follow quite faithfully the simulated curve. The experimental curve shows error bars of 2.5% of the measured power, according to the uncertainty of the powermeter measurements.

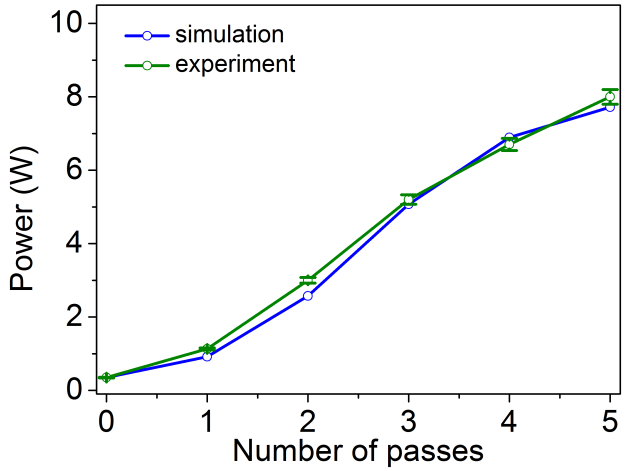

Figure 3.45: IR measured (green line) and simulated (blue line) power as function of the number of passes in the Ti:Sa for 18 W of pump power.

We secondly tested the amplifier in six-passes configuration, increasing the pump power to 22.5 W and injecting the IR seed in narrow band mode. The estimated and the measured power evolution for each pass is shown in figure 3.46a. The experimental data are in good

a) **b)**

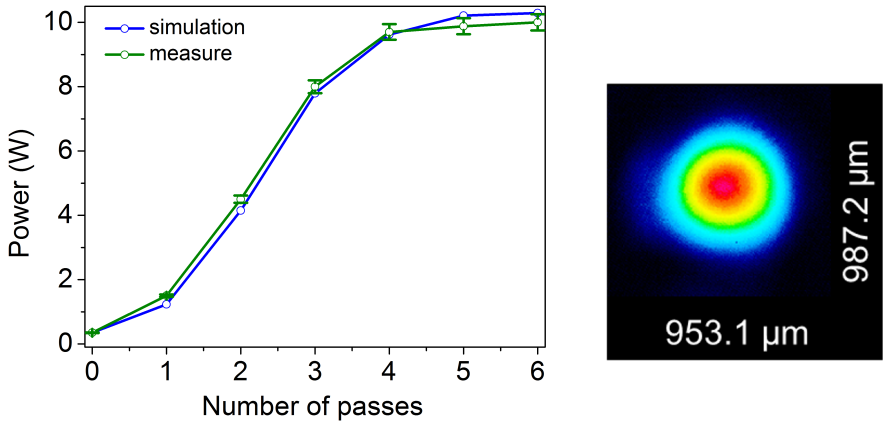

Figure 3.46: a) IR measured (green line) and simulated (blue line) power as function of the number of passes in the Ti:Sa for 22.5 W of pump power and narrow band regime. b) Corresponding IR output beam profile (diameter at $1/e^2$).

agreement with the simulation and the amplifier is well saturated after six passes. The IR

signal reaches 10 W at 1 kHz maintaining an excellent beam profile and RMS stability of 0.3% over ten minutes; this result is quite impressive for a water cooled amplifier. As we can notice in this configuration the sixth pass does not actually improve much the output power with respect to the fifth pass. However, we want the amplifier to work at saturation for both narrow band and broad band regime; considering that the input energy for broad band mode is nearly half of the energy in narrow band mode, a sixth pass in the amplifier will ensure the saturation condition for both the narrow and the broadband regime. Figure 3.46b shows the output beam profile after six passes in the amplifier. The ellipticity value of 96% confirms the excellent beam profile quality.
Figure 3.47a shows the input and output spectrum: the output spectrum is slightly red-shifted with respect to the input and no gain narrowing occurs during amplification. Figure 3.47b represents the Fourier transform temporal profile for the output spectrum of the amplifier. The transform limited pulse duration is 30 fs at FWHM. The temporal duration obtained from the spectrum corresponds to the calculation for a pulse with a square hyperbolic secant shape rather than gaussian.

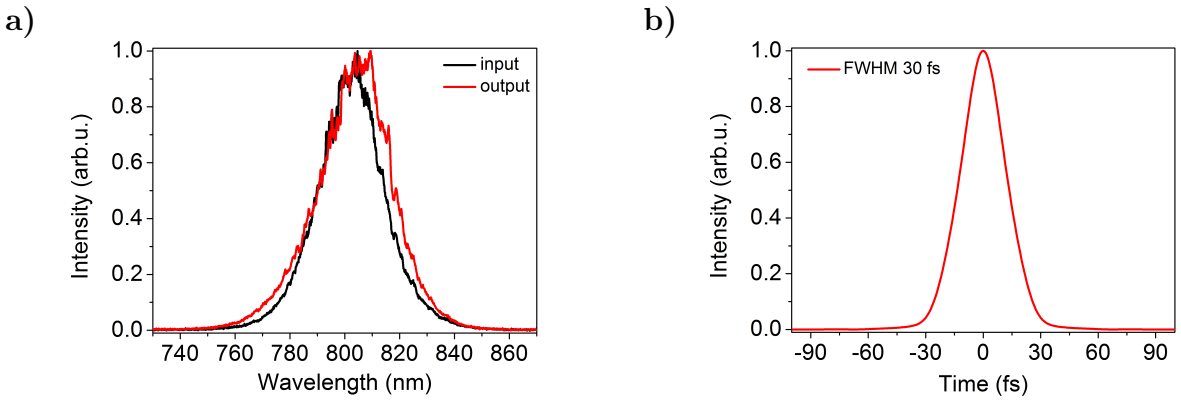

Figure 3.47: a)Input spectrum (black line) and output spectrum (red line) for narrow band regime of 1 kHz amplifier. b) Corresponding transform limited pulse duration for the output spectrum.

Finally we tested the amplifier in broad band regime, pumping with 22.5 W. In this case the IR injected energy reaching the crystal surface is limited to 0.17 mJ due to the losses induced by the Mazzler loops. Figure 3.48a represents the experimental and simulated data in terms of power.

The saturation regime of the amplifier allows to reach nearly the same level of output power for both narrow and broad band mode. In broad band mode the output power after six passes is measured to be 9.4 W. Figure 3.48b shows the final beam profile, with an ellipticity value of 95%. Figure 3.49a reports the comparison between input spectrum (black line) and output spectrum (red line). As shown in figure 3.49b, the output spectrum supports transform limited pulse duration as short as 17.5 fs at FWHM.

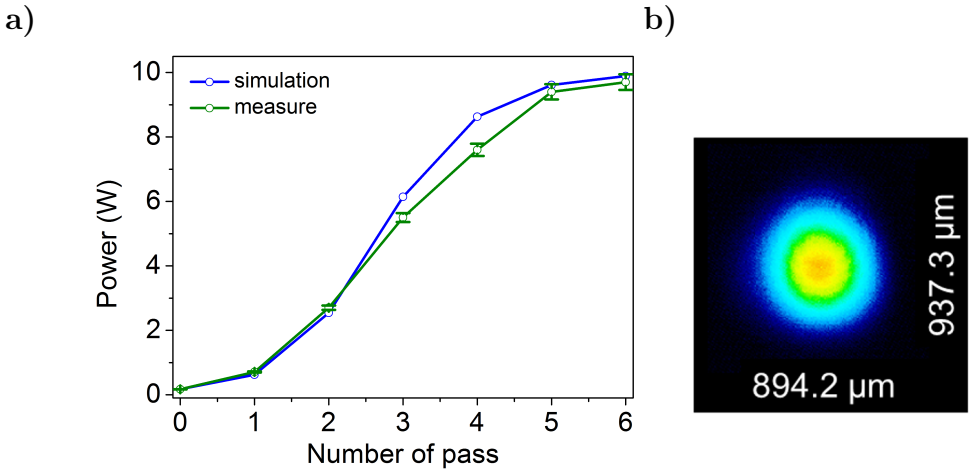

Figure 3.48: a) IR measured (green line) and simulated (blue line) power as function of the number of passes in the Ti:Sa for 22.5 W of pump power and broad band regime. b) Corresponding IR output beam profile (diameter at $1/e^2$).

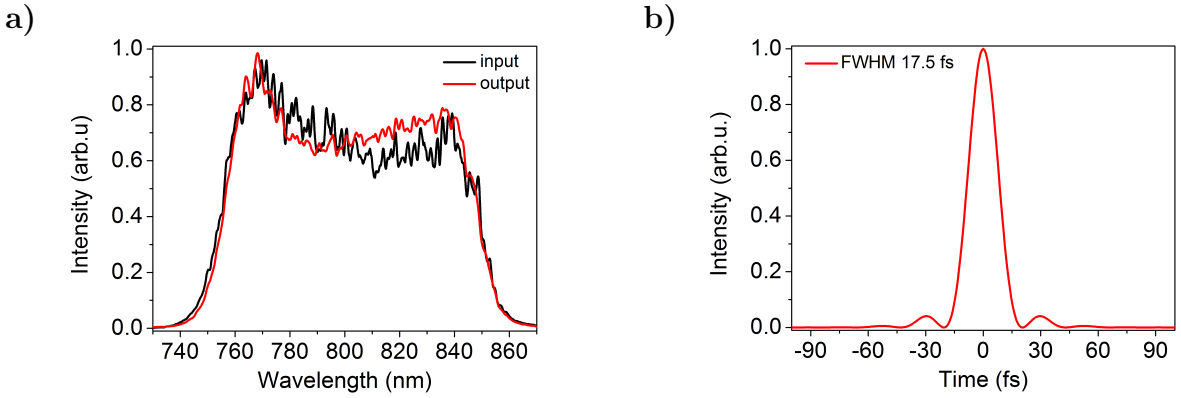

Figure 3.49: a)Input spectrum (black line) and output spectrum (red line) for broad band regime of 1 kHz amplifier. b) Corresponding transform limited pulse duration for the output spectrum.

3.4.3 Amplification at 1kHz repetition rate of tunable spectra

The 1 kHz multipass amplifier has been tested also in spectral tunable narrow band mode (TNB). Ti:Sa CPA laser system with tunability option has been demonstrated at 20 mJ, 100 Hz, delivering pulse with tunable central wavelength from 755 nm to 845 nm [75].
In this section we present the results obtained for our 1 kHz amplifier in tunable mode, delivering up to 10 mJ for tunable spectra centered at 800 nm.
Some of the spectra proposed in section 3.3 have been injected in the amplifier and the output spectra as well as their power is measured. Figure 3.50 shows the spectra at the output of the regenerative amplifier and after amplification in the 1 kHz amplifier for different central wavelengths.

We decided to limit the Dazzler injection bandwidth to a minimum width of 40 nm FWHM, in order to avoid damages of the optics and the crystal, considering the high level

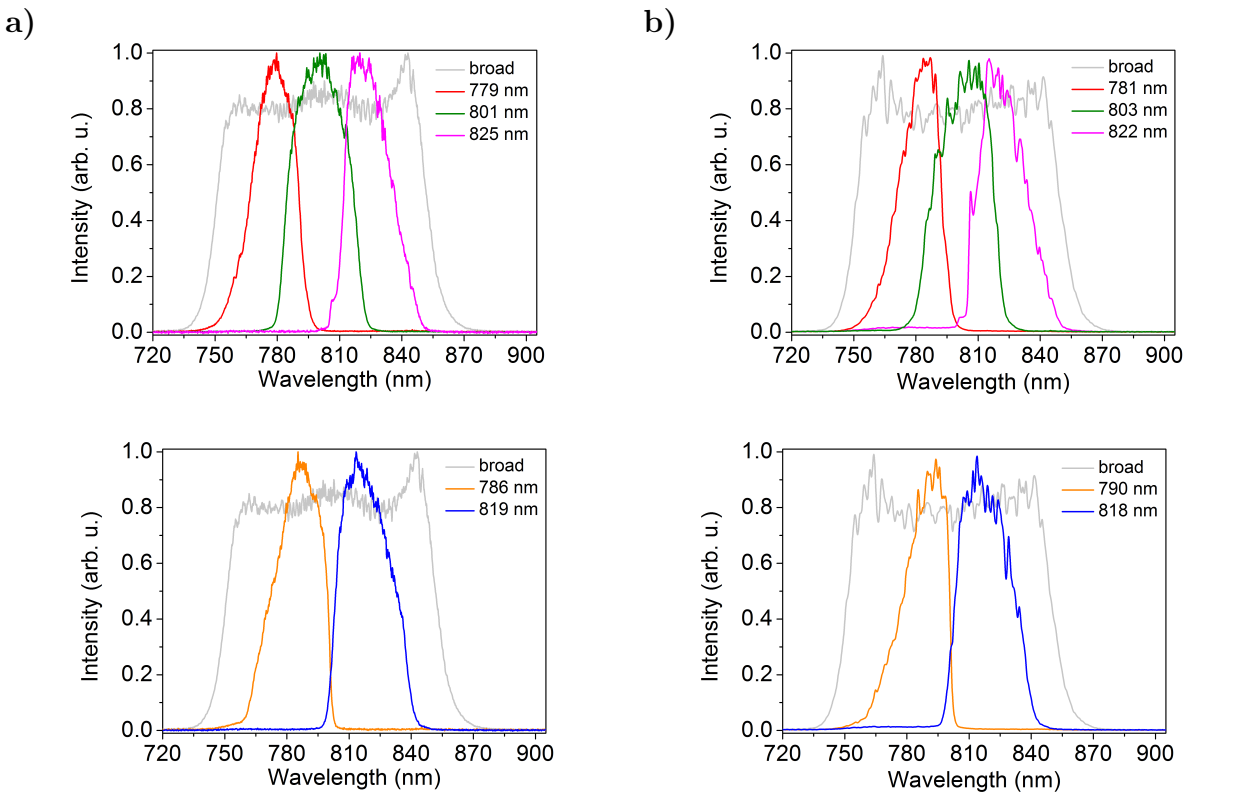

Figure 3.50: Output spectra after different stages of amplification. a) output spectra from the 10 kHz regenerative amplifier and b) the same spectra after amplification in the 1 kHz multipass amplifier.

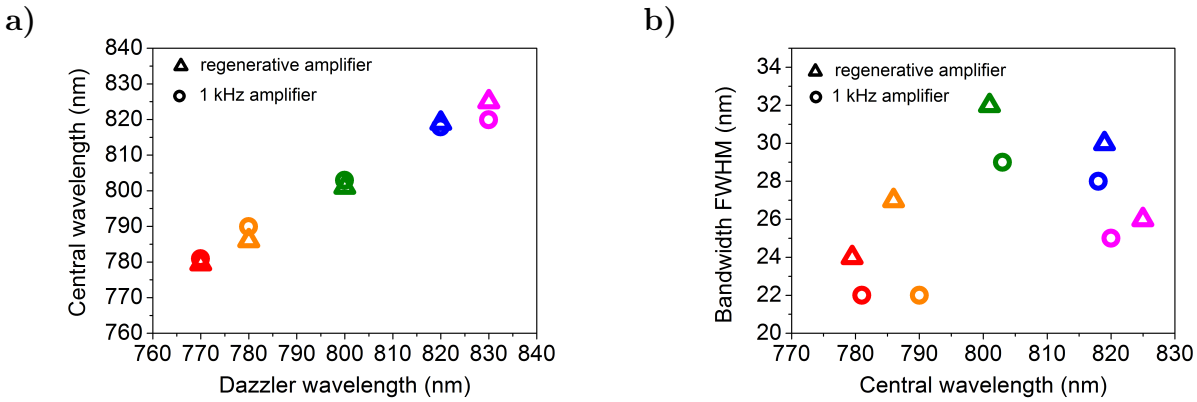

Figure 3.51: a) Spectra central wavelength as a function of the Dazzler selected wavelength and b) FWHM bandwidth after amplification in regenerative amplifier (triangles) and 1kHz multipass amplifier (circles).

of power that the pulses reach after amplification.
Figure 3.51a shows the spectra central wavelengths after regenerative amplifier (triangles) and 1kHz amplifier (circles) for the corresponding central wavelengths selected with Dazzler. As already explained in the section about spectral tunability at the regenerative amplifier

output, both red shift and higher gain centered at 800 nm contribute to the spectra shift towards 800 nm. This effect is less visible in the regenerative amplifier, where the Mazzler induces losses at 800 nm, while it is more pronounced after the 1 kHz amplifier, where the pulses are shifted towards the center of the spectral gain of the amplifier. This shift can be in principle compensated by performing the Mazzler loop for spectral broadening as well as the ASE gating taking as input the spectrum after the 1 kHz amplifier instead of the ones after the regenerative amplifier. Performing the Mazzler loop at the multipass amplifier level would also counteract the gain narrowing at this amplification stage, that is visible in figure 3.51b. The triangle represents the FWHM bandwidth of pulses after the regenerative amplifier, while the circles correspond to the output of the 1 kHz amplifier.

Figure 3.52 shows the regenerative amplifier output power and the 1 kHz amplifier output power for the spectra of figure 3.50. The amplifier works in saturation condition, so that even though the input power is different for different spectra, they attain almost the same output power after amplification, leading to spectral tunability with almost same energy after the compressor. In particular, the amplifier output energy varies of ±0.3 W around the central value of 10 W, while the output power of the regenerative amplifier changes from 2.2 W to 3.7 W. We underline that this graph gives the performances of the amplifier in

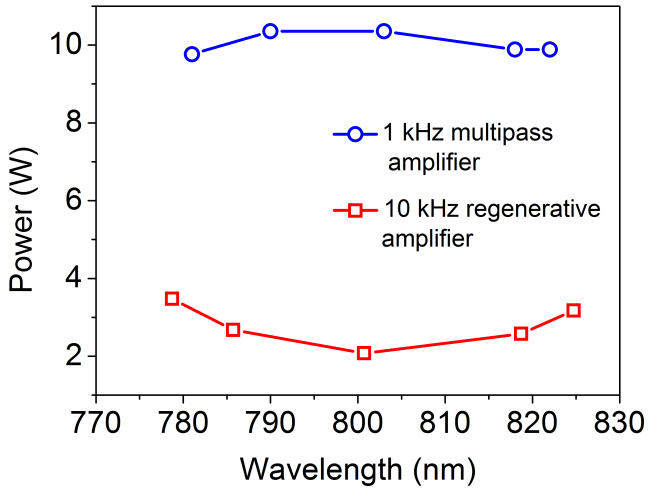

Figure 3.52: Output power of 10 kHz regenerative amplifier (red line) and 1 kHz multipass amplifier (blue line) for the spectra shown in figure 3.50.

terms of power, where the repetition rate should be taken into account. In terms of energy the multipass amplifier boost the output of the regenerative amplifier from 200-300 μJ up to 9-10 mJ, with an amplification factor of about 40.

3.5 Scaling the peak power to the TW level

The above described Ti:Sa front-end has been coupled to further amplification modules [107]. The schematic representation of the high power amplification chain is shown in figure 3.53. After the double-crystal regenerative amplifier, a double-crystal, single pass amplifier

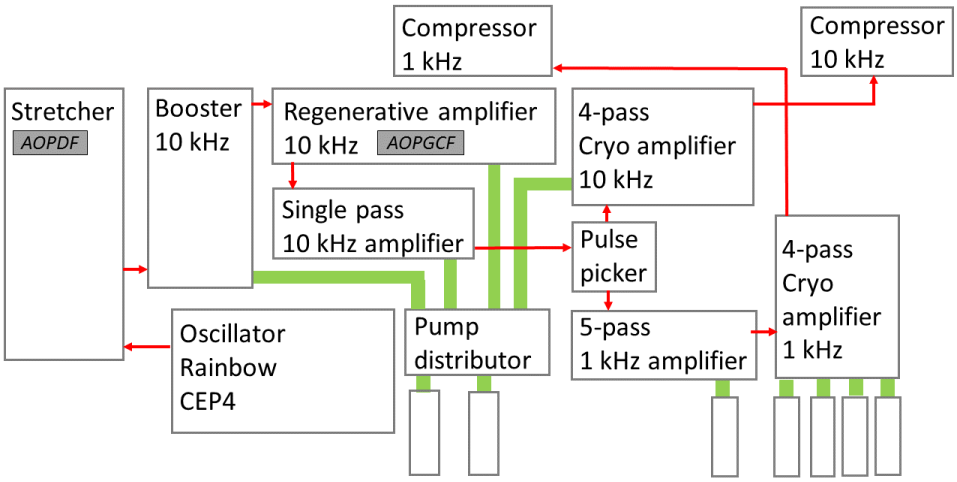

Figure 3.53: Schematic representation of the high power laser chain, with the 10 kHz arm and the TW level 1 kHz arm.

pumped with 25 W increases the pulse power up to 7 W at 10 kHz in broad band mode. Once again, the double crystal scheme is used in order to distribute the heat load and avoid beam profile deterioration due to thermal lensing. The pulse seeds again two separated high energy amplification lines. 30% of the energy (200 μJ) is sent to a pulse picker, composed by a Pockels cell and two pairs of thin polarizers, to reduce the repetition rate from 10 kHz to 1 kHz, resulting in a 180 μJ pulse in broad band mode. The pulse is amplified in a water-cooled 5 pass Ti:Sa amplifier, reaching 4.3 mJ. This amplifier is pumped by a commercial laser (Jade from Thales) with 15 W. A second 4-pass amplifier pumped with 75 W boosts the pulse energy up to 23 mJ at 1 kHz repetition rate, corresponding to 23 W. Due to the high average power in this last amplification stage, the Ti:Sa Brewster-cut crystal needs to be cooled under vacuum down to below -150° by means of a cryo-cooling system in order to counteract thermal effects. The cryogenic cooler is vibration-free, to minimize any possible source of CEP noise.
The residual part of the 10 kHz beam, 5 W in broad band mode, seeds another cryo-cooled amplifier. The Brewster-cut Ti:Sa crystal is cooled down to below -150° under vacuum. With 100 W of pump power, delivered by four Jade lasers, the output of the amplifier reaches 28 W at 10 kHz. Thanks to the cryo-cooling system in both the 1 kHz and the 10 kHz line, the IR final profiles maintain a good quality, as shown in figure 3.54.

Initially the output spectrum of the regenerative amplifier has been enlarged to 80 nm at $1/e^2$ with the Mazzler loop. The pulses from both amplification lines have been subsequently compressed by means of two grating based compressors. Thanks to the Wizzler-Dazzler coupling, optimal pulse compression leads to a 23.4 fs pulse duration at 1 kHz output, and 24.4 fs pulse duration simultaneously at 10 kHz. The compressor transmission reduces the final output energy to 16 mJ at 1 kHz and 2 mJ at 10 kHz.
Applying a further Mazzler loop allows to broaden the spectrum up to 100 nm at $1/e^2$. In order to compensate for further energy losses induced by Mazzler, the pumps power has been

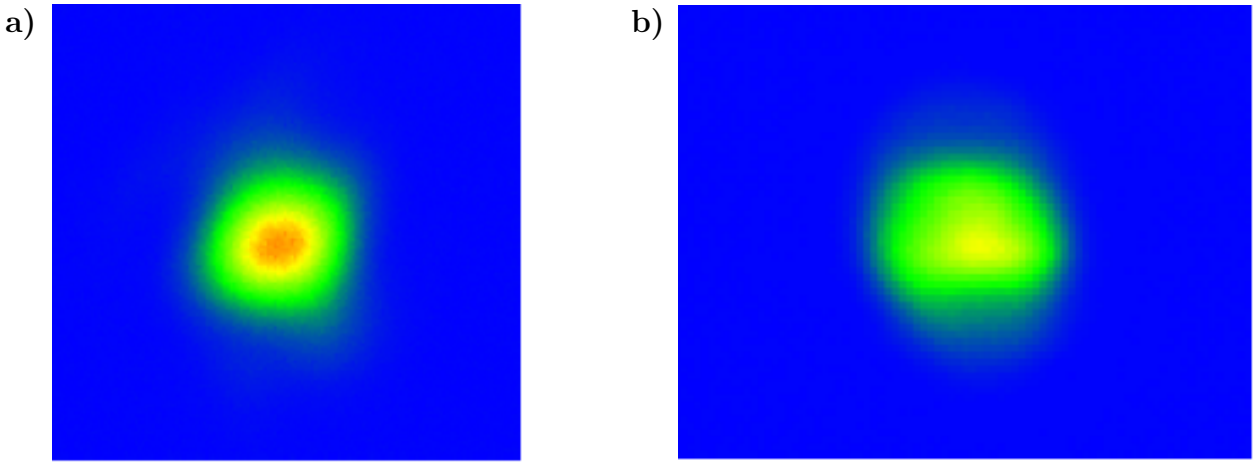

Figure 3.54: Beam profiles at the output of a) 1 kHz cryogenic amplifier and b) 10 kHz cryogenic amplifier.

increased. The optimal pulse compression is performed on the 1 kHz line. Red-shift and spectral narrowing occurring during amplification have been counteracted by performing a Mazzler spectral shaping with the output spectra of the amplification line. Figure 3.55a shows the 1 kHz compressor output spectrum: the spectrum remains as large as 100 nm at $1/e^2$. Optimal compression on the 1 kHz line has been obtained by coupling the Wizzler with the Dazzler: again figure 3.55a shows the measured spectral phase (red line). Figure 3.55b shows the transform limited (red dashed line) and the measured (black line) temporal profile for the 1 kHz amplification line. Pulse duration as short as 17.8 fs are generated with 16 mJ of energy leading to a peak power of 0.93 TW level, thus in the TW-class regime.

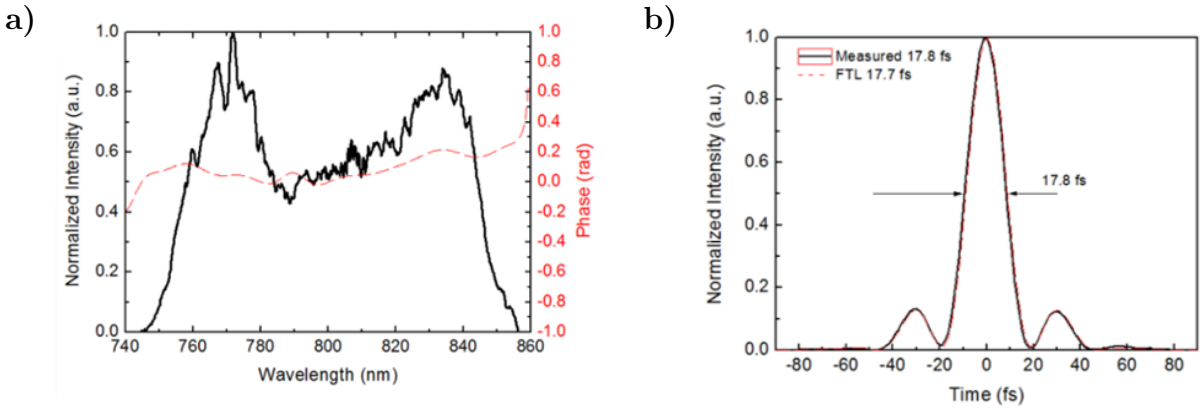

Figure 3.55: a) Measured broad band spectrum of a 16 mJ amplified pulse at 1 kHz (black line) and spectral phase after Wizzler-Dazzler loop (dashed red line). b) Corresponding temporal profile with 17.8 fs FWHM (black line) while its Fourier limited pulse duration is 17.7 fs (dashed red line).

The pulse duration on the 10 kHz line remains below-20 fs with 1.5 mJ pulse energy. The pulse duration difference between the two lines is due to the fact that the Dazzler

parameters are optimized for compression on the 1 kHz line. The energy decrease is due to the fact that it is not possible to further increase the pump power. On the contrary, on the 1 kHz line we benefit of some spare pump power for compensating energy losses in broad band regime. Figure 3.56 shows a picture of the total system. Thanks to the novel design of the

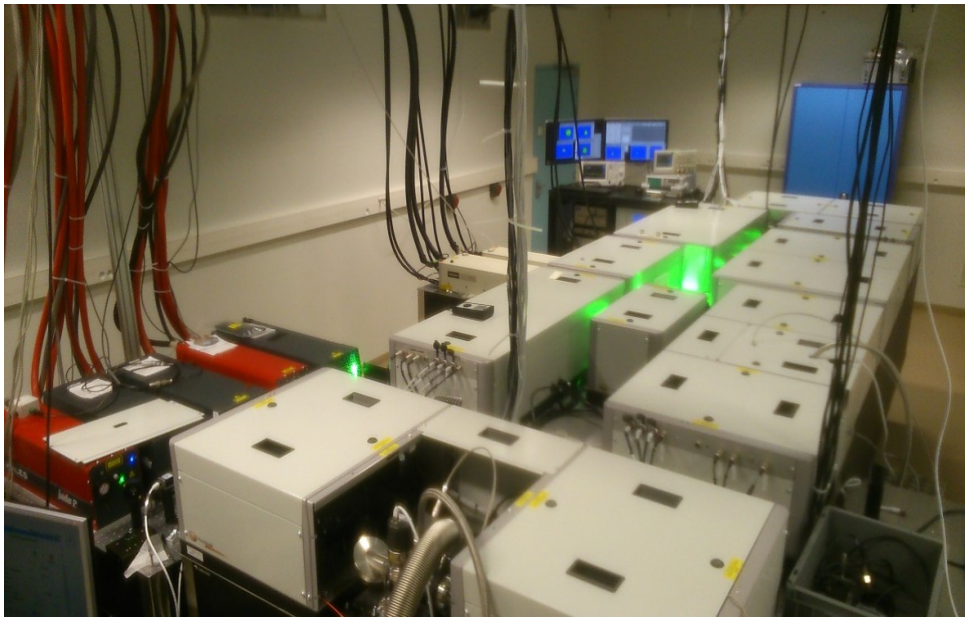

Figure 3.56: Picture of the laser chain comprising the 10 kHz laser front-end and the two high power amplification line at 1 kHz and 10 kHz.

regenerative amplifier detrimental thermal effects can be avoided maintaining a simple and economically convenient laser configuration. Once the front-end is coupled to high power amplifiers, it delivers more than 15 W simultaneously at 1 kHz and 10 kHz with sub-18 fs pulse duration.

Chapter 4

Thermal lensing study within the regenerative cavity

4.1 Introduction

The key factors defining the interaction of the laser pulse with the electron cloud are the beam focusability and beam pointing stability [108]. Eventual wavefront distortions may critically affect the focusability of the pulse, reducing the focus intensity and as a consequence the intensity of the radiation produced from the interaction with the electron bunch. Temporal variations of beam pointing distortion can in turn cause beam pointing fluctuations, introducing a source of instability in the experiment. Wavefront distortions can arise in high average power laser amplifier based on doped crystals, where pumping with high average power causes heat accumulation in the gain medium [26, 109, 110, 27, 111]. The amplified pulses can then be affected by thermal lensing, high order aberrations and beam profiles distortions. Especially thermal lensing should not be underestimated because it can lead to an important reduction of the beam size, causing damages on the optics, and resonator instability when propagating in the cavity. Precautions must be taken in order to minimize or compensate thermal effects while designing high average power, high repetition rate laser amplifiers based on crystal as active medium. The common approach consists in predicting and preventing heat load in the amplification medium. Several numerical approaches have been proposed to study temperature distribution in the pumped medium [112, 113, 114] or more specifically thermal lensing and aberration [115, 116, 117]. These models provide an understanding of the impact of the amplification conditions (pump power, gain medium refractive index or dimensioning) on the thermal lensing phenomenon. The amplifier design can then be scaled accounting for these considerations. Another way to deal with thermal effect is to compensate for it, using divergent lenses or through a specific amplifier configuration. Cooling systems have widely been demonstrated to reduce and in some cases eliminate the thermal effect, in YAG crystals [118] and Ti:Sa crystals [110], and among these the cryogenical cooling [29]. Minimizing the heat load, the cryogenic solution eliminates not only the thermal lensing but any aberration and distortion. The amplifier does not need any corrective optics and it maintains a simple design. As an example, 1 kHz laser systems approaching the TW level and equipped with cryogenical cooler for minimizing

thermal effects have succesfully been demonstrated [119, 83]. However, the cryogenic cooler is an expensive and cumbersome solution, that needs to be adapted to laser systems that require a high level of mechanical stability (CEP compatible chain).
On the other hand, thermal lensing can also be used as shown by Salin et al. [106]. The idea consists in exploiting the induced thermal lens to create an equivalent lens waveguide for generation of diffraction-limited beams in 1 kHz multipass amplifiers.

Despite the solution that can be proposed for preventing detrimental thermal effects, the first step consists in gaining an understanding of the phenomenon. Theoretical studies and experimental measurements have already been proposed in Ti:Sa crystal [108, 29] or in Yb-doped crystal [120]. However, many parameters participate in defining the thermal effect. Improving at its maximum the laser performances certainly requires a specific study considering the particular functioning conditions of amplification. For this reason we tailor a set of measurements of the thermal lens for our Ti:Sa regenerative amplifier.

In the next discussion we will introduce the thermal effect in Ti:Sa crystal for 10 kHz repetition rate pumping. We will firstly describe the existing theoretical model for the thermal lens and then show the results of our measurements.

4.2 Theoretical basics

Pumping the Ti:Sa crystal with high average power causes heat accumulation in the crystal. Thereby, the gradient of temperature appearing in the crystal modifies its mechanical and physical properties, inducing wavefront distortion on the pulse propagating through the medium. In first approximation the distortions induced in the wavefront are equivalent to that induced by a lens, characterized by a certain focal length and astigmatism. The characteristics of the equivalent thermal lens depends on the temperature distribution in the crystal, that needs to be evaluated. It is then necessary to identify the sources of heat. Literature [28] provides a solution of the heat equation in terms of temperature distribution on the crystal. This solution depends on the geometry and on the physical properties of the crystal, on the eventual cooling system and on the average power absorbed by the crystal. Once the temperature distribution is known, it is possible to formulate an equation for the thermal lens focal length.

4.2.1 Thermal sources

In this section we will describe the phenomena that lead to conversion of energy into heat during amplification. An overview of the main non-radiative processes contributing to heat accumulation in the gain medium will be provided.

4.2.1.1 Quantum defect

Upon absorption of one pump photon of energy $h\nu_p$, the d-electron of the Ti:Sa lattice is promoted from the ground state to one of the triplet excited levels. The interaction between

the excited electron and vibrational states causes non-radiative relaxation to a lower energy excited state. The decay to the ground state happens with emission of an IR photon $h\nu_e$. Due to non-radiative relaxation among excited states, the emitted photon energy is lower than the pump energy. The energy difference between pump and emission signal is dissipated in the lattice as heat. In order to quantify the conversion of absorbed energy into heat, it is necessary to introduce the so-called *quantum defect*:

$$\eta_q = \frac{h\nu_e}{h\nu_p} = \frac{\lambda_p}{\lambda_e} \tag{4.1}$$

The Ti:Sa crystal in our laser chain is pumped with the second harmonic of the Nd:YAG emission at 532 nm or Nd:YLF at 527 nm; the emission wavelength spans over a broad spectral range centered at 800 nm. The quantum defect is respectively:

$$\eta_{q,1} = \frac{532}{800} = 66.5\% \qquad\qquad \eta_{q,2} = \frac{527}{800} = 65.9\%$$

4.2.1.2 Quantum efficiency

The *quantum efficiency* accounts for the fact that only a fraction of the pump photons absorbed by the medium is converted into laser radiative emission. There are in fact other processes that contribute to energy damping in a non-radiative way and their probability of occurrence depends on the temperature. For temperature above 150 K, the electronic excited state has a certain probability to couple to lattice vibrational modes, leading to electron decay through non-radiative phonon emission [121]. The quantum efficiency η_c is the relation between the number of photons emitted at the lasing wavelength and the number of absorbed pump photons:

$$\eta_c = \frac{P_e}{P_{abs}} \frac{\nu_{abs}}{\nu_e} \tag{4.2}$$

where P_e and P_{abs} are respectively the emitted and absorbed average power, ν_e and ν_{abs} the emitted and the absorbed frequency, which corresponds to respectively 800 nm and 532 nm.

An equivalent way to describe the quantum efficiency is based on the dynamic of the excited state. The lifetime of the electronic excited state in Ti:Sa is $\tau_r = 3.87$ μs at 0 K [68]. The phonon emission process occurring for temperatures above 150 K causes the excited state lifetime to decrease as a function of the temperature:

$$\tau(T) = \left[\frac{1}{\tau_r} + \frac{1}{\tau_{nr}} exp\left(- \frac{\Delta E}{k_B T} \right) \right]^{-1} \tag{4.3}$$

where $\tau_{nr} = 2.93$ ns is the excited state non-radiative lifetime, $\Delta E = 1794$ cm^{-1} is the energy of the electronic transition, k_B the Boltzmann's constant. The process of lifetime decreasing due to temperature increasing is known as *quenching*.
It is possible to express the quantum efficiency in terms of the excited state lifetime:

$$\eta_c(T) = \frac{\tau(T)}{\tau_r} \tag{4.4}$$

At 300 K the lifetime of the excited state is calculated to be 3.15 μs. With this value the quantum efficiency is:

$$\eta_c(300K) = \frac{3.15\mu s}{3.87\mu s} = 81\%$$

At room temperature the quantum efficiency is 81%, whereas it approaches the unit value for T below 150 K.

The above-mentioned phenomena are the two main sources of heat accumulation during amplification in Ti:Sa crystal. It is possible to account for both of them and define the total absorbed pump energy that is converted into heat:

$$E_{th} = E_{abs}(1 - \eta_c\eta_q) \tag{4.5}$$

At room temperature, one can approximates that $(1 - 0.81 \cdot 0.665 =)$ 46% of the absorbed energy is converted into heat in the crystal. As a consequence, it is not possible to extract more than 54% of the energy deposited in the amplification medium.

4.2.1.3 Other thermal sources

For seek of completeness we cite further processes which contribute to heat accumulation in some gain media but they are negligible in Ti:Sa.

Some materials are characterized by further excited level whose energy is twice the pump photon energy. It can happen that a previously excited electron absorbs a pump photon and is promoted to a higher energy level. The consecutive decay is non-radiative: it contributes to the heat accumulation in the medium and it decreases the quantum efficiency. This phenomenon is called *two-photon absorption*. The electronic structure of the Ti:Sa crystal allows two-photon absorption for a pump wavelength around 350 nm, whereas it is negligible at 532 nm [122, 123].

Another case of heat accumulation concerns those materials where the energy gap between electronic state corresponds to the emitted photon energy. There is then a probability that an emitted photon is reabsorbed by the material. This phenomenon is more probable in materials where absorption and emission band are overlapped. For Ti:Sa, this overlap is limited to a narrow range of wavelengths around 600 nm. However the absorption coefficient at this wavelength is negligible compared to the maximal absorption coefficient at 532 nm.

Finally, we cite the process of *up-conversion*. This phenomenon concerns essentially the rare earth amplifiers. Two ions in excited state can interact one with each other and exchange energy: one of them is promoted to a higher energy level whereas the second decays on the ground state. The first ion decays from the higher to the lower excited state in a non-radiative way. This phenomenon leads to a decrease of population in excited state and to heat accumulation.

4.2.2 Thermal lens focal length

Once the sources of heat storage are identified and characterized, it is possible to deduce the temperature distribution inside the amplification medium. The temperature gradient is the solution of the heat equation. The analytical description that leads from the heat equation to its solution is beyond the purpose of this section. Nevertheless, this topic has been widely treated by several studies [124, 113]. Once we dispose of an equation for the temperature distribution inside the crystal, we can deduce the consecutive refractive index gradient. The refractive index variations as well as thermo-mechanical deformations of the crystal contribute to the wavefront distortion, that can be translated into a thermal lens with focal length [28, 26]:

$$f_{th} = \frac{2\pi r_1^2 K}{P_{th}\left[\left(\frac{\partial n}{\partial T}\right)_{T=T_0} + \frac{2r_2\alpha_{th}(n_0-1)}{L}\right]} \tag{4.6}$$

where r_1^2 is the radius of the pumped zone on the crystal, r_2 is the radius of the crystal, K is the thermal conductivity, $\partial n/\partial T$ is the refractive index gradient as a function of the temperature, α_{th} is the thermal expansion coefficient, L is the length of the crystal, P_{th} is the fraction of pump power converted into thermal power, and n_0 is the refractive index at temperature T_0.
It is clear from equation 4.6, that the dioptric power of the thermal lens strongly depends on the average pump power. The pump profile and size, as well as the geometrical parameters of the crystal, also affect the thermal lensing effect. Even though accurate dimensioning of the crystal and cooling system may help reducing the heat load, the thermal lens dioptric power critically depends on the pump average power.

4.3 Thermal lens measurement

In this section we will describe the setup designed for characterizing the thermal lensing in the Brewster-cut Ti:Sa crystal. The detector we used (SID4, Phasics) will be briefly introduced and then the measurements for different configurations of regenerative amplifier will be reported.

4.3.1 Detection device

The wavefront detector used for the following measurements is SID4 (Phasics) device, based on the *Multiple-Wave Lateral Shearing Interferometry* (MWLSI). The general working principle [125, 126] consists in generating a defined number of replica of the beam to be measured. The MWLSI method exists in different variants according to the number of generated replica: two-wave LSI [127, 128], three-waves LSI [129, 130, 131] or Quadriwave LSI [132, 133, 134] have been demonstrated for wavefront distortion measurements. These replica correspond to different diffraction orders from a diffraction grating and thus they are spatially separated. The angular separation of the replica depends on the wavelength and on

the grating pitch. Figure 4.1 represents schematically the concept of shearing interference in the case of quadri-waves (image modified from [133]).

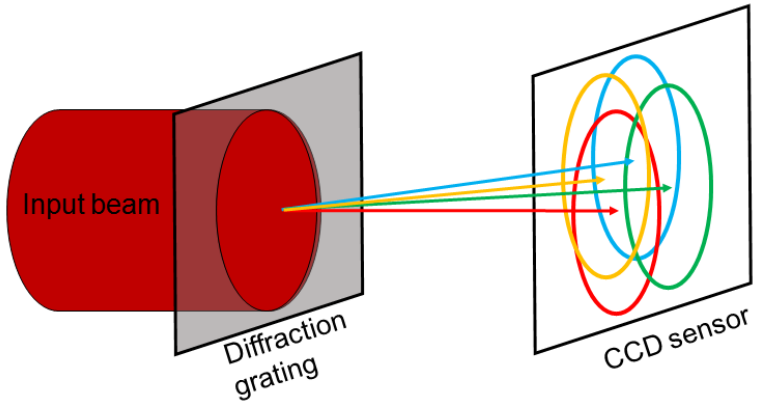

Figure 4.1: Quadri-Wave Lateral Shearing Interferometry. Image modified from [133]

When the waves overlap on the detector, the lateral shear is translated into an interferogram that is detected by a CCD sensor. The wavefront distortion can be retrieved from the interferogram, since the separation between the fringes (2 waves LSI) or the dots (3 and 4 waves LSI) is a function of the wavefront derivative. This technique is able to reach high values of precision of the order of $\lambda/50$ [127] or even $\lambda/200$ [131].

The SID4 uses the Quadriwave LSI technique and its output consists in the beam and wavefront profiles and its Zernike polynomial decomposition. The software calculates also the equivalent lens focal length and astigmatism corresponding to the measured wavefront distortion, thus providing an approximation for the thermal lens dioptric power.

4.3.2 Experimental setup

The thermal lensing has been measured on one of the two Brewster-cut Ti:Sa crystals used in the double-crystal regenerative cavity described in chapter 3. The round section crystal (3 mm radius, 20 mm length) is water-cooled at 17°. The experimental setup conceived for our thermal measurements is inspired by [120, 108] but it is specifically suited to fit in our regenerative cavity. In fact we want to test the thermal lensing under non-lasing and lasing conditions, thus the amplifier should not be influenced by the thermal lens diagnostic in any way.

As probe we used a HeNe laser emitting at 632 nm. In order to avoid spherical aberrations not related to thermal effects, the probe beam size should match with the the pump beam generating the thermal lensing. The scheme of our setup is shown in figure 4.2. At the output of the HeNe we placed an adjustable waveplate to match the probe and the seed polarization inside the regenerative cavity. A confocal telescope magnifies the HeNe beam by a factor of 2.5. Subsequently the beam is focused on the Ti:Sa crystal by a 800 mm lens. The difference in wavelength between pump, Ti:Sa emission and probe ensures that the probe beam can be transmitted through all the optics used in the regenerative cavity. Figure 4.3 shows the pump and the probe beam profiles at the crystal position with their diameters at $1/e^2$. The optical system on the probe injection line allows a perfect match

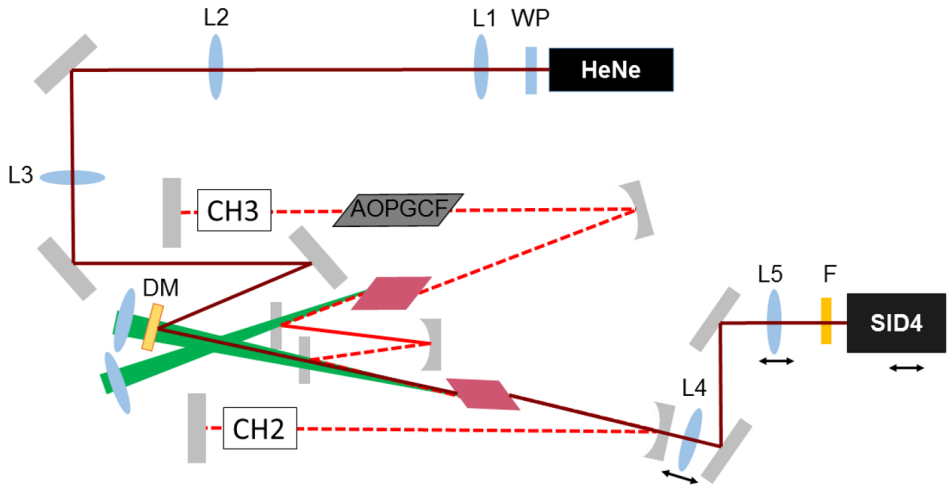

Figure 4.2: Schematic representation of the setup used for thermal lensing measurements. WP-wave plate. L1 and L2-telescope. L3-focusing lens. DM-dichroic mirror. L4 and L5-imaging system. F-filters.

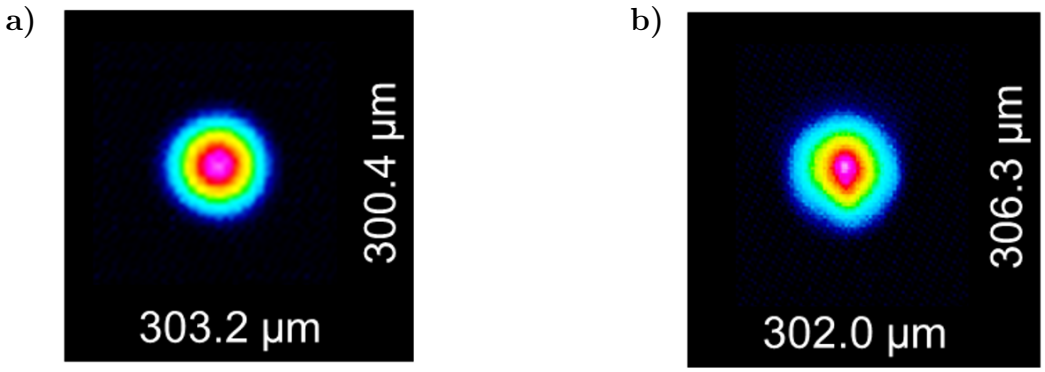

Figure 4.3: Probe (a) and pump (b) profiles at the crystal position (diameter at $1/e^2$).

between pump and probe. The last mirror before the crystal on the HeNe line is a dichroic mirror, with high transmission at 532 nm and high reflectivity from 700 to 900 nm. Even though the reflectivity bandwidth is not optimized for the probe wavelength, there is still enough energy reflected towards the crystal. Moreover, the transmission bandwidth of the mirror ensures negligible energy losses on the transmitted pump beam.
The dichroic mirror is aligned so that the probe beam propagates into the crystal according to the axis of the cavity. The alignment has been done by carefully overlapping the probe with the seed propagating in the cavity, when not pumping. This configuration allows to avoid any further optics inside the cavity that may cause a misalignment of the lasing axis. On the other side, the pump beam needs to be slightly re-aligned after transmission through the dichroic mirror. For this purpose, we switched off the probe beam, and found back the cavity performances in terms of IR output power and build-up time.

After propagating trough the crystal, the probe beam is imaged on the SID4 sensor with a 4f imaging system, comprising two lenses of 500 mm focal length. The imaging lenses and

the SID4 are mounted on horizontal translation stages to optimize the distances. We've been quite careful to image the probe profile at the crystal's output surface position. This choice ensures that the detected wavefront accounts for the thermal lensing integrated through all the crystal length; the thermal lens can in this case be considered as a thin lens placed at the output surface of the crystal. Moreover, since the thermal lens evolves over the crystal length, imaging a different plane would give a different wavefront distortion and thus a different value for the thermal lens. We underline that, considering the compactness of the regenerative amplifier design and the need of keeping unaltered its working regimes, it was experimentally quite difficult and time consuming to find the appropriate setup and carry these measurements.
Two filters are placed in front of the detector to extinguish any stray transmission at the pump and at the Ti:Sa emission wavelengths.
Before proceeding with measurement under pumping condition, the setup has been tested recording the wavefront distortion after propagation through a lens of known focal length, in our case 116 mm at 800 nm. The focal length has been previously measured with an autocollimator. The principle of the measurement is quite simple. We use a diode laser source emitting at 800 nm; the beam is collimated by a lens with known focal length ($f1$ in figure 4.4). The lens to be measured, with unknown focal length f, is placed on the beam optical path. A mirror is then placed at a certain distance from the lens. The mirror reflects back the rays which travel through the lenses towards a half-reflective plate, which deviates the beam on a detector. The distance between the unknown lens and the mirror is then adjusted until the image has precisely the same dimension of the object. The focal length is given by the distance between mirror and lens. Figure 4.4 represents schematically the principle of the autocollimator for focal length measurement. The image size is equal to the object size only if the distance d between lens and mirror is equal to the lens focal length f. The focal length of the lens ($f(\lambda)$) scales with wavelength (λ), thus its value changes at the probe wavelength. For thin lens approximation we can write:

$$\frac{f(\lambda_1)}{f(\lambda_2)} = \frac{n(\lambda_2) - 1}{n(\lambda_1) - 1} \tag{4.7}$$

for $\lambda_1 = 800$ nm and $\lambda_2 = 632$ nm, and BK7 material, the focal length deviation is only 1%, resulting in 115 mm at 632 nm.
A reference wavefront is recorded when the lens is not in place, including all the eventual static aberrations from the optical setup. The SID4 is programmed to acquire and average 100 images. The reference wavefront is subtracted to the measured one, so that the only phase distortions coming from the lens are detected. Figure 4.5 shows the wavefront without the lens (a) and the wavefront after placing the lens (b). The measured focal length is 106 mm and it deviates of 8% from the expected value. This small discrepancy may be due to the precision of the imaging system.

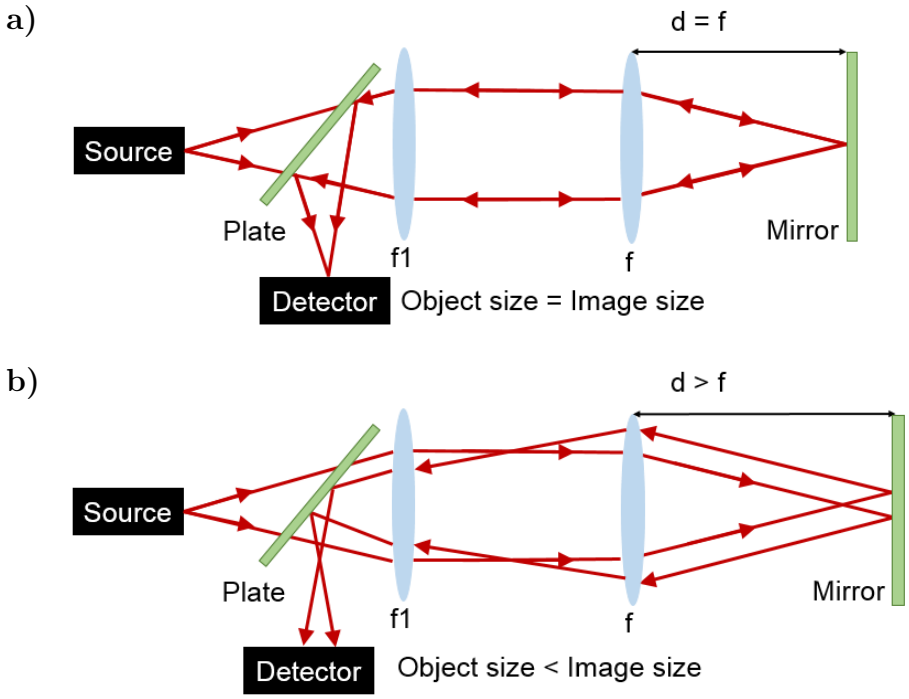

Figure 4.4: Schematic representation of autocollimator for focal length measurement. a) Object and image have the same size and the distance d between the unknown lens and mirror corresponds to the focal length. b) Object and image has different size and the distance between mirror and the unknown lens is not equivalent to the focal length. d-distance between lens and mirror; f-unknown lens focal length; f1-known focal length.

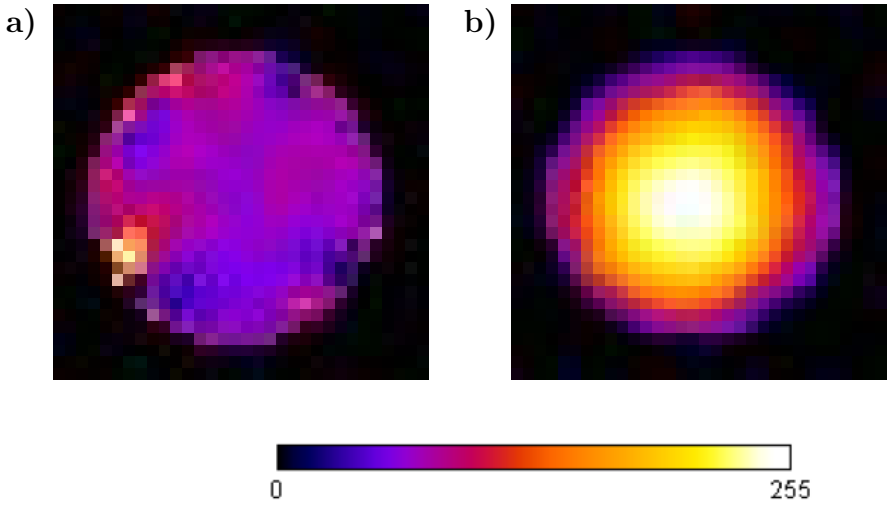

Figure 4.5: Referenced wavefront for a) no lens (flat wavefront) and b) 115 mm lens.

4.3.3 Results

With the previously described setup we ran a set of measurements to quantify the thermal lens focal length in the Ti:Sa crystal. For the first set of measurements, we recorded the effect of the pump on the crystal when the cavity is in non-lasing condition (injection Pockels cell off). The pump power is increased from 8 W to 14 W, that corresponds to the desired pump value for the amplifier routine functioning. The corresponding wavefront distortion is recorded. These data allow to reconstruct the thermal lens focal length variation as a function of the pump power and to compare it with the theoretical curve obtained from equation 4.6. This last one has been obtained with a software developed by Amplitude Laser Group. The code takes as input parameters: the pump beam size and projects the dimensions on the Brewster-cut crystal surface, the repetition rate, the crystal dimensions and the temperature of the cooling system. From these informations, together with the crystallographic parameters of the Ti:Sa ($\tau_r, \tau_n r, \Delta E$), the refractive index gradient is calculated and finally the value of the thermal lens focal length as for equation 4.6. Figure 4.6 reproduces in gray the dispersion of the experimental data, in black the mean value and in red the theoretical curve. As expected, the thermal lens focal length increases with decreasing pump power,

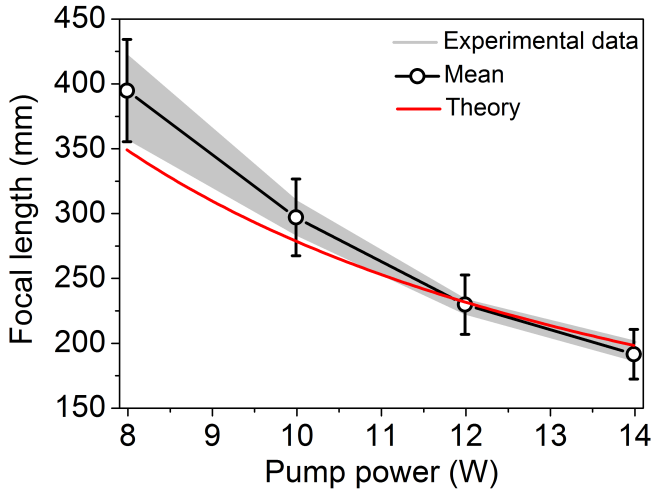

Figure 4.6: Thermal lens focal length as a function of the pump power. In gray, the dispersion of the experimental data, in black the mean. In red the simulated data from equation 4.6.

passing from around 180 mm at 14 W of pump to around 400 mm at 8 W. The measured values match the theoretical model especially for higher power, whereas a discrepancy is notable when the pump power decreases. In this condition the wavefront distortion is less pronounced and the detector is less precise, what also justifies the higher dispersion of the experimental values with decreasing pump power. On the other side, the theory and the experiments show a good agreement for the range of pump value that are actually meaningful for the desired cavity functioning, i.e. around 14 W. The SID4 measurements report also an astigmatism of about 40° on the wavefront. This value is independent from the pump power and it doesn't result from the measurement line, since a reference wavefront has been subtracted before running the measurements. The astigmatism is then part of the thermal

phenomenon, depending on the heat distribution inside the crystal. The projection of the pump beam on the Brewster cut crystal might also contribute to astigmatism.
The probe polarization has been rotated from P to S. The measurements don't show any dependency of the thermal effect with the probe polarization. As an example, the measured thermal lens focal length at 14 W of pump is 187 mm for P-polarization and 185 mm for S-polarization of the probe. The 2% of difference falls into the accuracy range of 8% defined for our setup.

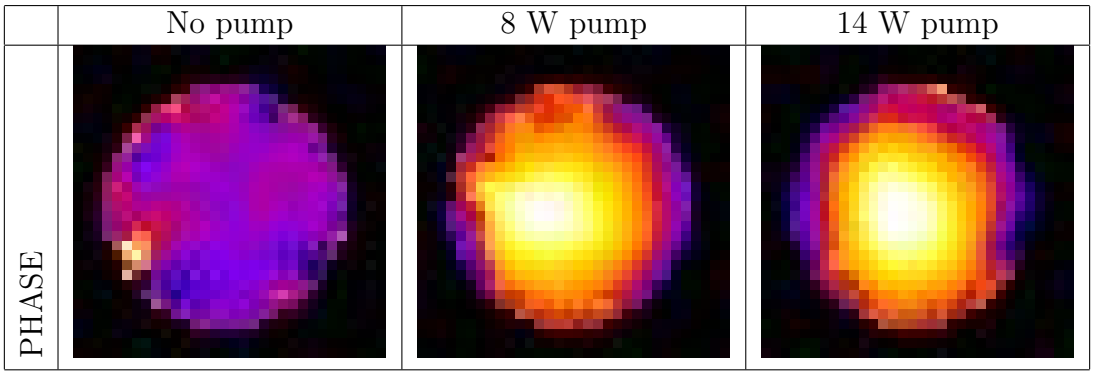

Table 4.1: Phase profiles of the probe beam for increasing pump power.

Table 4.1 shows the wavefronts for increasing pump power. Wavefront distortion should be taken into account when designing the regenerative cavity.

Before proceeding with the second set of experiments, the setup has been modified to detect the portion of the probe wavefront reflected by the Brewster cut crystal. This measurement allows us to verify that no deformation occurs at the crystal surfaces when increasing pump power, since no wavefront distortion of the reflected probe beam is detected by the camera. This justifies the fact that the theoretical description of the thermal lens (equation 4.6) does not include any term of surface deformation.

The second set of measurements consists in testing the thermal effect under different working regimes of the regenerative amplifier. We remind that the regenerative amplifier is designed in a W-like configuration, allowing to pump simultaneously two Ti:Sa crystals. The amplifier is composed by two sub-cavities and it can lase with only one crystal pumped or two crystals pumped. Obviously, the delay of the Pockels cell should be adjusted according to the desired regime.

We first configure the extraction delay of the Pockels cell to allow lasing from one crystal only, specifically the same crystal we use to record the probe's wavefront distortion as a function of pump power. The second crystal is not pumped. We acquired the wavefront distortion of the probe for increasing pump power. Figure 4.7 shows the curves for two lasing regimes, i.e. extracted nanosecond (red curve) and picosecond (blue curve) emission. The black curve reports the data already shown in figure 4.6 for non-lasing regime. The global thermal lens

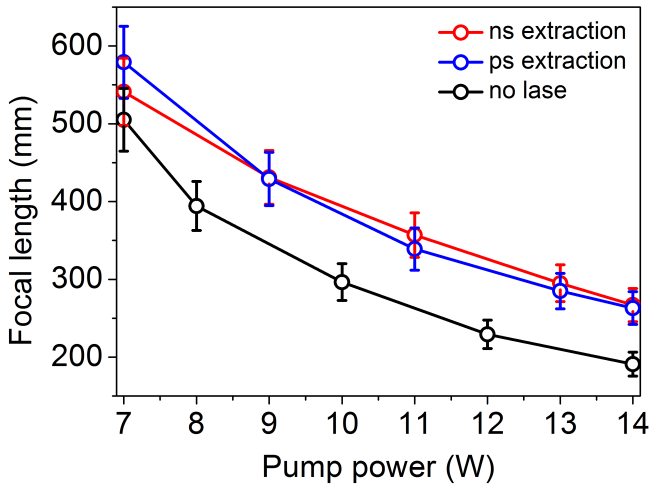

Figure 4.7: Thermal lens focal length as a function of the pump power for different working regime of the regenerative amplifier: non-lasing condition (black curve), extracted nanosecond (red curve) and picosecond (blue curve) emission.

effect becomes weaker when the cavity is lasing; the thermal focal length becomes longer. In fact in this configuration the radiative stimulated emission is encouraged: most of the electronic population is relaxed to the ground level with radiative emission, reducing the probability of non-radiative emission, which causes heat accumulation. The measured focal length for lasing condition is about 6.5 cm longer than in non-lasing condition. We did not notice any significant difference for nanosecond and picosecond regime, meaning that the injected seed does not contribute to heat load in the crystal.

We then measured the thermal lensing effect when both crystals are pumped and the cavity works in picosecond regime. This condition corresponds to the standard working regime of the amplifier. The thermal lensing is measured again through detection of probe wavefront distortion propagating on one of the two crystals. Figure 4.8 reproduces the measured thermal lens focal length as a function of pump power for double crystal picosecond regime. For equal pump power, the thermal effect is less strong when the cavity works in double crystal configuration. This means that stimulated radiative emission is more encouraged, reducing the probability of non-radiative process that would contribute to heat accumulation. For each pump power value, and depending on the cavity regime, the delay of the extraction Pockels cell has been adjusted in order to extract the maximal energy.

Finally we propose a measurement of thermal lensing as a function of the extraction

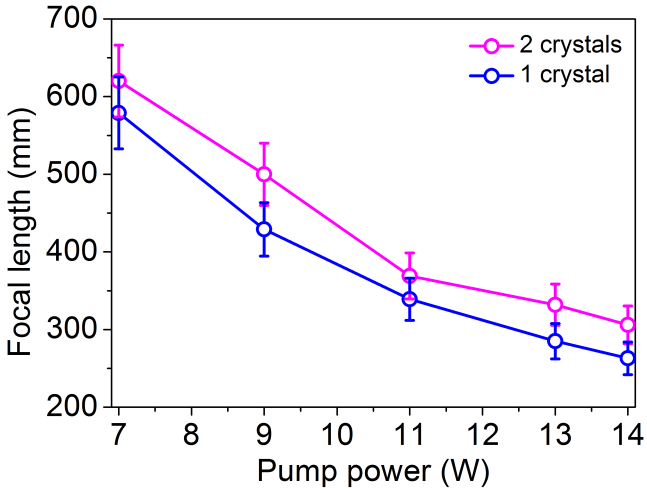

Figure 4.8: Thermal lens focal length as a function of the pump power for picosecond regime of the regenerative amplifier when pumping one crystal (blue curve) and two crystals (magenta curve).

delay, when pumping only one crystal with 14 W of pump. Figure 4.9 reports the thermal

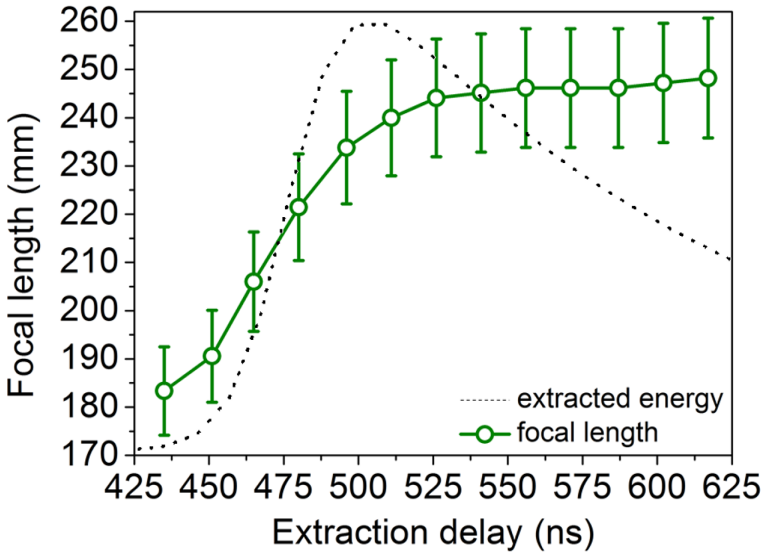

Figure 4.9: Thermal lens focal length as a function of the extraction delay for 14 W of pump power (green curve). The black dot curve corresponds to simulated extracted energy as function of the extraction delay.

lens focal length (green curve) as well as the simulated extracted energy as a function of the extraction delay. First, we set the extraction delay so that the IR signal is extracted before being amplified: this situation corresponds to non-lasing cavity. The thermal lens focal length value corresponds to that shown in figure 4.6, around 180 mm. We then gradually increased the extraction delay of defined steps, each of them equal to a cavity round trip time

(14 ns approximately), and for each step we recorded the wavefront distortion of the probe beam. As the dotted curve shows, with increasing delay the extracted IR pulse undergoes gradual amplification up to its maximum, corresponding to an extraction delay of 510 ns. In this delay range, the thermal lensing becomes weaker and the corresponding focal length longer, up to 240 mm, since more and more energy is extracted from the crystal, reducing the probability of non-radiative relaxation process. The optimal functioning of the amplifier requires to extract the IR beam at the delay of 510 ns. If the extraction delay is further increased, the energy balance between amplification and cavity losses becomes unfavourable, leading to a decrease of the extracted power with increasing extraction delay. On the other side, the thermal lens focal length plateaus at the values corresponding to maximal extracted energy, i.e. 240 mm. The thermal lensing depends in fact only on the amount of energy stored in the crystal, whereas the extracted energy depends on both the energy stored in the crystal and the losses of the cavity. After the optimal extraction time the thermal lensing does not change since there are no additional sources of heat accumulation, which would shorten the focal length, neither other radiative relaxation channel, which would increase the focal length.

We demonstrate that for 10 kHz repetition rate the thermal lensing can be rather strong corresponding to a focal length from 180 mm to 300 mm for 14 W of pump power, depending on the amplifier regime. These values are short considering that the total round trip length in the regenerative amplifier is of the order of the meter. While designing the regenerative amplifier, the thermal lens should be carefully taken into account in order to avoid instability of the resonator, and subsequently low energy conversion efficiency and bad beam profile. As described more in detail in chapter 3, the regenerative amplifier has been designed to support a thermal lens focal length as short as 180 mm, even though in lasing regime the actual thermal lens focal length is longer. The design chosen for the cavity ensures that the amplifier is stable over a large range of thermal lens focal length, from the strongest measured lens, 180 mm, up to 360 mm, ensuring an efficient functioning of the amplifier for different working conditions (one crystal or two crystals pumped, nanosecond or picosecond regime).

4.4 Study of thermal lensing through the crystal length

In the previous discussion we considered the crystal as a thin lens, and we carefully measured the probe wavefront at its output surface, in order to account for the global effect of heat accumulation over the whole crystal length. In this condition and thanks to the 4f-imaging system, the measured radius of curvature of the probe beam (R_{meas}) at the detector sensor corresponds to the wavefront radius of curvature at the output surface of the crystal and equivalently to the focal length of the thermal lens (f_{th}) generated through all the crystal by the pump (see figure 4.10). This method is the most appropriate for studying the global thermal lensing effect of the crystal, providing an equivalent focal length value that can be used to properly design the regenerative amplifier.

However, it might be interesting to also probe the thermal lensing evolution through the crystal length. This study could give a more complete insight of the phenomenon and it

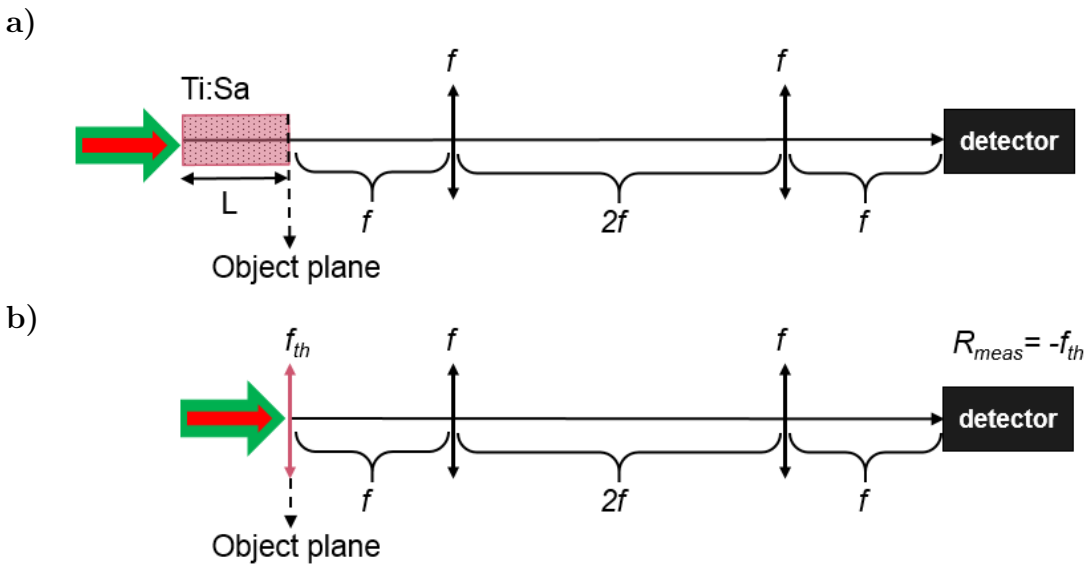

Figure 4.10: a) Schematic representation of the imaging system used for probe's wavefront detection at the output surface of the crystal and b) approximation of the crystal to a thin lens of focal length f_{th}. In green and red respectively the pump and the probe beam.

underlines the different approaches required for different initial hypothesis.
The idea is to measure the wavefront distortion of the probe beam occurring at different surfaces within the crystal length. In this condition, the crystal cannot be approximated to a thin lens anymore, but it should be rather considered in all its thickness. Figure 4.11 clarifies this concept.

A crystal of length L is placed on the axis of an 4f-imaging system, composed by the two lenses with focal f and the detection system. The first and the last crystal surfaces are indicated as S_0 and S_n and they are located at the coordinated z_0 and z_n respectively. If we want to measure the wavefront radius of curvature at a surface S_i with coordinate z_i inside the crystal, the 4f-imaging system and the detection device should be set up so that the image of the surface S_i is created at the detector sensor. The coordinate z_i represents the position of the object plane, and the distance between the surface S_i and the first lens is f (figure 4.11a). The lensing effect of the heat accumulation on the crystal over the length $z_i - z_0$ can be approximated to a thin lens of focal length $f_{th}(z_i)$, placed at the coordinate z_i. The other portion of the crystal within the coordinates z_i and z_n acts like a lens of thickness $d = z_n - z_i$ and unknown focal length f_x, positioned on the imaging system, and contributing to the ray-transfer matrix (figure 4.11b). In the hypothesis that the approximated thick lens has symmetrical radii of curvature of the two surfaces (R_x) and refractive index (n) of Ti:Sa, its transfer matrix can be written as:

$$T = \begin{bmatrix} A & B \\ C & D \end{bmatrix}_{thicklens} = \begin{bmatrix} 1 + \dfrac{d(1-n)}{R_x n} & \dfrac{d}{n} \\ \left(\dfrac{1-n}{R_x}\right)\left(2 + \dfrac{d(1-n)}{R_x n}\right) & 1 + \dfrac{d(1-n)}{R_x} \end{bmatrix}$$

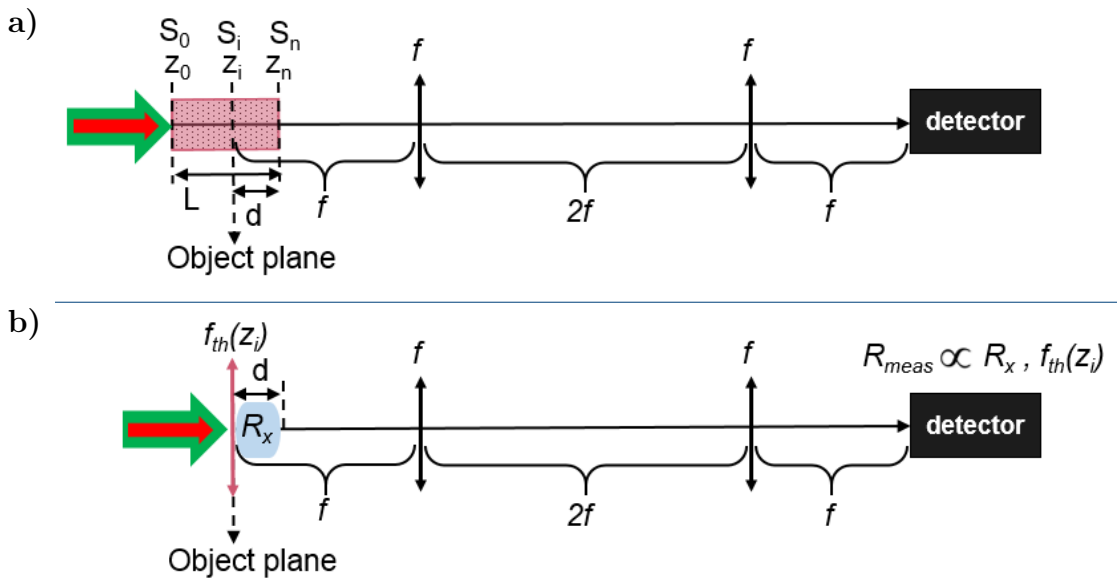

Figure 4.11: a) Schematic representation of the imaging system used for probe's wavefront detection at the surface S_i inside the crystal. b) Approximation of the crystal to a combination of a thin lens of focal length $f_{th}(z_i)$ located at the coordinate z_i, and a thick lens of length $d = z_n - z_i$, and unknown surface's radius of curvature R_x. In green and red respectively the pump and the probe beam.

and its focal length depends on R_x as follows:

$$\frac{1}{f_x} = (n-1)\left[\frac{2}{R_x} - \frac{d(n-1)}{nR_x^2}\right] \tag{4.8}$$

The approximation of thick lens is rather strong, since its transfer matrix is calculated as if the optics was in air, when, actually, it is not physically separated from the other portion of the crystal.

The wavefront radius of curvature measured by the detector (R_{meas}) does not correspond directly to the thermal lens focal length at the object plane ($f_{th}(z_i)$), but depends on both $f_{th}(z_i)$ and the radius of curvature of the thick lens R_x.
For a defined surface on the crystal (S_i), the dependency of the measured radius of curvature (R_{meas}) on the two unknown variables ($f_{th}(z_i)$ and R_x) is given by the ABCD transfer matrix of the imaging system of figure 4.11b:

$$\begin{bmatrix} A & B \\ C & D \end{bmatrix} = \begin{bmatrix} 1 & f \\ 0 & 1 \end{bmatrix} \begin{bmatrix} 1 & 0 \\ -1/f & 1 \end{bmatrix} \begin{bmatrix} 1 & 2f \\ 0 & 1 \end{bmatrix} \begin{bmatrix} 1 & 0 \\ -1/f & 1 \end{bmatrix} \begin{bmatrix} 1 & (f-d) \\ 0 & 1 \end{bmatrix} \begin{bmatrix} A & B \\ C & D \end{bmatrix}_{thicklens}$$

The probe Gaussian beam measured at the detector position is described by its complex parameter q_{meas}:

$$\frac{1}{q_{meas}} = \frac{1}{R_{meas}} - i\frac{\lambda}{\pi w_{meas}^2} \tag{4.9}$$

where R_{meas} is the radius of curvature, w_{meas} the beam spot size and λ the wavelength.
The measured complex parameter q_{meas} depends on the complex parameter at the input of

the imaging system, i.e. $q_i = q(zi)$:

$$q_{meas} = \frac{Aq_i + B}{Cq_i + D} \tag{4.10}$$

Since we can measure both the radius of curvature and the beam waist of the beam after propagation through the optical system, we have complete access to q_{meas}. As consequence, we can inverse equation 4.10 and write the initial complex parameter at the coordinate z_i as a function of the measured complex parameter q_{meas}:

$$q_i = \frac{Dq_{meas} - B}{A - Cq_{meas}} \quad \text{and} \quad Re\left\{\frac{1}{q_i}\right\} = \frac{1}{R_i} = -\frac{1}{f_{th}(z_i)} \tag{4.11}$$

However, since the elements of the transfer matrix ABCD depend on the unknown radius of curvature of the thick lens (R_x), equation 4.11 contains two unknowns (R_x and f_{th}) and it cannot be solved:

$$f_{th}(z_i) = h(R_x) \qquad \text{or equivalently} \qquad f_{th}(z_i) = g(f_x) \tag{4.12}$$

where h and g indicates two generic functions and the second equation is derived from equation 4.8.

If we want to solve equation 4.12 with respect to $f_{th}(z_i)$, we need another equation depending on the same parameter R_x of f_x, in order to build a system of two equations with two unknowns. The idea is then to perform a symmetrical measurement of the wavefront radius at the same surface $S_i = S(z_i)$ when the probe propagates in the opposite direction. Figure 4.12 shows schematically the two coupled measurements for the same surface S_i.

Figure 4.12a corresponds to the above-described case, whereas figure 4.12b represents the symmetrical measurements. In this second case the object plane corresponds again to the surface S_i at the coordinate z_i, and the thermal lensing effect is unchanged, since the pump is unchanged. However, the probe beam propagates in the opposite direction. As a consequence, the portion of crystal within the coordinate z_i and z_n is approximated to a thin lens of focal length $f'_{th}(z_i)$, in general different from $f_{th}(z_i)$, and the portion of crystal within z_0 and z_i can be thought as a thick lens of thickness $(L - d)$ and radius of curvature R'_x, different from R_x. As before, one can find an equation for $f'_{th}(z_i)$ as a function of R'_x:

$$f'_{th}(z_i) = h'(R'_x) \qquad \text{or equivalently} \qquad f'_{th}(z_i) = g'(f'_x) \tag{4.13}$$

where the generic functions h' and g', obtained from the ABCD matrix, differ from h and g because the length of the thick lens is different. Nevertheless, equation 4.13 can be coupled to equation 4.12 considering that:

- Both measurements occur at the same surface inside the crystal, $S_i = S(z_i)$.
- The equivalent focal length of the thick lens (f'_x) for the case of figure 4.12b verifies equation 4.12, providing that R_x is replaced with R'_x and d with $(L - d)$.

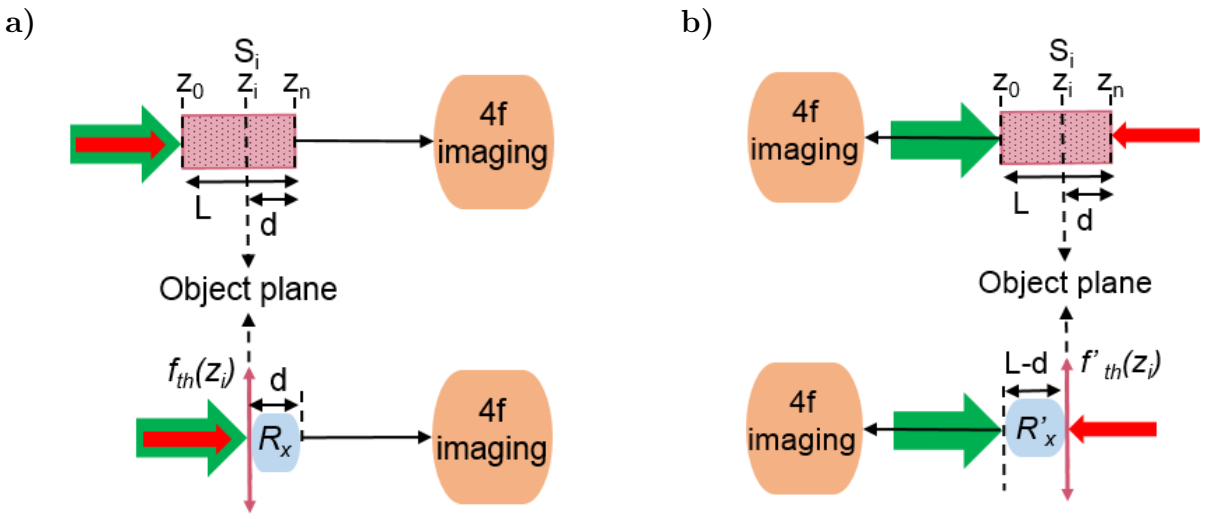

Figure 4.12: Coupled measurements for characterization of the focal length at a surface $S_i = S(z_i)$ in the crystal. a) On top, the first configuration with pump and probe propagating on the same direction in the crystal; on bottom, the approximation to a couple of thin lens with focal $f_{th}(z_i)$ and thick lens of radius R_x and length d. b) On top , the second configuration with pump and probe propagating in opposite directions; on bottom, the approximation to a couple of thin lens with focal $f'_{th}(z_i)$ and thick lens of radius R'_x and length $(L-d)$. Pump and probe are represented in green and red, respectively.

Based on these assumption, we can write:

$$\begin{cases} f_{th}(z_i) = g(f_x) \\ f'_{th}(z_i) = g'(f'_x) \end{cases} \qquad \begin{cases} f'_{th}(z_i) = f_x \\ f_{th}(z_i) = f'_x \end{cases} \tag{4.14}$$

leading to two systems of in total four equations in four variables that can be solved.

This method ideally allows to retrieve the thermal lens focal length induced by the pump at any coordinate within the crystal length, and to reconstruct the lensing effect evolution in the amplification medium. Practically some restrictions to our setup made these measurements rather complicated to implement with the degree of precision required by the experiment. As described in previous section, our setup for thermal lensing measurement is built around the regenerative cavity, to allow its characterization under different functioning regimes. The study proposed in this section requires two coupled measurements in the two opposite directions: one should be able to switch from one configuration to the other, keeping a certain precision on the position of the imaging system, in order to carefully image a defined surface in the crystal. Considering the optics density of the regenerative setup and the limited space, it was impossible to simultaneously set up two symmetrical injection and imaging lines for the probe beam. Nevertheless we tried to first set up one configuration and acquire measurements for a defined number of surfaces inside the crystal and subsequently re-build the symmetrical configuration and measure the same surfaces. However, building

a new configuration was quite time consuming and necessarily this procedure induced an added degree of uncertainty in the measurements, due to design, alignment and eventual environmental variations. Thus, measurements can be affected by perturbations occurring from one configuration to the other and the data cannot be compared. Considering the level of precision required by the experiment, we judge it necessary to run the two symmetrical measurements simultaneously, in order to ensure that the data are acquired under the same conditions.
A solution for simplifying the experiment would be to extract the crystal from the cavity and run the measurements on an independent setup. A new line for the pump must be conceived and the thermal effect cannot be tested under functioning regime of the amplifier.

Finally, also the detection device sets a limitation to the experiment. Our wavefront sensor provides the equivalent focal length for a measured wavefront ray of curvature. The focal length is given as the distance between the camera sensor and the focus of the detected beam. The detection device was calibrated: the camera cannot distinguish between a 10 cm focal length lens placed at 10 cm from the object plane and a 20 cm focal length lens placed exactly in the object plane; the measure gives a focal length of 20 cm in both cases. This effect adds further uncertainty in the measurement of the thermal lensing for a defined surface inside the crystal. On the other side, we can state that the measurement of the thermal lensing at the output surface of the crystal is the most appropriate to globally evaluate the thermal effect.

Chapter 5

The Carrier Envelope Phase

5.1 Introduction

The wide range of applications of ultrafast laser demands an increasing degree of control over all the parameters of intense ultrashort pulses. Well-established methods for pulse diagnostic are nowadays in use in most of the systems and they allow to characterize the envelope in terms of pulse duration, spectral phase and residual chirp [135, 136, 137, 138, 139, 140]. Envelope characterization is exhaustive for describing non linear phenomena in the perturbative regime (intensity $< 10^{13}$ W/cm^2); on the contrary, strong field applications, like high harmonic generation, demand a more detailed degree of control. As the pulse intensity increases due to pulse duration reduction, the light-matter interaction triggers phenomena that are sensitive to the pulse electric field rather than its envelope. Recent advancements in laser technology gave rise to ultrashort system approaching the single-cycle regime [141, 142, 143], with pulse duration of 5 fs [77] and 4 fs [144]. In this condition the electric field varies substantially in the time range of the pulse duration. In order to benefit from complete control of light-matter interaction in the strong field regime, it is necessary to control the mutual position of electric field and envelope maximum. The parameter that defines the position of the main peak of the electric field with respect to the envelope maximum is know as the Carrier Envelope Phase (CEP). A pulse-to-pulse change on the CEP corresponds to a slippage of the electric field under the envelope, and the maximum field strength changes for two consecutive pulses.
At the end of the nineties, first estimations of CEP noise in conventional mode-locked oscillators [145] triggered a rapid development of CEP stabilization techniques [146]. CEP oscillators [147, 148] as well as amplifiers [149] represented a significant step towards the full control of pulse parameters. High harmonic generation processes and in particular isolated attosecond pulse generation [150, 151, 152] benefits from time domain complete control of the driving pulse's electric field. In the frequency domain a train of CEP stabilized pulses corresponds to a steady and defined comb of modes across the laser bandwidth and provides a proper tool for frequency metrology [153].
This chapter provides a definition of the CEP in time and frequency domain; sources of CEP noise for oscillator and amplifier will be identified.

The reader will find many analogies in terms of noise source for oscillator and ampli-

fier. However, due to substantial differences between the two modules, like the energy level and the repetition rate, their respective CEP measurement and stabilization methods are conceptually different.

5.2 Definitions

As introduced in chapter 2, the electric field of a short pulse can be defined as:

$$\mathbf{E}(t) = \mathbf{E}_0(t)cos[\omega_0 t + \varphi_{CE}] \tag{5.1}$$

where $\mathbf{E}_0(t)$ is the envelope, ω_0 the carrier frequency and φ_{ce} the Carrier Envelope Phase (CEP), i.e. the position of the carrier wave with respect to the maximum of the envelope (see figure 5.1). The above formalism is simplified for a transform limited pulse, where no chirp

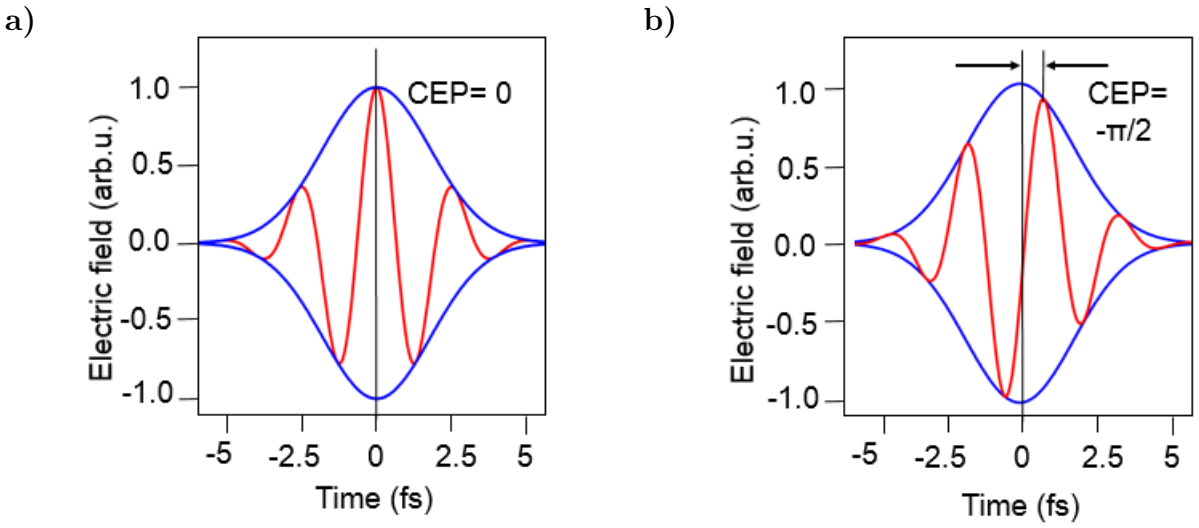

Figure 5.1: Definition of Carrier Envelope Phase for a laser pulse. The envelope is shown in blue line and the carrier in red line for a) CEP = 0 and b) CEP = $-\pi/2$.

nor self phase modulation are taken into account; a complete description of these phenomena and their impact on the envelope shape and instantaneous frequency can be found in chapter 2. The phase relation between carrier and envelope changes with propagation and equation (5.1) is valid for a specific position in space. The carrier phase slips through the envelope during propagation due to the difference between the carrier velocity (phase velocity v_p) and envelope velocity (group velocity v_g).

Considering a pulse with an initial CEP $\varphi_{CE}(z = 0) = \varphi_0$, after propagation through a dispersive medium, the CEP in z is:

$$\varphi_{CE}(z) = \varphi_0 + \omega_0 z \left(\frac{1}{v_g} - \frac{1}{v_p} \right) \Bigg|_{\omega_0} \tag{5.2}$$

$$\Delta\varphi_{CE} = \omega_0 z \left(\frac{1}{v_g} - \frac{1}{v_p} \right) \Bigg|_{\omega_0} \tag{5.3}$$

The difference between group and phase velocity originates from the dependence of the refractive index on the frequency.

$$\frac{1}{v_p} = \frac{n(\omega_0)}{c}$$
$$\frac{1}{v_p} = \frac{\partial}{\partial\omega}\left[\frac{\omega}{c}n(\omega)\right]_{\omega_0}$$

so that

$$\Delta\varphi_{CE}(z) = \frac{z\omega_0^2}{c}\frac{\partial n(\omega)}{\partial\omega}\bigg|_{\omega_0} \tag{5.4}$$

Since

$$\frac{\partial n}{\partial\omega} = \frac{\partial n}{\partial\lambda}\frac{\partial\lambda}{\partial\omega} = -2\pi\frac{c}{\omega_0^2}\frac{\partial n}{\partial\lambda}$$

the carrier envelope shift can also be expressed in terms of refractive index:

$$\Delta\varphi_{CE}(z) = -2\pi z\frac{\partial n}{\partial\lambda}\bigg|_{\lambda_0} \tag{5.5}$$

For example, at 800 nm the chromatic dispersion of fused silica is $\partial n/\partial\lambda = -0.017288$ μm^{-1}, and propagation through 58 μm of fused silica results in a CEP shift of 2π rad. As comparison, the same propagation length induces on a 5 fs pulse a dispersion that broadens the pulse to 5.13 fs, that can be considered negligible. The carrier-envelope phase shift does not depend on the temporal pulse broadening nor on its absolute duration even thought it becomes significant only for quasi-single cycle pulses (sub-10 fs at 800 nm).

5.3 Carrier Envelope Phase in Laser Oscillator

A mode-locked oscillator produces a train of femtosecond pulses spaced in time by the round trip period T_R.
Two consecutive pulses of the train undergo different dispersion, since the second one travels one round trip more in the cavity. For consecutive pulses the CEP varies according to the equation (5.5) with z equal to the propagation length through the dispersive gain medium (see figure 5.2[154]).
Considering in first approximation no perturbation of the laser cavity, we can state that the CEP shift of consecutive pulses, $\Delta\varphi_{CE}$, from an oscillator is constant. The condition of no perturbation will be relaxed in the next section, and CEP shift variation with time will be discussed.
The time between two pulses with same value of CEP is defined as the *carrier envelope phase offset time*:

$$T_{CEO} = T_R\frac{2\pi}{\Delta\varphi_{CE}} \tag{5.6}$$

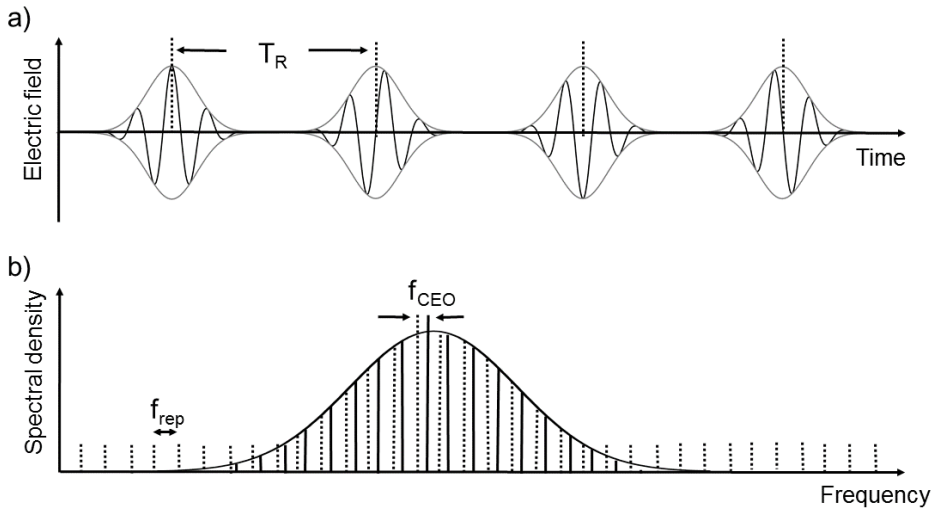

Figure 5.2: a) Time and b) frequency domain representation of the output of a mode-locked oscillator. The spectral comb of longitudinal modes corresponds to a train of pulses spaced in time by T_R. The frequency offset of the comb f_{CEO} is related to the pulse-to-pulse phase shift [154].

Ignoring for now $\Delta\varphi_{CE}$, in the time domain the electric field of a train of identical pulses can be written as:

$$E(t) = \sum_n E_p(t - nT_R) \tag{5.7}$$

Using the Poisson sum formula, the above-mentioned electric field can be re-written as a function of its Fourier transform $\tilde{E}$ [154]:

$$E(t) = \sum_n E_p(t - nT_R) = \sum_{k=-\infty}^{+\infty} \frac{1}{T_R} \tilde{E}\left(\frac{k}{T_R}\right) e^{i2\pi kt/T_R} \tag{5.8}$$

Equation (5.8) shows that in the frequency domain the electric field of a train of pulses consists of a comb of discrete frequencies, integer multiples of the repetition rate $f_{rep} = 1/T_R$. If the pulse-to-pulse phase shift $\Delta\varphi_{CE}$ is included, the absolute phases of consecutive pulses of the train are not identical and, for the n-th pulse of the train, it can be written as $\varphi_{CE} = \varphi_0 + n\Delta\varphi_{CE}$, where φ_0 is the CEP of the initial pulse. The electric field of the train of pulses is then:

$$E(t) = \sum_n E_0(t - nT_R) e^{i(\omega_0 t - n\omega_0 T_R + n\Delta\varphi_{CE} + \varphi_0)} \tag{5.9}$$

$$= \sum_n E_0(t - nT_R) e^{i(\omega_0 t + n(\Delta\varphi_{CE} - \omega_0 T_R) + \varphi_0)} \tag{5.10}$$

Fourier-transforming the equation for $E(t)$ leads to:

$$\tilde{E}(\omega) = \int \sum_n E_0(t - nT_R) e^{i(\omega_0 t + n(\Delta\varphi_{CE} - \omega_0 T_R) + \varphi_0)} e^{-i\omega t} \tag{5.11}$$

which, after further manipulation[154], leads to:

$$\tilde{E}(\omega) = e^{i\varphi_0}\tilde{E}_0(\omega - \omega_0)\sum_m \delta(\Delta\varphi_{CE} - \omega t - 2\pi m) \tag{5.12}$$

The resulting electric field is a comb of frequencies:

$$\omega_m = \frac{2m\pi}{T_R} - \frac{\Delta\varphi_{CE}}{T_R} \tag{5.13}$$

$$f_m = mf_{rep} + f_{CEO} \tag{5.14}$$

where the *carrier envelope phase offset frequency* - f_{CEO} is defined as:

$$f_{CEO} = -\frac{\Delta\varphi_{CE}}{2\pi T_R} = \frac{\Delta\varphi_{CE} f_{rep}}{2\pi} \tag{5.15}$$

Equation (5.14) shows that the frequency comb is shifted from integer multiples of the repetition rate by a value f_{CEO} that depends on the pulse-to-pulse carrier envelope phase shift (see figure 5.2).

5.3.1 CEP noise sources

Equation (5.5) underlines the direct link between chromatic dispersion and CEP shift. If the dispersion is time independent, the frequency offset (f_{CEO}) of the oscillator spectral comb stays constant as well as the pulse-to-pulse CEP shift ($\Delta\varphi_{CE}$). There are actually various factors that may induce a time dependency on the chromatic dispersion and as a consequence the CEP shift may not be constant with time. Such different sources of noise inducing a time dependency on the dispersion can be classified according to their time characteristic.

Environment temperature variations, together with pressure and humidity changes can induce perturbations of the gain medium refractive index in a long time scale (minutes or hours).

Faster variations, inducing a pulse-to-pulse noise on the CEP shift, originate from the Kerr effect. Typical commercial oscillators deliver pulses with energy of the order of 5 nJ and few cycle pulse duration, approximately 5 fs, at 75 MHz repetition rate. With these performances, the average power and the peak power reach respectively 0.5 W and 1 MW. The resulting intracavity intensity is high enough to induce nonlinear phenomena, first and foremost the Kerr effect, causing the dependency of the refractive index on the intensity, according to the equation $n(I) = n_0 + n_2 I$ (cfr chapter 2). Variation in time of the IR intensity circulating inside the cavity induces a time dependency on the refractive index; this energy variation is in turn directly correlated to the energy stability of the pump beam. Studies [155, 156] confirmed the CEP noise caused directly by intensity fluctuations.
Another side effect directly correlated to intensity fluctuations must be taken into account: changes of the refractive index cause in turn the incident beam to propagate inside the crystal in a different direction due to the Snell law of refraction. The consequent beam depointing has a direct influence on the CEP shift and it has been measured to be even more critical than the refractive index variation [156].

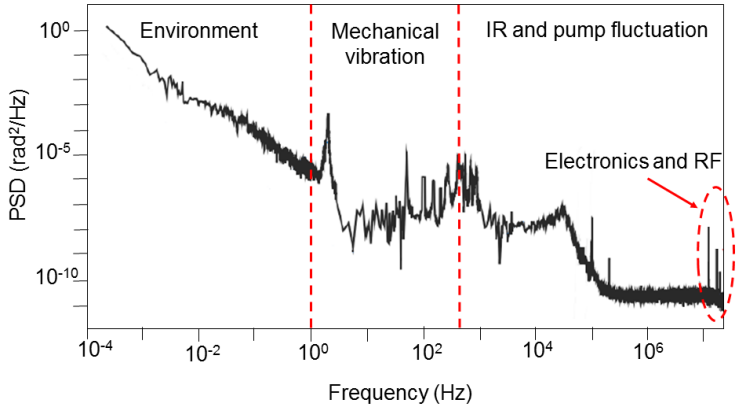

Figure 5.3: CEP noise power spectral density for an oscillator working at 75 MHz and different noise ranges.

Figure 5.3 depicts the CEP noise Power Spectral Density (PSD) for typical oscillator operating at 75 MHz[1]. The PSD, expressed in rad^2/Hz, gives information about the noise power distribution over frequency range and it is defined as the Fourier transform of the autocorrelation function of the noise signal. For lower frequency components up to the Hz level, the main contribution to noise is given by environment perturbations, like temperature or humidity variations. The broadband noise extending from the Hz up to the 100 Hz level is mainly due to mechanical vibrations. For faster variation the main noise sources are IR and pump intensity variations. The narrowband peaks at the upper edge of the spectrum are due to electronics and RF noises.

5.3.2 CEP shift detection

The first successful measure of CEP shift in the time domain dates back to 1996 and was performed using an interferometric cross-correlator [145]. The technique is based on a Michelson interferometer followed by a second harmonic crystal. One arm of the interferometer is properly delayed so that two consecutive pulses interact in the second harmonic crystal. A detector tuned on the second harmonic field acquires the signal that contains informations about $\Delta\varphi_{CE}$. Since this time domain technique compares two consecutive pulses, it is not sensitive to rapid jitter that may not affect critically the CEP shift of the above-mentioned pulses but on the contrary may be detrimental for highly separated pulses due to a sum-up effect.

The breakthrough came with a self-referencing technique based on the so-called *f-to-2f interferometer*. Instead of measuring the $\Delta\varphi_{CE}$ of two subsequent pulses, this frequency domain method provides a way to directly detect the f_{CEO}. Figure 5.4 [157] shows the working principle of the f-to-2f interferometer. A frequency $f_m = mf_{rep} + f_{CEO}$ in the lower part of the spectral comb undergoes frequency doubling in a proper crystal, generating the component $2f_m = 2(mf_{rep} + f_{CEO})$. If the fundamental spectrum spans over an entire

[1]http://www.medea-horizon2020.eu/wp-content/uploads/2016/04/MEDEA_Webinar_2016-03-16_CEP-Stabilization_Luecking.pdf

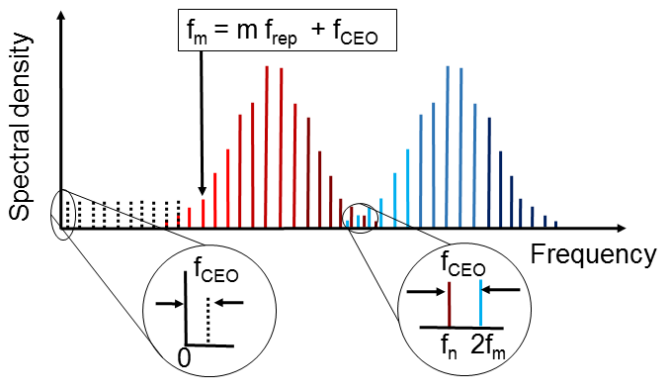

Figure 5.4: Principle of f-to-2f interferometer. The fundamental spectrum (red comb) undergoes frequency doubling (blue comb). The superposition of the newly-generated component $2f_m$ and the f_n component of the fundamental spectrum results in the heterodyne beat-signal f_{CEO} [157].

octave, it naturally contains components close to the newly-generated frequency, with index $n = 2m$ so that $f_n = 2mf_{rep} + f_{CEO}$. The superposition of the two frequencies $2f_m$ and f_n on a detector results in the heterodyne beat-signal at frequency f_{CEO}.

$$2f_m - f_n = 2(mf_{rep} + f_{CEO}) - (2mf_{rep} + f_{CEO}) = f_{CEO} \tag{5.16}$$

The beat frequency f_{CEO} becomes accessible as an RF signal and can be tracked using a radio-frequency spectrum analyser. A delay line is required in order to compensate the group delay between the low and the high components of the comb. Note that neither the cross-correlation nor the self-referencing technique can determine the absolute value of the CEP for a given pulse, but rather its pulse-to-pulse change in terms of phase $\Delta\varphi_{CE}$ or offset frequency f_{CEO}.

Typical spectra of commercial oscillator, albeit broad, do not cover an entire octave. Applying the self-referencing technique requires then a preliminary broadening of the spectrum. Octave spanning spectra can be produced using self-phase modulation in non linear media. Microstructured fiber [158] have been used to successfully generated wide spanning spectra[159][160], as well as photonic-crystal fiber [161], keeping unaltered the structure of the comb. An alternative self-referencing technique used for measuring the offset frequency employs the difference frequency generation [162, 163]. This method requires a large but non necessarily octave-spanning spectrum [164]. In this case three teeth are considered $f_q = qf_{rep} + f_{CEO}$, $f_p = pf_{rep} + f_{CEO}$ and $f_r = rf_{rep} + f_{CEO}$, where the three integers numbers satisfy the relation $q - p = r$. The two components f_q and f_p interact in a non linear medium and generate the difference frequency $f_q - f_p = (q - p)f_{rep} = rf_{rep}$. The difference frequency interacts with the comb tooth f_r and the resulting beat-signal $(f_q - f_p) - f_r = f_{CEO}$ is acquired on the detector.
Different versions of frequency mixing have been proposed for f_{CEO} detection, like for example the *2f-to-3f* interferometer [165], where a PPLN crystal has been used in order to generate the second harmonic frequency $2f$ and the sum frequency $3f$.

5.3.3 Carrier Envelope Offset frequency stabilization

Once the offset frequency is detected, it is possible to draw up a feedback system that allows to minimize its time drift and stabilize its value. In general, the method to stabilize f_{CEO} is to control the source that causes its drift. As mentioned in the first section, the offset frequency noise originates from the difference between group and phase velocity. A first intuitive method consists in inserting different thickness of a wedge glass plate in the beam path, in order to change roughly the dispersion. Secondly it is possible to implement a faster feedback loop acting on the end cavity mirror of the oscillator. With a motorized mount, the tilt of the mirror is finely tuned in order to slightly change the incidence angle of the beam in the dispersive medium and consequently change the dispersion.

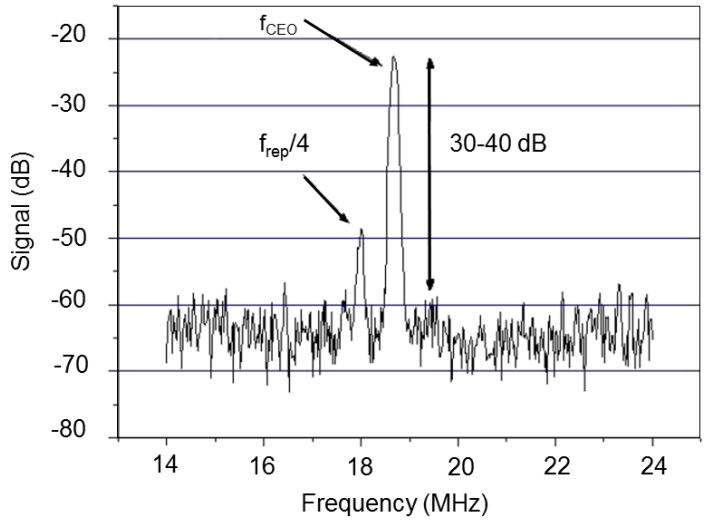

Figure 5.5: Beat-signal f_{CEO} and reference signal $f_{rep}/4$ at the input of the phase-detector for a 75 MHz oscillator.

Since the time stability of the offset frequency is strongly dependent on the energy stability of the pump, another more efficient method to tailor its value is to directly vary the pump energy. This is possible using an acousto-optic modulator (AOM), which partially diffracts the pump beam, allowing to finely adjust its value and consequently the Kerr effect.

Electronic systems for locking the CE offset frequency are commercially available, such as the Menlo Systems product. Initially a fast photodiode detects the repetition rate frequency f_{rep} and the reference signal $f_{rep}/4$ is generated. At the same time, the offset frequency f_{CEO} is detected at the output of an f-to-2f interferometer. Figure 5.5 shows the beat-signal f_{CEO} from an f-to-2f interferometer and the $f_{rep}/4$ signal. The two signals, $f_{rep}/4$ and f_{CEO} are sent to two inputs of a phase-detector, which gives at the output a periodic signal modulated at the frequency difference of the inputs ($f_{rep}/4 - f_{CEO}$). The error signal is sent to the input of a proportional integral controller that acts on the acousto-optic modulator for tuning the pump power and minimizing the error signal; f_{CEO} is consequently stabilized at $f_{rep}/4$. Figure 5.6 depicts the working principle of the earliest commercial CEP stabilized oscillator (Rainbow CEP3 from Spectra Physics) based on the above described feedback method. The CEP noise correction bandwidth is limited to 100 kHz and can stabilize the train of pulses

with residual CEP noise of 100-150 mrad.

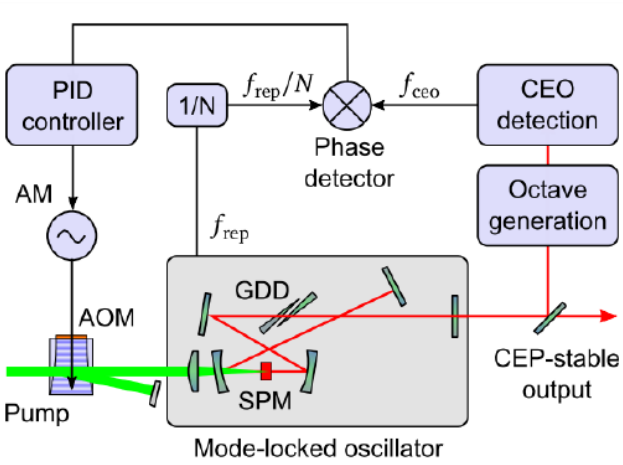

Figure 5.6: Working principle of a commercial CEP stabilized oscillator based on the feedback technique.

The latest improvement in the CEP locking technique gave rise to a new generation of CEP stabilized oscillator based on the so-called feed-forward technique, referring to the fact that the correction applied to the frequency comb does not affect the f_{CEO} measurement. The working principle has been firstly described by Koke et al. and is depicted in figure 5.7[166].

The frequency comb from the femtosecond, not CEP stabilized oscillator is injected in the AOFS, that acts like a transmission diffractive element. The input beam is therefore divided into two parts according to the diffraction order zero and one. The comb of the transmitted beam (zero order) remains unaffected whereas the diffracted comb is shifted by the frequency f_{RF}, that is the input of the acousto-optics device. It is then sufficient to set $f_{RF} = f_{CEO}(t)$ in order to shift the diffracted comb to exactly zero offset. In order to do this, the order zero comb is used as a measurement source and the result of the measurement is used to power the AOFS. The first order comb is stabilized to $f_{CEO} = 0$ that corresponds in time domain to a train of pulses with the same electric field. In order to maximize diffraction efficiency in the first order the set-up satisfies the Bragg condition: $2\lambda_{ac} sin\alpha = \lambda n$, where λ_{ac} is the acoustic wavelength, $\alpha = \alpha_{in} = \alpha_{out}$ are the input and diffracted angles, λ the optical wavelength and n the refractive index of the AOFS. With a diffraction efficiency of about 60-70%, this technique allows a large stabilization bandwidth up to the MHz range. Oscillators based on this stabilization method are nowadays commercially available (Rainbow CEP4 from Spectra Physics), demonstrating CEP stabilization with residual noise of 30 mrad on a 20 seconds time scale [167] and less than 100 mrad over hours.
Both of the oscillators described in this section (Rainbow CEP3 and CEP4) have been used during the thesis for different developments.

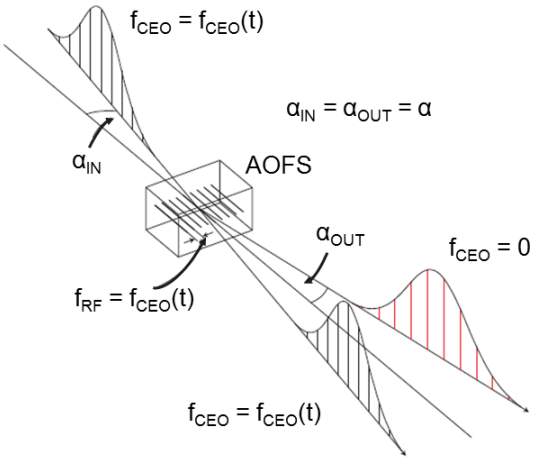

Figure 5.7: Representation of the feed-forward principle. The Acousto Optics Frequency Shifter (AOFS) splits the input comb into two beams. The transmitted comb (black) is used to measured $f_{CEO}(t)$; the diffracted comb (red) is CEP stabilized to $f_{CEO} = 0$ as long as the acousto-optics frequency which powers the AOFS f_{RF} is set equal to the measured $f_{CEO}(t)$. Figure taken from [166].

5.4 Carrier Envelope Phase in Amplifiers

In the previous chapter we discussed the necessity of amplifying the train of pulses from the oscillator in order to reach peak powers that allow to access physical phenomena beyond the perturbative regime. Monitoring the electric field of amplified pulses is necessary for a complete control of the strong field experiment. For this purpose CEP stabilization at the oscillator level is essential but not sufficient since different noise sources in the typical Chirp Pulse Amplification design affect the CEP stabilization. As we will see in the next discussion, upon detection of these noise sources, it is possible to correct the CEP noise of the amplified pulses. Since the limit to noise detection is imposed by the amplifier repetition rate, we have no access to noise at frequencies higher than the repetition rate. However higher frequency noise can be detected and stabilized at the oscillator output. For this reason it is necessary to reduce as much as possible the CEP noise at the output of the oscillator, and to benefit from the highest detector's acquisition speed, that in the best case is equal to the repetition rate.

5.4.1 CEP noise sources in amplified chains

Even if CEP fluctuations at the oscillator level can be successfully detected and to some extent controlled, additional noise sources influence the CEP at the output of an amplified chain. The CEP noise introduced by the amplification chain originates mainly from three sources [168]: i) changes on the material path lengths due to temperature variations and beam pointing fluctuations; ii) non linear refractive index variations caused by laser intensity fluctuations; iii) beam pointing and mechanical perturbations of highly dispersive module

such as stretcher and compressor.

In the following text each of these sources will be analysed, providing some reference values of the corresponding CEP shift.

Starting from the first noise source, air turbulences and mechanical vibrations cause shot-to-shot beam pointing fluctuations which in turn change the path length travelled by the pulse in the amplification medium or refractive optics. The following CEP change due to beam pointing (bp) can be evaluate as: $\delta\varphi_{bp} = 2\pi(\Delta L/L_{2\pi,bp})$, where ΔL is the the change of the optical path length and $L_{2\pi,bp}$ is the propagation length which corresponds to a CEP change of 2π. Values of $L_{2\pi,bp}$ for different materials at 800 nm are given in table 5.1 [168].

Material	$L_{2\pi}$ at 800 nm
Air	157×10^3 μm
Sapphire	37 μm
Fused Silica	58 μm

Table 5.1: Values of propagation lengths corresponding to a CEP shift of 2π for different materials.

For good experimental conditions [169] where beam pointing fluctuations do not exceed several μrad, the corresponding CEP fluctuation is in the sub-mrad regime, then negligible. Giving an example, we study here the case of a pulse propagating through a fused silica plate of d =10 cm thickness. Considering a beam depointing of 20 μrad, the corresponding difference in propagation length can be found considering the Snell law of refraction. At the interface between two media, the refraction angle θ_2 is given by the relation $n_2 sin\theta_2 = n_1 sin\theta_1$ where n_1 and θ_1 are respectively the refractive index and the incidence angle of the first medium , n_2 is the refractive index of the second medium. Considering a first pulse with normal incidence direction ($\theta_1 = 0$): its refraction angle is $\theta_2 = 0$ and the optical path length through the fused silica plate L_1 corresponds to exactly the plate thickness d multiplied by n_2. If a second pulse carries a depointing $\delta\theta$, the new refractive angle θ_{2bp} will be given by $n_2 sin\theta_{2bp} = n_1 sin(\theta_1 + \delta\theta)$. The second pulse propagates then through a distance $L_2 = n_2 d/cos\theta_{2bp}$. The change on the optical path length is then $\Delta L = L_2 - L_1 = n_2 d(1/cos\theta_{2bp} - 1)$. For $\delta\theta = 20\mu rad$, $n_1 = 1$ and $n_2 = 1.4533$ (pulse propagating from air to fused silica), d = 10 cm, and $L_{2\pi}$ as in table 5.1 and as calculated in section 5.2, the corresponding $\delta\varphi_{bp}$ is of the order of the μrad.

Environment as well as gain medium temperature fluctuations can induce a greater CEP noise, but they occur on a minute time scale, leading to a very slow drift. In conclusion, temperature variations and beam pointing in low dispersive media cause a negligible shift in the CEP.

The second source of noise is correlated to pulse intensity fluctuations.
As already listed among the main sources of CEP noise in oscillators, the Kerr effect is once again a critical factor for CEP noise in amplifiers. Fluctuations of the amplified intensity lead to changes in the refractive index of the propagation medium, and subsequently to

CEP shift. The CEP shift due to the non linear refractive index (nl) can be expressed as: $\delta\varphi_{nl} = 2\pi L/L_{2\pi,nl}$, where L is the medium length and $L_{2\pi,nl}$ is the propagation length corresponding to 2π CEP shift. As already mentioned, for a specific medium the refractive index is: $n = n_0 + n_2 I$, being I the pulse intensity. The variation of refractive index due to intensity fluctuations depends on the term $n_2 I$. It is then possible to write $L_{2\pi,nl}$ as function of the refractive index variation: $L_{2\pi,nl} = 1/[I(dn_2/d\lambda)]$. In the previous chapter the B-integral has been introduced as the total phase change due to non-linear refractive index: $B = 2\pi/(\lambda)\int_0^L n_2 I dz$. For simplicity, the intensity is assumed to be constant over the length L and the B-integral becomes: $B = IL2\pi n_2/(\lambda)$.
It is possible to express the CEP shift due to non linear refractive index in terms of B-integral:

$$\delta\varphi_{nl} = \frac{\lambda}{n_2}\frac{dn_2}{d\lambda}B \tag{5.17}$$

The CEP change due to relative intensity fluctuation of the amplified pulse ΔI is given by $\delta\varphi_{nl}\Delta I$.
For propagation through typical materials of an amplified chain, like Ti:Sa as amplification medium and fused silica for refractive optics, the values of n_2 and $dn_2/d\lambda$ at 800 nm are listed the table 5.2[168]. When amplifying short pulses at high energy level it is important to

Material	n_2 (m^2/W)	$dn_2/d\lambda$ (m/W)
Fused Silica	3.3×10^{-20}	-0.98×10^{-14}
Sapphire	3.0×10^{-20}	-1.03×10^{-14}

Table 5.2: Non linear refractive index and chromatic dispersion for Fused Silica and Sapphire [168].

keep the B-integral to reasonable value (3-5). Table 5.3 below resumes the torelable values of relative intensity pulse-to-pulse fluctuation ΔI for ensuring that the corresponding CEP noise does not exceed 50 mrad, for B-integral increasing form 1 to 3 and 5.

Material	$B = 1$	$B = 3$	$B = 5$
Fused Silica	$\Delta I < 20\%$	$\Delta I < 7\%$	$\Delta I < 4\%$
Sapphire	$\Delta I < 18\%$	$\Delta I < 6.1\%$	$\Delta I < 3.7\%$

Table 5.3: Torelable values of ΔI for different values of B-integral ensuring CEP noise not exceeding 50 mrad, for propagation in Fused Silica and Sapphire .

Since the intensity fluctuations can vary between two consecutive pulses, the corresponding noise is on the shot-to-shot scale and introduces a CEP shift that becomes difficult to compensate at the kHz repetition rate. The train of amplified pulses generated by the double crystal regenerative amplifier described in chapter 3 is characterized by RMS stability of 0.3%. For this values and typical unit value of the B-integral the CEP noise is of the order

of the mrad, thus negligible.

The third source of CEP noise of amplified pulses is dispersion fluctuations in stretcher and compressor. In the previous chapter we demonstrated that grating based stretcher and compressor are the most suitable dispersive modules for high amplification systems, where large stretching and compression factors are demanded. On the other side, these modules are more sensitive to mechanical vibrations and beam pointing fluctuation because of their cumbersome design, which includes further optics. The influence of grating based dispersive modules on the CEP will be deepened in the next chapter, where existing theoretical models for CEP shift in grating based modules will be compared to simulation based on ray tracing software.
In this section we introduce the topic considering a typical design for grating-based stretcher and compressor. As already mentioned in the previous chapter, the spectral phase $\varphi(\omega)$ and the group delay τ_g induced by a single pass in the grating pair are:

$$\varphi(\omega) = \frac{\omega p}{c} + R(\omega) \quad \text{and} \quad \tau_g = \frac{\partial \varphi}{\partial \omega} = \frac{p}{c}$$

where p is the total path length in the dispersive module, c is the speed of light. $R(\omega)$ is the phase-correction term introduced by Treacy (chapter 2) and is given by $R(\omega) = -2\pi G(tan\theta_d(\omega))/d$, where G is the perpendicular gratings distance, d the grating constant and θ_d the diffracted angle which depends on the spectral component.

The CEP shift experienced by a specific pulse after one passage on the grating pair is then:

$$\omega_0 \frac{\partial \varphi}{\partial \omega} - \varphi(\omega_0) = -R(\omega_0) = 2\pi \frac{G}{d}(tan\theta_d(\omega_0)) \tag{5.18}$$

If no perturbation occurs in the grating-based module, two consecutive pulses experience the same CEP shift. On the contrary, perturbations of one, or more, of the parameters of equation (5.18) lead to a pulse-to-pulse CEP noise.

In the following discussion we will consider separately the effect of beam pointing, that induce a shot-to-shot variation of the diffracted angle θ_d, and the effect of mechanical vibrations, that in first approximation affect only the grating distance G.

We first consider the effect of mechanical vibrations, which induce a grating distance variation δG. The derivative of $R(\omega_0)$ with respect to the grating distance G, gives the CEP shift for the distance variation δG.

$$\delta\varphi_{CE} = \delta G \frac{\partial R(\omega_0)}{\partial G} = 2\pi \frac{\delta G}{d} tan\theta_d \tag{5.19}$$

For a grating constant $1/d = 1480$ lines/mm, carrier wavelength 800 nm and incidence angle 45°, the diffracted angle is 23° and a δG of 1.5 μm is enough to give a 2π CEP shift on single pass in the grating pair. For double pass (compressor configuration) a δG of the order of the wavelength gives a CEP shift of 2π.
Same considerations can be applied to the stretcher even thought its design complexity makes it more sensitive to mechanical vibration. In the case of the stretcher the grating distance G should be replaced by the effective perpendicular distance G_s that depends not only on

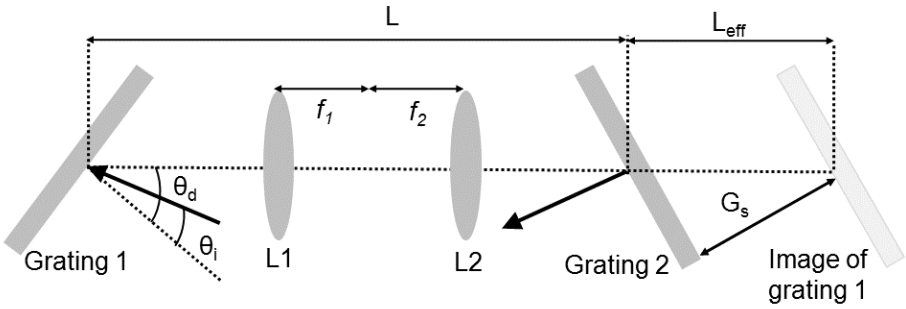

Figure 5.8: Grating based stretcher with a two lenses telescope. L1 and L2 are two lenses of focal length respectively f_1 and f_2; L_{eff} is the effective negative distance between the two gratings (Grating 1 and Grating 2) and G_s is the perpendicular grating distance.

the grating position but also on the position of the optics of the imaging system. As shown in Figure 5.8, $G_s = L_{eff}cos(\theta_d)$, where θ_d is the diffraction angle and L_{eff} is the effective linear distance between the gratings.
If the two lenses of the imaging system are confocal then [170]:

$$L_{eff} = [l - 2(f_1 + f_2)]\left(\frac{f_1}{f_2}\right)^2$$

if $f_1 = f_2$ then

$$L_{eff} = l - 4$$

where f_1 and f_2 are the focal lengths of the lenses of the imaging system, l is the geometrical distance between the two gratings. Considering a perturbation on the effective distance δL_{eff} due to mechanical vibrations, the corresponding CEP shift is:

$$\delta\varphi_{CE} = 2\pi\frac{\delta L_{eff}}{d}sin(\theta_d) \tag{5.20}$$

where the change of L_{eff} can originate from displacement of either lenses and gratings.
The effect on the CEP noise of variations of the effective length has been studied by Li et al. [149] for a grating based stretcher with 1200 lines/mm, f =250 mm and diffracted angle θ_d= 23.3°; a variation of only 2μm in the effective length leads to a CEP shift of 2π.

Same considerations can be applied for beam pointing fluctuations, which induce a change in the incident angle θ_i and, as consequence, in the diffraction angle θ_d. Recalling equation (5.18), referring to a typical compressor configuration based on a pair of grating spaced by G, for a given variation of $\delta\theta_i$ the corresponding CEP shift is:

$$\delta\varphi_{CE} = \delta\theta_i\frac{\partial R(\omega_0)}{\partial\theta_d} = 2\pi\frac{G}{d}cos\theta_i\frac{(1 + tan^2(\theta_d))}{cos\theta_d}\delta\theta_i \tag{5.21}$$

Recalling the same compressor parameters used previously, at 800 nm, for G= 1 m, 1/d = 1480 lines/mm, and $\theta_i = 45°$, a $\delta\theta_i = 10$ μrad produces a CEP fluctuation of 96 rad for a

single pass in the grating pair. This value is rather high but in first approximation we can consider that the CEP shift resulting from a single pass is compensated by the second pass in the grating pair since the sign of the beam pointing fluctuation $\delta\theta_i$ at the input of the grating pair is reversed for the second pass. In the next chapter evidences that actually also in a double pass configuration the CEP noise is not completely compensated will be provided. Anyway, the residual CEP noise due to beam pointing fluctuation is less detrimental than the shift induced by mechanical vibrations, implying a grating distance variation.

Finally we cite the case of grating angle variation due to mechanical vibrations. The case of both gratings moving by the same angle, thus remaining parallel, can be treated as the case of beam pointing variation since only the incidence angle and consequently the diffracted angle changes, keeping unaltered the mutual gratings position. On the contrary if the angular position of only one grating changes due to vibrations, two possible interpretations can be given. In first approximation we can consider that, if the angular variation is small enough (μrad), the gratings conserve their paralellism and G does not change; again only the position of the grating with respect to the input beam changes, that is equivalent to say that only the incident and the diffracted angle change; the case can again be treated as for beam pointing variation. If this approximation is relaxed and the gratings are considered not parallel anymore, it is no longer possible to define a perpendicular distance G. This case has been treated by [171], considering the optical separation of the grating ($G/cos\theta_d$) instead of their perpendicular distance (G). For a variation $\delta\theta_i$ of the grating angle, the corresponding CEP shift can be written as:

$$\delta\phi_{CE} = 2\frac{4\pi G}{d} cos\theta_i (1 + tan^2\theta_d)\delta\theta_i \tag{5.22}$$

Also in this case the double pass configuration of the dispersive module allows for partial compensation of the CEP shift induced for one pass configuration. In this case however, the total CEP shift for equal angle fluctuation is higher than the previous case (beam pointing) since not only the incidence angle is changed but in addition also the grating parallelism is lost. CEP noise induced by both beam pointing fluctuation and single grating vibration will be detailed in Chapter 6, giving numerical estimations.

5.4.2 Amplified pulses CEP shift detection

Detection of the CEP drift in amplifiers differs from the case of oscillator for two main reasons. First, the availability of high energy pulses simplifies the generation of octave spanning spectrum, which can be easily achieved in bulk material or via filamentation in gas, avoiding the need of micro structured fibers. Second, the repetition rate of the amplifier is lower than that of the oscillator. In fact, the average power of amplified pulses is limited by both the available pump sources and thermal effects and, as consequence, in order to obtain high pulse energy is necessary to reduce the repetition rate. The heterodyne technique used in the oscillator for MHz signals cannot be applied to amplified pulses, due to excess of 1/f noise [172]. The CEP shift detection of amplified pulse is still possible with an f-to-2f interferometer but in this case, instead of detecting electronically the narrow-band beat signal, the interference spectrum between the fundamental signal and its second harmonic is analysed.

For a Ti:Sa laser system, a small portion (μJ) of the laser pulse is firstly focused on a sapphire plate, which benefits of a large value of n_2 and high damage threshold. The peak power exceeds the critical power of the sapphire plate and a single filament is generated. The pulse undergoes self-phase modulation and its bandwidth is broadened so that it covers an octave, including f and 2f components. Typically for Ti:Sa laser the f component is chosen to be >1000 nm and the 2f is >500 nm. In first approximation we consider that the white light generated from self phase modulation maintains the same CEP information of the original input pulse. Actually studies [173] have revealed that, since spectral broadening is an intensity-dependent non linear interaction, pulse-to-pulse intensity fluctuations can vary the accumulated phase throughout the white-light, compromising the phase coherence of input pulse and white light and consequently the fidelity of the measurement. It is then essential to maintain a stable white light in order to guarantee the credibility of the measurement. The octave spanning pulse is sent to a BBO crystal for second harmonic generation of the 1000 nm component. The generated 500 nm signal has crossed polarization with respect to the same spectral component of the white-light. A polarizer is necessary to select a common polarization for the two signals to interfere. Due to propagation in the crystal the two 500 nm signals undergo dispersion which results in a delay τ. The interference spectrum detected

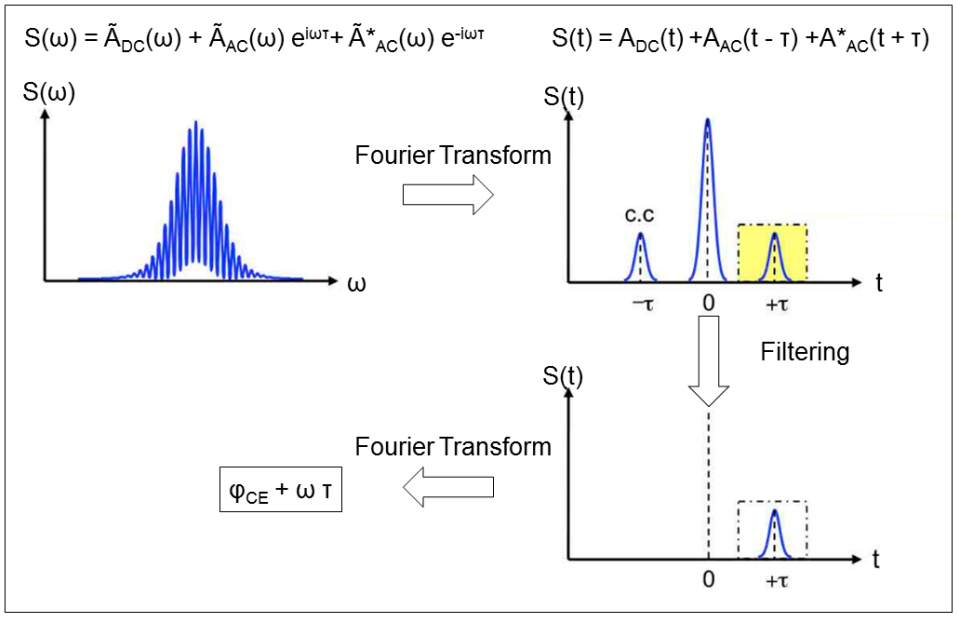

Figure 5.9: Schematic representation of the Fourier Transform Spectral Interferometry.

by the spectrometer shows a modulation with period determined by the delay τ. It can be demonstrated that the interferogram contains information about the CEP.
Re-calling equation (5.1), the electric field of the fundamental pulse in time and frequency domain can be written:

$$E_f(t) = E_{f,0}(t)cos[\omega_0 t + \varphi_{CE}] \qquad \tilde{E}_f(\omega) = \tilde{E}_{f,0}(\omega)exp(i\varphi_{CE}) \tag{5.23}$$

The second harmonic generation process leads to a pulse with twice the CEP of the fundamental and phase jump of $\pi/2$; the dispersion due to propagation in the BBO crystal leads

to a time delay τ which is expressed as a phase shift $exp(i\omega\tau)$ [174]:

$$\tilde{E}_{2\omega}(\omega) = \tilde{E}_{0,2\omega}(\omega) exp\left(i\Big(2\varphi_{CE} + \frac{\pi}{2} + \omega\tau\Big)\right) \tag{5.24}$$

The spectral interference pattern from the superposition of the signals is:

$$\tilde{S}(\omega) = |\tilde{E}_f(\omega) + \tilde{E}_{2\omega}(\omega)|^2 \tag{5.25}$$

$$= |\tilde{E}_f(\omega)|^2 + |\tilde{E}_{2\omega}(\omega)|^2 + 2\tilde{E}_f(\omega)\tilde{E}_{2\omega}(\omega) \cdot cos(\omega\tau + \varphi_{CE} + \pi/2) \tag{5.26}$$

The interference patter contains an oscillation terms $\omega\tau$ with period determined by the delay τ between the two signals, and phase proportional to the CEP. The CEP contained in the interference term can be extracted using the *Fourier Transform Spectral Interferometry* (FTSI), represented schematically in figure 5.9. Equation (5.26) can be re-written as:

$$\begin{aligned}\tilde{S}(\omega) = \tilde{A}_{DC}(\omega) &+ |\tilde{E}_f(\omega)||\tilde{E}_{2\omega}(\omega)|^* e^{i(\varphi_{ce}+\pi/2)} e^{i\omega\tau} \\ &+ |\tilde{E}_f(\omega)|^* |\tilde{E}_{2\omega}(\omega)| e^{-i(\varphi_{ce}+\pi/2)} e^{-i\omega\tau}\end{aligned}$$

$$\tilde{S}(\omega) = \tilde{A}_{DC}(\omega) + \tilde{A}_{AC}(\omega) e^{i\omega\tau} + \tilde{A}^*_{AC}(\omega\tau) e^{-i\omega\tau} \tag{5.27}$$

where the interferogram has been expressed as the sum of a DC signal and two oscillating signals containing the information of CEP. The inverse Fourier transform of equation (5.27) leads to

$$S(t) = A_{DC}(t) + A_{AC}(t-\tau) + A^*_{AC}(t+\tau) \tag{5.28}$$

In the time domain the interference pattern corresponds to one gaussian signal centered at $t = 0$, and two sidebands centered at $t_{1,2} = \pm\tau$, whose phase contains the information of CEP. Only one of the two sidebands is filtered and Fourier transformed in order to retrieve its argument $\varphi_{CE} + \omega\tau$. Note that both non linearity and dispersion in the crystal cause an unknown phase shift that is not taken into account in the demonstration above. Consequently the CEP retrieved from the input pulse reflects the phase jump with respect to a reference pulse measured previously. Upon acquiring interference spectra of consecutive pulses the CEP shift between the two pulses is retrieved and the error signal feeds back to an actuator for CEP shift correction.
The self-referencing technique described above does not require a delay line, allowing a collinear and compact geometry. On the other hand digital acquisition of the spectra and phase retrieval can be time-consuming. Earlier spectral interferometer supported acquisition speed of the order of the millisecond [168] and their acquisition bandwidth extended to hundreds of Hz. Latest digital detection can reach the kilohertz acquisition range making possible single-shot detection in the multi-kHz range [172]. Recently analog detection systems replacing the spectrometer have been used to obviate the digital data processing and allowing shot-to-shot measurement up to 1 kHz [175], 3 kHz [176] and 5 kHz [172, 177].

If the pulse energy approaches the millijoule, is possible to measure the CEP exploiting phenomena that depend directly on the electric field. The high harmonic spectrum of the laser fundamental pulse (peak intensity 10^{14} W/cm^2) depends on the CEP and its stability

can be evaluated upon generation and detection of harmonics spectra [178, 179]. The angular distribution of photoemitted electrons from an atomic gas depends on the CEP of the driving pulse and this phenomenon can be used to extimate its stability [180, 181]. Laser pulses with peak intensity of 10^{15} W/cm^2 (energy of 100 μJ) have been used for this experiment. Another way to estimate the single-shot CEP noise consists in comparing the asymmetries of photoemitted electrons in the two different directions parallel to the pulse's polarization [182]. These experimental evidences represent an alternative method for CEP measurement, as well as clear proof of the impact of CEP stability on high field experiments. On the other hand the complexity of these set-ups and the low signal-to-noise ratio make nowadays the self-referencing f-to-2f technique the most used.

It is clear now that, even if the sources of noise for oscillators and amplifiers have the same nature, the differences between the two modules, in particular the repetition rate, give rise to the necessity of two different detection systems. For the oscillator, working at the MHz repetition rate, the f_{CEO} is obtained as an heterodyne beat-signal that is therefore accessible to a radio-frequency spectrum analyser. On the contrary, due to the lower repetition rate, the CEP shift of the amplified train of a few kHz (or less) pulses is reconstructed from the interference pattern of the f-to-2f interferometer through the FTSI method.

5.4.3 CEP stabilization after amplification

Successful CEP stabilization of amplified pulses asks for fast detection as well as fast feedback actuators. According to the Nyquist theorem, in order to reconstruct faithfully a band-limited analogic signal without loosing informations due to aliasing, the sampling rate should be twice the maximum frequency of the signal. If, in the best case, the acquisition or sampling rate is equal to the repetition rate, then the signal can be reconstructed up to $f_{rep}/2$. Consequently, also the feedback correction speed is limited to half of the repetition rate. However, in the previous section we saw that the detection, in turn, is limited by its post processing bandwidth, thus limiting the acquisition rate to less than the repetition rate; recent developments gave rise to digital and analog detection schemes in the multikHz range. It is straightforward that higher repetition rate lasers can be more efficiently stabilized since in principle higher frequency noise can be detected, if a spectrometer with enough bandwidth is available, and corrected with fast actuators .

Different feedback methods have been proposed during the last decade. As for the oscillator, the idea is to control the sources of CEP noise in the amplification chain. Figure 5.10 shows the CEP noise spectral distribution in terms of PSD for a 10 kHz laser system, seeded by a CEP stabilized oscillator and before stabilization after amplification. As for figure 5.3, figure 5.10 summarizes the different spectral ranges for the CEP noise sources affecting the amplified pulses.

For perturbations that take place on a long time scale (minutes), due to temperature and humidity changes, the CEP shift can be held back with a sufficiently precise control of the laser environment. For faster perturbations, a feed back loop is required. The bibliography provides some example of CEP stabilization of amplified femtosecond pulses. The CEP noise correction can be implemented by feeding back again the oscillator, with a slower loop compared with the one for oscillator CEP noise correction. Imran et al. provides an example of a 1 kHz, grating based stretcher and compressor system CEP stabilized with a double

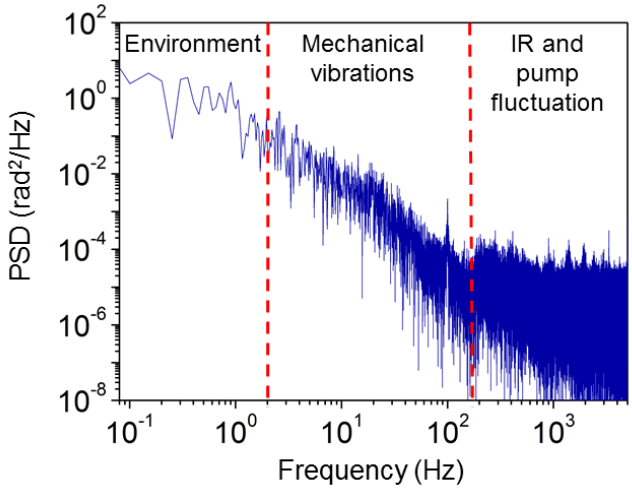

Figure 5.10: Power spectral density of CEP noise for a train of amplified pulses at 10 kHz system and different spectral ranges for different noise sources.

feedback to the oscillator. The train of pulses from the oscillator is CEP stabilized with the direct locking technique [183], feeding back the error signal from an f-to-2f interferometer to an AOM which controls the oscillator pump power. The CEP shift after amplification is measured with an f-to-2f interferometer coupled to a 50 Hz bandwidth digital spectrometer and the detected noise signal is averaged over 20 shots. Again the measured error signal feeds back to the same AOM in the oscillator. The measured CEP residual noise is 180 mrad averaged over 20 pulses.
In general averaging over multiple pulses decreases the noise signal, and as a consequence the CEP noise is underestimated. Nevertheless, some authors claim that the shot-to-shot CEP noise can be approximated by the measured noise averaged over N-pulses and multiplied by $\sqrt{N}$ so that $RMS_{shot-to-shot} = RMS_{N-averaged}\sqrt{N}$. This approximation is valid only for white noise, i.e. a random noise, with equal intensity over all the frequency range and giving a constant PSD. As we see in 5.10 this is not the case for the different noise sources participating to the total CEP noise PSD. It has been also experimentally demonstrated [177] that averaging over a large number of shots (>20) leads to a CEP standard deviation that is independent on the number of laser pulses. In conclusion averaging the measurement over multiple pulses cannot give any useful information about the shot-to-shot noise.
The first CEP measurements were averaged over multiple shots; only with the advent of faster detection system shot-to-shot CEP measurements became possible.
Shot-to-shot CEP stabilization with residual noise of 950 mrad of amplified pulses is demonstrated by Hong et al. [184] for a 500 Hz system equipped with grating based stretcher and compressor. The shot-to-shot CEP stabilization is again achieved with a double feedback loop to the oscillator's pump controller. The remarkable features of this laser is that CEP stabilization is maintained for high intensity pulse (10^{18} W/cm^2) that reaches the relativistic regime.

Alternatively, it is possible to minimize the CEP shift feeding back on an electronic device that controls the position of one optic in the stretcher or compressor. Chen et al.

[185] stabilize to 90 mrad residual noise the CEP of a 1kHz train of amplified pulses. The measure is averaged over 50 pulses and the noise is underestimated. The oscillator is CEP stabilized with the monolithic stabilization scheme [186]. The CEP shift of amplified pulses is measured with an interferometer and the error signal feeds back a piezoelectric transducer in the compressor which controls the position of one of the gratings. The main advantage of this approach with respect to feeding back in the oscillator is that any interference between the two stabilization loops is avoided, because the two feedback signals control two different actuators.
Li et al. [149] stabilize the CEP of a grating based, 1kHz system feeding back a piezo controller which finely tunes the position of one of the stretcher mirrors. The CEP noise is measured with an f-to-2f interferometer coupled to a digital spectrometer. The oscillator is stabilized with the above mentioned direct locking technique. CEP residual noise of amplified pulse when both loops are active is measured to be as low as 180 mrad. The author does not specify if the measure is single shot or averaged.

In all the previous examples the common principle for CEP stabilization consists in acting on the noise source in order to correct it. CEP stabilization of amplified pulses can also be achieved by inserting on the laser chain a programmable dispersive element for phase control. Lucking et al. [172] demonstrated a residual CEP noise of 140 mrad on a 10 kHz system, using as actuator an Acousto Optics Frequency Shifter placed after the oscillator. The laser system is seeded by a CEP stable oscillator (Rainbow CEP4 by Spectra Physics) based on the feed-forward method described in section 5.3.3. The CEP noise of amplified pulses is subsequently detected with two f-to-2f interferometers respectively coupled to two different feedback loops. The slow loop, working at 125 Hz, feeds back a Piezo stage placed in the stretcher and controlling the insertion of a prism in the optical path. The faster loop, working at 10 kHz repetition rate, feeds back to the same AOFS used in the oscillator. Instead of controlling the frequency of the acoustic wave, as for the CEP stabilization of the oscillator output, the loop controls its phase: the acoustic wave imprints its phase on the optical diffracted wave. By this method, it is possible to produce a train of pulses with a constant and specific value of CEP.
Acousto Optics Programmable Filters (AOPDF)[187, 188] have also beeen demonstrated as fast actuators for CEP correction of amplified pulses. The AOPDF is a birifringent crystal seeded by an acoustic wave that generates a transient diffraction pattern. The phase of the acoustic wave is imprinted on the diffracted optical wave so that it is possible to control the CEP shift from pulse to pulse by only changing the phase of the acoustic wave. The process of CEP control in the AOPDF is completely decoupled from spectral phase and intensity control (this device is also used to precompensate dispersions and improve the pulse compression, see chapter 3 for details). Moreover this actuator does not involve moving elements, which would slow down the correction speed, and it is rather insensitive to beam pointing fluctuation. Electro-optical crystals have further been demonstrated to be a suitable tool for CEP stabilization [189]. The refractive index of the electro-optical crystal can be varied by applying a proper voltage to the element allowing to modify group and phase velocities, keeping all the other pulse parameters untouched. The CEP shift introduced by the crystal is proportional to its length, extraordinary refractive index and electro-optical coefficient as well as to the applied electric field and to the carrier wavelength. The use of an electro-optical crystal, the $LiNbO_3$, coupled to and f-to-2f interferometer has successfully

been demonstrated as a proper actuator for fast CEP correction loop. The first demonstration of this method [190] led to a 15 Hz single shot CEP stabilization of a 1 kHz amplified system with residual CEP noise as low as 320 mrad over half an hour. Since no mechanical displacement is involved in the correction method, this actuator can be applied also to higher repetition rate. This technique has also been demonstrated on a larger repetition rate laser giving similar results as AOPDF feedback loop [177].

In conclusion this chapter underlines that CEP stabilization of an amplified chain should account for different constraints. First of all, it is necessary to seed the amplifier with a CEP stabilized primary source, i.e. the oscillator. Secondly, since CEP noise sources spread over a large range of frequency and are various, one should minimize as much as possible those sources of noise that are controllable, like environment fluctuations (temperature, humidity etc.) and mechanical vibrations deriving from influences of the noisy components in the laser room. For those sources of noise that are not directly controllable, it is necessary to implement a detection and stabilization system. The detection tools should ideally be limited only by the laser repetition rate, and thus be able to acquire at the shot-to-shot rate. The stabilization system in turn should ideally be limited only by the Nyquist theorem of sampling, to half of the detection rate.

Chapter 6

Carrier Envelope Phase stabilization of the 10 kHz laser system

6.1 Introduction

From the beginning of the century the growing interest for CEP stabilized systems triggered several studies on Ti:Sa CPA laser. CEP stabilization was previously demonstrated in kHz laser systems with low stretching factor, where the compression takes place in chirped mirrors [147, 79, 178]. With the need of increasing the pulse energy, grating based stretcher and compressor with higher dispersion coefficient became soon an exigence, with the drawback of a higher level of sensitivity of gratings to mechanical vibrations. CEP stabilization of grating based stretcher and compressor have been widely studied [170, 168, 171, 149] and demonstrated for amplified pulses through regenerative [177, 185, 191] or multipass amplifier [192, 193, 194]. Hybrid dispersive modules, constituted by prism stretcher and transmission grating compressor [188] or grism compressor [62], have also been demonstrated for CEP stable laser systems. CEP noise detection and stabilization improvements lead in the last decade to CEP compatible systems at 1 kHz [190] and 10 kHz [177] with high average output power (20 W) as well as high peak power, at the TW level, for repetition rate of tens of Hz [195, 196] and even kHz [197, 198]. Defining a reference value for CEP stability at the state of the art is rather complicated. Some authors provide the residual CEP noise averaged over a certain number of shots, which results in an underestimated value as low as 90 mrad [185], whereas the actual shot-to-shot noise can be of the order of 500 mrad. We can state that nowadays a satyfying threshold for CEP stability is 250 mrad of residual noise, while below 200 mrad may be considered as an exceptional result when considering highly stretched amplifier systems using grating based dispersive devices [172, 199].

A different case that has to be cited is represented by the OPA and OPCPA systems: passively CEP stabilized pulses are generated through difference frequency generation with less limitation of power and repetition rate. Nevertheless, a slow active loop has in general to be added in order to counteract minute or hours time scale environmental perturbations. CEP passive stabilization assisted by slow active loop has been achieved on a 1 kHz, 0.5 mJ OPA based amplifier, seeded by Ti:Sa CPA system [200], with a RMS value as low as 180 mrad. Also OPCPA systems have been demonstrated to reach CEP stability below 250

mrad at 1 kHz repetition rate for mJ level output pulses [44, 201] and even below 100 mrad, for a mid-infrared laser source (3 μm), at 100 kHz repetition rate and μJ pulse energy[202].

Nowadays challenge in the field of Ti:Sa CPA system consists in improving the CEP stability with increasing average and peak powers. Scaling the pulse peak power demands for grating based dispersive module, as well as cryo-cooling devices that influence the overall system stability. Reducing the source of CEP noise in high power Ti:Sa systems raises the demand of a continuous investigation of laser designs and stabilization methods capable of increasing the CEP stability of the laser source. In the previous chapter about theoretical fundamentals of CEP stabilization several ways for actively stabilizing the CEP of amplified pulses have been described. Nevertheless, the routine for improving at its maximum the CEP stability can be resumed in three conditions. First of all, the laser front-end should be seeded by a CEP stabilized train of pulses. The stabilization at the oscillator output is essential for compensating for high frequency noise that downgrades the CEP stability and cannot be detected after the amplification chain, that works at a lower repetition rate. Secondly, a fast acquisition system is required for detecting the wider range of frequency noise that affects the CEP stability. Ideally the detection speed should be limited only by the repetition rate. Thirdly, the stabilization loop coupled to the acquisition should also provide a fast response, only limited by the Nyquist theorem to half of the detection rate, i.e. the laser repetition rate.

In this chapter we present the results obtained in terms of CEP stabilization of the 10 kHz laser chain described in chapter 3 The stabilization system is based on a completely analog detection and feedback loop, ensuring a shot-to-shot acquisition and stabilization up to the kHz frequency range. We experimentally studied the effect of two of the main CEP noise sources: environment perturbations and the compressor's optical mounts mechanical sensibility. In particular two different grating's mounts have been tested in term of CEP stability, applying environmental perturbation in order to prove their solidity. After identifying the best configuration for CEP stability, we ran a set of CEP residual noise measurements for proving the stability of our system.

We also present a newly conceived numerical approach to evaluate the effect of perturbations on dispersive module in terms of CEP stability. As already mentioned, grating based modules are quite susceptible to mechanical vibrations, which represent a source of CEP noise that extends over a broad range of frequencies. The bibliography provides an analytical approach that can be applied to a limited set of well defined perturbations. With the numerical approach based on an optical design software we hope to provide a powerful and flexible tool for evaluating the CEP dependency on grating based module perturbations, that can be applied to any user designed geometry of the dispersive module.

6.2 Experimental conditions

The main goal of the measurements presented in this chapter is to test the CEP stability of the 10 kHz laser front-end described in chapter 3 and in particular the performances of the newly-designed double-crystal regenerative amplifier. Even though the fundamental design of the laser system remains unchanged, two modifications have been applied before performing CEP measurements [199]. First, the Rainbow CEP3 has been replaced with

Rainbow CEP4. The performances of the two oscillators in terms of repetition rate, output pulse energy and duration are equivalent, whereas the CEP stabilization method is quite different. As mention in chapter 5, the Rainbow CEP4 is based on the feed-forward method and the residual theoretical CEP noise is below 60 mrad [167]. Secondly, the laser system is equipped of a third stage of amplification, following booster and regenerative amplifier. The module is a single pass double-crystal (Ti:Sa, flat surface) 10 kHz amplifier. Pumped with 25 W by a commercial pump laser (MESA from Continuum), the amplifier releases 7 W (0.35% RMS stability) of IR power in broad band mode. Since the amplifier is also affected by gain narrowing and red-shifting, the pulse shaping via Mazzler is performed using the output spectrum of the amplifier. Dichroic mirrors as well as IR high-reflectivity optics are used in this module and the design is adjusted to ensure a good overlap between pump and IR beam. The amplified train of pulses is then compressed in the reflection grating based compressor described in chapter 3, designed with solid CEP-compatible optical mounts. The output spectrum after compression is shown in figure 6.1 together with its transform limited and measured pulse duration. The final output power after compression is lowered down to 5 W due to the compressor transmission.

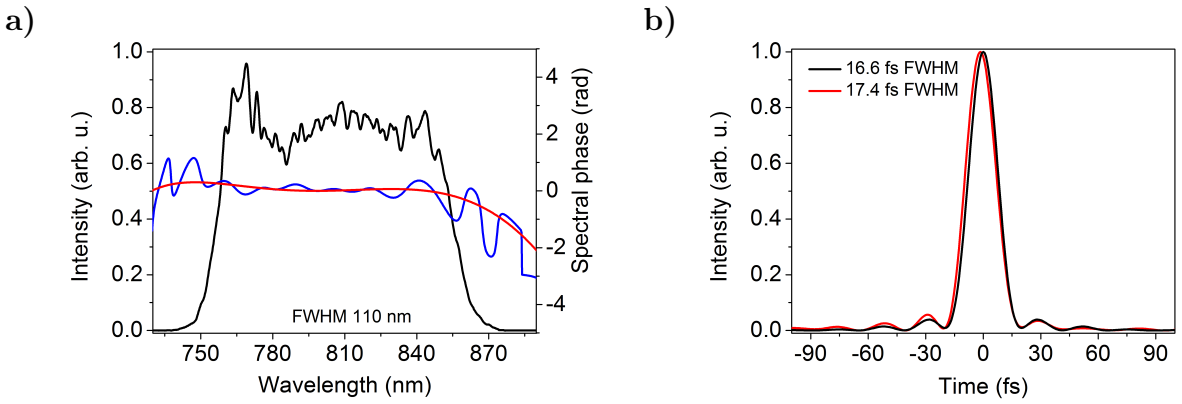

Figure 6.1: a) Pulse spectrum (black line), measured (blue line) and fitted (red line) spectral phase. b) Corresponding transform limited (black line) and measured (red line) pulse duration.

6.3 Analog control of the Carrier-Envelope Phase

The CEP measurement and stabilization of the amplified femtosecond pulses are performed with a complete analog method based on the Amplitude Laser Group product BIRD (Beat Interferometer for Rapid Detection). The BIRD is a nonlinear interferometer (f-to-2f interferometer, cf chapter 5), through which interference patterns encoding CEP are produced by white light generation followed by its second harmonic generation. The CEP dependent signal is sampled using two photomultipliers (PMs), instead of conventional visible-infrared spectrometer, thus ensuring a much faster acquisition rate. The data analysis also relies on analog electronics, allowing the elimination of any additional delay for numerical post processing. The scheme enables single-shot CEP detection at multi-kilohertz rates.
We remind that the CEP stabilization in our laser chain occurs at the oscillator level, with a fast feed-forward stabilization loop, and after amplification, whit a slow feedback loop. The CEP noise detection is coupled to a fast actuator, the Dazzler, that allows correction of the noise up to the kHz frequency range.

The BIRD design is shown in figure 6.2. A small portion of the femtosecond pulse, of

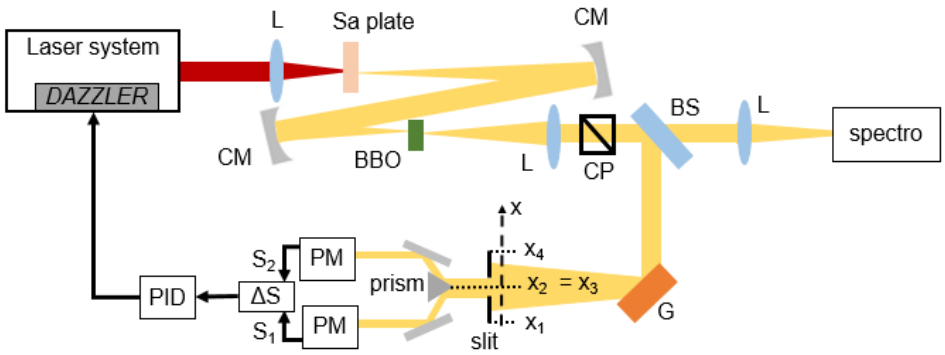

Figure 6.2: Schematic representation of the CEP noise analog detection system BIRD, coupled to the fast actuator Dazzler in the laser chain. L-lens; CM-concave mirror; CP-cube polarizer; BS-beam splitter; G-diffraction grating; PM-photomultiplier.

the order of few μJ, is sent to the interferometer. The pulses are focused on a 2 mm thick sapphire plate for continuum generation spanning over an octave, which corresponds to the signal at frequency f. The beam is recollimated and focused by means of two concave mirrors in a 1.5 mm thick BBO crystal cut for second harmonic generation at 1064 nm. The 2f signal at 532 nm is cross-polarized with respect to the fundamental white light. A lens images with magnification the signal at the slit position. A cube polarizer projects the polarization of the two beams on the same directions, allowing interference between the newly-generated second harmonic signal and the signal at the same frequency already composing the white light spectrum. A 50/50 broadband beam splitter divides the signal in two parts. One fraction of the beam from the beam splitter is focused at the input of a fast spectrometer that acquires the spectral interferometer pattern. The CEP noise is encoded in the spectral shift of the fringes and can be retrieved applying the FTSI algorithm (cf. chapter 5). The spectrometer can acquire in single shot mode up to 1 kHz. The digital acquisition is coupled

to the analog detection in order to allow long term measurement. However, the feedback loop is based on the analog acquisition. The coupling with the spectrometer has also the advantage of monitoring the spectral fringes, even when the resolving power of the human eye doesn't allow to distinguish them in the analog setup.
The other fraction of the beam from the beam splitter is sent to a diffraction grating. The spectral interference pattern is then transferred in spatial domain. A slit selects a single fringe that is divided in two parts by the apex of a prism. The two signals are sent respectively to two photomultipliers that integrate the signals over two spatial ranges indicated as (x_1, x_2) and (x_3, x_4) (cf. figure 6.2). The outputs of the two PMs (S_1 and S_2) are analogically subtracted ($\Delta S = S_2 - S_1$), providing the error signal $\Delta\varepsilon$. For symmetrical alignment of the prism with respect to the slit ($x_4 - x_3 = x_2 - x_1 = \Delta x$ and $x_2 = x_3$), the difference signal ΔS is demonstrated to depend on the CEP φ according to the relation [177]:

$$\Delta S(\varphi) \propto \frac{1}{\alpha} sin^2(\alpha \Delta x/2) sin(\alpha x_1 + \varphi) \tag{6.1}$$

where α is a parameter depending on the grating dispersion and the distance between the grating and the detectors. The shot-to-shot difference signal is acquired by an oscilloscope that displays it on a time scale of some tens of seconds. Since the shot-to-shot CEP shift can be traced on this short time scale, the coupling with the digital, 1 kHz single shot detection system provides an alternative measurement on a longer time scale.
Equation 6.1 shows that the difference signal generated by the PMs is not linear with the CEP but changes as a sine function. It is thus necessary to apply an arcsinus calibration on ΔS in order to retrieve the CEP shift that is resolved in a $\left[-\frac{\pi}{2}, +\frac{\pi}{2}\right]$ range. This trend is experimentally demonstrated. We configured the Dazzler in order to insert a linear variation of the CEP with time while acquiring the CEP noise with the BIRD. Figure 6.3 shows the signal applied with the Dazzler (red curve) and the corresponding measure acquired with the BIRD (black curve).
While the digital spectrometer and the FTSI algorithm give a sawtooth wrapped signal, confined between $[-\pi, +\pi]$, that can be directly unwrapped, the BIRD gives a sinusoidal signal that requires a preliminary arcsinus calibration before unwrapping.
After detection, the error signal is sent to a PID controller which drives the Dazzler. The analog input of the Dazzler controller generates a specific acoustic wave that permits to precompensate the CEP shift. In fact the phase of the acoustic wave can be imprinted on the optical wave. We point out that a fine tuning of the PID parameters is important for obtaining an efficient correction loop, over a broad range of frequencies.

Experimentally we observe that the most critical factor of the f-to-2f interferometer for obtaining a reliable measurement is the quality of the white light. Energy instabilities in the continuum generation can couple to CEP drifts, resulting in an unreliable measurement. The input pulse energy , as well as the positioning of the sapphire plate must be precisely adjusted in order to obtain a stable and homogeneous continuum generation. The pulse compression is a critical parameter that needs to be optimized for improving the white light stability. In our measurement, after achieving pulse compression with grating alignment and Wizzler-Dazzler loop, the white light is optimized changing finely the second order dispersion

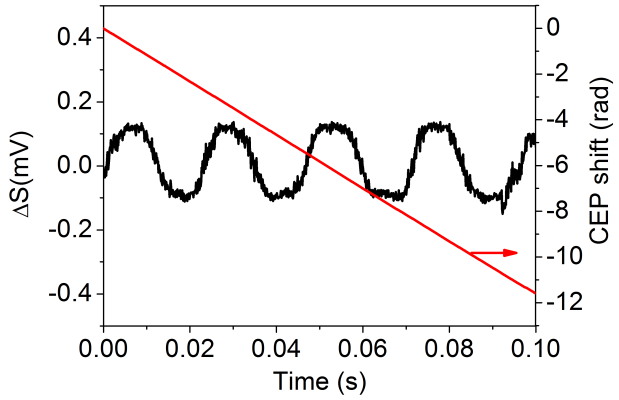

Figure 6.3: Ramp signal for linear CEP shift applied to the Dazzler (red line) and corresponding CEP shift, in terms of difference signal ΔS, measured by the BIRD and the oscilloscope (black curve).

with the Dazzler. In this condition, we noticed that the continuum generation is sensitive to dispersion variation of the order of 50 fs^2 for a pulse duration of 17 fs. Figure 6.4 is a picture of the spatial fringes just before the slit selection. We use the most contrasted fringes that can be seen on the right part of the picture.

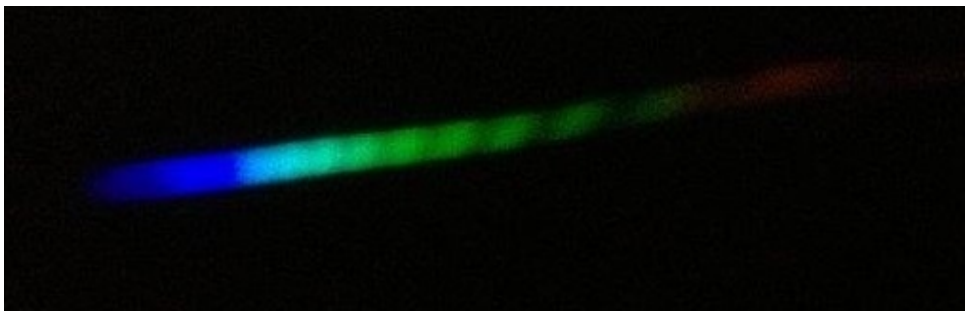

Figure 6.4: Spatial fringes from f-to-2f interferometer encoding the CEP information.

We finally can state that the feedback loop based on the complete analog detection with the PMs, together with the fast acousto-optics actuator makes this scheme appropriate for laser repetition rate up to few hundred kHz.

6.4 CEP measurement for different compressor designs

As discussed in previous chapter, many noise sources can influence the CEP stability of an amplified train of pulses. When measuring the laser performances in terms of CEP stability it is important to define the experimental conditions because environmental perturbations or apparently trivial modifications in the laser design may actually have a detrimental effect on the CEP stability. The preliminary measurements proposed in this section have the

purpose of testing the CEP stability of the 10 kHz front-end described in section 6.2 and in particular to quantify the influence of two of the main CEP noise sources: environmental condition and compressor design. In particular, we ran a set of comparative measurements of the CEP residual noise for two different compressor's designs. The two compressors are equivalent in terms of dispersion induced on the pulse and both of them are grating based; the only difference consists in the optical mounts used for the module. The first compressor uses standard adjustable optical mounts, that allows to finely tune the grating translation and rotation and ensure mechanical stability thanks to the spring-based construction. The second compressor has already been introduced in chapter 3 on the compression section. This newly-designed compressor is equipped with solid, tuning-free optical mounts. The position and rotation of the gratings cannot be finely adjusted, allowing only the manually alignment. This compressor has been specifically designed for being CEP compatible. The comparison between the two compressor's designs has the goal of verifying and quantifying the improvement in terms of CEP stability of the newly-design compressor as well as its robustness and reliability.

We decided to test both compressors in two different environmental conditions: without and with external perturbations. For this purpose, we divided the laser chain into two parts: the primary source together with stretcher and amplification stages is installed in an isolated room, to improve the control on the environment parameters and minimize any CEP perturbation that is not related to the compressor. On the contrary the compressor is placed in the user room where two setups for strong field experiments are installed, and includes two couples of primary and turbo vacuum pumps. This environment represents a good testing condition of compressor stability. We could in fact create some perturbations by starting the vacuum pumps: in this condition the compressor might be influenced by the users' setup and in particular by vibrations propagating from noisy vacuum pumps to the optical table where the compressor is located. Moreover the pulse propagation length reaches several meters from the last stage of amplification to the compressor, and represents a source of instability for the pulse CEP.
This testing situation actually represents the real final configuration of the laser system. The compressor should in fact be placed as close as possible to the user input, to minimize dispersion due to propagation of the beam and ensure a nearly transform limited measured pulse duration. The following measurements quantify in terms of CEP stability the influence of the surrounding environment on the two different compressors and the difference between the two designs.

6.4.1 CEP stability after standard compressor

The first set of CEP residual noise measurements has been performed on the standard compressor, with optical mounts equipped with motorized translation and rotational stages. We compare the CEP stabilization performances for different environmental conditions surrounding the compressor: when users vacuum pump are off and when they are on.

We firstly detect CEP residual noise after analog stabilization with 1 kHz single shot digital acquisition on a minute time scale. Figure 6.5.a shows the CEP noise Power Spectral Density (PSD) when all the vacuum pump are off.

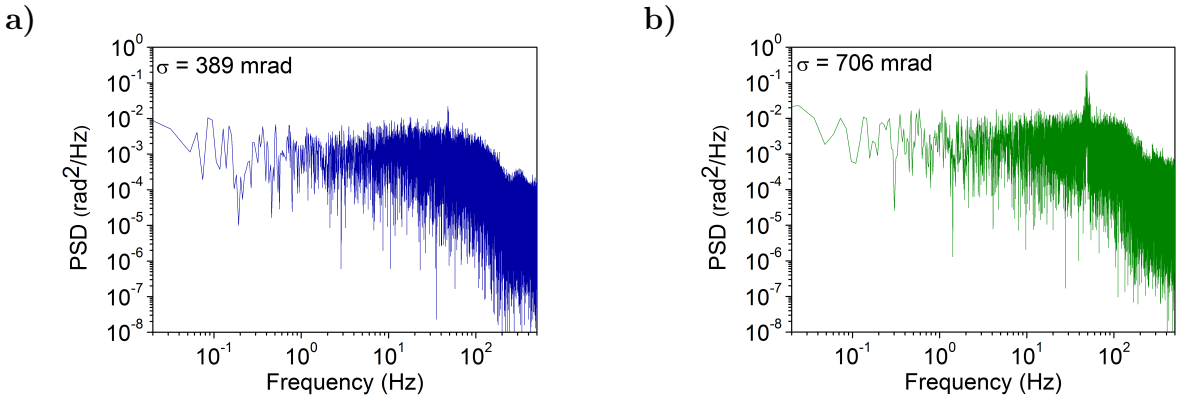

Figure 6.5: PSD of CEP noise for 1 kHz single shot digital acquisition on a minute time scale when using a standard compressor and complete analog stabilization loop. The two figures represents the two cases of a) vacuum pumps off b) vacuum pumps on.

A small noise peak arises at 50 Hz and it is likely associated to the alternating current supply; the residual RMS CEP noise is 389 mrad. When all the vacuum pumps are switched on, the residual RMS CEP noise reaches 706 mrad (6.5b) and the feedback correction loop is not able anymore to efficiently correct the CEP drifts. Besides the noise peak at 50 Hz, the worsening of the CEP stability can be explained assuming the presence of high frequency noise, in the kHz frequency range, that cannot be digitally detected by the spectrometer. The spectral noise reconstruction is in fact limited by the Nyquist theorem to half of the acquisition rate: in the case of digital acquisition at 1 kHz, noise sources in the kHz spectral range cannot be resolved.

In order to get some more informations about detrimental high frequency noise, it is useful to perform shot-to-shot CEP noise measurements at the laser repetition rate. Figure 6.6 shows the PSD with slow stabilization loop active and in the two cases of vacuum pumps off (figure 6.6.a) and on (figure 6.6.b).

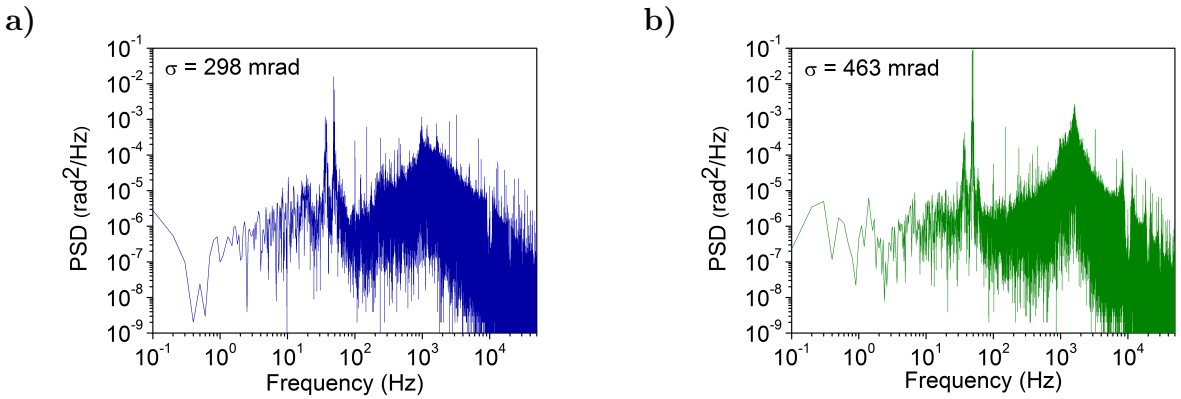

Figure 6.6: CEP noise PSD for 10 kHz shot-to-shot analog acquisition and stabilization on a second scale when using a standard compressor. The two figures represents the two cases of a) vacuum pumps off and b) on.

In the first case, without external perturbations, the RMS residual noise is 298 mrad, whereas when perturbations are switched on the residual noise grows to 463 mrad. In both cases a sharp peak is visible at 50 Hz, and a bump in the kHz range, but when the pumps are on, the bump in the kHz range gets narrower and more intense. The spectral position of the bump is typically related to noise sources arising from mechanical vibrations. We can suppose that vibrations coming from functioning vacuum pumps propagate through the floor and the optical table to the compressor optical mounts. Even if the slow stabilization loop is active, a worsening on the CEP stabilization is clearly due to vibrations. One may notice that the residual RMS noise values are in this case lower than the values obtained with the 1 kHz, minute long, acquisition. This can be explained considering the different acquisition times. The shot-to-shot 10 kHz acquisition is performed with a fast oscilloscope that limits the acquisition length to the second time scale. In this time interval, the CEP is not influenced by low frequency noises, happening on the minute time scales. However, fast shot-to-shot acquisition gives information about high frequency noise, that is not resolvable by the 1 kHz acquisition. This justifies the importance of coupling two acquisition systems, a shot-to-shot for high frequency noise, and a long, single shot for slow noise.

Finally we performed 10 kHz shot-to-shot analog acquisition on 10 seconds time scale, when the slow stabilization feedback loop is off. In this condition the CEP does not change randomly from pulse to pulse but it's stabilized at the oscillator level with the fast feedback loop.

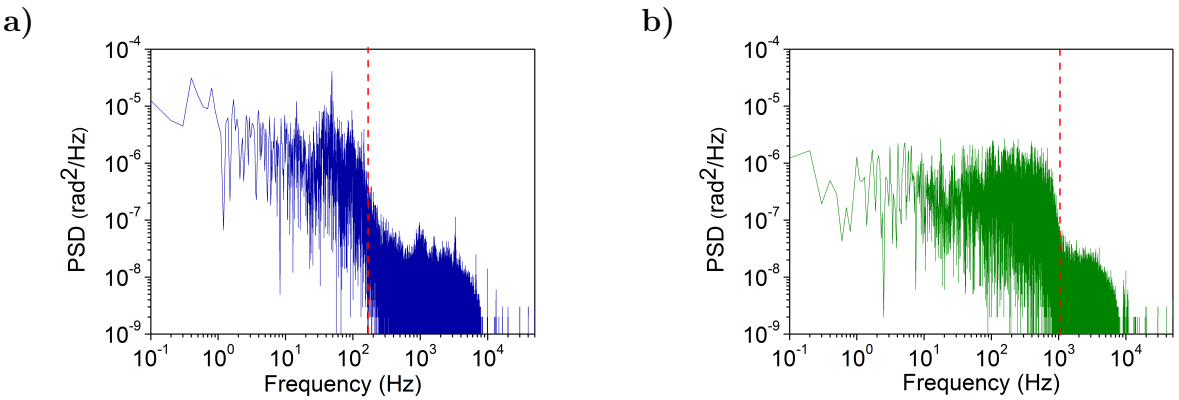

Figure 6.7: 10 kHz shot-to-shot free-running CEP noise. The slow stabilization loop is off and the system is stabilized only at the oscillator level. The standard compressor is in place and a) vacuum pumps are off and b) vacuum pumps are on. The red dashed lines delimit the frequency range of major noise contribution.

This kind of measurements gives informations about the free noise distribution when no slow loop is applied. Figure 6.7.a shows the CEP noise PSD when all the vacuum pumps are switched off. The main noise contribution is spectrally located below 200 Hz (dashed red line in figure 6.7.a) and it is typical of environment parameter changes. When user's pumps are switched on, (PSD in 6.7.b) the main noise contribution extends over a larger spectral range, up to 1 kHz (red dashed line in figure 6.7.b), again associated to noise sources arising from mechanical vibrations. In figure 6.7a the PSD reaches higher values compared with the

PSD of figure 6.7b. Actually, since no correction loop is applied, the integrated PSD over the frequency, which represents the CEP noise information, is the same for both cases. The interest of these figure lies in the informations about the frequency distribution of the noise, rather than its value.

In conclusion, a standard compressor, equipped with tunable optical mounts appears to be sensitive to perturbations, such as mechanical vibrations. Even whit slow feedback loop on, the noise arising from mechanical vibrations cannot be compensated and the residual shot-to-shot CEP noise is not better than 463 mrad on a second time scale.

6.4.2 CEP stability after CEP compatible compressor

The second set of measurements has been performed upon installation of the CEP compatible compressor, precisely designed to reduce the impact of vibrations and environmental perturbations on the CEP stability. The grating mounts are particularly solid and tuning-free.

The shot-to-shot CEP stability is achieved with the complete analog method described in section 6.3. The CEP residual noise is measured using a 10 kHz shot-to-shot oscilloscope acquisition coupled with a 1 kHz single shot digital spectrometer for long term measurements.

The first set of measurements is performed with a kHz spectrometer on a minute time scale. The CEP shot-to-shot stabilization loop is active. Figure 6.8 shows the CEP noise

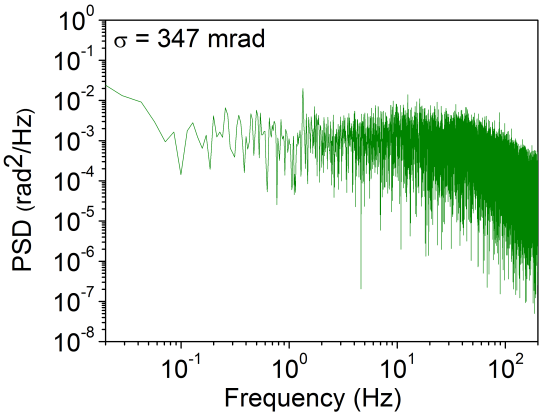

Figure 6.8: 1 kHz single shot CEP noise digital acquisition when the analog stabilization loop is active and the newly-designed compressor is used. All the vacuum pumps are on.

PSD when all the vacuum pumps are running. The RMS CEP residual noise is as low as 347 mrad, even when perturbing the compressor. This result is better than those obtained on the standard compressor not only in the same environmental condition but also for no perturbation applied on the standard compressor. As visible for the PSD, the peak at 50 Hz due to alternating current supply does not affect the CEP, meaning that the solid, tuning-free optical mounts are more reliable in terms of CEP than the standard tunable mounts.

Moreover, considering the low RMS residual noise, it is reasonable to suppose that also noises in the kHz frequency range are lowered by the solid optical mounts.

In order to confirm the previous hypothesis, we performed 10 kHz shot-to-shot CEP noise measurement. Figure 6.9 represents the PSD of CEP noise when the analog stabilization

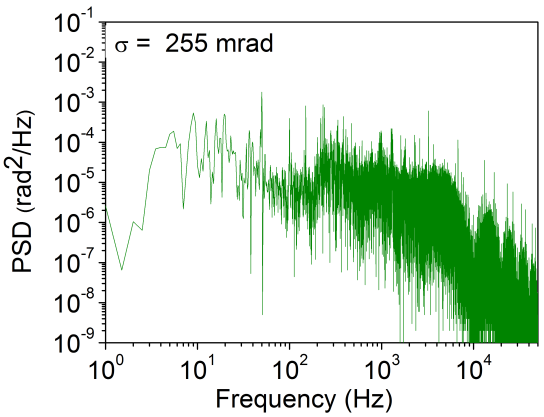

Figure 6.9: 10 kHz shot-to-shot CEP noise when the analog stabilization loop is active and the newly-designed compressor is used. All the vacuum pumps are on.

loop is active, and all the vacuum pumps are on. On a second time scale, the RMS residual noise is as low as 255 mrad. The major contribution to CEP noise located in the kHz range, as well as the 50 Hz noise peak, is not visible anymore, confirming the priceless stability of the new compressor design.

In order to summarize the results of the test performed on the two compressors, we resume in table 6.1 the main measurements when all the pumps are running.

PUMP ON	**Standard compressor**	**CEP compatible compressor**
1 kHz acqusition	706 mrad	347 mrad
10 kHz acquisition	463 mrad	255 mrad

Table 6.1: Comparison between standard and CEP compatible compressor in terms of residual CEP noise measured at 1 kHz and 10 kHz when all the vacuum pumps are running.

From the 1 kHz single shot acquisition over a minute time scale, the residual RMS CEP noise for the standard compressor is 706 mrad, twice higher than the residual noise measured in the case of newly-designed compressor.
At 10 kHz shot-to-shot acquisition, the main contributions to CEP noise in the case of standard compressor are the alternating current supply, represented by a peak at 50 Hz , and the mechanical vibrations propagating through the compressor optical mounts, represented

by a bump in the kHz frequency range (cf figure 6.6). The lower RMS residual CEP noise measured with the new compressor demonstrates its incomparable stability and reliability, introducing an important improvement in CEP stability. This result confirms that also perturbations arising from sources external to the laser system have to be taken into account while conceiving the laser installation. It also shows that high dispersive modules are really sensitive to mechanical vibrations and need to be properly designed in order to achieve a good CEP stability.

6.5 CEP stabilization at the front-end output

From the comparative measurements described in the previous section we can confirm that both the surrounding environment and the compressor design have a strong influence on the CEP stability. In this section we propose the best results in terms of CEP stability, measured at the right output of the laser system, thus in the same controlled room, and with the newly-designed tuning-free grating's mounts.
The experimental conditions are described more in detail in section 6.2: we use the front-end output delivering 17 fs pulses with 0.5 mJ at 10 kHz. The CEP detection and stabilization is performed with the completely analog method of section 6.3. We report below the shot-to-shot residual CEP noise together with the measured PSD over 20 seconds acquired with the fast oscilloscope.

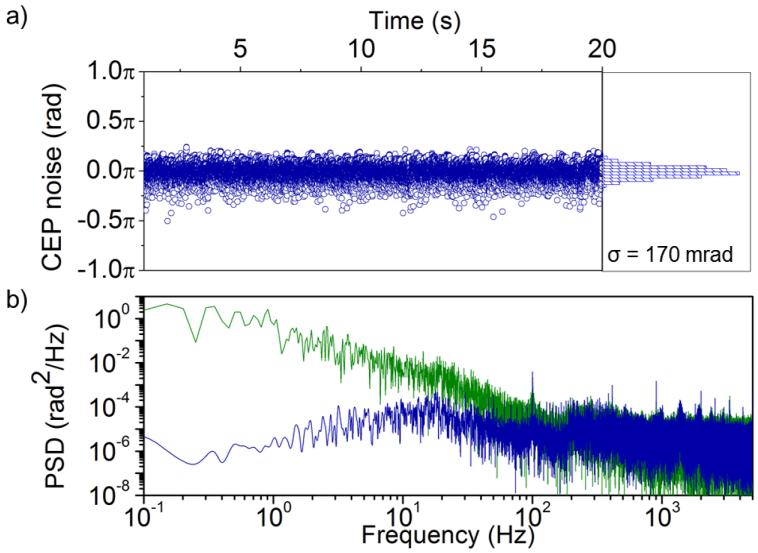

Figure 6.10: (a) 10 kHz shot-to-shot CEP residual noise over 20 seconds performed with the fast oscilloscope. The residual CEP noise is as low as 170 mrad (RMS). (b) Comparison between the power spectral density of CEP noise when the analog stabilization loop is off (green curve) and when it is on (blue curve).

Figure 6.10a shows that the CEP residual noise is reduced to 170 mrad (RMS) over 20 seconds. Figure 6.10b shows the comparison between the two PSD of CEP noise with slow feedback loop off (green curve) and on (blue curve). The combination of analog detection

and stabilization loop allows a clear stabilization up to 200 Hz, and a small improvement is visible also at in the kHz range.

Figure 6.11a represents the 1 kHz single shot residual CEP noise acquired with the digital fast spectrometer over 120 seconds. In the first 60 seconds the slow stabilization loop is off and only the fast oscillator loop in active. From the 60th seconds onwards, the analog shot-to-shot stabilization loop is switched on and a clear reduction of the CEP noise is achieved. The CEP residual noise is as low as 206 mrad. As comparison Figure 6.11b shows the CEP residual noise over 60 seconds after averaging over 20 shots, with the same correction loop. In this case the residual noise is underestimated to a value as low as 110 mrad. In the literature we can find examples [185] of approximation of the shot-to-shot CEP residual noise to the measured CEP average noise divided by the square root of the integrated shot number. This approximation is valid only for white noise, i.e. noise that remains constant over the range of measured frequencies. Since this is not the case for the CEP noise, our effort to acquired and correct as fast as possible are justified by the need of providing a realistic estimation of the CEP noise.

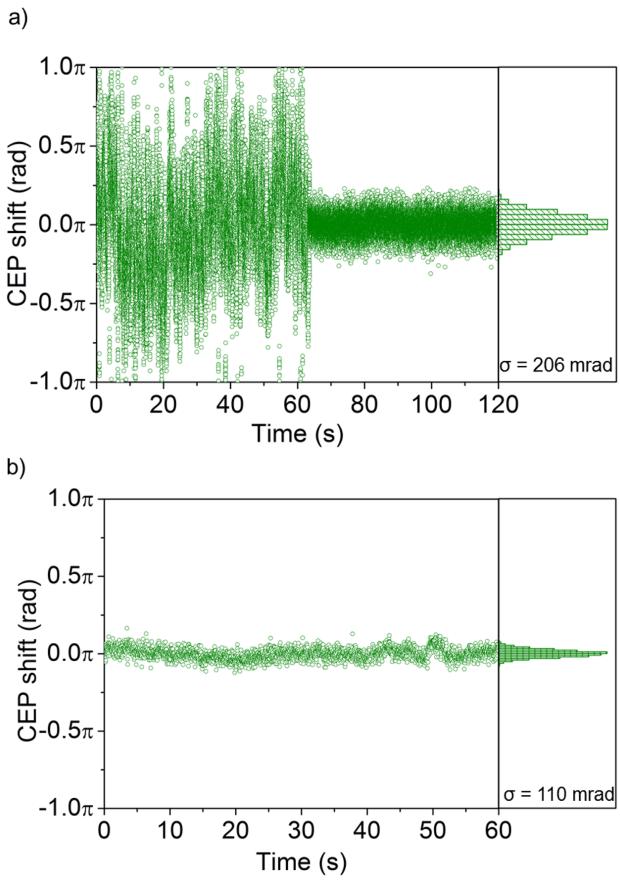

Figure 6.11: (a) 1kHz single shot CEP noise measurement performed with the spectrometer over 120 seconds; the first 60 seconds the slow loop is off, while at the 60th second the active stabilization loop is switched on; in this case the CEP noise is minimized to 206 mrad. (b) 20 shots averaged CEP residual noise over 20 seconds; the residual CEP noise is as low as 110 mrad.

Finally figure 6.12 shows the CEP residual noise over 3 hours, that is as low as 210 mrad, confirming the robustness of the system.

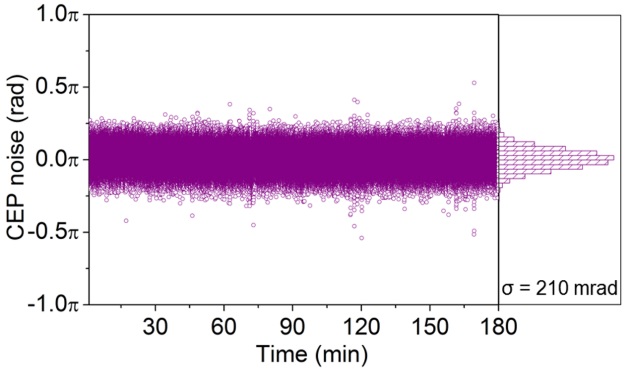

Figure 6.12: CEP measurement performed with the spectrometer over 3 hours; the residual CEP noise is 210 mrad.

The results listed above in terms of CEP stabilization are quite remarkable considering the architecture of our system using a regenerative amplifier and in particular the choice of reflection grating based stretcher and compressor. Even though solid optical mounts can increase the mechanical stability, the grating based dispersive modules remain intrinsically a critical factor for CEP stability, due to the big size and the long propagation path of the beam. However the grating based modules carry the priceless benefits of large dispersion values, which is compatible with high amplification. As comparison with our system, the literature provides an example of shot-to-shot CEP stabilization down to 98 mrad, on short time scale, of a 10 kHz Ti:Sa laser delivering 0.8 mJ [172], where the compressor is constitutes by a couple of transmission gratings and the stretcher is a pair of prisms. The fact that the gratings of dispersive module are in transmission and not in reflection minimizes the system sensitivity to mechanical vibrations, but also the value of dispersion, especially concerning the stretcher. Our stretching factor is rather high, ensuring a low value of B-integral when applying a high amplification factor to the pulse. On the other side, since it is based on reflection gratings, and due to its high value of dispersion, our stretcher is more sensitive to vibrations. The same author demonstrated that long term CEP residual noise stays as low as 150 mrad; this remarkable values is close to what we demonstrated (210 mrad) on a more demanding laser system.
In conclusion we believe that the limit to CEP stabilization in our system is imposed by the architecture that we necessarily choose for our system, rather than the complete analog detection and stabilization loop, that is demonstrated to be quite flexible and powerful.

6.6 CEP stabilization of high power laser system

Earlier in this work we discussed the possibility of coupling the 10 kHz front-end to further amplification stages. We demonstrated the generation of simultaneously two trains of pulses, one at 10 kHz, 24.4 fs and 2 mJ pulse energy and the other at 1 kHz, 23.4 fs and

16 mJ after compression. We also described how the 1 kHz train of pulses can be scaled to shorter pulse duration, 17 fs, maintaining the same pulse energy, thus approaching the TW-level.
In order to have a complete view of our high power laser system, we characterized both arms in term of CEP stability. Measures are performed on the 23.4 fs and 24.4 fs pulses respectively at 1 kHz and 10 kHz repetition rates. The detection and stabilization methods are the same as those described for the 10 kHz front-end. The measurements presented in this section have been recorded in the users experimental room, where the compressor is placed at at least five meters away from the output of the amplification line.
The residual RMS CEP noise over 30 minutes is 350 mrad at 1 kHz (figure 6.13a) and 260 mrad at 10 kHz (figure 6.13b).

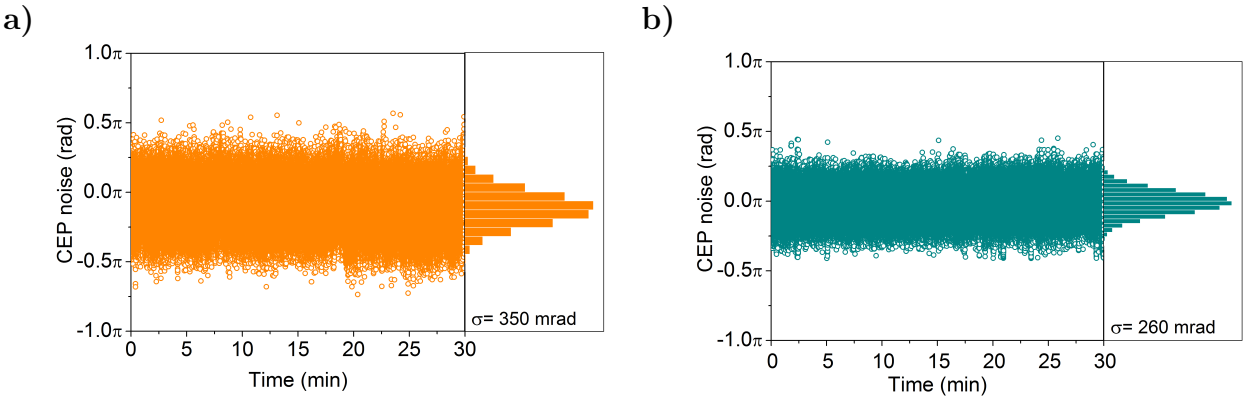

Figure 6.13: RMS CEP residual noise measured over 30 minutes for a) 1 kHz and b) 10 kHz train of pulses.

Thanks to a larger correction bandwidth due to the higher repetition rate as well as less amplification stages, the 10 kHz CEP residual noise is lower than the 1 kHz.
Comparing these results with those reported in section 6.4, we notice that the CEP residual noise at 10 kHz is now lower than the one measured previously. The reason of this discrepancy may be identified in the different environmental conditions where the two sets of measurements have been ran.
These better results have been obtained without any experiment running thus with limited vibrations in the experimental rooms since no vacuum pump was used.

The values presented here are quite remarkable considering that they have been recorded at a long distance from the amplifier.
The literature provides other example of TW-class or lower laser system at 1 kHz repetition rate and CEP stabilized. These lasers are quite similar to our system, consisting on grating based stretcher and compressor and amplification line comprising regenerative and multipass amplifiers. Chen et al. [185] presented the results of CEP stabilization obtained on a Ti:Sa laser, with grating based stretcher and compressor, delivering 6 mJ, 30 fs pulses at 1 kHz. The measured valued of residual RMS CEP noise is as low as 90 mrad. Actually this value is averaged over a number of shots and the author approximates the shot-to-shot residual noise as a white noise with RMS 600 mrad. Fordell et al. [191] demonstrated CEP stabilization down to 470 mrad residual noise of a 1 kHz, 6 mJ train of pulses.

This comparison underlines the uniqueness of our system in terms of power scalability, pulse duration and CEP stability.

6.7 Computing the CEP shift in dispersive modules with an optical design program

As shown in the previous section, a grating based dispersive module is critical for CEP stability. The sensibility to mechanical vibrations, due to the big size of the optics, constitutes one of the main sources of noise that extends over a broad range of frequencies. Many efforts have been made for increasing the stability of the optical mounts and reduce at its minimum the impact of environment and mechanical vibrations on the CEP (cf. section 6.4)[197, 203]. Nevertheless, a realistic estimation of the impact of mechanical perturbations on the CEP remains necessary for a preliminary evaluation of the system's performances in terms of stability. The literature presents an analytical approach providing a formula for evaluating the CEP shift occurring during propagation in a grating pair and for specific perturbation of this design [204, 170]. Even though these equations represent a useful and simple tool for preliminary evaluation of the impact of perturbations in the dispersive module on its CEP compatibility, as we will see in the next discussion their application is limited to a grating pair design and can account for only few specific perturbations applied to it. In fact the input variable to these equations are the grating pair parameters and no other type of design can be tested. It may then be convenient for engineering applications to dispose of a more complete tool for evaluating the influence of a stretcher/compressor design and perturbation on the CEP stability. This tool ideally models and permits to analyse any technically feasible geometry of the module and any possible perturbation it might be subjected to. This can be done with a numerical approach applied to a user defined module design. Optical design programs already exist and they represent a powerful tool for custom design and analysis. Once the user has correctly set the geometry of the module, these programs compute the optical paths for a user defined ray source, no matter the complexity of the system using a ray-tracing approach. The source is assumed to continuously emit rays at defined wavelengths so that time dependency is not taken into account. From the path lengths the phase of each wavelength can be directly calculated and consecutively also informations about high order dispersion or CEP variation become accessible. Since the phase is retrieved from ray-tracing and not from analytical formula depending on the design parameter, any configuration can be tested. Moreover, these programs rely on a wide database of optical components and often no user treatment is needed for defining their optical properties. For example, the phase correction factor introduced by the propagation through a grating is already taken into account by the program.

In the next discussion we first describe the existing analytical approach and then we propose a new approach for studying the CEP compatibility of a grating based module, with a ray tracing software.

6.7.1 Analytical approach

The literature [170, 171] provides equations for evaluating the CEP shift after propagation throug a grating pair. The following derivation is conducted on a compressor design with G defined as perpendicular distance between gratings, $1/d$ groove density, θ_i incidence angle and $\theta_d(\omega)$ diffracted angle for the specific component ω. We remind that the phase φ of a spectral component of an ultrashort pulse defined by the frequency ω and propagating through a pair of grating is given by [57]:

$$\varphi(\omega) = \frac{\omega}{c}p + R(\omega) \tag{6.2}$$

where p is the optical path through the grating pair and $R(\omega)$ is the correction factor. For a single pass in the grating pair the expression of the phase becomes:

$$\varphi(\omega) = \frac{\omega}{c}p - 2\pi\frac{G}{d}tan(\theta_d) \tag{6.3}$$

The dispersive nature of the compressor introduces a CEP shift on the propagating pulse that is [170]:

$$\phi'_{CE} - \phi_{CE} = \omega_0\tau_g(\omega_0) - \varphi(\omega_0) \tag{6.4}$$

where ϕ'_{CE} and ϕ_{CE} are respectively the output and the input pulse carrier envelope phase, ω_0 the carrier frequency and $\tau_g = \partial\varphi/\partial\omega$ the group delay. Differentiation of the equation 6.2 leads to the expression for τ_g:

$$\tau_g = \frac{\partial\varphi}{\partial\omega} = \frac{p}{c} + \left(\frac{\omega}{c}\right)\frac{\partial p}{\partial\omega} - 2\pi\frac{G}{d}\frac{\partial tan(\theta_d)}{\partial\omega} \tag{6.5}$$

The second term is shown to be equal in module and of opposite sign to the third term providing that $\tau_g = p/c$. The CEP shift after one pass on the grating pair can be expressed as:

$$\begin{aligned}\phi'_{CE} - \phi_{CE} &= \omega_0\tau(\omega_0) - \varphi(\omega_0)\\ &= -R(\omega_0)\\ &= 2\pi\frac{G}{d}tan(\theta_d(\omega_0))\end{aligned}$$

For a double pass in the grating pair (the case of compressor) it is necessary to multiply by a factor 2 the above-mentioned equation. As already mentioned, it is possible to derive analytically the CEP shift after propagation through the compressor's grating pair from its parameter, that is essentially equal to the phase correction $R(\omega)$ evaluated at the carrier frequency ω_0.
The pulse to pulse CEP shift due to perturbation of the grating pair can be found derivating $R(\omega_0)$ with respect to the compressor parameters. For example, a change of the grating separation δG leads to a pulse to pulse CEP fluctuation ($\Delta\phi_{CE_G}$) of:

$$\Delta\phi_{CE_G} = -\frac{\partial R(\omega_0)}{\partial G}\delta G = 2\pi\frac{\delta G}{d}tan\theta_d \tag{6.6}$$

for a single pass on the grating pair. For a double pass equation 6.6 has to be multiplied by a factor 2. Figure 6.14 represents the CEP shift for grating distance variation in a compressor. The graph is plotted from equation 6.6, considering the following compressor's parameters:

$$\begin{cases} G = 382.843 \text{ mm} \\ \frac{1}{d} = 1480 \text{ lines/mm} \\ \lambda = 800 \text{ nm} \\ \theta_i = 45.45° \end{cases} \tag{6.7}$$

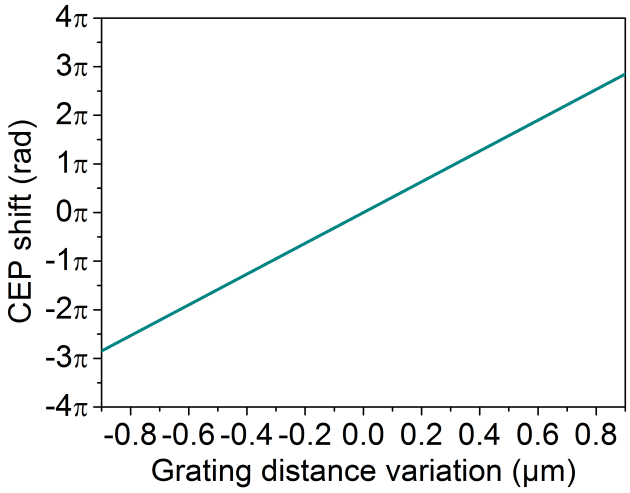

Figure 6.14: CEP shift caused by grating distance variation from equation 6.6 on a double pass in the grating pair with parameters 6.13

Same consideration can be applied to beam pointing fluctuation. It results in a change of the incident angle θ_i and consecutively a change of the diffraction angle θ_d. Thus a beam pointing fluctuation of $\delta\theta_i$ results in a CEP fluctuation ($\Delta\phi_{CE_{BP}}$) of:

$$\Delta\phi_{CE_{BP}} = -\frac{\partial R(\omega_0)}{\partial\theta_i}\delta\theta_i = \frac{2\pi G}{d} cos\theta_i \frac{1 + tan^2\theta_d}{cos\theta_d}\delta\theta_i \tag{6.8}$$

for a single pass in the grating pair. In a double-pass configuration the increase of incidence angle in the first pass leads to a decrease of the same angle in the second pass: the double pass configuration compensates for incidence angle variation, as depicted in figure 6.15 (taken from [204]).

As shown if figure 6.16, the compensation is not complete and this process results in a residual CEP variation.

In figure 6.16 we plot the curve obtained from equation 6.8. The equation gives the CEP fluctuation for a single pass in the grating pair. It is then necessary to calculate the CEP shift for the first pass (black curve in figure 6.16) and for the second pass (red curve in figure 6.16) independently, considering that the incident angle changes in sign for the two different

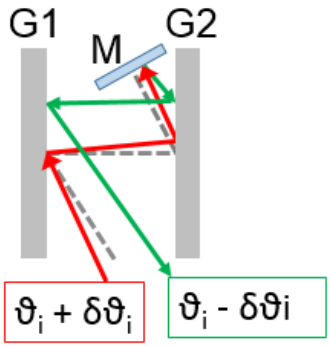

Figure 6.15: Compensation of beam pointing fluctuation on double pass in a grating pair. A change in the incidence angle θ_i of $+\delta\theta_i$ corresponds to an output angle $\theta_i - \delta\theta_i$ (taken from [204]). G1, G2-diffraction gratings. M-folding mirror.

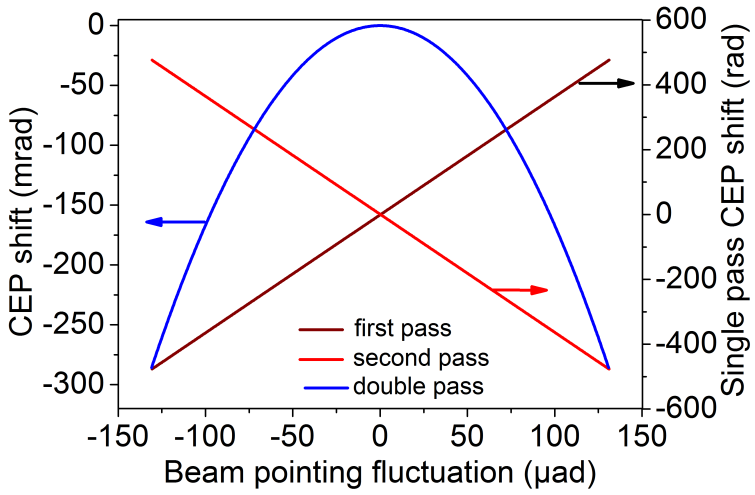

Figure 6.16: CEP shift caused by beam pointing fluctuation in the grating pair on a double pass configuration with parameters 6.13.

passes. The two curves are summed up, resulting in the double pass CEP shift.

Finally one can find a formula for CEP variation when only one grating of the pair undergoes angular tilt ($\Delta\phi_{CE_T}$) [171]:

$$\Delta\phi_{CE_T} = 2\frac{4\pi G}{d} cos\theta_i(1 + tan^2\theta_d)\delta\theta_i \tag{6.9}$$

for a single pass in the grating pair. In this case, both the incidence angle and the mutual position of the two gratings are changed. We expect that in this case the CEP shift is more important than the case of beam pointing fluctuation, for equal angle variation. As for the previous case, the double pass configuration compensate for the CEP variation. The CEP shift for double pass in the grating pair is found by calculating the shift for each pass as for

equation 6.9, and summing them up. The results is shown in figure 6.17. The CEP shift

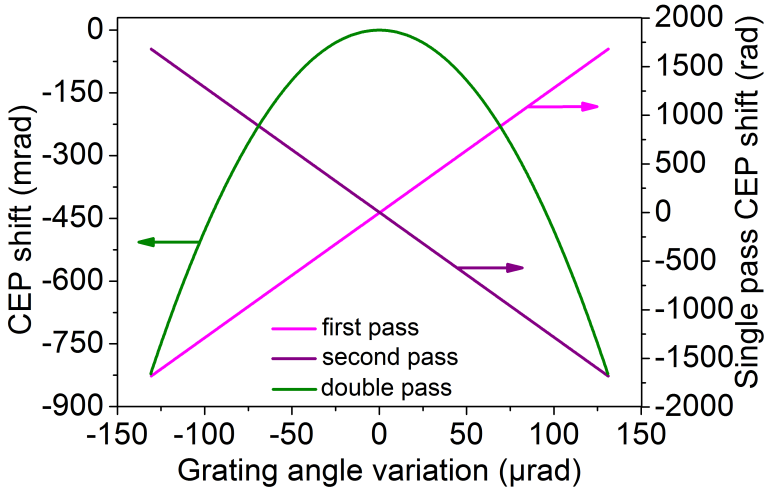

Figure 6.17: CEP shift caused by angle variation of one of the two gratings of the pair on a double pass configuration with parameters 6.13.

for double pass in the grating pair is a quadratic function depending on the grating angular shift. As expected, in this case the CEP shift is bigger compared with the beam pointing case, for equal angle variation.

6.7.2 Numerical approach

The starting point of the numerical approach is equation 6.4. The routine is the following:

1. Design the compressor with an optical design program. Define the source of light and its spectral components. The software allows to retrieve with great accuracy the optical path of the user defined spectrum propagating through the system. With the help of a macro, calculate the phase acquired by each user defined wavelength after propagation in the system.

2. Export the spectral phase information to a post-processing software (Matlab or equivalently Octave); calculate the group delay as the derivative of the phases. All the informations are known for calculating the CEP[1] from equation 6.4.

3. Consider a perturbation to the compressor (for example grating distance variation); this corresponds to a different Zemax design. Apply again the routine described in point 1 and 2 for the new configuration.

[1]From now on we will use the term CEP to indicate the CEP difference between the input pulse and the output pulse of the dispersive module, i.e. the CEP terms added by the module. This notation allows to ease the discussion and to create a distinction from what we call CEP shift, that is the pulse to pulse variation occurring for perturbations of the dispersive module.

4. Obtain a collection of CEP values for each value of the perturbed parameter. For example, if a grating distance perturbation is considered, the final output will be a two vectors matrix where the first vector corresponds to different values of grating distance perturbation (δG) and the second vector is the corresponding value of CEP. Use these two vectors to calculate $\partial CEP/\partial G$ that is the CEP shift rate. For a user defined perturbation ΔG it is possible to obtain the corresponding CEP variation: $\Delta G(\partial CEP/\partial G)$.

6.7.2.1 Computing spectral phase and dispersion with Zemax

The compressor has been simulated using Zemax[2] optical design software. Figure 6.18 shows the ray-tracing program output for a spectrum of wavelengths spanning from 760 nm to 840 nm. The compression configuration appears unfolded. In order to validate the design

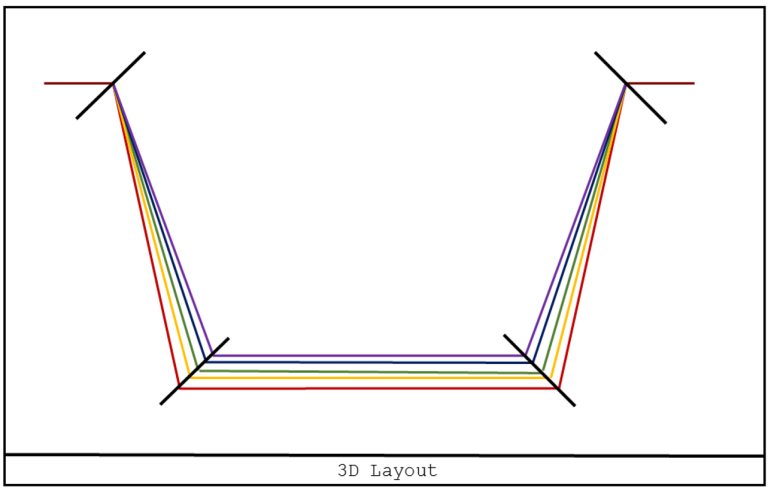

Figure 6.18: Zemax output sketch for compressor design.

we reproduced the grating compressor proposed by Fork et al. [205, 206], and compared the values of GDD and TOD obtained with our design, with the values proposed by the literature and those obtained with direct dispersion calculation with equations. We remind that for a grating compressor GDD and TOD are given by:

$$GDD = \frac{\partial^2 \varphi}{\partial \omega^2} = -2\frac{\frac{G\lambda^3}{d^2}}{2\pi c^2 cos^3(\theta_d)} \tag{6.10}$$

$$TOD = \frac{\partial^3 \varphi}{\partial \omega^3} = 2\frac{3G}{4d^2}\frac{\lambda^4}{\pi^2 c^3 cos^5(\theta_d)}(1 + sin(\theta_i)sin(\theta_d)) \tag{6.11}$$

where the factor 2 indicated the double pass in the grating pair.
The Zemax macro for extracting the GDD and TOD has been proposed by O'Shea [207]. The macro consists in the following steps:

[2]ZEMAX is a program licensed by ZEMAX Development Corporation, Bellevue, Wash. 98004-8017 (http://www.zemax.com).

- The user defines the central wavelength λ_0 and the wavelength differential $\Delta\lambda$. The program calculates and propagates through the system 4 wavelengths centred on λ_0 and spaced by $\Delta\lambda$. Convert the wavelengths in radian frequencies.
- Retrieve the optical path (OP) for each frequency after propagation through the system.
- Convert the optical path in phase $\varphi = 2\pi OP/\lambda$
- Calculate the vector of phase differences $\Delta\varphi$ and the corresponding radian frequencies $\Delta\omega$.
- Calculate the time delay $\tau = \Delta\varphi/\Delta\omega$.
- Calculate the delay differences $\Delta\tau$, and GDD = $\Delta\tau/\Delta\omega$.
- Calculate the TOD = $\Delta GDD/\Delta\omega$

The routine starts from a quartet of wavelengths. The GDD is then a vector of two elements whose values are close to each other. This expedient allows to calculate also the TOD. The final value of GDD is calculated as the average values of the two vector's elements.
It is important to underline that Zemax provides three built-in functions for retrieving the wavelength optical path: RAYO, RAYT and OPTH. As specified in the user manual, unlike RAYT and RAYO, OPTH considers also the phase added by diffractive surfaces such as gratings. As explained after equation 6.5, this does not influence the calculation of τ_g, and then of GDD and TOD, because the contribution of the phase correction factor is deleted after calculating the phase derivative. However, it is of essential importance when computing the CEP, since, as already mentioned, it corresponds exactly to the correction factor $R(\omega)$.

We applied the above-mentioned macro to the compressor design for the parameters given by Fork et al.:

$$\begin{cases} G = 7 \text{ mm} \\ \dfrac{1}{d} = 600 \text{ lines/mm} \\ \lambda = 620 \text{ nm} \\ \theta_i = 45^\circ \end{cases} \tag{6.12}$$

where G is the perpendicular grating distance, 1/d the grating's groove density, λ the spectrum central wavelength, θ_i the incidence angle. The results obtained from the Zemax simulation are listed in table 6.2 together with the comparison with the equations and the data provided by Fork et al. As evident from table 6.2, the Zemax design reproduces faithfully the expected results obtained with the equations.

Once the Zemax routine have been verified, the same routine has been applied to the compressor design used in the 10 kHz front-end; the parameters are resumed here below:

$$\begin{cases} G = 382.843 \text{ mm} \\ \dfrac{1}{d} = 1480 \text{ lines/mm} \\ \lambda = 800 \text{ nm} \\ \theta_i = 45.45^\circ \end{cases} \tag{6.13}$$

Dispersion	Fork et al.	Equation	Zemax
GDD (fs^2)	-2540	-2539.694	-2539.691
TOD (fs^2)	+2184	+2154.143	+2154.141

Table 6.2: Comparison between second and third order dispersion calculation for the compressor with parameters 6.12

Again a spectrum of four wavelengths centred at 800 nm is propagating through the compressor. Applying the same Zemax macro to this design, we obtained a good agreement with the theory. The results are shown in table 6.3.

Dispersion	Equation	Zemax
GDD (fs^2)	$-2.213626 \cdot 10^6$	$-2.213641 \cdot 10^6$
TOD (fs^3)	$+4.840761 \cdot 10^6$	$+4.840787 \cdot 10^6$

Table 6.3: Comparison between second and third order dispersion calculation for the compressor of parameters 6.13

6.7.2.2 Post-processing

The information of phases and wavelengths obtained with the same macro for the compressor with parameters defined in 6.13 is exported to a post-processing code (Octave) for calculation of the CEP. First, the wavelength vector is converted in an evenly spaced vector of radian frequencies and its sampling dimension is increased. Secondly, the phase vector is interpolated in the frequency vector to obtain more points. The group delay τ_g is computed as diffφ/diffω. In order to again verify the routine, we apply subsequently the diff function to calculate the GDD and TOD as two vectors. The average calculated on the vector represents their value: $-2.213626 \cdot 10^6$ fs^2 for the GDD and $+4.879283 \cdot 10^6$ fs^3 for the TOD. The GDD values perfectly matches with the Zemax macro and the equation (cf table 6.3) while the TOD value differs from the equation value; however the percentage difference is really small (0.6%) and can be attributed to the diff built-in function. Once the Octave algorithm has been proven to provide the same results as the Zemax macro and the analytical equations, we can proceed calculating the CEP value. We first calculate the correction factor vector $R(\omega)$ for every frequency of the frequency vector:

$$R(\omega) = -\omega\tau(\omega) + \varphi(\omega) \tag{6.14}$$

This is possible since the information of optical path for each frequency has been extrapolated from Zemax using the OPTH function, that accounts for the phase correction factor at the grating surface. We extract then the vector element corresponding to the index of ω_0, since $R(\omega)$ evaluated in ω_0 gives the CEP:

$$\phi'_{CE} - \phi_{CE} = -R(\omega_0) = [\omega\tau(\omega) - \varphi(\omega)]|_{\omega_0}. \tag{6.15}$$

In order to evaluate the results, we compare the vector $R(\omega)$ obtained with the numerical approach described above with the vector $R_{eq}(\omega)$ obtained with the analytical equation, remembering that $R_{eq}(\omega) = -4\pi(G/d)tan(\theta_d(\omega))$, for a double pass in the grating pair. Disregarding for the moment the CEP calculation, Treacy [57] introduced $R(\omega)$ in the phase calculation in order to correctly take into account the additional phase difference at the grating surface between two different spectral components, that necessarily hit the second grating in two different positions. What is really meaningful for evaluating the compressor dispersion and the temporal shape of the output pulse is the difference between the values of phase for different frequencies, and as consequence the difference between values of $R(\omega)$, rather than their absolute values. Figure 6.19 reminds the meaning of the term $R(\omega)$.

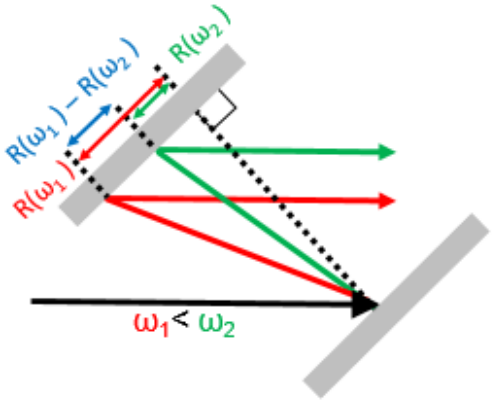

Figure 6.19: Schematic representation of the meaning of the term $R(\omega)$.

If we extract the single element $R(\omega_0)$ from the numerically calculated vector, its value is much different with respect to the equivalent element $R_{eq}(\omega_0)$, obtained with analytical calculation. However, if we compute the consecutive differences between each element of both vectors separately, applying the function diff($R_{eq}(\omega)$) and diff($R(\omega)$), we obtain the two vectors of differences, whose values are consistent. For example, we extract the central value for both vectors obtaining: $[\text{diff}(R_{eq}(\omega))]|_{\omega_0}$ = -76.80705 rad and $[\text{diff}(R(\omega))]|_{\omega_0}$ = -76.80646, where the two values differ for less than 0.001%.

In conclusion, the numerical approach provides an absolute value of CEP that is different from the one obtained with equation; however the absolute values are physically not really meaningful. On the contrary, we demonstrated that the numerical approach correctly accounts for phase differences between different spectral components propagating through the compressor. As a consequence, the same approach can correctly calculate, for any specific spectral component, the phase difference that occurs if the compressor design is modified, simulating a perturbation. Considering then two compressor designs, respectively modelling the non-perturbed condition and a perturbed condition, we can calculate and extract for both design the two values of $R(\omega_0)$, named $R_1(\omega_0)$ and $R_2(\omega_0)$. Their difference will be used to calculate the CEP shift caused by the specific perturbation.

6.7.2.3 Applying perturbations to compressor

The above-mentioned routine allows to extract the values of CEP= $-R(\omega_0)$ for a specific value of carrier frequency ω_0 and for a defined compressor configuration designed with Zemax. Equivalently, given the same propagating spectrum, a defined compressor configuration corresponds to one value of CEP. If now a perturbation is applied to the compressor, its configuration changes as well as the Zemax design. It is then possible to build two vectors: the first one is composed by the values of the perturbed parameter (that could be for example the grating distance or the incidence angle), the second contains the corresponding values of CEP. It is then sufficient to apply the derivative of the CEP with respect to the varying parameter for accessing the CEP fluctuation rate.

We studied the case of mechanical vibrations inducing a variation of the grating distance G. We first define a set of values for G, centred at the equilibrium value G_0. For each value we designed the corresponding Zemax compressor and we calculate the CEP with the routine defined above. We obtain two vectors, one with the values of G and the second with the corresponding values of CEP= $-R(\omega_0)$:

$$\mathbf{G}\text{ vector} \qquad\qquad \mathbf{CEP}\text{ vector}$$

$$\begin{cases} G_1 = G_0 - 1000\text{ nm} \\ G_2 = G_0 - 500\text{ nm} \\ G_3 = G_0 \\ G_4 = G_0 + 500\text{ nm} \\ G_5 = G_0 + 1000\text{ nm} \end{cases} \qquad \begin{cases} CEP_1 = -R_1(\omega_0) \\ CEP_2 = -R_2(\omega_0) \\ CEP_3 = -R_3(\omega_0) \\ CEP_4 = -R_4(\omega_0) \\ CEP_5 = -R_5(\omega_0) \end{cases}$$

After interpolating for increasing the vector sampling, the CEP shift rate can be calculated as diff(**CEP**)/diff(**G**) as for equation 6.6. The result is shown in figure 6.20 where the CEP shift as a function of the grating distance variation is plotted in orange line. In order to plot this curve, it is sufficient to multiply the CEP shift rate (diff(**CEP**)/diff(**G**)) by the grating distance variation δG, obtaining $\Delta\phi_{CE_G} = \delta G(\text{diff}(\mathbf{CEP})/\text{diff}(\mathbf{G}))$. The dashed black line in figure 6.20 is the same curve calculated with analytical equation 6.6 for a double pass in the grating pair: $\Delta\phi_{CE_G} = 4\pi(G/d)tan(\theta_d(\omega_0))$ (cf figure 6.14). Figure 6.20 shows an excellent agreement between the analytical and the numerical approach. For a grating distance variation of the order of the wavelength (0.8 μm) from the equilibrium position G_0, the corresponding CEP shift is of the order of 2.5310π radiant calculated with numerical approach, and 2.5312π extracted from the equation. This results confirm also that a grating distance variation of the order of the wavelength has a detrimental effect on the CEP stability.

We apply the same routine in the case of beam pointing fluctuation. In order to simulate this in Zemax, it is sufficient to add a tilting angle to the emitting source, so that the incidence angle θ_{i0} undergoes a variation. As before, we collect two vectors of incident

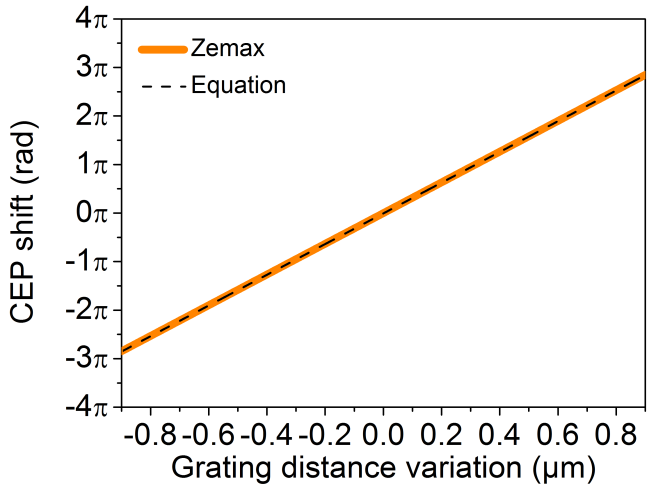

Figure 6.20: Comparison between the numerical approach (orange line) and analytical approach (black dashed line) for CEP shift caused by grating distance variation.

angles and corresponding CEP values.

$\boldsymbol{\theta_i}$ vector

$$\begin{cases} \theta_{i1} = \theta_{i0} - 130\ \mu\text{rad} \\ \theta_{i2} = \theta_{i0} - 85\ \mu\text{rad} \\ \theta_{i3} = \theta_{i0} - 45\ \mu\text{rad} \\ \theta_{i4} = \theta_{i0} \\ \theta_{i5} = \theta_{i0} + 45\ \mu\text{rad} \\ \theta_{i6} = \theta_{i0} + 85\ \mu\text{rad} \\ \theta_{i7} = \theta_{i0} + 130\ \mu\text{rad} \end{cases}$$

CEP vector

$$\begin{cases} CEP_1 = -R_1(\omega_0) \\ CEP_2 = -R_2(\omega_0) \\ CEP_3 = -R_3(\omega_0) \\ CEP_4 = -R_4(\omega_0) \\ CEP_5 = -R_5(\omega_0) \\ CEP_6 = -R_6(\omega_0) \\ CEP_7 = -R_7(\omega_0) \end{cases}$$

We calculate the CEP shift rate as diff(**CEP**)/diff($\boldsymbol{\theta_i}$) and multiply it for a vector of angle variation $\delta\theta_i$, obtaining $\Delta_{CE_{BP}} = \delta\theta_i(\text{diff}(\mathbf{CEP})/\text{diff}(\boldsymbol{\theta_i}))$. The curve obtained is shown in 6.21, orange curve, whereas the black dashed curve is that obtained with the analytical approach (cf figure 6.16). For a beam pointing fluctuation of 100 μrad the corresponding CEP shift calculated with the equation is in module 166.57 mrad and 167.32 mrad with the numerical approach. Again the numerical approach is in good agreement with the analytical approach. We notice that for a double pass geometry, the CEP shift is not totally compensated, even though the CEP stability for beam pointing fluctuation is less affected than in the case of grating distance variation. Thus beam pointing instability should not be an issue for CEP stability using grating based compressor.

In order to complete the study of the compressor, we simulate an angular tilt on the first grating. The routine is the same as that described for the previous case except that the elements of the vector of angles are now represented by the tilt of the first grating. In

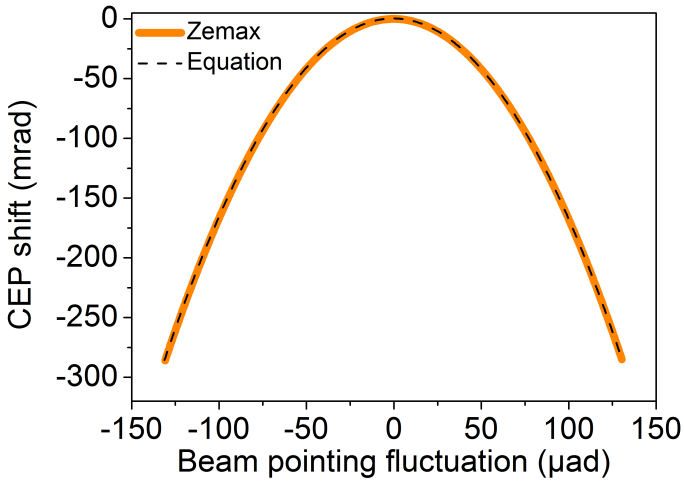

Figure 6.21: Comparison between the numerical approach (orange line) and analytical approach (black dashed line) for CEP shift caused by beam pointing fluctuation.

order to compare the effect of beam pointing and grating tilt we apply to the grating the same tilt we applied to the emitting source in the previous case. Figure 6.22a reports the results obtained with the numerical approach (orange curve) and the analytical approach (black dashed curve) for grating angular tilt. Figure 6.22b displays the CEP shift as a

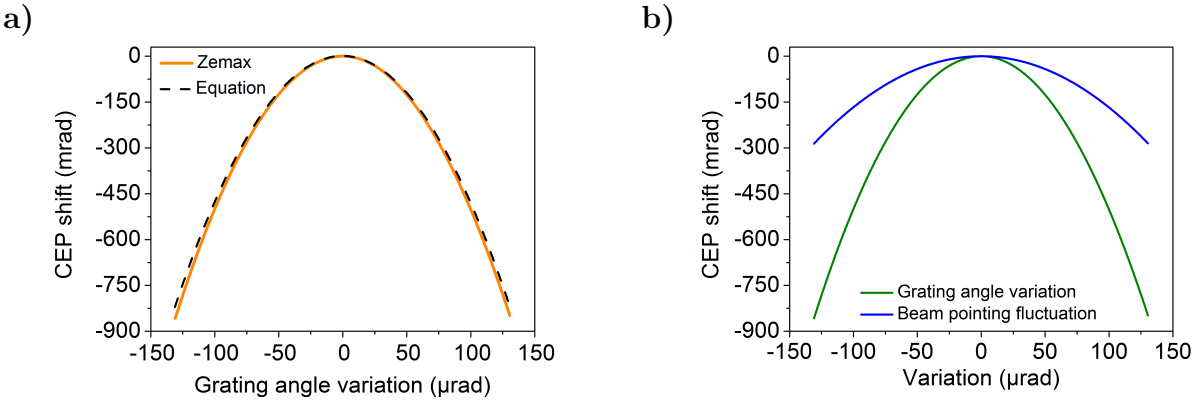

Figure 6.22: a) CEP shift induced by angular tilt of the first grating with the numerical (orange) and analytical approach (black dashed curve). b) Comparison between grating tilt (green curve) and beam pointing (blue curve) on CEP shift.

function of beam pointing (blue curve) and grating angle variation (green curve). A beam pointing fluctuation of 100 μrad induces a CEP shift of 167 mrad in module, whereas the same amount of tilt applied to the first grating results in a CEP shift of 500 mrad. In fact in this second case a misalignment of the grating pair must be added to the effect of incidence angle variation.

6.7.2.4 Study of Öffner stretcher designs on CEP stability

The numerical approach can be applied to more complex optical designs like the Öffner stretcher configuration. The complexity of this design comes from the aberration-free imaging system, composed by two curved mirrors. Even thought calculation of dispersion induced by a Öffner stretcher is well described by the equations for a pair of gratings (cf equations 6.10 and 6.11), approximating the stretcher to a couple of grating might lead to an underestimated value of CEP shift. We then studied theoretically the CEP dependency on the Öffner stretcher design applying the numerical approach, allowing us to ideally have an understanding of how each optics composing the module affect the CEP sensitivity.

We used the Zemax ray-tracing software for simulating the module used in the 10 kHz front-end described in chapter 3. The stretcher parameters are listed below:

$$\begin{cases} s = 200 \text{ mm} \rightarrow G_s = -2scos\theta_d = 299.226 \text{ mm} \\ R_{conc} = 1000 \text{ mm}, R_{conv} = -500 \text{ mm} \\ \dfrac{1}{d} = 1200 \text{ lines/mm} \\ \lambda = 800 \text{ nm} \\ \theta_i = 17.24° \\ \theta_d = 41.58° \end{cases} \tag{6.16}$$

where s is the distance between the grating and the mirror's center of curvature, G_s is the equivalent parallel grating distance (cf. chapter 2), R_{conc} and R_{conv} the radius of curvature of the concave and the convex mirrors, $1/d$ the groove density, λ the spectrum central wavelength, θ_i and θ_d the incidence and diffraction angles at 800 nm respectively. Figure 6.23 shows the Zemax design for a spectrum of wavelengths centered at 800 nm and spanning from 760 nm to 840 nm. After the first pass in the triplet grating-concave-convex, the beam

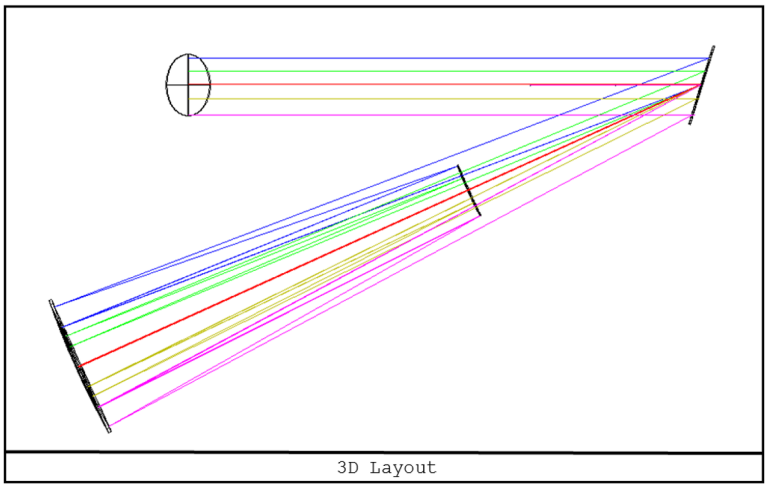

Figure 6.23: Zemax output sketch for Öffner stretcher design.

is reflected back by a dihedral mirror, for spatial chirp compensation. In total the beam travels twice in the triplet, i.e. in the grating pair.

As for the compressor, the stretcher design has been validated comparing the GDD and the TOD obtained with Zemax macro and with equations. We remind that for the stretcher GDD and TOD are described by the same equation as those for the compressor (cf. equation 6.10 and 6.11), providing that G is replaced with G_s.

Dispersion	Equation	Zemax
GDD (fs^2)	$1.863890 \cdot 10^6$	$1.860749 \cdot 10^6$
TOD (fs^3)	$-5.087625 \cdot 10^6$	$-5.074940 \cdot 10^6$

Table 6.4: Comparison between second and third order dispersion terms calculated for the stretcher of parameters 6.16

Table 6.4 shows the results. The errors in GDD and TOD calculation between the numerical and the analytical approach are respectively 0.17% and 0.25%, thus negligible.

The analysis carried out on the stretcher has the purpose of comparing the Öffner configuration used in our front-end (parameters 6.16), with two alternative configurations inducing the same value of GDD. The two newly-conceived configurations differ in the values of the radius of curvature of the mirrors, in the grating groove density and in the equivalent grating's perpendicular distance. The incidence angle is unchanged, the diffracted angle depends on the groove density. The parameters describing each design are resumed in table 6.5, where we identify as "Design 1" the one used in our 10 kHz front-end.

Parameter	Design 1	Design 2	Design 3
ROC concave (mm)	1000	2000	500
s (mm)	200	384	84.5
Gs (mm)	-299.226	-663.492	-95.846
1/d (lines/mm)	1200	1000	1400
GDD (fs^2)	$1.860749 \cdot 10^6$	$1.862271 \cdot 10^6$	$1.852827 \cdot 10^6$
TOD (fs^3)	$-5.087625 \cdot 10^6$	$-3.558260 \cdot 10^6$	$-9.015001 \cdot 10^6$

Table 6.5: Parameters of the three different Öffner configurations and corresponding GDD and TOD.

The three configurations require a double pass in the grating pair for ensuring the desired value of GDD, that is equivalent for the three designs (the errors are below 0.05%). On the other hand, the values of TOD are different and can be compensated with a proper design of the coupled compressors.

We focused our interest on the effect of beam pointing fluctuations on CEP stability for the three configurations. For each of them we applied the routine described for the case of compressor, considering that beam pointing fluctuations can be translated into incidence angle variations. In synthesis, for each of the three configurations:

- We define a vector of incidence angles, each of them corresponding to an angular tilt of the emitting source in Zemax design.
- With the previously described macro, we propagate a spectrum of defined wavelengths centered at 800 nm and we export the information of phase acquired by each component during propagation in the module.
- For each incidence angle we calculate the corresponding CEP from the phase informations. We dispose of two vectors: the incidence angles and the corresponding CEP values.
- We calculate the derivative of the CEP with respect to the incidence angle and multiply the result by a vector of incidence angle variation: we obtain thus a curve of CEP shift as a function of beam pointing fluctuation.

The same routine is repeated for the three configurations with the same vector of incidence angles, resulting in three comparable curves. The result of this simulation is shown in figure 6.24.

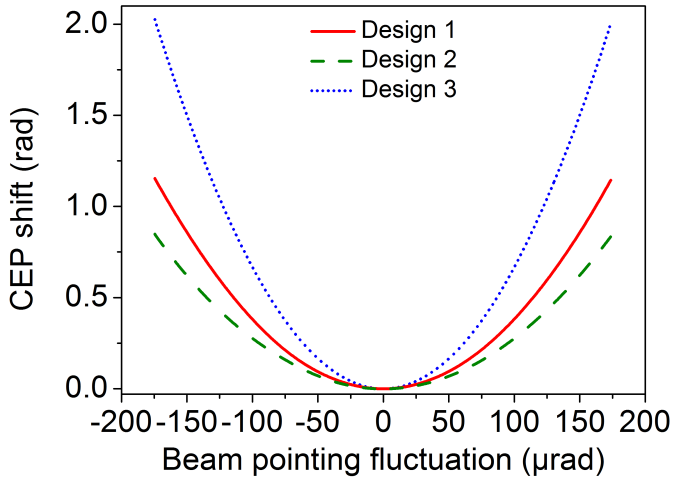

Figure 6.24: CEP shift as a function of beam pointing fluctuations for the three Öffner designs defined by the parameter of table 6.5.

We notice that in general the stretcher is more sensitive to beam pointing fluctuation than the compressor. We can for example compare the stretcher of design 1 (parameter 6.16) with the compressor of parameter 6.13 (cf figure 6.21); the two modules are in fact coupled in the 10 kHz front-end of chapter 3. For 100 μrad of beam pointing fluctuation, the compressor gives a CEP shift, in module, of 167 mrad whereas the CEP shift for the stretcher reaches the value of 380 mrad. The stretcher sensitivity comes most probably from the fact that also its imaging system is affected by the beam pointing fluctuation. We also notice that the parabolas defining the shift for compressor and stretcher have opposite sign. This is due to the stretcher imaging system, that inverts the sign of the mutual grating distance.

Even though the total CEP shift on a stretcher cannot be simply described by equation 6.4, because it is influenced also by the imaging system, we can suppose that the CEP depends anyway on the grating distance.
Secondly, we notice that a more compact stretcher design, with higher groove density (design 3) is more sensitive to beam pointing fluctuation. The CEP shift for 100 μrad of beam pointing variation increases from 270 mrad of design 2, up to 670 mrad for the most compact design 3. Figure 6.25 plots the leading coefficient[3] for the three parabolas of figure 6.24 as function of the equivalent perpendicular grating distance, the grating groove density and the concave mirror radius of curvature. From this first analysis we deduce that a less compact

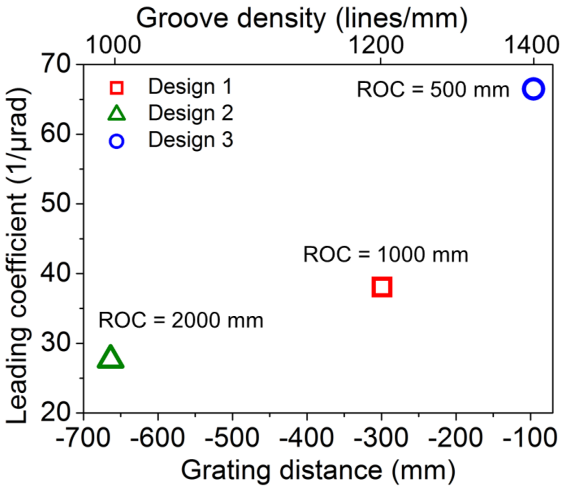

Figure 6.25: Leading coefficient for the three parabolas of figure 6.24 as a function of grating groove density, equivalent perpendicular grating distance and concave mirror radius of curvature.

stretcher design coupled to a lower groove density can be more stable in terms of CEP noise induced by beam pointing fluctuation.

It would be interesting to understand which parameter, among the three of figure 6.25, affects most the stretcher stability. For this purpose we conceive a fourth Öffner design, in double pass. This configuration uses the same radius of curvature of design 3, but different groove density. Its parameters are listed in table 6.6, together with those of design 3. The comparison between these two designs gives information on the influence of the groove density on the CEP sensitivity, for equal concave mirror radius of curvature. We underline that design 4 induces half of the dispersion provided by design 3: the two configurations are not equivalent in terms of dispersion. Figure 6.26a shows the results. For equal radius of curvature, the groove density parameter has a strong influence on the CEP sensitivity. A smaller value of groove density implies smaller value of GDD. Less dispersion in turn causes less CEP shift for a defined beam pointing shift: for 100 μrad, the CEP shift rises from 180 mrad (design 4) to 670 mrad (design 3).

[3]For a parabola defined as $y = ax^2$, its leading coefficient is a.

Parameter	Design 3	Design 4	Design 1
ROC concave (mm)	500	500	1000
s (mm)	84.5	100	200
Gs (mm)	-95.846	-149.613	-299.226
1/d (lines/mm)	1400	1200	1200
GDD (fs^2)	$1.852827 \cdot 10^6$	$0.928612 \cdot 10^6$	$1.860749 \cdot 10^6$
TOD (fs^3)	$-9.015001 \cdot 10^6$	$-2.515627 \cdot 10^6$	$-5.087625 \cdot 10^6$

Table 6.6: Parameters of Öffner configurations in design 1, 3 and 4, and corresponding GDD and TOD.

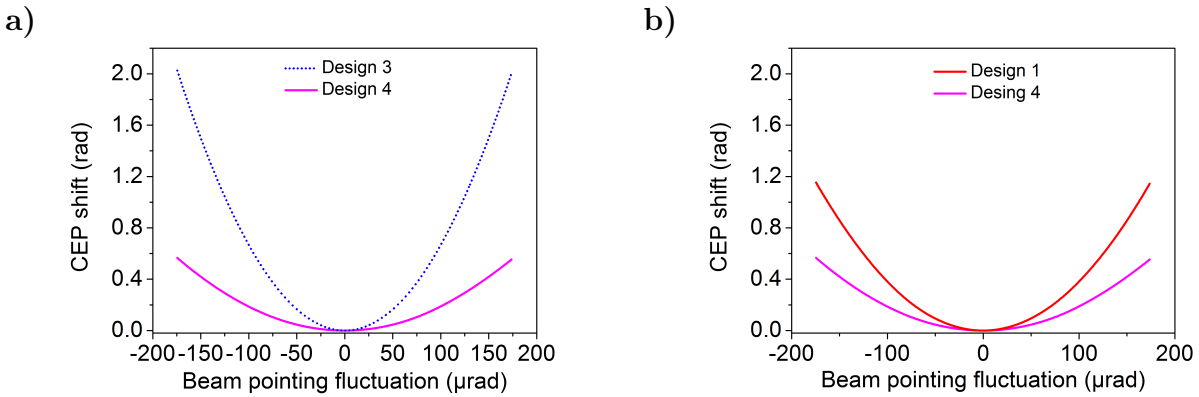

Figure 6.26: CEP shift as a function of beam pointing fluctuations in different Öffner configurations. a) Comparison between design 3 and 4 with same radius of curvature and different groove density. b) Comparison between design 1 and 4 with same groove density and different radius of curvature. The designs are defined by the parameters of table 6.6.

More interesting is the case of two Öffner configurations with same groove density and different radius of curvature. Design 4 can be compared to design 1, providing an insight on how the radius of curvature influences the CEP sensitivity. The result of the comparison is shown in figure 6.26b. The result obtained are in this case unexpected. We expect that since design 4 uses a more compact configuration with a smaller radius of curvature, it is also more sensitive to beam pointing fluctuation. However, the results shows the opposite. For fixed value of beam pointing fluctuation (100 μrad), design 4 gives 180 mrad, while design 1 gives 367 mrad. It is necessary then to re-think how the different parameters influence the module sensitivity. What actually counts in defining the stretcher characteristic is the total imaging system, (not only the radius of curvature), i.e the couple of radius of curvature (ROC) and grating-center of curvature distance (s). Two imaging systems can be equivalent (same ratio between ROC and s) but define different gratings distances G_s, thus different dispersion. Then what mostly defines the module sensitivity is the dispersive power of the design so that:

- For equivalent imaging system and same groove density, the most dispersive configu-

ration is the most sensitive (higher values of G_s), as for the result of figure 6.26b.

- For equivalent value of dispersion induced, equivalent imaging system, different G_s and different groove density (the three configurations of figure 6.24), the most sensitive configuration to CEP shift is that using higher value of groove density which compensates smaller grating distance value.

As reported in table 6.6, design 4 differs from the other designs for its value of GDD that is twice smaller. In order to increase the value of dispersion, after a double pass in the grating pair, one can deviate the beam back again into the stretcher: in this case the pulse travels through the triplet grating-concave-convex four times, equivalent to four passes in the grating pair. If double passing the stretcher has the trivial effect on the GDD of doubling its value, the effect on the CEP needs to be studied. We analysed this case after designing a fifth stretcher configuration, using the same optics as design 4, and including also a prism at its output, that reflects the beam back into the stretcher. Table 6.7 resumes the parameters and the dispersion values of design 5, compared with those of design 4.

Parameter	Design 4	Design 5
ROC concave (mm)	500	500
s (mm)	100	100
Gs (mm)	-149.613	-149.613
1/d (lines/mm)	1200	1200
GDD (fs^2)	$0.928612 \cdot 10^6$	$1.858448 \cdot 10^6$
TOD (fs^3)	$-2.515627 \cdot 10^6$	$-5.153186 \cdot 10^6$

Table 6.7: Parameters of Öffner configurations in design 4 and design 5 and corresponding GDD and TOD. Design 4 and design 5 allow respectively two and four passes in the grating pair.

From figure 6.27, for equivalent design, the most dispersive module (design 5) is more sensitive to beam pointing fluctuation.

Finally figure 6.28 compares the four configurations inducing the same GDD, where design 5 uses four passes in the grating pair, the three other two passes. Form table 6.7 and table 6.5, we notice that design 5 is really similar to design 1 in terms of induced GDD and TOD. This similarity is translated also in terms of CEP sensitivity, since the two parabolas of figure 6.28 for the two designs are really close to each other. However, design 5 seems to be more stable than design 1. This slight difference comes probably from the fact that, in order to ensure the same value of GDD for only two passes in the grating pair, the equivalent grating distance on design 1 must be twice the distance of design 5. In terms of dispersion, design 5 can be thought as design 4 with twice the value of grating distance (-149.613·2 mm), that is exactly the same value used in design 1 (-299.226 mm); however, this approximation is too strong when considering the CEP stability, that is affected by the whole stretcher design. Even though design 5 seems to be quite stable, one should consider that the prism insertion for double passing the module induces an added source of noise, since it can be affected by mechanical vibrations.

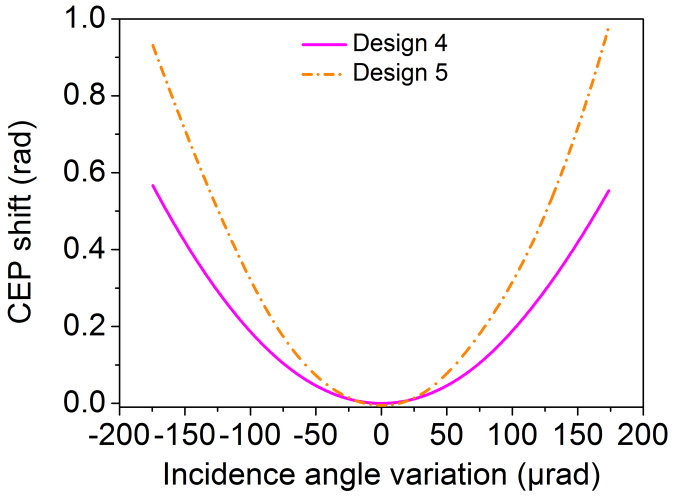

Figure 6.27: CEP shift as a function of beam pointing fluctuations for two passes (design 4) and four passes in the grating pair (design 5).

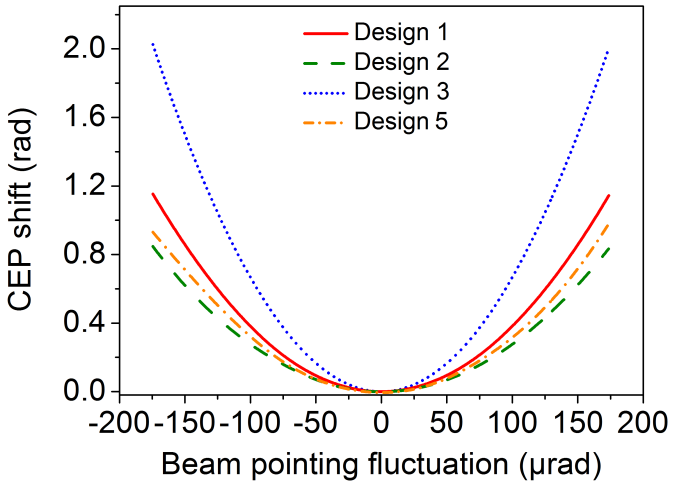

Figure 6.28: Comparison of four designs inducing the same GDD in term of CEP stability as a function of beam pointing fluctuation.

In conclusion, for equal value of GDD, a more compact design, that necessarily uses higher values of groove density, is more sensitive to beam pointing fluctuation. The analysis shown in this section is limited to the effect of only one source of CEP noise. It has been demonstrated that the numerical approach can efficiently predict the CEP shift for different designs, and it represents a powerful and useful device for engineering. Our approach can be ideally used to study any perturbation that can affect the module, like distance variation between the imaging optics or angular tilt of any stretcher's component that may be affected by mechanical vibrations.

Chapter 7

Conclusions and perspectives

This thesis has been dedicated to the development and demonstration of methods to improve the performances of a CPA Ti:Sa laser system according to the requirements needed by attosecond science. We demonstrate that, although alternative laser technologies (like OPA, OPCPA and fiber lasers) conceived during the past decade are little by little gaining importance as sources for attosecond science, there is still room of improvement for Ti:Sa CPA lasers. The first observation of high harmonics generation dates back to 1987-1988 [16, 208], period when CPA and Ti:Sa laser were firstly demonstrated. Fast development of the laser technique caused that at the beginning of the century many laboratories working on harmonics generation and strong field applications choose a Ti:Sa CPA laser as driving source for their experiments. The interplay between laser source and attosecond science implied that the development of one was reflected on the advancement of the other. Thus Ti:Sa lasers owed their success to the novelty of their applications, that were possible only upon development of the laser technology.
Nowadays still many laboratories working on attosecond science are equipped with Ti:Sa lasers, reason why any possibility of improvement should be pursued.

We focused our research on two main lines: generation of high average power pulses and CEP stabilization. The first research branch is focused on overcoming two limitations: thermal heat load at high repetition rate and gain narrowing in amplification medium. After deepening the study of thermal effect in Ti:Sa amplifier, we demonstrate a 10 kHz front-end capable of working in three different regimes: narrow band, broad band and tunability mode. The core of the amplifier is the double crystal regenerative cavity for thermal effect management, delivering pulses up to three times more powerful than a standard regenerative amplifier. In narrowband mode (measured pulse duration of 35 fs), the module delivers pulses with more than 5 W of power, i.e. 500 μJ. When applying the spectral broadening through programmable filter, the measured pulse duration is shortened to 17 fs with 2.7 W of power at 10 kHz and a good beam profile. The 110 nm broad spectrum supports also spectral tunability performed thanks to the coupled functioning of Dazzler and Mazzler. Prerequisite to high amplification without incurring in dramatic values of B-integral is high stretching factor, obtained with high dispersion grating based stretcher and compensated with grating based compressor. A completely water-cooled lens-less multipass amplifier has been designed to boost the pulse's power up to 10 W at 1 kHz. The saturation of the amplifier ensures

that the output power undergoes negligible variation when switching from narrow band to broad band mode and again to tunability mode. In parallel to this specific study and in order to demonstrate the energy scalability of our front-end, it has been coupled to further cryogenically cooled amplification stages at 10 kHz and 1 kHz, reaching the TW class regime. This led to the new FAB1/10 laser equipping ATTOlab platform.
The novel amplifier designs demonstrated on our front-end also have an impact on the international market of Amplitude Laser Group. During these three years, both the 10 kHz double crystal regenerative amplifier and the 1 kHz fully water-cooled lens-less multipass amplifier became well-established modules included in commercially available Amplitude Laser products. The company already sold three lasers equipped with the double crystal regenerative amplifier and three others with the 1 kHz multipass amplifier to international customers.

CEP stabilization of the amplified pulses has been performed with a complete analog detection and feedback tool, allowing 10 kHz shot-to-shot stabilization with residual CEP noise of 170 mrad on a 10 seconds time scale, and 210 mrad over three hours. The newly designed tunable-free compressor's optical mounts are engineered to improve CEP stability. The performances of the grating based compressor equipped with solid CEP- compatible mounts have been tested in a controlled environment where perturbations can be applied to the module. The priceless stability of this new design is demonstrated by the measurement of CEP stability at its output, with a RMS residual shot-to-shot noise of 255 mrad, compared with a standard compressor with residual CEP noise of 463 mrad, in same conditions.
Finally we presented a new simulation tool based on a commercial ray-tracing software (Zemax) for predicting the CEP shift in dispersive modules (stretcher or compressor) for any particular design of the module. The strength of the tool consists in providing the CEP shift for any perturbation, independently of the complexity of the design of the dispersive module. Thus the routine can account for CEP perturbations arising from parameter that are not taken into consideration by existing equations.

Even though Ti:Sa laser technology has already been largely exploited, perspectives of further improvements are feasible.
Concerning the amplification line, the double crystal regenerative amplifier is designed to support a large range of thermal lens focal length values. As a consequence, we could in principle increase the pump power on both crystals in order to gain more IR output power, keeping unaltered the cavity stability. Simultaneously it is necessary to properly dimension the beams (both pump and seed) size, in order to avoid permanent damages of the optics. In fact it has been demonstrated that the beam size on the folding mirrors in the W-like amplifier is rather small, and the beam intensity approaches the damage threshold of the optics. At the same time, the position of these mirrors cannot be changed because it represents a critical parameter for cavity stability. Besides the optics damage threshold, also the Mazzler constitutes a delicate element concerned by power scaling. In fact the size of the beam propagating through the Mazzler should not exceed few mm in diameter $1/e^2$ in order to avoid spatial cutting of the beam. On the other side, increasing the beam energy without increasing its size might lead to critically intense beam propagating through the Mazzler. A solution could be represented by replacing the Mazzler with spectral filters, that allow to scale the beam dimension, or to benefit from a larger Mazzler size.

Even thought Ti:Sa laser systems reaching the PW level have been currently demonstrated, Ti:Sa technology has a significant drawback: heat accumulation in the crystal causes thermal lensing that deteriorates the beam profile quality, and in worst case, can cause damage of the amplification medium. This limitation prevents Ti:Sa amplifiers to be scaled to high repetition rate and high average power. As consequence, scaling the peak power calls for decreasing the repetition rate. In this manuscript we described a TW-class laser working at 1 kHz; 100 TW lasers have been demonstrated at 10 Hz [73] and 100 Hz, whilst further scaling the power to the PW level has been reported for 1 Hz operation [209, 210, 211]. Amplitude Laser Group recently designed and bulit a Ti:Sa system delivering 2 PW at 10 Hz for the facility of ELI-ALPS [212]. The thin-disk technology applied to Ti:Sa crystal may offer the possibility to scale the laser average power to higher values [213, 214]. The main difference from conventional rod or slab lasers is the geometry of the gain medium: the crystal is a disk with considerably smaller thickness than its diameter. Heat extraction occurs in the longitudinal rather than transversal direction, through cooling of one of the end face of the disk. This new geometry ensures a more efficient heat extraction and offers the possibility of scaling the output average power, while keeping a good beam profile. The small thickness of the medium reduces also the mechanical stress due to heat accumulation. An issue to be considered for thin disk geometry is Amplified Spontaneous Emission (ASE) in the transversal direction, that may reduce the achievable gain. A solution to suppress transversal ASE is to use a composite disk, with an undoped part on top of a doped layer. Extraction During Pumping (EDP) method has also been suggested [215]. Numerical simulation of heat transfer for Ti:Sa in thin-disk geometry in combination with EDP has shown the possibility of scaling Ti:Sa laser system to 100 TW at 100 Hz repetition rate [216].

The two amplification lines at 1 kHz and 10 kHz repetition rate seeded by the 10 kHz front-end described in chapter 3 have already been demonstrated to be suitable for high order harmonic generation. Spectral tunability at the end of each amplified line will be shortly experimented, keeping in mind that pulse amplification up to more than tens of Watts of narrow spectra might result in B-integral increase in the amplification stages.

The role of the driving pulse's CEP in high harmonics generation is clearly evidenced for pulse duration approaching the single cycle. However influence of CEP for multi-optical-cycle has also been demonstrated [217]. High order harmonics are generated from interaction of the intense driving pulse with an atomic or molecular target. Ionized electrons travel a certain path before recombining with the parent ion. The recombination happens with emission of XUV light. For defined experimental conditions, the generated harmonics spectrum is given by contribution of long and short trajectories of electrons. Figure 7.1 represents some preliminary results obtained with FAB1 laser. These are premature measurements obtained with generation conditions that need to be optimized. However, they are clear enough to show the principle of an XUV experiment included in the laser CEP stabilization loop.

The figure shows an image of harmonics emissions (a) and harmonic spectrum (b) generated in Argon with the 1 kHz TW-class CEP stable Ti:Sa laser described in chapter 3. The rings surrounding each maxima of intensity in figure 7.1a are given by the contribution of long trajectories. Their XUV emissions are spatially overlapped and result in an interference

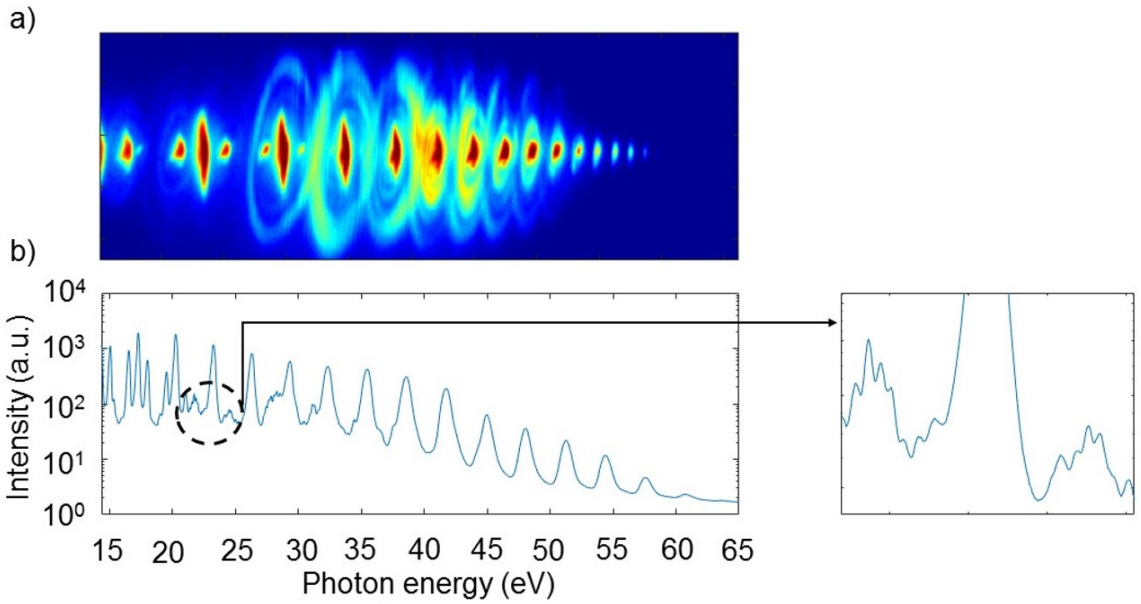

Figure 7.1: a) Image of the high order harmonics emission and b) harmonics spectrum generated with the 1 kHz TW-class laser described in chapter 3. The position of the interference pattern showed in the inset depends on the CEP of the driving pulse.

pattern spectrally located at each side of the odd harmonics. This effect is visible in figure 7.1b, when the CEP stabilization loop of the driving laser is running. Without CEP stabilization, it is not possible to observe these interference patterns. Long electron trajectories are influenced by the CEP of the driving pulse and consequently the position of the fringes depends on this laser parameter. Detecting the pulse-to-pulse interference pattern of long trajectories and its shift could be used to monitor the stability of the driving pulse CEP and apply a feedback loop to the laser CEP stabilization actuator. The fact that the stabilization loop includes the XUV experiment represents the best solution for CEP stabilization at the experiment stage.

Bibliography

[1] P. Krehl and S. Engemann. August Toepler - The first who visualized shock waves. *Shock Waves*, 5(1-2):1–18, 1995.

[2] V. Gruson, L. Barreau, Jiménez-Galan, F. Risoud, J. Caillat, A. Maquet, B. Carré, F. Lepetit, J. F. Hergott, T. Ruchon, L. Argenti, R. Taïeb, F. Martín, and P. Salières. Attosecond dynamics through a Fano resonance: Monitoring the birth of a photoelectron. *Science*, 354(6313):734–738, 2016.

[3] T. H. Maimain. Stimulated Optical Radiation in Ruby. *Nature*, 187(4736):493–494, 1960.

[4] F. J. McClung and R. W. Hellwarth. Giant optical pulsations from ruby. *Journal of Applied Physics*, 33(3):828–829, 1962.

[5] M. Didomenico, J. E. Geusic, H. M. Marcos, and R. G. Smith. Generation of ultrashort optical pulses by mode locking the YAIG: Nd laser. *Applied Physics Letters*, 8(7):180–183, 1966.

[6] Paul Michael, William French, and B Sc. NEW FEMTOSECOND DYE LASER SYSTEMS. *Thesis*, (January), 1987.

[7] De Spence, Pn Kean, and W Sibbett. 60-fsec pulse generation from a self-mode-locked Ti: sapphire laser. *Optics Letters*, 16(1):42–44, 1991.

[8] P. Moulton. Ti-doped sapphire Tunable Solid-State Laser. *Optics News*, 8(9):9, 1982.

[9] R. L. Fork, O. E. Martinez, and J. P. Gordon. Negative dispersion using pairs of prisms. *Optics Letters*, 9(5):150, 1984.

[10] Robert Szipöcs, Christian Spielmann, Ferenc Krausz, and Kárpát Ferencz. Chirped multilayer coatings for broadband dispersion control in femtosecond lasers. *Optics Letters*, 19(3):201, 1994.

[11] A Stingl, M Lenzner, Ch Spielmann, and F Krausz. Sub-10-fs mirror-dispersion-controlled Ti : sapphire laser. *Optics Letters*, 20(6):602–604, 1995.

[12] a Kasper and K J Witte. 10-fs pulse generation from a unidirectional Kerr-lens mode-locked Ti:sapphire ring laser. *Optics Letters*, 21(5):360, 1996.

[13] L. Xu, G. Tempea, A. Poppe, M. Lenzner, Ch Spielmann, F. Krausz, A. Stingl, and K. Ferencz. High-power sub-10-fs Ti:sapphire oscillators. *Applied Physics B: Lasers and Optics*, 65(2):151–159, 1997.

[14] T Beddard, W Sibbett, D T Reid, J. Garduno-Meija, N Jamasbi, and M Mohebi. High-average-power, 1-MW peak-power self-mode-locked Ti:sapphire oscillator. *Optics Letters*, 24(3):163–165, 1999.

[15] Donna Strickland and Gerard Mourou. Compression of amplified chirped optical pulses. *Optics Communications*, 56(3):219–221, 1985.

[16] A. McPherson, G. Gibson, H. Jara, U. Johann, T. S. Luk, I. A. McIntyre, K. Boyer, and C. K. Rhodes. Studies of multiphoton production of vacuum-ultraviolet radiation in the rare gases. *Journal of the Optical Society of America B*, 4(4):595, 1987.

[17] J. J. Macklin, J. D. Kmetec, and C. L. Gordon. High-order harmonic generation using intense femtosecond pulses. *Physical Review Letters*, 70(6):766–769, 1993.

[18] T. D. Donnelly, T. Ditmire, K. Neuman, M. D. Perry, and R. W. Falcone. High-Order Harmonic Generation in Atom Clusters. *Physical Review Letters*, 76(14):2472–2475, 1996.

[19] S. X. Hu and Z. Z. Xu. Enhanced harmonic emission from ionized clusters in intense laser pulses. *Applied Physics Letters*, 71(18):2605–2607, 1997.

[20] M. Yu. Ivanov and P. B. Corkum. Generation of high-order harmonics from inertially confined molecular ions. *Physical Review A*, 48(1), 1993.

[21] Y. Liang, S. Augst, S. L. Chin, Y. Beaudoin, and M. Chaker. High harmonic generation in atomic and diatomic molecular gases using intense picosecond laser pulses-a comparison. *Journal of Physics B: Atomic, Molecular and Optical Physics*, 27(20):5119–5130, 1994.

[22] Philippe Antoine, Anne L'huillier, and Maciej Lewenstein. Attosecond pulse trains using highorder harmonics. *Physical Review Letters*, 77(7):1234–1237, 1996.

[23] Pascal Salières and Maciej Lewenstein. Generation of ultrashort coherent XUV pulses by harmonic conversion of intense laser pulses in gases: Towards attosecond pulses. *Measurement Science and Technology*, 12(11):1818–1827, 2001.

[24] Gérard A Mourou. TENDANCES ACTUELLES Ultraintense lasers : relativistic nonlinear optics and applications. 2147(01):1407–1414, 2001.

[25] Steffen Hädrich, Manuel Krebs, Armin Hoffmann, Arno Klenke, Jan Rothhardt, Jens Limpert, and Andreas Tünnermann. Exploring new avenues in high repetition rate table-top coherent extreme ultraviolet sources. *Light: Science and Applications*, 4(8), 2015.

[26] W. Koechner. *Solid-State Laser Engineering*. 1976.

[27] Mark D. Skeldon, Rolf B. Saager, and Wolf Seka. Quantitative Pump-Induced Wavefront Distortions in Laser-Diode- and Flashlamp-Pumped Nd:YLF Laser Rods. *IEEE Journal of Quantum Electronics*, 35(3):381–386, 1999.

[28] Serge Ferré. *Caractérisation expérimentale et simulation des effets thermiques d'une chaîne laser ultra-intense à base de saphir dopé au titane.* PhD thesis, 2002.

[29] M. Zavelani-Rossi, F. Lindner, C. Le Blanc, G. Chériaux, and J.P. Chambaret. Control of thermal effects for high-intensity Ti:sapphire laser chains. *Applied Physics B*, 70(S1):S193–S196, 2000.

[30] Isao Matsushima, Hidehiko Yashiro, and Toshihisa Tomie. 10 kHz 40 W Ti: sapphire regenerative ring amplifier. *Optics letters*, 31(13):2066–2068, 2006.

[31] David F Hotz. Gain Narrowing in a Laser Amplifier. *Applied Optics*, 4(5):527–530, 1965.

[32] C P Barty, T Guo, C Le Blanc, F Raksi, C Rose-Petruck, J Squier, K R Wilson, V V Yakovlev, and K Yamakawa. Generation of 18-fs, multiterawatt pulses by regenerative pulse shaping and chirped-pulse amplification. *Optics letters*, 21(9):668–670, 1996.

[33] C P J Barty, C L Gordon III, and B E Lemoff. Multiterawatt 30-fs Ti : sapphire laser system. 19(18):1442–1444, 1994.

[34] Thomas Oksenhendler, Daniel Kaplan, Pierre Tournois, Gregory M. Greetham, and Frédéric Estable. Ultrawideband regenerative amplifiers via intracavity acousto-optic programmable gain control. *Springer Series in Optical Sciences*, 132:421–426, 2007.

[35] M. Nisoli, S. De Silvestri, and O. Svelto. Generation of high energy 10 fs pulses by a new pulse compression technique. *Applied Physics Letters*, 68(20):2793–2795, 1996.

[36] Andreas Hoffmann, Michael Zürch, Maximilian Gräfe, and Christian Spielmann. Spectral broadening and compression of sub-millijoule laser pulses in hollow-core fibers filled with sulfur hexafluoride. *Optics Express*, 22(10):12038, 2014.

[37] Frederik Böhle, Martin Kretschmar, Aurélie Jullien, Mate Kovacs, Miguel Miranda, Rosa Romero, Helder Crespo, Uwe Morgner, Peter Simon, Rodrigo Lopez-martens, and Tamas Nagy. Compression of CEP-stable multi-mJ laser pulses down to 4 fs in long hollow fibers. *Submitted to Laser Physics Letters*.

[38] C. Li, K. P. M. Rishad, P. Horak, Y. Matsuura, and D. Faccio. Spectral broadening and temporal compression of 100 fs pulses in air-filled hollow core capillary fibers. *Optics Express*, 22(1):1143, 2014.

[39] A. Mysyrowicz, A. Couairon, and U. Keller. Self-compression of optical laser pulses by filamentation. *New Journal of Physics*, 10, 2008.

[40] Stefan Skupin, Gero Stibenz, Luc Bergé, Falk Lederer, Thomas Sokollik, Matthias Schnürer, Nickolai Zhavoronkov, and Günter Steinmeyer. Self-compression by femtosecond pulse filamentation: Experiments versus numerical simulations. *Physical Review E - Statistical, Nonlinear, and Soft Matter Physics*, 74(5):1–9, 2006.

[41] Luis Plaja, Ricardo Torres, and Amelle Zai. *Attosecond Physics*. 2013.

[42] Andreas Vaupel, Nathan Bodnar, Benjamin Webb, Lawrence Shah, and Martin Richardson. Concepts, performance review, and prospects of table-top, few-cycle optical parametric chirped-pulse amplification. *Optical Engineering*, 53(5):051507, 2013.

[43] C. Vozzi, G. Cirmi, C. Manzoni, E. Benedetti, F. Calegari, G. Sansone, S. Stagira, O. Svelto, S. De Silvestri, M. Nisoli, and G. Cerullo. High-energy, few-optical-cycle pulses at 1.5 m with passive carrier-envelope phase stabilization. *Optics Express*, 14(21):10109, 2006.

[44] Rimantas Budrinas, Tomas Stanislauskas, Jonas Adamonis, Aidas Aleknavičius, Gediminas Veitas, Darius Gadonas, Stanislovas Balickas, Andrejus Michailovas, and Arnas Varanavičius. 53 W average power CEP-stabilized OPCPA system delivering 55 TW few cycle pulses at 1 kHz repetition rate. *Optics Express*, 25(5):5797, 2017.

[45] Shunsuke Adachi, Nobuhisa Ishii, Yohei Kobayashi, Yutaka Nomura, Jiro Itatani, Teruto Kanai, and Shuntaro Watanabe. Carrier-envelope phase control of few-cycle parametric chirped-pulse amplifier. *Japanese Journal of Applied Physics*, 49(3R):032703, 2010.

[46] O. V. Chekhlov Y. Tang, A. Lyachev, C. Hernandez-Gomez, I. Musgrave, I. N. Ross and J. L. Collier. High performance Ti:Sa amplifier for 10PW front-end system. *Laser Science and Development*, pages 2008–2010, 2009.

[47] J. P. Zou, C. Le Blanc, D. N. Papadopoulos, G. Chériaux, P. Georges, G. Mennerat, F. Druon, L. Lecherbourg, A. Pellegrina, P. Ramirez, F. Giambruno, A. Fréneaux, F. Leconte, D. Badarau, J. M. Boudenne, D. Fournet, T. Valloton, J. L. Paillard, J. L. Veray, M. Pina, P. Monot, J. P. Chambaret, P. Martin, F. Mathieu, P. Audebert, and F. Amiranoff. Design and current progress of the Apollon 10 PW project. *High Power Laser Science and Engineering*, 3:1–4, 2015.

[48] D. J. Richardson, J. Nilsson, and W. A. Clarkson. High power fiber lasers: current status and future perspectives [Invited]. *Journal of the Optical Society of America B*, 27(11):B63, 2010.

[49] Michalis N. Zervas and Christophe A. Codemard. High Power Fiber Lasers: A Review. *IEEE Journal of Selected Topics in Quantum Electronics*, 20(5):219–241, 2014.

[50] L. Lavenu, M. Natile, F. Guichard, Y. Zaouter, X. Delen, M. Hanna, E. Mottay, and P. Georges. Nonlinear pulse compression in a gas-filled multipass cell. *Optics Letters*, 43(10):2252, 2018.

[51] Thomas Deutsch. Mode-locking effects in an internally modulated ruby laser. *Applied Physics Letters*, 7(4):80–82, 1965.

[52] A. Schmackpfeffer and H. Weber. Mode-locking and mode competition by saturable absorber in a ruby-laser. *Physics Letters*, 24(3):190–191, 1967.

[53] Fritz P. Schäfer, Werner Schmidt, and Jürgen Volze. Organic dye solution laser. *Applied Physics Letters*, 9(8):306–309, 1966.

[54] M D Perry, O L Landen, J Weston, and R Ettlebrick. Design and performance of a high-power, synchronized Nd:YAG-dye laser system. *Optics letters*, 14(1):42–4, 1989.

[55] P. Maine, D. Strickland, P. Bado, M. Pessot, and G. Mourou. Generation of Ultrahigh Peak Power Pulses by Chirped Pulse Amplification. *IEEE Journal of Quantum Electronics*, 24(2):398–403, 1988.

[56] Oscar Eduardo Martinez. 3000 times grating compressor with positive group velocity dispersion: Application to fiber compensation in 1.3-1.6 m region. *IEEE Journal of Quantum Electronics*, 23(1):59–64, 1987.

[57] E. B. Treacy. Optical Pulse Compression With Diffraction Gratings. *IEEE Journal of Quantum Electronics*, 5(9):454–458, 1969.

[58] G. Cheriaux, Barry Walker, L. F. Dimauro, P. Rousseau, F. Salin, and J. P. Chambaret. Aberration-free stretcher design for ultrashort-pulse amplification. *Optics Letters*, 21(6):414, 1996.

[59] B E Lemoff and C P Barty. Quintic-phase-limited, spatially uniform expansion and recompression of ultrashort optical pulses. *Optics letters*, 18(19):1651–1653, 1993.

[60] C P J Barty, C L Gordon III, and B E Lemoff. Multiterawatt 30-fs Ti : sapphire laser system. *Optics letters*, 19(18):1442–1444, 1994.

[61] Gerard A. Mourou, Toshiki Tajima, and Sergei V. Bulanov. Optics in the relativistic regime. *Reviews of Modern Physics*, 78(2), 2006.

[62] A. Ricci, Aurélie Jullien, Nicolas Forget, Vincent Crozatier, Pierre Tournois, and R. Lopez-Martens. Grism compressor for carrier-envelope phase-stable millijoule-energy chirped pulse amplifier lasers featuring bulk material stretcher. *Optics Letters*, 37(7):1196, 2012.

[63] J Squier, C P Barty, F O Salin, C Le Blanc, and S Kane. Use of mismatched grating pairs in chirped-pulse amplification systems. *Applied optics*, 37(9):1638–1641, 1998.

[64] V. Bagnoud and F. Salin. Global optimization of pulse compression in chirped pulse amplification. *IEEE Journal of Selected Topics in Quantum Electronics*, 4(2):445–448, 1998.

[65] S. Kane and J. Squier. Fourth-order-dispersion limitations of aberration-free chirped-pulse amplification systems. *Journal of the Optical Society of America B*, 14(5):1237, 1997.

[66] Lee M. Frantz and John S. Nodvik. Theory of pulse propagation in a laser amplifier. *Journal of Applied Physics*, 34(8):2346–2349, 1963.

[67] W. H. Lowdermilk and J. E. Murray. The multipass amplifier: Theory and numerical analysis. *Journal of Applied Physics*, 51(5):2436–2444, 1980.

[68] P. F. Moulton. Spectroscopic and laser characteristics of Ti:Al_2O_3. *Journal of the Optical Society of America B*, 3(1):125, 1986.

[69] R E Fahey, A J Strauss, A Sanchez, and R L Aggarwal. Growth of Laser-Quality Ti:Al_2O_3 Crystals by a Seeded Gradient-Freeze Technique. *Tunable Solide-State Laser II*, pages 82–88, 1986.

[70] A. Abragam and B. Bleany. Electron paramagnetic resonance of transitionions Ions. 11:1992, 1970.

[71] Wall K. F. A. and Sanchez. Titanium sapphire laser. *The Lincoln Laboratory Journal*, 3(3):447–461, 1993.

[72] J P Chambaret, C Le Blanc, G Chériaux, P Curley, G Darpentigny, P Rousseau, G Hamoniaux, A Antonetti, and F Salin. Generation of 25-TW, 32-fs pulses at 10 Hz. *Optics Letters*, 21(23):1921, 1996.

[73] K. Yamakawa, M. Aoyama, S. Matsuoka, T. Kase, Y. Akahane, and H. Takuma. 100-TW sub-20-fs Ti:sapphire laser system operating at a 10-Hz repetition rate. *Optics Letters*, 23(18):1468, 1998.

[74] W Sandner, M P Kalachnikov, P V Nickles, and H Sch. On the way to 100 TW 10 Hz titanium sapphire laser facilities. 472:254–259, 2001.

[75] Alexandre Trisorio, Pierre M. Paul, Fabien Ple, Clemens Ruchert, Carlo Vicario, and Christoph P. Hauri. Ultrabroadband TW-class Ti:sapphire laser system with adjustable central wavelength, bandwidth and multi-color operation. *Optics Express*, 19(21):20128, 2011.

[76] C. P. J. Barty, G. Korn, F Raksi, A.-C. Tien, K R Wilson, V V Yakovlev, C Rose-Petruck, J Squier, and K Yamakawa. Regenerative pulse shaping and amplification of ultrabroadband optical pulses. *Optics Letters*, 21(3):219, 1996.

[77] Samuel Bohman, Akira Suda, Tsuneto Kanai, Shigeru Yamaguchi, and Katsumi Midorikawa. Generation of 50 fs, 50 mJ pulses at 1kHz using hollow-fiber pulse compression. *Optics Letters*, 35(11):1887, 2010.

[78] Stibenz G Et Al. Self compression of millijoule pulses to 7.8fs duration in a white-light filament. *Opt. Lett*, 31(274):274–276, 2006.

[79] C. P. Hauri, W. Kornelis, F. W. Helbing, A. Heinrich, A. Couairon, A. Mysyrowicz, J. Biegert, and U. Keller. Generation of intense, carrier-envelope phase-locked few-cycle laser pulses through filamentation. *Applied Physics B: Lasers and Optics*, 79(6):673–677, 2004.

[80] D Busto, L Barreau, M Isinger, M Turconi, and C Alexandridi. Time frequency representation of autoionization dynamics in helium. *Journal of Physics B*, 51, 2018.

[81] Alexander Zholents. Next-generation x-ray free-electron lasers. *IEEE Journal on Selected Topics in Quantum Electronics*, 18(1):248–257, 2012.

[82] M. Sabbar, S. Heuser, R. Boge, M. Lucchini, L. Gallmann, C. Cirelli, and U. Keller. Combining attosecond XUV pulses with coincidence spectroscopy. *Review of Scientific Instruments*, 85(10):1–7, 2014.

[83] Charles G. Durfee, Sterling Backus, Margaret M. Murnane, and Henry C. Kapteyn. Design and implementation of a TW-class high-average power laser system. *IEEE Journal on Selected Topics in Quantum Electronics*, 4(2):395–405, 1998.

[84] Jochen Speiser. Scaling of thin-disk lasersinfluence of amplified spontaneous emission. *Journal of the Optical Society of America B*, 26(1):26, 2009.

[85] Vladimir Chvykov, Huabao Cao, Roland Nagymihaly, Mikhail P. Kalashnikov, Nikita Khodakovskiy, Richard Glassock, Lutz Ehrentraut, Matthias Schnuerer, and Károly Osvay. High peak and average power Ti:sapphire thin disk amplifier with extraction during pumping. *Optics Letters*, 41(13):3017, 2016.

[86] V. Chvykov, R. Nagymihaly, H. Cao, M. Kalashnikov, and K. Osvay. High peak power and repetition rate laser systems with thin disk Ti: Sa amplifiers. *Frontiers in Optics 2017, OSA technical digest*, LW5F.2.:3–4, 2017.

[87] Anne-Laure Calendron, Hüseyin Çankaya, and Franz X. Kärtner. High-energy kHz Yb:KYW dual-crystal regenerative amplifier. *Optics Express*, 22(20):24752, 2014.

[88] A. Jaffrès, S. Ricaud, A. Suganuma, B. Viana, P. Loiseau, P. Georges, and F. Druon. Yb :CALGO as material for high power ultrafast laser and focus on thermal conductivity variation. *Proc. SPIE 8621, Optical Components and Materials X*, page 86211S, 2013.

[89] Alexander Büttner, Udo Bünting, Dieter Wandt, Uwe Morgner, Dietmar Kracht, and Jörg Neumann. Ultrafast double-slab regenerative amplifier with combined gain spectra. *CLEO/Europe - EQEC 2009 - European Conference on Lasers and Electro-Optics and the European Quantum Electronics Conference*, 18(21):21973–21980, 2009.

[90] Orazio Svelto. *Principles of lasers*. 2010.

[91] J. M. Eggleston. Periodic resonators for average-power scaling of stable-resonator solid-state lasers. *IEEE Journal of Quantum Electronics*, 24(9):1821–1824, Sep. 1988.

[92] Patterson F.G. and M.D. Perry. Design and performance of a multiterawatt , subpicosecond neodymium : glass laser. *Ieee Journal of Quantum Electronics*, 8(11):2384–2391, 1991.

[93] Jeff Squier, Scott Coe, G M, and Don Harter. An alexandrite pumped Nd : glass regenerative amplifier for chirped pulse amplification. *Optics Communications*, 92:73–78, 1992.

[94] I P Christov. Amplification of femtosecond pulses in a spatially dispersive scheme. *Optics letters*, 17(10):742–4, 1992.

[95] M. B. Danailov and I. P. Christov. A novel method of ultrabroadband laser generation. *Optics Communications*, 73(3):235–238, 1989.

[96] C. P. Hauri, M. Bruck, W. Kornelis, J. Biegert, and U. Keller. Generation of 148-fs pulses in a spatially dispersed amplifier. *Optics Letters*, 29(2):201, 2004.

[97] A. M. Weiner, D. E. Leaird, J. S. Patel, and J. R. Wullert. Programmable femtosecond pulse shaping by use of a multielement liquid-crystal phase modulator. *Optics Letters*, 15(6):326, 1990.

[98] F. Verluise, V. Laude, Z. Cheng, Ch. Spielmann, and P. Tournois. Amplitude and phase control of ultrashort pulses by use of an acousto-optic programmable dispersive filter:pulse compression and shaping. *Optics Letters*, 25(8):575, 2000.

[99] Thomas Oksenhendler, P. Rousseau, R. Herzog, O. Gobert, M. Perdrix, and P. Meynadier. 20hz femtosecond laser amplifier optimization using an aopdf pulse shaper and a spider. In *Conference on Lasers and Electro-Optics/Quantum Electronics and Laser Science Conference*, page CWE1. Optical Society of America, 2003.

[100] N. Minkovski, G. I. Petrov, S. M. Saltiel, O. Albert, and J. Etchepare. Nonlinear polarization rotation and orthogonal polarization generation experienced in a single-beam configuration. *Journal of the Optical Society of America B*, 21(9):1659, 2004.

[101] Aurélie Jullien, Olivier Albert, Gilles Chériaux, Jean Etchepare, Stoyan Kourtev, Nikolay Minkovski, and Solomon M. Saltiel. Nonlinear polarization rotation of elliptical light in cubic crystals, with application to cross-polarized wave generation. *Journal of the Optical Society of America B*, 22(12):2635, 2005.

[102] L. Canova, O. Albert, N. Forget, B. Mercier, S. Kourtev, N. Minkovski, S. M. Saltiel, and R. Lopez Martens. Influence of spectral phase on cross-polarized wave generation with short femtosecond pulses. *Applied Physics B: Lasers and Optics*, 93(2-3):443–453, 2008.

[103] D. Kaplan and P. Tournois. Theory and performance of the acousto optic programmable dispersive filter used for femtosecond laser pulse shaping. *Journal de Physique IV (Proceedings)*, 12(5):69–75, 2002.

[104] M. Kotur, D. Guénot, Jiménez-Galán, D. Kroon, E. W. Larsen, M. Louisy, S. Bengtsson, M. Miranda, J. Mauritsson, C. L. Arnold, S. E. Canton, M. Gisselbrecht, T. Carette, J. M. Dahlström, E. Lindroth, A. Maquet, L. Argenti, F. Martín, and A. L'Huillier. Spectral phase measurement of a Fano resonance using tunable attosecond pulses. *Nature Communications*, 7:1–6, 2016.

[105] B. Shan, A. Cavalieri, and Z. Chang. Tunable high harmonic generation with an optical parametric amplifier. *Applied Physics B: Lasers and Optics*, 74(SUPPL.):23–26, 2002.

[106] François Salin, Catherine Le Blanc, Jeff Squier, and Chris Barty. Thermal eigenmode amplifiers for diffraction-limited amplification of ultrashort pulses. *Optics Letters*, 23(9):718720, 1998.

[107] A. Golinelli X. Chen B. Bussire E. Gontier P.-M. Paul O. Tcherbakoff P. dOliveira J.-F. Hergott. Cep-stabilized, sub-18 fs, 10 khz and tw-class 1 khz dual output ti: Sa laser with wavelength tunability option. *Opt. Expr. in preparation*, 2019.

[108] S. Ito, H. Nagaoka, T. Miura, K. Kobayashi, A. Endo, and K. Torizuka. Measurement of thermal lensing in a power amplifier of a terawatt Ti: sapphire laser. *Applied Physics B: Lasers and Optics*, 74(4-5):343–347, 2002.

[109] Sandro D E Silvestri Paolo and Vittorio Magni. Pump Power Stability Range of single-Mode Solid-State Laser with Rod Thermal Lensing. *IEEE Journal of Quantum Electronics*, (11):3–8, 1999.

[110] Peter A Schulz and Scott R Henion. Liquid-Nitrogen-Cooled Ti : A12 O3 Laser. *IEEE Journal of Quantum Electronics*, 21(4):1039–1047, 1991.

[111] J Frauchiger, Peter Albers, and Heinz P Weber. Modeling of Thermal Lensing and Higher Order Ring Mode Oscillation in End-Pumped CW Nd Lasers. *IEEE Journal of Quantum Electronics*, 28(4), 1992.

[112] S J Sheldon, L V Knight, and J M Thorne. Laser-induced thermal lens effect: a new theoretical model. *Applied Optics*, 21(9):1663, 1982.

[113] U O Farrukh and P Brockman. Temperature distribution in side- and end-pumped laser crystal rods: temporal and spatial variations. *Applied optics*, 32(12):2075–81, 1993.

[114] M. E. Innocenzi, H. T. Yura, C. L. Fincher, and R. A. Fields. Thermal modeling of continuous-wave end-pumped solid-state lasers. *Applied Physics Letters*, 56(19):1831–1833, 1990.

[115] Christine A Carter and Joel M Harris. Comparison of models describing the thermal lens effect. *Appl. Opt.*, 23(3):476–481, 1984.

[116] Jun Shen, Roger D. Lowe, and Richard D. Snook. A model for cw laser induced mode-mismatched dual-beam thermal lens spectrometry. *Chemical Physics*, 165(2-3):385–396, 1992.

[117] F Jürgensen and W Schröer. Studies on the diffraction image of a thermal lens. *Applied optics*, 34(1):41–50, 1995.

[118] David C. Brown. Heat, fluorescence, and stimulated-emission power densities and fractions in Nd:YAG. *IEEE Journal of Quantum Electronics*, 34(3):560–571, 1998.

[119] Sterling Backus, Charles G. Durfee, Gerard Mourou, Henry C. Kapteyn, and Margaret M. Murnane. 02-TW laser system at 1kHz. *Optics Letters*, 22(16):1256, 1997.

[120] S. Chénais, F. Druon, F. Balembois, G. Lucas-Leclin, Y. Fichot, P. Georges, R. Gaumé, B. Viana, G. P. Aka, and D. Vivien. Thermal lensing measurements in diode-pumped Yb-doped GdCOB, YCOB, YSO, YAG and KGW. *Optical Materials*, 22(2):129–137, 2003.

[121] P. Albers, E. Stark, and G. Huber. Continuous-wave laser operation and quantum efficiency of titanium-doped sapphire. *Journal of the Optical Society of America B*, 3(1):134, 1986.

[122] T. Danger, K. Petermann, and G. Huber. Polarized and time-resolved measurements of excited-state absorption and stimulated emission in Ti:YAlO3 and Ti:Al2O3. *Applied Physics A Solids and Surfaces*, 57(4):309–313, 1993.

[123] T Wegner and K Petermann. Excited State Absorption of Ti 3 + YAIO3 *. *Applied Physics B*, 49(1989):275–278, 1989.

[124] Usamah O. Farrukh, A. Martin Buoncristiani, and Charles E. Byvik. An Analysis of the Temperature Distribution in Finite Solidstate Laser Rods. *IEEE Journal of Quantum Electronics*, 24(11):2253–2263, 1988.

[125] Sabrina Velghe, Jérôme Primot, Nicolas Guérineau, Riad Haïdar, Sébastien Demoustier, Mathieu Cohen, and Benoît Wattellier. Advanced wave-front sensing by quadri-wave lateral shearing interferometry. *Proceeding of SPIE*, 6292:62920E–1, 2006.

[126] Sébastien Chénais, Frédéric Druon, Sébastien Forget, François Balembois, and Patrick Georges. On thermal effects in solid-state lasers: The case of ytterbium-doped materials. *Progress in Quantum Electronics*, 30(4):89–153, 2006.

[127] Justin L. Blows, Judith M. Dawes, and Takashige Omatsu. Thermal lensing measurements in line-focus end-pumped neodymium yttrium aluminium garnet using holographic lateral shearing interferometry. *Journal of Applied Physics*, 83(6):2901–2906, 1998.

[128] J. L. Blows, P. Dekker, P. Wang, J. M. Dawes, and T. Omatsu. Thermal lensing measurements and thermal conductivity of Yb:YAB. *Applied Physics B: Lasers and Optics*, 76(3):289–292, 2003.

[129] J. Primot and L. Sogno. Achromatic three-wave (or more) lateral shearing interferometer. *J. Opt. Soc. Am A*, 12(12), 1995.

[130] J C Chanteloup, F Druon, M Nantel, a Maksimchuk, and G Mourou. Single-shot wave-front measurements of high-intensity ultrashort laser pulses with a three-wave interferometer. *Optics letters*, 23(8):621–623, 1998.

[131] Jérôme Primot. Three-wave lateral shearing interferometer. *Applied optics*, 32(31):6242–9, 1993.

[132] Pierre Bon, Guillaume Maucort, Benoit Wattellier, and Serge Monneret. Quadriwave lateral shearing interferometry for quantitative phase microscopy of living cells. *Optics Express*, 17(15):13080, 2009.

[133] J.-C. Chanteloup. Multiple-wave lateral shearing interferometry for wave-front sensing. *Applied Optics*, 44(9):1559, 2005.

[134] Soazic Mousset, Claude Rouyer, Gabrielle Marre, Nathalie Blanchot, Sébastien Montant, and Benoit Wattellier. Piston measurement by quadriwave lateral shearing interferometry. *Optics Letters*, 31(17):2634, 2006.

[135] Rick Trebino, Kenneth W Delong, David N Fittinghoff, John N Sweetser, Bruce A Richman, Marco A Krumbu, and Daniel J Kane. Measuring ultrashort laser pulses in the time-frequency domain using frequency-resolved optical gating. 68(9):3277–3295, 1997.

[136] C. Iaconis and I. A. Walmsley. Spectral phase interferometry for direct electric-field reconstruction of ultrashort optical pulses. *Optics Letters*, 23(10):792, 1998.

[137] Guan Xinan, M. Lambsdorff, J. Kuhl, and Wu Biachang. Fast-scanning autocorrelator with 1-ns scanning range for characterization of mode-locked ion lasers. *Review of Scientific Instruments*, 59(9):2088–2090, 1988.

[138] Kenneth L Sala, Geraldine A Kenney-wallace, and Gregory E Hall. CW Autocorrelation Measurements of picosecond Laser Pulses. *IEEE Journal of Quantum Electronics*, 2(9):990–996, 1980.

[139] A. Gutierrez, P. Dorn, J. Zeller, D. King, L. F. Lester, W. Rudolph, and M. Sheik-Bahae. Autocorrelation measurement of femtosecond laser pulses by use of a ZnSe two-photon detector array. *Optics Letters*, 24(16):1175, 1999.

[140] Maïté Louisy, Chen Guo, Lana Neoričić, Shiyang Zhong, Anne L'Huillier, Cord L. Arnold, and Miguel Miranda. Compact single-shot d-scan setup for the characterization of few-cycle laser pulses. *Applied Optics*, 56(32):9084, 2017.

[141] G.Steinmeyer, D.H.Sutter, L.Gallmann, N.Matuschek, and U.Keller. Frontiers in Ultrashort Pulse Generation: Pushing the Limits in Linear and Nonlinear Optics. *Science*, 286:1507, 1999.

[142] Wolfgang Schweinberger, Annkatrin Sommer, Elisabeth Bothschafter, Jiang Li, Ferenc Krausz, Reinhard Kienberger, and Martin Schultze. Waveform-controlled near-single-cycle milli-joule laser pulses generate sub-10 nm extreme ultraviolet continua. *Optics Letters*, 37(17):3573, 2012.

[143] P. Dombi, A. Apolonski, Ch L. Emell, G. G. Paulus, M. Kakehata, R. Holzwarth, Th Udem, K. Torizuka, J. Burgdörfer, T. W. Hänsch, and F. Krausz. Direct measurement and analysis of the carrier-envelope phase in light pulses approaching the single-cycle regime. *New Journal of Physics*, 6, 2004.

[144] Frederik Böhle, Martin Kretschmar, Aurélie Jullien, Mate Kovacs, Miguel Miranda, Rosa Romero, Helder Crespo, Uwe Morgner, Peter Simon, Rodrigo Lopez-Martens, and Tamas Nagy. Compression of CEP-stable multi-mJ laser pulses down to 4 fs in long hollow fibers. *Laser Physics Letters*, 11(9), 2014.

[145] L. Xu, T. W. Hänsch, Ch. Spielmann, A. Poppe, T. Brabec, and F. Krausz. Route to phase control of ultrashort light pulses. *Optics Letters*, 21(24):2008, 1996.

[146] H.R. Telle et al. Carrier-envelope offset phase control: A novel concept for absolute optical frequency measurement and ultrashort pulse generation. *Applied Physics B*, 69:327–332, 1999.

[147] A. Apolonski, A. Poppe, G. Tempea, Ch Spielmann, Th Udem, R. Holzwarth, T. W. Hänsch, and F. Krausz. Controlling the phase evolution of few-cycle light pulses. *Physical Review Letters*, 85(4):740–743, 2000.

[148] David J Jones, Scott A Diddams, Jinendra K Ranka, Andrew Stentz, Robert S Windeler, John L Hall, and Steven T Cundiff. Carrier-Envelope Phase Control of Femtosecond Mode-Locked Lasers and Direct Optical Frequency Synthesis Carrier-Envelope Phase Control of Femtosecond Mode-Locked Lasers and Direct Optical Frequency Synthesis. *Science*, 288(5466):635–639, 2000.

[149] Chengquan Li, Eric Moon, and Zenghu Chang. Carrier-envelope phase shift caused by variation of grating separation. *Optics Letters*, 31(21):3113, 2006.

[150] G. Sansone, E. Benedetti, F. Calegari, C. Vozzi, L. Avaldi, R. Flammini, L. Poletto, P Villoresi, C Altucci, R Velotta, S Stagira, S De Silvestri, and M Nisoli. Isolated Single-Cycle Attosecond Pulses. *Science*, 314:443–447, 2006.

[151] Michael Chini, Kun Zhao, and Zenghu Chang. The generation, characterization and applications of broadband isolated attosecond pulses. *Nature Photonics*, 8(3):178–186, 2014.

[152] Bin Zeng, Yongli Yu, Wei Chu, Jinping Yao, Yuxi Fu, Hui Xiong, Han Xu, Ya Cheng, and Zhizhan Xu. Generation of an intense single isolated attosecond pulse by use of two-colour waveform control. *Journal of Physics B: Atomic, Molecular and Optical Physics*, 42(14), 2009.

[153] R. Holzwarth, Th Udem, T. W. Hänsch, J. C. Knight, W. J. Wadsworth, and P. St J. Russell. Optical frequency synthesizer for precision spectroscopy. *Physical Review Letters*, 85(11):2264–2267, 2000.

[154] Steven T Cundiff. Phase stabilization of ultrashort optical pulses. *Journal of Applied Physics D*, 43, 2002.

[155] S. Witte, R.T. Zinkstok, W. Hogervorst, and K.S.E. Eikema. Control and precise measurement of carrier-envelope phase dynamics. *Applied Physics B: Lasers and Optics*, 78(1):5–12, 2004.

[156] F. W. Helbing, G. Steinmeyer, J. Stenger, H. R. Telle, and U. Keller. Carrier-envelope-offset dynamics and stabilization of femtosecond pulses. *Applied Physics B: Lasers and Optics*, 74:35–42, 2002.

[157] U. Keller. Ultrafast solid-state laser oscillators: A success story for the last 20 years with no end in sight. *Applied Physics B: Lasers and Optics*, 100(1):15–28, 2010.

[158] Benjamin Eggleton, Charles Kerbage, Paul Westbrook, Robert Windeler, and Arturo Hale. Microstructured optical fiber devices. *Optics Express*, 9(13):698, 2001.

[159] Jinendra K. Ranka, Robert S. Windeler, and Andrew J. Stentz. Visible continuum generation in airsilica microstructure optical fibers with anomalous dispersion at 800 nm. *Optics Letters*, 25(1):25, 2000.

[160] Jinendra K. Ranka, Robert S. Windeler, and Andrew J. Stentz. Optical properties of high-delta airsilica microstructure optical fibers. *Optics Letters*, 25(11):796, 2000.

[161] J. C. Knight, J. Broeng, T. A. Birks, and P. St J. Russell. Photonic band gap guidance in optical fibers. *Science*, 282(5393):1476–1478, 1998.

[162] Takao Fuji, Alexander Apolonski, and Ferenc Krausz. Self-stabilization of carrier-envelope offset phase by use of difference-frequency generation. *Optics Letters*, 29(6):632, 2004.

[163] Marcus Zimmermann, Christoph Gohle, Ronald Holzwarth, Thomas Udem, and Theodor W. Hänsch. Optical clockwork with an offset-free difference-frequency comb:accuracy of sum- and difference-frequency generation. *Optics Letters*, 29(3):310, 2004.

[164] Z. Chang. *Fundamentals of Attosecond Optics*. 2011.

[165] Kenichi Hitachi, Atsushi Ishizawa, Tadashi Nishikawa, Masaki Asobe, and Tetsuomi Sogawa. Carrier-envelope offset locking with a 2f-to-3f self-referencing interferometer using a dual-pitch PPLN ridge waveguide. *Optics Express*, 22(2):1629, 2014.

[166] Sebastian Koke, Christian Grebing, Harald Frei, Alexandria Anderson, Andreas Assion, and Günter Steinmeyer. Direct frequency comb synthesis with arbitrary offset and shot-noise-limited phase noise. *Nature Photonics*, 4(7):462–465, 2010.

[167] Fabian Lücking, Andreas Assion, Alexander Apolonski, Ferenc Krausz, and Günter Steinmeyer. Long-term carrier-envelope-phase-stable few-cycle pulses by use of the feed-forward method. *Optics Letters*, 37(11):2076, 2012.

[168] M. Kakehata, Y. Fujihira, H. Takada, Y. Kobayashi, K. Torizuka, T. Homma, and H. Takahashi. Measurements of carrier-envelope phase changes of 100-Hz amplified laser pulses. *Applied Physics B: Lasers and Optics*, 74:43–50, 2002.

[169] X. Chen, L. Canova, A. Malvache, A. Jullien, R. Lopez-Martens, C. Durfee, D. Papadopoulos, and F. Druon. 1-mJ, sub-5-fs carrier-envelope phase-locked pulses. *Applied Physics B: Lasers and Optics*, 99(1-2):149–157, 2010.

[170] Zenghu Chang. Carrier-envelope phase shift caused by grating-based stretchers and compressors. *Applied Optics*, 45(32):8350, 2006.

[171] Chengquan Li. CARRIER ENVELOPE PHASE STABILIZATION OF AN OPTICAL AMPLIFER. *Patent Apllication Publication, Santa Clara (CA)*, US 2011/0019267 A1, 2011.

[172] Fabian Lücking, Vincent Crozatier, Nicolas Forget, Andreas Assion, and Ferenc Krausz. Approaching the limits of carrier-envelope phase stability in a millijoule-class amplifier. *Optics Letters*, 39(13):3884, 2014.

[173] Andrius Baltuška, Matthias Uiberacker, Eleftherios Goulielmakis, Reinhard Kienberger, Vladislav S. Yakovlev, Thomas Udem, Theodor W. Hänsch, and Ferenc Krausz. Phase-Controlled Amplification of Few-Cycle Laser Pulses. *IEEE Journal on Selected Topics in Quantum Electronics*, 9(4):972–989, 2003.

[174] Fabian Lücking. *Carrier-Envelope Phase Control for the Advancement of Attosecond Pulse Generation*. PhD thesis, 2014.

[175] T. Fordell, M. Miranda, C. L. Arnold, and A. L'Huillier. High-speed carrier-envelope phase drift detection of amplified laser pulses. *Optics Express*, 19(24):23652, 2011.

[176] Sebastian Koke, Christian Grebing, Bastian Manschwetus, and Günter Steinmeyer. Fast f-to-2f interferometer for a direct measurement of the carrier-envelope phase drift of ultrashort amplified laser pulses. *Optics Letters*, 33(21):2545, 2008.

[177] C. Feng, J.-F. Hergott, P.-M. Paul, X. Chen, O. Tcherbakoff, M. Comte, O. Gobert, M. Reduzzi, F. Calegari, C. Manzoni, M. Nisoli, and G. Sansone. Complete analog control of the carrier-envelope-phase of a high-power laser amplifier. *Optics Express*, 21(21):25248, 2013.

[178] M. Nisoli, G. Sansone, S. Stagira, S. De Silvestri, C. Vozzi, M. Pascolini, L. Poletto, P. Villoresi, and G. Tondello. Effects of carrier-envelope phase differences of few-optical-cycle light pulses in single-shot high-order-harmonic spectra. *Physical Review Letters*, 91(21):1–4, 2003.

[179] Giuseppe Sansone, Francesca Calegari, and Mauro Nisoli. Attosecond technology and science. *IEEE Journal on Selected Topics in Quantum Electronics*, 18(1):507–519, 2012.

[180] Masayuki Kakehata, Yohei Kobayashi, Hideyuki Takada, and Kenji Torizuka. Single-shot measurement of a carrier-envelope phase by use of a time-dependent polarization pulse. *Optics Letters*, 27(14):1247, 2002.

[181] P. Dietrich, F. Krausz, and P. B. Corkum. Determining the absolute carrier phase of a few-cycle laser pulse. *Optics Letters*, 25(1):16, 2000.

[182] T. Wittmann, B. Horvath, W. Helml, M. G. Schätzel, X. Gu, A. L. Cavalieri, G. G. Paulus, and R. Kienberger. Single-shot carrier-envelope phase measurement of few-cycle laser pulses. *Nature Physics*, 5(5):357–362, 2009.

[183] Yong Soo Lee, Jae Sung, Chang Nam, Tae Yu, and Kyung-Han Hong. Novel method for carrier-envelope-phase stabilization of femtosecond laser pulses. *Optics Express*, 13(8):2969–2976, 2005.

[184] Kyung Han Hong, Jongmin Lee, Bixue Hou, John A. Nees, Erik Power, and Gerard A. Mourou. Carrier-envelope phase stabilization of high-contrast femtosecond laser pulses with a relativistic intensity. *Applied Physics Letters*, 89(3):3–5, 2006.

[185] Shouyuan Chen, Michael Chini, He Wang, Chenxia Yun, Hiroki Mashiko, Yi Wu, and Zenghu Chang. Carrier-envelope phase stabilization and control of 1 kHz, 6 mJ, 30 fs laser pulses from a Ti:sapphire regenerative amplifier. *Applied Optics*, 48:5692, 2009.

[186] Takao Fuji, Jens Rauschenberger, Alexander Apolonski, Vladislav S. Yakovlev, Gabriel Tempea, Thomas Udem, Christoph Gohle, Theodor W. Hänsch, Walter Lehnert, Michael Scherer, and Ferenc Krausz. Monolithic carrier-envelope phase-stabilization scheme. *Optics Letters*, 30(3):332, 2005.

[187] N. Forget, L. Canova, X. Chen, A. Jullien, and R. Lopez-Martens. Closed-loop carrier-envelope phase stabilization with an acousto-optic programmable dispersive filter. *Optics Letters*, 34(23):3647, 2009.

[188] Lorenzo Canova, Xiaowei Chen, Alexandre Trisorio, Aurélie Jullien, Andreas Assion, Gabriel Tempea, Nicolas Forget, Thomas Oksenhendler, and Rodrigo Lopez-Martens. Carrier-envelope phase stabilization and control using a transmission grating compressor and an AOPDF. *Optics letters*, 34(9):1333–1335, 2009.

[189] O. Gobert, P.M Paul, J.F Hergott, O. Tcherbakoff, F. Lepetit, P. D 'Oliveira, F. Viala, and M. Comte. Carrier-envelope phase control using linear electro-optic effect. *Optics Express*, 19(6):5410, 2011.

[190] J.-F. Hergott, O. Tcherbakoff, P.-M. Paul, Ph. Demengeot, M. Perdrix, F. Lepetit, D. Garzella, D. Guillaumet, M. Comte, P. D' Oliveira, and O. Gobert. Carrier-Envelope Phase stabilization of a 20 W, grating based, chirped-pulse amplified laser, using Electro-Optic effect in a LiNbO_3 crystal. *Optics Express*, 19(21):19935, 2011.

[191] T Fordell, M Miranda, A Persson, and A L'Huillier. Carrier-envelope phase stabilization of a multi-millijoule, regenerative-amplifier-based chirped-pulse amplifier system. *Optics Express*, 17(23):21091, 2009.

[192] Etienne Gagnon, Isabell Thomann, Ariel Paul, Amy L Lytle, Sterling Backus, Margaret M Murnane, Henry C Kapteyn, and Arvinder S Sandhu. Long-term carrier-envelope phase stability from a grating-based, chirped pulse amplifier. *Optics letters*, 31(12):1866–1868, 2006.

[193] Kyung Han Hong, Jongmin Lee, Bixue Hou, John A. Nees, Erik Power, and Gerard A. Mourou. Carrier-envelope phase stabilization of high-contrast femtosecond laser pulses with a relativistic intensity. *Applied Physics Letters*, 89(3):3–5, 2006.

[194] Hiroki Mashiko, Christopher M. Nakamura, Chengquan Li, Eric Moon, He Wang, Jason Tackett, and Zenghu Chang. Carrier-envelope phase stabilized 5.6 fs, 1.2 mJ pulses. *Conference on Lasers and Electro-Optics, 2007, CLEO 2007*, 121109(2010):1–4, 2007.

[195] Georg Gademann, Fabien Plé, Pierre-Mary Paul, and Marc J.J. Vrakking. Carrier-envelope phase stabilization of a terawatt level chirped pulse amplifier for generation of intense isolated attosecond pulses. *Optics Express*, 19(25):24922, 2011.

[196] E. Cunningham, Y. Wu, and Zenghu Chang. Carrier-envelope phase control of a 10 Hz, 25 TW laser for high-flux extreme ultraviolet quasi-continuum generation. *Applied Physics Letters*, 107(20):2013–2016, 2015.

[197] Benjamin Langdon, Jonathan Garlick, Xiaoming Ren, Derrek J. Wilson, Adam M. Summers, Stefan Zigo, Matthias F. Kling, Shuting Lei, Christopher G. Elles, Eric Wells, Erwin D. Poliakoff, Kevin D. Carnes, Vinod Kumarappan, Itzik Ben-Itzhak, and Carlos A. Trallero-Herrero. Carrier-envelope-phase stabilized terawatt class laser at 1 kHz with a wavelength tunable option. *Optics Express*, 23(4):4563, 2015.

[198] A. Golinelli, X. Chen, B. Bussière, E. Gontier, P-M. Paul, O. Tcherbakoff, P. D'Oliveira, and J-F. Hergott. CEP-Stabilized, sub-18 fs, 10 kHz and TW-Class 1 kHz Dual Output Ti: Sa Laser with Wavelength Tunability Option (in preparation), 2018.

[199] A. Golinelli, X. Chen, E. Gontier, B. Bussière, O. Tcherbakoff, M. Natile, P. D'Oliveira, P.-M. Paul, and J.-F. Hergott. Original Ti:Sa 10kHz front-end design delivering 17fs, 170mrad CEP stabilized pulses up to 5W. *Optics Letters*, 42(12):2326, 2017.

[200] Matteo Negro, Martino Quintavalla, Jacopo Mocci, Anna G. Ciriolo, Michele Devetta, Riccardo Muradore, Salvatore Stagira, Caterina Vozzi, and Stefano Bonora. Fast stabilization of a high-energy ultrafast OPA with adaptive lenses. *Scientific Reports*, 8(1):4–9, 2018.

[201] Shunsuke Adachi, Nobuhisa Ishii, Yohei Kobayashi, Yutaka Nomura, Jiro Itatani, Teruto Kanai, and Shuntaro Watanabe. Carrier-envelope phase control of few-cycle parametric chirped-pulse amplifier. *Japanese Journal of Applied Physics*, 49(3 PART 1):4–7, 2010.

[202] N. Thiré, R. Maksimenka, B. Kiss, F. Clément, P. Bizouard, E. Cormier, K. Osvay, and N. Forget. 4-W, 100-kHz, few-cycle mid-infrared source with sub-100-mrad carrier-envelope phase noise. *Optics Express*, 25(2):1505–1514, 2017.

[203] Isabell Thomann, Etienne Gagnon, R. Jason Jones, Arvinder S. Sandhu, Amy Lytle, Ryan Anderson, Jun Ye, Margaret Murnane, and Henry Kapteyn. Investigation of a grating-based stretcher/compressor for carrier-envelope phase stabilized fs pulses. *Optics Express*, 12(15):3493, 2004.

[204] M. Kakehata, Y. Fujihira, H. Takada, Y. Kobayashi, K. Torizuka, T. Homma, and H. Takahashi. Measurements of carrier-envelope phase changes of 100-Hz amplified laser pulses. *Applied Physics B: Lasers and Optics*, 74:43–50, 2002.

[205] R. L. Fork, C. H. Brito Cruz, P. C. Becker, and C. V. Shank. Compression of optical pulses to six femtoseconds by using cubic phase compensation. *Optics Letters*, 12(7):483, 1987.

[206] C H Brito Cruz, P C Becker, R L Fork, and C V Shank. Phase correction of femtosecond optical pulses using a combination of prisms and gratings. *Optics Letters*, 13(2):123, 1988.

[207] Donald C O'Shea. Group velocity dispersion using commercial optical design programs. *Applied optics*, 45(19):4740–6, 2006.

[208] M Ferray, A L'Huillier, X F Li, L A Lomprk, G Mainfray, and C Manus. Multiple-harmonic conversion of 1064 nm radiationin rare gases. *Journal of Physics B: Atomic, Molecular and Optical Physics*, 21:31–35, 1988.

[209] Yuxi Chu, Xiaoyan Liang, Lianghong Yu, Yi Xu, Lu Xu, Lin Ma, Xiaoming Lu, Yanqi Liu, Yuxin Leng, Ruxin Li, and Zhizhan Xu. High-contrast 2.0 petawatt ti:sapphire laser system. *Opt. Express*, 21(24):29231–29239, Dec 2013.

[210] Tae Jun Yu, Seong Ku Lee, Jae Hee Sung, Jin Woo Yoon, Tae Moon Jeong, and Jongmin Lee. Generation of high-contrast, 30 fs, 1.5 pw laser pulses from chirped-pulse amplification ti:sapphire laser. *Opt. Express*, 20(10):10807–10815, May 2012.

[211] Jae Hee Sung, Seong Ku Lee, Tae Jun Yu, Tae Moon Jeong, and Jongmin Lee. 0.1 hz 1.0 pw ti:sapphire laser. *Opt. Lett.*, 35(18):3021–3023, Sep 2010.

[212] Sergei Khn, Mathieu Dumergue, Subhendu Kahaly, Sudipta Mondal, Mikls Fle, Tams Csizmadia, Balzs Farkas, Balzs Major, Zoltn Vrallyay, Eric Cormier, Mikhail Kalashnikov, Francesca Calegari, Michele Devetta, Fabio Frassetto, Erik Mnsson, Luca Poletto, Salvatore Stagira, Caterina Vozzi, Mauro Nisoli, Piotr Rudawski, Sylvain Maclot, Filippo Campi, Hampus Wikmark, Cord L Arnold, Christoph M Heyl, Per Johnsson, Anne LHuillier, Rodrigo Lopez-Martens, Stefan Haessler, Mamona Bocoum, Frederik Boehle, Aline Vernier, Gregory Iaquaniello, Emmanuel Skantzakis, Nikos Papadakis, Constantinos Kalpouzos, Paraskevas Tzallas, Franck Lpine, Dimitris Charalambidis, Katalin Varj, Kroly Osvay, and Giuseppe Sansone. The eli-alps facility: the next generation of attosecond sources. *Journal of Physics B: Atomic, Molecular and Optical Physics*, 50(13):132002, 2017.

[213] Yuan Han Peng, Yu Xian Lim, James Cheng, Yipei Guo, Yan Ying Cheah, and Kin Seng Lai. Near fundamental mode 11 kW Yb:YAG thin-disk laser. *Optics Letters*, 38(10):1709, 2013.

[214] Clara J. Saraceno, Florian Emaury, Cinia Schriber, Martin Hoffmann, Matthias Golling, Thomas Südmeyer, and Ursula Keller. Ultrafast thin-disk laser with 80μJ pulse energy and 242W of average power. *Optics Letters*, 39(1):9, 2014.

[215] Vladimir Chvykov, Huabao Cao, Roland Nagymihaly, Mikhail P. Kalashnikov, Nikita Khodakovskiy, Richard Glassock, Lutz Ehrentraut, Matthias Schnuerer, and Károly Osvay. High peak and average power Ti:sapphire thin disk amplifier with extraction during pumping. *Optics Letters*, 41(13):3017, 2016.

[216] R. S. Nagymihaly, H. Cao, D. Papp, G. Hajas, M. Kalashnikov, K. Osvay, and V. Chvykov. Liquid-cooled Ti:Sapphire thin disk amplifiers for high average power 100-TW systems. *Optics Express*, 25(6):6664, 2017.

[217] G. Sansone, C. Vozzi, S. Stagira, M. Pascolini, L. Poletto, P. Villoresi, G. Tondello, S. De Silvestri, and M. Nisoli. Observation of Carrier-Envelope Phase Phenomena in the Multi-Optical-Cycle Regime. *Physical Review Letters*, 92(11):1–4, 2004.

université PARIS-SACLAY | ÉCOLE DOCTORALE Ondes et Matière (EDOM)

Titre : Développement d'une nouvelle configuration de cavité régénérative à 10 kHz, permettant l'amplification à 1 kHz d'impulsions de durée 17 fs, stabilisées en CEP dans la classe TW ou accordables en longueur d'onde à 10 ou 1 kHz.

Mots clés : Laser ultra-rapide, stabilisation de la CEP, accordabilité spectrale, courte durée d'impulsion

Résumé: Au cours de dix dernières années la science aux attoseconde ou Physique au champ-fort a été l'objet d'un fort développement. La production d'impulsions laser énergétiques de courte durée à haute cadence et stabilisées en CEP constitue la première étape pour accéder aux dynamiques ultra-rapides caractérisant l'interaction de la matière avec une source de lumière cohérente, intense et ultra-rapide. Le travail de cette thèse consiste à améliorer globalement les performances d'un système laser Ti:Sa à haute cadence optimisé pour la génération des impulsions attoseconde. Nous avons développé une nouvelle configuration de cavité régénérative fonctionnant à 10 kHz qui permet une meilleure gestion des effets thermiques dans le cristal. En sortie de l'amplificateur les impulsions atteignent des valeurs de puissance de 5 W en bande étroite (35 fs), ou 2.7 W en bande spectrale large permettant une compression des impulsions proche de 17 fs. La CEP des impulsions en sortie d'amplificateur a été stabilisée ; le bruit résiduel mesuré tir-à-tir est de 210 mrad pendant trois heures. L'amplificateur peut supporter également le fonctionnement en mode accordable, en sélectionnant des spectres de 30 à 40 nm de largeur à mi-hauteur et en accordant leur longueur d'onde centrale dans une gamme de 80 nm autour de 800 nm. Nous avons conçu et mis en fonctionnement un amplificateur multi-passages non-cryogéné à imagerie par lentille thermique pour accroître la puissance des impulsions jusqu'à 10 W à une cadence de 1 kHz. Le régime de forte saturation d'amplificateur garantit une variation négligeable (±3% pic à pic) de la puissance des impulsions en sortie du module, face à une variation importante de la puissance en entrée (±25% pic à pic) sur la bande spectrale accordable. L'amplification peut encore être plus importante grâce à une ligne d'amplification à refroidissement cryogénique, qui permet d'atteindre des puissances au niveau TW, à la cadence de 1 kHz, tout en maintenant un régime de courte durée (17.5 fs) et stabilité en CEP (350 mrad de bruit résiduel tir-à-tir). Nous proposons aussi une étude des sources de bruit de CEP dans les modules hautement dispersifs : nous avons conçu une nouvelle approche numérique sur la base d'un logiciel de tracé de rayon commercial (Zemax) pour évaluer les variations de CEP dans les modules contenant réseaux de diffraction.

Title : Development of an original 10 kHz Ti :Sa regenerative cavity allowing 17 fs CEP stable 1 kHz TW-class amplification or wavelength tunability

Keywords : Ultrafast lasers, CEP stabilization, spectral tunability, short pulse duration

Abstract: The last decade has seen a lot of progress in attosecond science or in strong field physics. Generating energetic, few-cycle laser pulses with stabilized Carrier-Envelope Phase at high repetition rate constitutes the first step to access the ultra-fast dynamics underlying the interaction of matter with intense, ultrashort coherent light source. The work of this thesis consists in globally improving the performances of a high repetition rate Ti:Sa laser system optimized for attosecond science. We present an original 10 kHz Ti:Sa CPA laser based on an newly-designed double-crystal cavity for thermal lensing management. The amplifier delivers up to 5 W in narrow band mode (35 fs pulses), or 2.7 W in broad band mode, supporting 17 fs pulses after temporal compression. We demonstrate shot-to-shot CEP stabilization with a remaining noise of 210 mrad over three hours at the front-end output. In parallel to the short pulse duration operation mode, it is possible to use the front end in a wavelength tunability mode within a 80 nm range around 800 nm, with a resolution of 1 nm and 30 to 40 nm of bandwidth. We designed and demonstrated a complete water-cooled lens-less multipass amplifier using thermal lensing for mode adaptation boosting the pulse energy up to 10mJ at 1 kHz repetition rate (up to 10 W). The saturation regime of the amplifier ensures negligible variation (±3% peak to peak) of the output power for significant variation of the input power (±25% peak to peak) over the tunability range. The energy scalability of the front-end is demonstrated by coupling its output to cryogenically cooled amplifier, delivering 1 kHz, TW-class pulses at 17.5 fs and CEP stabilized with a residual noise of 350 mrad. A study of CEP noise sources in high dispersive module is also addressed, proposing a numerical approach based on a commercial ray-tracing software (Zemax) for predicting CEP fluctuation in grating based modules.